ENHANCED DUCTILITY OF MASONRY SHEAR WALLS USING LATERALLY CONFINED (SELF-REINFORCED) CONCRETE BLOCK

ENHANCED DUCTILITY OF MASONRY SHEAR WALLS USING LATERALLY CONFINED (SELF-REINFORCED) CONCRETE BLOCK

By

MADELEINE PATRICIA JOYAL
B.Eng (McMaster University)

A Thesis Submitted to the School of Graduate Studies

in Partial Fulfilment of the Requirements for the Degree of

Master of Applied Science

McMaster University

MASTER OF APPLIED SCIENCE (2014) McMaster University

(CIVIL ENGINEERING) Hamilton, Ontario

Title: Enhanced Ductility of Masonry Shear Walls Using Laterally Confined (Self-Reinforced) Concrete Block

Author: Madeleine Joyal, B.Eng (McMaster University)

Advisors: Dr. M.J. Tait and Dr. R.G. Drysdale

Number of Pages: xvi, 165

ABSTRACT

The aim of the study presented in this dissertation was to investigate a new method of improving the ductility of masonry shear walls by means of confinement. This proprietary method, referred to as Self-Reinforced Concrete Block (SR Block) employs a previously untried technique of molding lateral confining devices into concrete block. This internal reinforcement provides lateral confinement to the enclosed volume of block and grout material. The resulting triaxial state of compressive stress under axial load allows the confined material to maintain high compressive capacity while undergoing high axial compressive strains. The results from a proof-of-concept program indicated improved plasticity due to the presence of the confining devices within the block. Despite spalling of the unconfined portions of the block at high strains, the SR Block specimens retained load carrying capacities in excess of the peak capacity of similar unreinforced/unconfined block prisms at strains beyond 2% with no visible damage to the confining devices or to the confined material. Further to this proof-of-concept study, an experimental program was undertaken involving additional prism tests as well as testing of shear walls constructed with the SR Block. This program proved the efficacy of a second confining device design in enabling prisms to retain compressive load capacity to strains over six times larger than that of standard grouted masonry. Additionally, the results of the shear wall program indicated that these desirable characteristics were effective in a wall configuration and led to significant increases in the displacement ductility of the walls when compared to similar, unconfined walls. The data presented is expected to serve as a basis for future testing and acceptance of SR Block as a method of increasing the compressive strain capacity of reinforced masonry in order to improve the ductility of masonry shear walls as a lateral force resisting system.

ACKNOWLEDGEMENTS

The research presented in this paper was funded by an I2I Grant from the Natural Science and Engineering Research Council (NSERC) of Canada. Financial support of the author by the NSERC CGS Master's Program and by the Ontario Graduate Scholarship (OGS) Program is gratefully acknowledged. Provision of mason time by the Ontario Masonry Contactors Association (OMCA) and the Canada Masonry Design Centre is appreciated. Block manufacture and time contributed by Paul Hargest and Boehmers Block is also appreciated.

I would like to acknowledge and thank my co-supervisors. Dr. Drysdale for his guidance and unwavering support, even across oceans, and for his taking an interest not only in this project but in my personal success. Dr. Tait for his faith in me from the outset and for his timely input and direction when I needed it most.

Credit for the completion of my experimental work must be shared. The help of my right hand man, Alexander Sciascetti, was invaluable and I cannot thank him enough for putting up with me day in and day out. Ian Blechta, who rounded out our lab team in the later stages of this research is also deserving of my utmost thanks. Of course, I would like to acknowledge the help of my friends and colleagues Omar El-Azizy, Niel Van Engelen and Brent Wybenga, all of whom lent a hand in the construction or testing of my specimens. Finally, the completion of my experimental work would not have been possible without the dynamic duo of the ADL, Kent Wheeler and Paul Heerema, who not only offered guidance and assistance, but also the antics and laughs that made my time in the lab a joy.

Thank you to my family for their support and encouragement, both in pursuing this degree and in my daily life. My final thanks is to Nick Smith, who was graciously on call anytime I needed an extra hand with construction or testing, and who provided editorial, intellectual and emotional support throughout the entirety of my degree program.

TABLE OF CONTENTS

LIST OF FIGURES

LIST OF TABLES

LIST OF SYMBOLS

A_n	average net cross-sectional area of block
A_R	height-to-length ratio (aspect ratio) of wall shear wall
A_s	area of reinforcing steel
A_{sp}	bar area of the hoop or spiral
d_{cd}	diameter of the centerline of confining device
d_s	diameter of hoop or spiral
f_1	maximum effective lateral confining stress
f'_1	lateral confining stress acting on concrete
f'_c	compressive strength of concrete (unconfined)
f'_{cc}	compressive strength of confined concrete
f'_{cm}	compressive strength of confined masonry
f'_m	compressive strength of masonry assemblage (unconfined)
f_y	yield strength of reinforcing steel
f_{yh}	yield strength of lateral confining steel
H	block height
h	height of a wall segment
h_p	assumed plastic hinge length
h_w	height of wall
k_1, k_2	empirical coefficients to describe the confined behaviour of concrete
K_e	confinement effectiveness coefficient (from Paulay and Priestley 1992)
l_w	length of wall
M_d	oven-dried block mass
M_i	immersed (buoyant) block mass
M_s	saturated block mass
P	axial load applied to wall
Q_u	ultimate lateral force resistance of wall
Q_y	lateral force resistance of wall at the first yielding of tension reinforcement
R_d	design force reduction factor relating to ductility
s_{cd}	spacing of lateral steel in confining device
s_h	longitudinal spacing of the hoops or spiral
T_{cf}	tension force in confining steel
V_m	shear strength of wall provided by axial loading and masonry strength
V_n	net volume of block
V_r	total shear strength of wall
V_s	shear strength of wall provided by shear reinforcement
Δ_C, Δ_T	increment of vertical displacement of wall segment under compression or tension
Δ_{Q_u}	lateral displacement of wall corresponding to ultimate load

$\Delta_{0.8Q_u}$ lateral displacement of wall corresponding to 20% decrease from ultimate load
Δ_u ultimate lateral displacement of wall
Δ_y lateral displacement of wall at the first yielding of tension reinforcement
Δ'_y ideal yield displacement of wall
ε_c compressive strain of concrete corresponding to compressive strength
ε_{cc} compressive strain of concrete corresponding to the confined compressive strength
ε_m compressive strain of masonry
ε_{mu} ultimate compressive strain of masonry
ε_s strain of steel reinforcement
ε_{sm} strain of steel at maximum tensile stress
$\mu_{\Delta Qu}$ displacement ductility (direct ratio) corresponding to ultimate load
$\mu_{1\%}$ displacement ductility (direct ratio) corresponding to 1% drift
$\mu_{\Delta 0.8Qu}$ displacement ductility (direct ratio) corresponding to 20% decrease from ultimate load
$\mu^{ep}_{\Delta 0.8Qu}$ idealized (elasto-plastic) displacement ductility
$\mu^{ep}_{\Delta u}$ idealized (elasto-plastic) displacement ductility (calculated using ultimate wall displacement)
ϕ average curvature of wall
ρ density of block
ρ_h horizontal steel reinforcement ratio in wall
ρ_{H_2O} density of water at room temperature
ρ_s volumetric ratio of confining steel
ρ_v vertical steel reinforcement ratio in wall
σ_1 longitudinal stress
σ_3 lateral stress originating from constant fluid pressure

DECLARATION OF ACADEMIC ACHIEVEMENT

This research encompasses experimental and analytical work carried out solely by Madeleine Joyal with advice and guidance provided by the academic supervisors Dr. Michael Tait and Dr. Robert Drysdale. Information that is presented from outside sources, which has been used towards analysis or discussion, has been cited when appropriate, all other materials are the sole work of the author.

CHAPTER 1

INTRODUCTION

1.1. Background

Until recently, reinforced masonry has been perceived as a form of construction having very limited ductility with correspondingly restricted applications in design for seismic loading. As a brittle material, masonry has generally been judged as unable to achieve comparable levels of ductility to other forms of construction including reinforced concrete and steel. However, standard reinforced concrete block construction adhering to easy-to-satisfy design and detailing requirements has recently been documented (Shedid 2006; Ahmadi Koutalan 2012; Banting 2013) to have much more ductility than previously credited in Canada and elsewhere. Nonetheless, there is potential for further improvements to provide even more enhanced seismic performance.

A major avenue to enhancing the ductility of reinforced masonry is to increase its capacity to withstand much higher compressive strains without significant loss of strength and to eliminate sudden brittle failure of the masonry. To this end, research reported in this thesis documents the development of the use of a new confinement method in concrete block construction.

Past work related to increasing the ductility of concrete masonry has focused on lateral confinement techniques which are external to the block. Confinement of this nature presents a number of limitations and challenges which have restricted the effectiveness and consequently the industry adoption of these techniques. Due to the geometry of concrete blocks, the area available for confinement is very limited. This reduces both the amount of confining material that may be used as well as the volume of concrete material that may be confined. Additionally, techniques which are external to the block rely on consistency of placement by a mason on-site, causing both an increase in labour time and the possibility of variations in quality due to construction tolerances. Also, confinement material in and around the block units can congest the already limited area present for grout flow and consolidation, which is another factor that can impact the quality of construction.

1.2. Objectives and Scope

The focus of this research was to investigate a new application of confinement in masonry construction in the form of Self-Reinforced Concrete Block (SR Block). This study follows some preliminary research (Toopchi-Nezhad et al. 2011a) which validated the concept and led to filing of a patent application (Toopchi-Nezhad et

al. 2011b). This new technique involved an untried method of molding steel confining devices into concrete block during the standard block manufacturing process. Following a proof-of-concept study, further objectives of this research were to optimize the block design, document the detailed behaviour of SR Block for implementation in industry applications, document the effects of the block on ductility in full scale shear wall tests, and test possible retrofitting procedures for the confined material to repair damage following an extreme loading event.

To test the concept of using SR Block under axial compressive loading and to optimize the prototype block design, the first part of this study involved prism testing documented in Chapters 2 and 3. As presented in Chapter 4, following selection of the optimum block design, the next stage of the study involved constructing a second complete set of prisms to test the effectiveness of a secondary design for the confining device within the SR Block. This series allowed not only the comparison of the behaviour of SR Block containing the new device design with that of standard block, but also a direct comparison between the performances of the two different confining devices under identical loading conditions.

The third part of this study, as presented in Chapter 5, was designed to test applications of the SR Block to improve the performance characteristics of concrete block shear walls. This research documented the results of three tests conducted on shear walls containing the SR Block. In Chapter 6, the behaviours and calculated ductilities of these walls were compared to one another as well as to a series of similar unconfined wall tests conducted previously at McMaster University. This allowed quantification of the behaviour induced by the inclusion of the SR Block in shear wall construction including increased lateral capacity and ductility.

1.3. Literature Review

1.3.1. Masonry Shear Wall Behaviour

A brief review of the flexural and shear behaviour of reinforced masonry shear walls is presented here; it pertains to the final phase of the reported research related directly to shear wall behaviour. Much of the research relating to structural masonry walls has focused on the behaviour of shear walls under in-plane loading and varying levels of axial load (Shedid 2009). This research has provided insight into flexural failure and shear failure mechanisms expected for reinforced masonry shear walls. Flexural behaviour of a shear wall is identified as more desirable as it results in a more ductile failure, exhibiting effective energy dissipation, and is simple to predict using flexural theory (Shedid, 2009). This type of behaviour is characterized by horizontal bed joint cracking and yielding of vertical steel, which extend to form a plastic hinging zone within which wall curvature is concentrated.

This is followed by crushing of the masonry and grout at the critical compression zone and eventual failure of the vertical reinforcement either in the form of buckling under compression or fracture under tension (Banting 2013).

Shear failure results from diagonal tension shear or sliding shear at the base and mortar bed joints (Shedid 2009). This potentially brittle failure mode involves much more rapid strength degradation as progressive damage along the shear interface reduces the mechanisms for force transfer. Shear forces are transferred by a combination of tension strength of the masonry (prior to cracking), aggregate interlock (increased by the application of axial load), and the presence of horizontal and vertical reinforcement (Shedid 2009). Failure under shear is characterized by the formation of diagonal cracks along the length of the wall which widen and can result in crushing of a diagonal strut in compression.

Combined shear-compression failures have also been observed in which a wall, upon reaching flexural strength and undergoing some inelastic deformation, experiences a shear failure mechanism due to the reduced ability of the damaged masonry to transfer shear forces (Banting 2013). Figure 1.1 displays the expected behaviour envelopes for each type of failure.

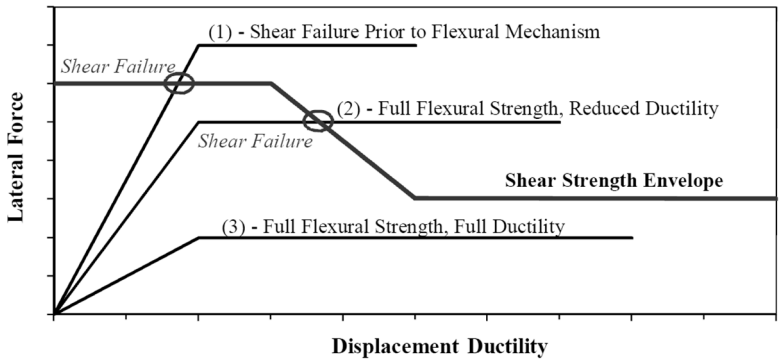

Figure 1.1. Shear, Flexural and Combined Failure Envelopes (from Banting 2013)

The performance of reinforced masonry shear walls has been thoroughly researched and the described expected behaviours are well established (Paulay & Priestley 1992). For this reason, this overview of reinforced masonry shear walls has been limited to the presentation of key aspects. A more thorough and detailed review of these established behaviours and failure mechanisms was presented by Banting (2013).

1.3.2. The Concept of Confinement

As reviewed below, previous research has demonstrated the beneficial effect of various types of confinement on the ductility and compressive strength capacity of

reinforced concrete and concrete block. The concept of confinement is well-established within engineering and is also applied in other disciplines for enhancement of desired properties. One simple example of this is in soil mechanics where the uniaxial loading properties of a soil are enhanced by the lateral confining pressure of the surrounding material. Confinement increases the bearing pressure of soils which "depend both on the undrained shear strength… and the lateral confining pressure of the surrounding soil." (Craig 2004) It is clear from this and many other examples that confinement and the resulting triaxial state of stress is a significant factor in the stress and strain characteristics of materials.

Specifically within the field of masonry construction, lateral reinforcement in the compression zone can serve to limit the lateral expansion of the masonry materials which is associated with failure under uniaxial compression. As lateral expansion occurs under axial compression, the lateral reinforcement resists and limits the expansion resulting in a triaxial compression state of stress in the confined material. As is well documented (MacGregor & Wight 2004), a triaxial compression state of stress leads to an increase in axial capacity as well as an increase in the ultimate strain achievable while maintaining this capacity. Tests on concrete cylinders subjected to a constant lateral fluid pressure with increasing longitudinal stress suggested that the longitudinal stress at failure could be represented by the following empirical equation (MacGregor & Wight 2004).

$$\sigma_1 = f'_c + 4.1\sigma_3 \tag{1.1}$$

These property improvements consisting of increased axial strength and increased axial strain capacity are especially important in the compression zones of shear walls and can lead to increased ductility of the element. An additional advantage of confinement within these compression zones is the provision of support for the vertical reinforcement resulting in delay or prevention of buckling and increased strength and stability. The following literature review summarizes past research relating to increasing the ductility of concrete masonry by use of various confinement techniques.

1.3.3. Behaviour of Unconfined and Confined Concrete

The precedent for improving the structural characteristics of a brittle material by use of confinement stems from extensive research in the fields of soils and reinforced concrete. In unconfined concrete columns, failure is generally characterized by the splitting and crushing of concrete followed by the buckling of longitudinal reinforcement in the absence of lateral support (MacGregor & Wight 2004). It is well accepted that confinement in the form of ties, hoops or spirals has a significant effect on the axial capacity and ductility of reinforced concrete

columns and, as such, requirements to ensure ductility in this manner appear in codes such as in Clause 7.6 of CSA A23.3 (CSA 2004b). Studies by Mander et al. (1988a) examined the behaviour of axially loaded concrete columns and wall sections to observe the effects of the spacing and configuration of transverse reinforcement. These tests concluded that the most significant parameter affecting the extent of confinement is the quantity of confining reinforcement provided, as defined by the spacing of confining elements. The effectiveness of confining reinforcement is also largely dependent on the configuration of reinforcement. Square ties are a less effective form of confinement than circular or spiral ties as there can be significant sections of unsupported length between longitudinal bars in a square/rectangle configuration that allow for dilation of the core concrete in these areas. Figure 1.2 illustrates this concept along with the effect of spacing of confinement reinforcement. Furthermore, studies by Sheikh and Toklucu (1993) compared the behaviour of hoop and spiral reinforcement patterns and concluded that, while the behaviour of the two configurations is generally comparable, hoops may be more effective under extreme strains because the rupture of one hoop has no effect on the integrity of adjacent hoops while a fracture at any point in a spiral is detrimental to the spiral structure as a whole.

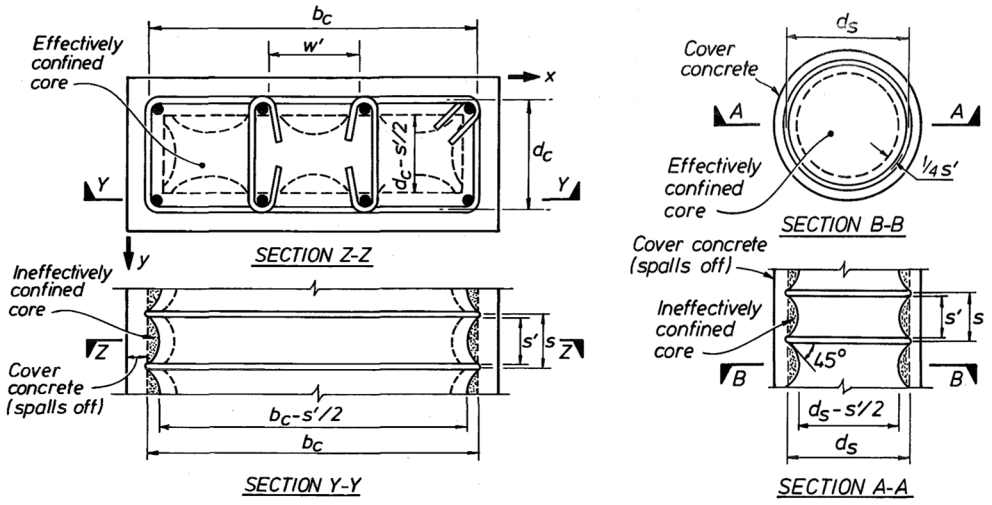

Figure 1.2. Effectively Confined Core of Rectangular and Circular Reinforcement (from Mander et al. 1988b)

1.3.4. Overview of Confined Concrete Masonry

Like concrete, grouted masonry assemblages constitute a very brittle construction material. Failure under compressive loads is defined as a combined tension-compression failure in which lateral expansion of the mortar and grout under compression leads to tensile splitting of the block face shells and compression-tension failure of the unconfined grout cores (Drysdale & Hamid 2005). In

reinforced specimens, this failure is accompanied by a subsequent buckling of vertical reinforcement. Confinement in masonry to restrict lateral expansion and prevent these brittle failure mechanisms has been the subject of various tests and trials but without the corresponding widespread implementation present in the reinforced concrete industry. This is due to the limitations associated with block construction which restrict the space that can be employed for reinforcement. Past work relating to increasing the ductility of concrete masonry using confinement has focused on techniques which are external to the block.

1.3.4.1. Bed Joint Confinement Techniques

The first accepted methods of confining masonry assemblages involved confinement placed within the bed joint mortar to laterally support the block concrete and delay splitting. While it was Scrivener (1972) who originally recognized the advantages of confining bed joints to reduce the lateral expansion of mortar, Priestly and Bridgeman (1974) were the first to produce consistently positive results from confinement in the form of what has become known as a Priestly Plate. This confinement plate, depicted in Figure 1.3 is formed from a 3 mm thick stainless (or galvanized) steel plate with dimensions corresponding to block size, small holes to facilitate mortar bonding, and larger holes corresponding to block cells to accommodate vertical reinforcement and grout placement. The plate is designed to restrict not only lateral expansion of the bed joint mortar in order to reduce vertical splitting pressure on the block concrete but also the natural lateral expansion of the block under compression. Additionally, it provides support against the buckling of vertical compression steel grouted into the cells of the block.

Various forms of bed joint reinforcement, including the Priestly Plate, were tested by Hart et al. (1988). As shown in Figure 1.3, these included a closed wire mesh which, with similar aims to the Priestly Plate, provides confinement not only to the mortar but also to the grout column. A second, open wire mesh (confining comb) was also tested which provides confinement without requiring threading of devices over longitudinal reinforcement, thereby increasing ease of construction.

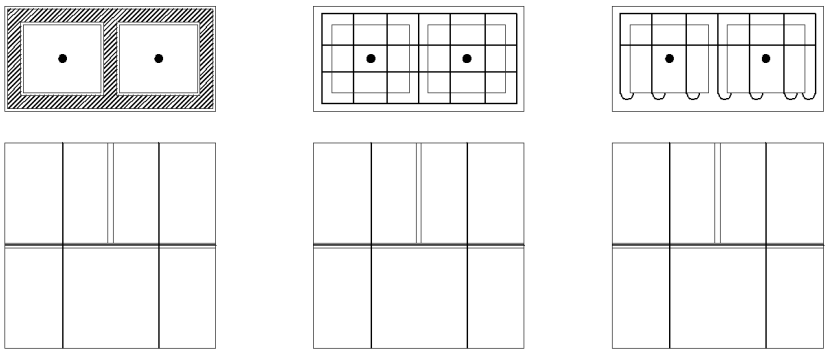

Figure 1.3. Bed Joint Confinement Techniques (redrawn from Hart et al. (1988))

1.3.4.2. In-Cell Confinement Techniques

One of the limitations of using bed joint reinforcement for confinement is the restricted spacing of the confining reinforcement. As has been observed in reinforced concrete, spacing is an important factor in the effectiveness of confinement; with bed joint reinforcement, spacing is dictated by block height. One proposed solution to this was to introduce confinement reinforcement within the cells of the concrete block. The study by Hart et al. (1988) compared the following four different in-cell confinement techniques (illustrated in Figure 1.4):

- Square steel ties equivalent to the minimum confinement reinforcement required by the 1988 UBC for masonry (#3 bars (9.5 mm diameter) at 8" (203 mm) spacing)
- Cage (hoop) reinforcement
- Spiral reinforcement
- Cage (spiral) reinforcement

Prisms made with each type of confinement were tested under axial compression. The intent was to provide reinforcement within the grout column similar to that of a confined reinforced concrete column. These confinement methods in block assemblages, however, differed from those in reinforced concrete in several respects. First, in using traditional block molds, the open space within each cell is very limited which, in turn, limits the volume of grout that can be confined. This leaves more than 50% of the cross-sectional area unconfined and subject to spalling under compressive loads. Additionally, in typical running-bond construction with standard concrete blocks, the block cells do not align from course to course. This forces in-cell confined grout to also be offset from course to course and does not result in a fully continuous cross sectional area of the confined grout column. This issue was raised by Paturova (2006) who recommended that a new configuration of

blocks be adopted for confinement to avoid this offset problem. Finally, researchers testing these types of confinement have reported that the presence of in-cell confinement can decrease the quality of the grouted columns due to improper grout consolidation in the congested space around the device (Paturova 2006). This introduction of unexpected voids has led to lower compressive capacities of the grouted assemblage.

Another form of in-cell confinement that has been tested is the use of fibre reinforcement in the grout. While this method does not alleviate the problem of vertical alignment within the grout column, it eases grout placement and, therefore, grout consolidation can be more easily assured. A blend of two polymers: polypropylene and polyethylene, was tested at Washington State University (Hervillard 2005) to increase the ductility of the grout concrete. Tests revealed that use of the fibres was effective in increasing peak stress and in increasing strain at the point of 50% reduction of stress following the peak but the results were highly dependent on the amount of fibres present in the grout mix.

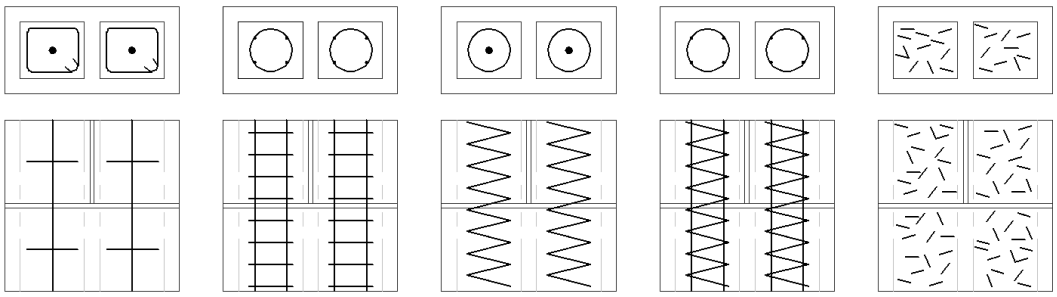

Figure 1.4. In-Cell Confinement Techniques
(redrawn from Hart et al. (1988) and Hervillard (2005))

1.3.5. Performance under Axial Compression

As described above, prism tests conducted by Hart et al. (1988) documented the effects of different types of bed joint and in-cell confinement methods under concentric axial compression. Based on results for each confinement type as reproduced in Figure 1.5, they defined a typical confined concrete masonry stress-strain curve as shown in Figure 1.6 (a). The study concluded that all confinement types, while having a negligible effect on the ascending portion of the stress-strain curve, had a positive effect of the descending (post-peak) portion of the curve, thereby increasing the area under the curve which is representative of the energy stored. The study also concluded that the Priestly Plate was the most effective confining method of all of the tested techniques. Tests by Hervillard (2005) compared performance of fibre reinforced masonry to other confinement

techniques and concluded that performance improvements attributed to the fibres were less effective than those previously reported for techniques such as steel plates and meshes.

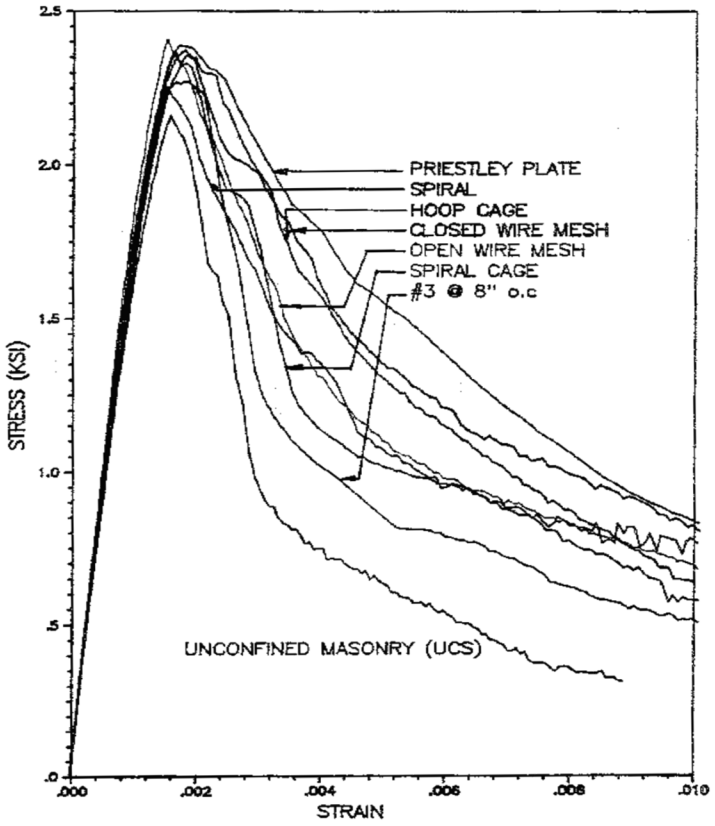

Figure 1.5. Stress-Strain Curves for Unconfined and Confined Prism Tests (from Hart et al. 1988)

For comparison purposes a representative confined concrete stress-strain curve is presented in Figure 1.6 (b). As can be seen, confinement in reinforced concrete is able to induce much higher ductility than the restricted techniques presented to date in masonry research as reported above. This is due to the limitations expressed above with respect to the confinement of concrete masonry. Restrictions on the spacing of confining elements and/or on the volume of material that may be confined in concrete block construction limit the effectiveness of confinement and therefore the achievable ductility when compared to that of reinforced concrete.

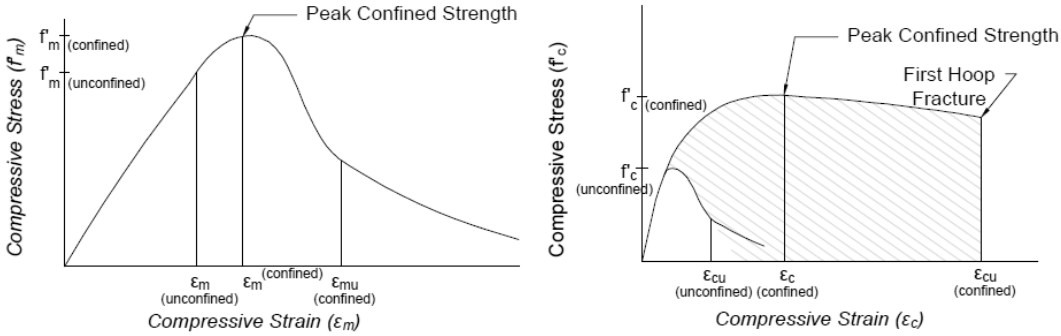

a) Confined concrete block
(redrawn from Hart et al. 1988)

b) Confined Concrete
(redrawn from Mander et al. 1988b)

Figure 1.6. Idealized Compressive Stress-Strain Curves

Conclusions related to the effect of confinement on strength and strain values in the field of reinforced concrete have been found in some cases to apply well to masonry applications (Hervillard 2005). Historically (Mander et al. 1988b), basic equations for confined concrete strength and strain based on the strength of unconfined concrete and the lateral pressure of the confinement formed the basis for confinement calculations and are presented as:

$$f'_{cc} = f'_c + k_1 f_1 \tag{1.2}$$

$$\varepsilon_{cc} = \varepsilon_c [1 + k_2 (f_1 / f'_c)] \tag{1.3}$$

Where f'_{cc} is the enhanced or confined concrete strength
ε_{cc} is the strain corresponding to f'_{cc}
f_1 is the lateral confining pressure
f'_c is the equivalent, unconfined concrete strength
ε_c is the strain corresponding to f'_c

These equations represented strength and corresponding longitudinal strain of concrete confined laterally in an active manner by fluid pressure. Richart et al. (1929) showed that passive confinement pressure from steel spirals produced a lateral pressure equivalent to this active fluid pressure and empirically defined the coefficients k_1 and k_2 as 4.1 and $5k_1$, respectively. Paulay and Priestly (1992) and Mander et al. (1988b) defined a series of equations for circular/spiral reinforced concrete in the form of the above basic equations but with the coefficients derived from a more fundamental basis as presented below.

The maximum effective lateral pressure (f_1) provided by the confinement is:

$$f_1 = \frac{2f_{yh}A_{sp}}{d_s s_h} \tag{1.4}$$

Where d_s is the diameter of the hoop or spiral
A_{sp} is the bar area of the hoop or spiral
s_h is the longitudinal spacing of the hoops or spiral
f_{yh} is the yield strength of the confining steel

The confining stress on the concrete (f'_1) is then given by:

$$f'_1 = K_e f_1 \tag{1.5}$$

Where K_e is a confinement effectiveness coefficient (typically 0.95 for circular confinement)

The compression strength (f'_{cc}) and corresponding strain (ε_{cc}) of the confined circular sections are:

$$f'_{cc} = -1.254f'_c + 2.254\sqrt{f'^2_c + 7.94f'_c f'_1} - 2f'_1 \tag{1.6}$$

$$\varepsilon_{cc} = 0.002[1 + 5(f'_{cc}/f'_c - 1)] \tag{1.7}$$

Where f'_c is the strength of the unconfined concrete

And a conservative, empirical estimate for the ultimate compressive strain (ε_{cu}) is:

$$\varepsilon_{cu} = 0.004 + 1.4\rho_s f_{yh}\,\varepsilon_{sm}/f'_{cc} \tag{1.8}$$

Where ε_{sm} is the steel strain at maximum tensile stress
ρ_s is the volumetric ratio of confining steel

Further to these empirical relationships, Kent and Park (1971) derived a more complex model which was adapted to square concrete columns and then to masonry applications by Priestley and Elder (1983) in a form which had good results for confinement in the form of bed-joint plates. However, the concrete models were expected to be the most applicable to this study due to the nature of confinement being investigated.

1.3.6. Confined Wall Systems

In addition to confinement on a unit-by-unit or course-by-course basis in masonry assemblages, some recent research has investigated confinement at the element level. Shear walls confined by flanges and boundary elements have been a focus of study at McMaster University for enhancing the seismic performance of masonry shear walls.

One of the undesirable potential failure mechanisms of reinforced concrete block shear walls is out-of-plane movement or buckling of vertical reinforcing bars in compression. This instability of the compression zone is due to the crushing of end concrete and the presence of only one, untied vertical bar in the extreme compression cell. In reinforced concrete shear walls, end regions that contain two or more parallel layers of vertical bars within closed ties exhibit much higher stability and ductility. As this configuration may be impractical within the construction limitations associated with a single concrete block, the addition of an element connected to the end of a wall can serve to provide this level of confinement in an easily constructed manner.

Three types of end-confinement were investigated and compared by Shedid (2009). The first, a flanged wall (as depicted in Figure 1.7) occurs naturally in building construction if intersecting structural walls are tied together. This link allows a perpendicular wall flange to contribute to the compression zone of what would otherwise be a rectangular wall. For the second and third types of end-confinement, the two types of boundary elements illustrated in Figure 1.7, involve construction of a confined zone with increased thickness at the end of a wall. All three of these methods provide multiple layers of vertical bars in parallel within the compression zone which leads to increased stability. In the boundary element configurations, the tied vertical bars form a reinforcing cage within which the masonry material remains reasonably intact. This material maintains support for the vertical bars throughout loading, resisting buckling and further increasing stability.

With the presence of each of these types of end confinement, the length of the compression zone decreases due to the greater thickness which in turn leads to increased curvature at peak capacity. Increases in maximum curvature result in increased displacement ductility of the wall.

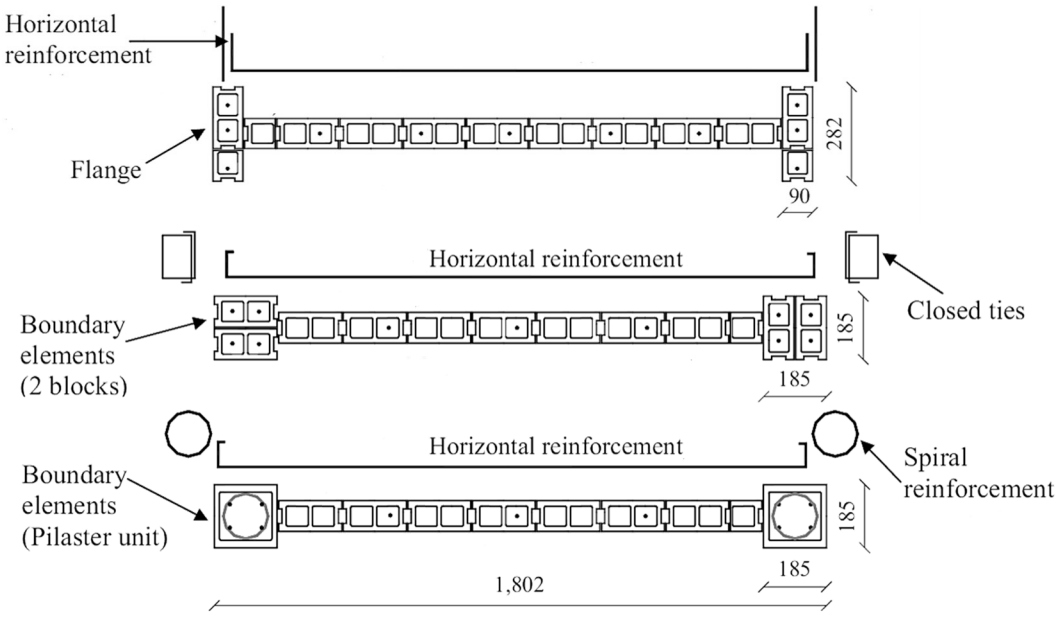

Figure 1.7. End-Confined Wall Configurations (from Shedid 2010)

1.3.7. Shear Wall Performance

The behaviour of shear walls with different forms of confinement has been compared in two theses referenced below. Sajjad (1990) at the University of California investigated the effects of three types of confinement: a cage (hoop) reinforcement equivalent to the minimum confinement reinforcement required by the 1988 UBC but in a supported configuration, a confining comb, and a spiral cage reinforcement. The results from three walls (one with each confinement technique employed throughout the wall) were compared to results for a similar wall without confinement. All four walls had identical properties including: vertical reinforcement ratio, horizontal reinforcement ratio, dimensions (aspect ratio of 1) and applied axial load. The results of the tests, summarized in Table 1.1, along with hysteresis loops for each wall, allowed Sajjad (1990) to draw the following conclusions:

- "The confined walls demonstrated superior performance at the Maximum Load Limit State and the load corresponding to the maximum drift ratio [over that of] the unconfined walls."
- "The maximum load at the Maximum Load Limit State increases by 6% to 14% for confined walls when compared to the unconfined wall." (Wherein "the Maximum Load Limit State exists when the strain in concrete masonry in the extreme compression fibre is equal to the maximum usable strain.")
- "The drift ratio associated with the maximum load increased by about 60%, on average, for the confined walls as compared to the unconfined wall."

- "Similarly, the maximum drift ratio [for the confined walls] increased by up to 123% over the unconfined wall."
- "It was shown that by providing confinement in a concrete masonry wall, its ability to sustain high drift ratio levels is improved remarkably."

Table 1.1. Results from Testing of Unconfined and Confined Shear Walls (from Sajjad 1990)

		Unconfined Wall	**Confined Walls**		
			Hoops Spaced at 8" (supported)	**Confining Comb**	**Spiral Cage**
Ratio of Confinement Reinforcement (volumetric)		-	0.0042	0.0022	0.0029
Max Force (kN)	Mean	352.7	374.1	403.0	374.5
	Ratio to Unconfined	1.00	1.06	1.14	1.06
Drift (%) at Maximum Force	Mean	0.73	1.22	1.16	1.20
	Ratio to Unconfined	1.00	1.66	1.58	1.64
Force (kN) at Maximum Drift	Mean	181.9	165.0	338.5	230.0
	Ratio to Unconfined	1.00	0.91	1.86	1.26
Maximum Drift (%)	Mean	1.17	1.70	2.15	2.61
	Ratio to Unconfined	1.00	1.45	1.83	2.24

A more recent study by Shedid (2009) at McMaster University included tests of a set of four equivalent walls to compare the effects of confining elements connected to wall ends. These tests included a flanged wall, a wall with two-block boundary elements and a wall with pilaster boundary elements (see Figure 1.7), all with identical reinforcement ratios and overall dimensions, and a fourth, unconfined wall in which the vertical reinforcement ratio was doubled in an attempt to achieve consistent peak loads with each test. All of the walls were constructed of half-scale blocks, had an aspect ratio of 1.5, and were subjected to identical axial loading. The data from these wall tests, presented in Table 1.2, led Shedid (2010) to conclude the following:

- "The ductilities of the proposed flanged and end-confined masonry walls were at least 39 and 106% higher than that of the rectangular walls having the same properties."
- "Drifts at 20% strength degradation were at least 1.0, 1.5, and 2.0% corresponding to the rectangular, flanged, and end-confined walls, respectively."
- "The test results showed that all the walls tested within each phase had almost the same capacity and the same elastic stiffness when subjected to

the same axial loads… [despite] a saving of more than 40% in amount of vertical reinforcement [in the end-confined walls].” This is as a result of the increased presence of longitudinal steel at farther distance from the neutral axis as well as additional compressive strength present in the end-confining elements.

Table 1.2. Results from Testing of Unconfined and End-Confined Shear Walls (from Shedid 2010)

		Unconfined Wall	**Confined Walls**		
			Flanged	**Two-Block Boundary Element**	**Pilaster Boundary Element**
Max Force (kN)	Mean	266	242	238	238
Drift at Maximum Force	Mean	0.50	0.75	0.91	0.76
	Ratio to Unconfined	1.00	1.50	1.82	1.52
Drift at 20% Strength Degradation	Mean	1.04	1.64	2.05	2.42
	Ratio to Unconfined	1.00	1.58	1.97	2.33
Displacement Ductility (idealized elastic-plastic)		4.8	6.6	9.8	9.7

It is evident from the results of both of the aforementioned studies that providing confinement in shear walls results in significant improvements in the wall performance under lateral loading. All forms of confinement tested led to an increase in the maximum lateral load capacities of the shear walls over unconfined counterparts. Additionally, the ultimate displacement and therefore the ductility capacity of each confined wall configuration tested in these studies exceeded that of the similar unconfined walls by a significant margin (generally an increase of over 100% in ultimate displacement).

1.3.8. Design Code Provisions

While the use of confinement has significant coverage in design codes for reinforced concrete, its presence is minor or nonexistent in current masonry design codes. In the past, the Uniform Building Code (ICBO 1997) stated minimum size and spacing requirements for in-cell stirrups (as tested by Hart et al. (1988)) to provide confinement allowing for compressive masonry strains up to 0.006. However, when the UBC (ICBO 1997) was abandoned in 2000 in favour of the IBC (ICC 2000), the specifications were removed and the MSJC (2011) opted to leave the responsibility of selecting and detailing an appropriate confinement technique to the designer. Presently, the only remaining specification for a particular confinement technique is in the New Zealand masonry design code

(SANZ, 2004) which allows for compressive masonry strains up to 0.008 in ductile walls with the use of confinement plates.

Both the American (MSJC 2011) and Canadian (CSA Draft Standard for Public Review, CSA S304-14 Design of Masonry Structures (CSA 2014)) masonry design provisions provide the designer with an option to increase the ultimate compression strain of concrete masonry construction above the current code ultimate, $\varepsilon_{mu} = 0.0025$, in shear wall design if confinement is provided. However, without the provision of specific guidelines relating to acceptability of certain types of confinement, the designer is left with the responsibility of proving the effectiveness of the method used. In Clauses 3.3.6.5.3 and 3.3.6.5.4, the MSJC (2011) states that confinement is required at all edges and around openings in shear walls if the extreme fibre compressive strain at the critical section exceeds ε_{mu} or if extreme fibre compressive stress corresponding to factored forces exceeds $0.2f'_m$. Information in Clause 3.3.6.5.5 and accompanying commentary explains that "unlike in the case of concrete where prescriptive detailing require[ments] for the specially confined boundary element are given, this Code requires that testing be done to verify that the detailing provided shall be capable of developing a strain in excess of the maximum imposed strain." (MSJC 2011) Additionally, the commentary advises that "It is hoped that reasonably extensive tests will be conducted in the near future, leading to the development of prescriptive detailing requirements for specially confined boundary elements of … reinforced masonry shear walls." (MSJC 2011).

CSA S304 (CSA 2014) has recently adopted a similar philosophy, introducing within the moderately ductile and ductile wall provisions, a clause (16.10.2) relating to confinement of masonry which allows ε_{mu} to be taken as greater than 0.0025 (up to a maximum of 0.008) in cases where the walls are detailed to develop the increased compressive strain capacity. These include cases where a tied boundary element is provided, or where "any other technique which can be shown through testing and analysis to satisfy the necessary requirements for the specified level of strain and required ductility capacity of the wall" (CSA 2014) is provided. Both this and the MSJC clauses enable the implementation of proven confinement techniques for improved stress and strain properties in the design of shear walls.

1.4. Closure

This review focused on the methods and effectiveness of confinement to improve the ductility of masonry construction for enhanced seismic performance. From the research presented, it is evident that many different forms of confinement have been tested with masonry assemblages with varying degrees of positive result. All forms

of confinement were able to effect some increase in the axial load capacity as well as an increase in the ultimate compressive strain of the masonry. Finally, when applied at an element level (shear walls), confinement has resulted in an increase in displacement ductility and therefore an improvement of the overall seismic performance of masonry.

While confinement has been shown to have obvious benefits for improved ductility, there is room for development of improved forms of confinement for concrete masonry. Additionally, there is currently a need in both the MSJC (2011) and the CSA S304 (CSA 2014) design codes to prove that enhanced strain and other aspects of behaviour can be achieved. Research in this area can provide proof that would lead to easier-to-use, specific requirements in these design standards in the future, eliminating the burden currently on the designer to provide these proofs.

The object of the study documented in this thesis was to achieve the results expected of confined reinforced concrete construction in concrete block construction using a proprietary method referred to as SR Block. Preliminary test data from this study was presented previously in two conference papers (Joyal et al. 2013; Sciascetti et al. 2013). A total of three test programs will be presented herein, each designed to test a different aspect or application of SR Block under specific loading conditions.

CHAPTER 2

PROOF-OF-CONCEPT PROGRAM FOR SELF-REINFORCED CONCRETE BLOCK

2.1. Introduction

The experimental program presented in this chapter was designed to serve as a proof-of-concept for using confining devices, which are molded into concrete block to provide increased ductility. This concept has been named Self-Reinforced Block (SR Block). As an extension of this proof, the program was designed to provide directly useable information regarding the extent to which the proposed method of confining a portion of concrete block provides enhancement of the desired properties; namely retained capacity and improved ductility. For this proof-of-concept stage, it was decided that tests of concrete block prisms under axial compression would best serve this purpose as this would provide uniform compression conditions. This eliminated the potential for the fundamental effects of the confining device to be obscured by other factors such as might be the case if shear walls were constructed for the initial testing. The program included testing of both prototype specimens and standard specimens in order that the effect of the confining devices could be isolated and compared to traditional construction.

To minimize the potential effects of platen constraint and the need to try to account for height-to-thickness ratio effect, four-block high prisms were chosen. Although two-course prisms (height-to-thickness ratio of 2:1) are the standard test method prescribed by the MSJC for obtaining masonry assemblage strength f'_m (MSJC 2011), past research at McMaster University has identified that two-course prisms do not produce a failure mode resembling that in full-scale masonry walls and that the "end effects significantly affect the state of stress in the prism" (Chahine 1989; Liu 2012). Chahine's research found that four-course prisms (height-to-thickness ratio of 4:1) gave more representative strengths and failure mechanisms and could "more directly and reasonably be related to full-scale walls" (Chahine 1989). For this reason, the results from the four-block high prisms tested are presented without scaling and it is expected that the data can be applied directly in developing design criteria.

2.2. Design and Manufacture of SR Block

2.2.1. Design and Manufacture of Confining Devices

Drawing from previous research related to confinement in concrete columns (MacGregor & Wight 2004; Mander et al. 1988a), the most effective shape for confinement was determined to be a circular device running the height of the block. Figure 2.1 illustrates the equilibrium conditions for a semi-circular segment of a confining device under tension resulting from the outward pressure from lateral expansion of the confined concrete block, mortar and grout encased within the confining device. For use of individual confining devices around each of the two cells in a 20 cm hollow concrete block, a circular shape is efficient in terms of satisfying minimum cover requirements and confining a large part of the block. This condition coincides with use of 20 cm block in the vast majority of concrete block construction; the application to other block sizes will be discussed in the final chapter of this thesis.

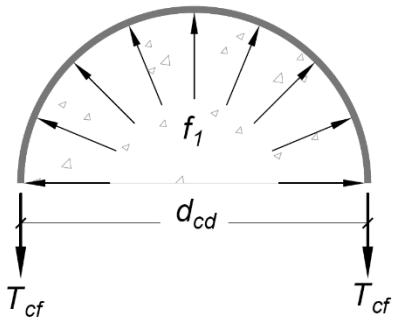

Figure 2.1. Equilibrium of Forces Acting on a Confining Hoop/Spiral

In running bond construction, for ideally confined conditions, the objective was to form semi-continuous columns of confined material over several courses of block. As blocks are manufactured as independent units, the mortar, block, and grout in the local region of the mortar bed joints depend on the near proximity of devices above and below for confinement. A 6 mm clearance from the top of the block to the confining device was chosen to allow a 6 mm notch to be formed in the block webs which, when combined with the 10 mm mortar bed joint, permits positioning of up to 10 mm nominal diameter horizontal reinforcement (shear reinforcement) in walls. For this proof-of-concept study, the selected confining devices were fabricated from 2.90 mm thick sheet steel with 19.1 mm square punched holes spaced at 25.4 mm on centre in both directions. This provided strips with a width of 6.3 mm on all sides of the punched holes.

With these dimensions, the resulting steel area of each lateral strip ($A_s = 6.3\text{ mm } x\ 2.9\text{ mm} = 18.3\text{ mm}^2$), was expected to provide a confining force

of $T_{cf} = A_s f_y = 7.3$ kN for an assumed 400 MPa steel yield stress. Referring to Figure 2.1, the corresponding maximum effective lateral confining pressure, f_1, is then dependent on the diameter of the device, d_{cd}, and the spacing, s_{cd} of each strip and is expressed as $f_1 = 2T_{cf}/(d_{cd}s_{cd}) = 3.5$ MPa where the diameter of the centerline of the device, d_{cd}, is taken as 164 mm and the spacing, s_{cd}, is 25.4 mm as mentioned above. From research on confinement of concrete, the strength of the confined material could then be empirically estimated (MacGregor & Wight 2004; Mander et al. 1988b) as $f'_{cm} = f'_m + 4.1f'_1 = f'_m + 14.4$ MPa. This would double an original uniaxial strength, f'_m, of 14.4 MPa which was within the range of expected uniaxial strength for unconfined masonry. On the basis of this calculation and considering that material outside of the confined region would spall away at high strains, to maintain the original compressive capacity of the block assembly, it was apparent that the cross-sectional area of the remaining confined material should exceed 50% of the original total area of the block. This was achieved with a device diameter of 164 mm, which resulted in a confined area equal to 57% of the original gross area of the block.

The sheets of punched confining device material were cut to a height of 184 mm, allowing 6 mm of clearance at the top of the 190 mm high finished block. The 514 mm long punched sheet was wrapped into a tubular shape with an outside diameter of 167 mm and the tube was welded along the abutting vertical end strips to complete manufacture of the confining device shown in Figure 2.2. The horizontal strips of the device provided the desired confining hoops while the vertical strips provided stiffness to the cage in the vertical direction to prevent collapse during compaction of concrete in the mold during block manufacture. The openings in the cage between strips were maximized to enhance concrete filling of the block mold and to facilitate bond between the outer concrete and the enclosed concrete. As discussed above, the size of the strips was chosen to ensure that the high strain compressive capacity of the confined volume would equal or exceed the capacity of similar unreinforced/unconfined block masonry.

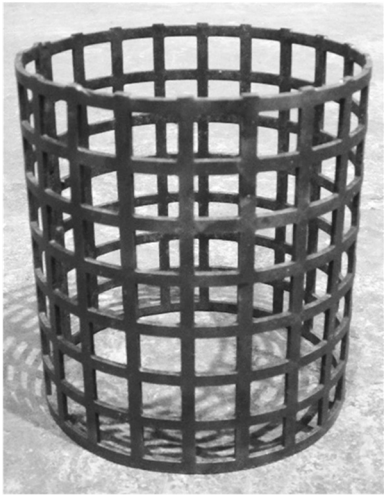

Figure 2.2. Confining Device

2.2.2. Block Design and Manufacture

To increase the effectiveness of the confining device by maximizing the volume of enclosed concrete, it was necessary to fit the largest possible cylindrical confining device around each block cell while leaving sufficient clearance inside and outside of the device to facilitate placement and compaction of the zero slump concrete used in block manufacture. For the first trials conducted in the block plant, a prototype block with small circular cells was used to maximize space between the confining device and the cell (core) part of the block mold to help ensure complete filling of the mold and proper embedment of the device within the finished block. Using a standard 20 cm splitter block mold (190 mm x 190 mm x 390 mm), in the first trials, mold inserts were machined to create 101.6 mm diameter cylindrical cells to replace the more traditional tapered, pear-shaped cells.

After the above trial confirmed that placement and compaction of the zero slump concrete did not present a significant problem, a new prototype block with larger, nearly circular cells was adopted in order to reduce the block mass to the range of traditional hollow block and increase the cell size for ease of placement of reinforcement and grout. For this block, new mold inserts were machined to create 152.4 mm diameter cells with flattened sides as depicted in Figure 2.3. The objective was to minimize block weight and have the block look as nearly as possible like a standard two-cell block while maximizing the volume of confined material. The flattened sides of the cell were introduced to produce a minimum 30 mm face shell thickness to satisfy the requirements of CSA A165.1 (CSA 2004d).

The cells were positioned to ensure their vertical alignment in a running bond pattern so that the confined volume would provide a straight member after spalling

of the outer shell. However, adjustments to the mold during the block plant trials caused some minor misalignment of the cells which resulted in an approximately 5 mm offset of the cells in some prisms in this proof-of-concept part of the research program.

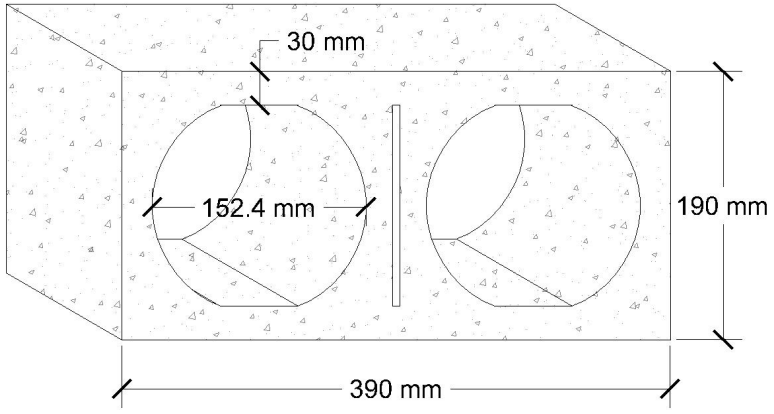

Figure 2.3. Prototype Block Design

Manufacture of the SR Block and similar block without confining devices was performed in an automated plant used for commercial mass production. The production line, using a "Besser" block machine, compacts a zero-slump concrete into three block molds during each cycle as shown in Figure 2.4 a). For this study, a prototype block (of either cell size) with or without confining devices, a standard splitter, and a standard hollow stretcher unit were produced in each cycle to ensure consistent concrete and compaction properties for test comparisons. To manufacture the SR Blocks, the production line was paused to allow manual centering of the confining devices on the base plate beneath the prototype mold. After positioning, the manufacturing process was resumed and the base plate was raised into position under the mold, which was then filled with concrete and vibrated for compaction.

To check that the concrete was being properly compacted and that no voids were created around the confining device, in the first production runs, the device was exposed by removing portions of the face-shell concrete to permit visual inspection of some trial blocks. As shown in Figure 2.4 b), filling of the mold and compaction of the concrete was complete; the confining device was not deformed during the manufacturing process. This block production trial indicated that, with some streamlining involving automated positioning of the confining devices, mass production of SR Block is feasible with existing manufacturing processes.

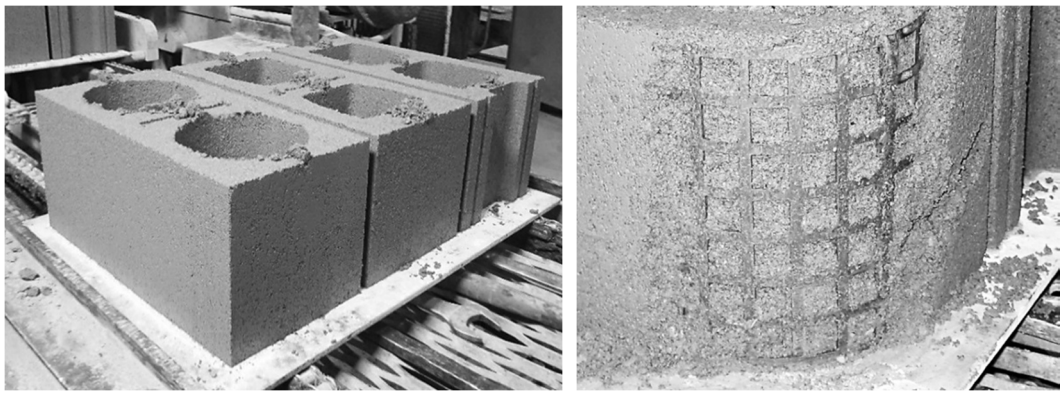

a) Three Block Types Produced in One Manufacturing Cycle

b) Confining Device Exposed by Removal of Compacted Exterior Concrete

Figure 2.4. SR Block Manufacturing

2.3. Design and Construction of Test Prisms

2.3.1. Design of the Test Program

To document the effect of the confining device, it was necessary to perform similar prism tests using comparable unconfined block manufactured in parallel with the SR Block. This avoided the potential of having to try to account for influences of variations in material properties, construction and test procedure. To create a broad basis for comparisons, a test program totalling 51 prisms was divided into various series to include standard and prototype units in both ungrouted and grouted states as shown in Table 2.1. This allowed for direct comparison of results for the new prototype block types with results using existing standard block. Within the category of prototype block, Type I had 101.6 mm diameter cells and Type II had 152.4 mm diameter cells. Of central interest was comparison of the grouted prism compression behaviour using block with and without the confining devices. At least three test repetitions were required for each series to enable statistical comparisons and, where possible for the more important series, five repetitions were planned for improved confidence.

As part of the program, seven prisms built with the confined prototype Type II block were grouted using two different compositions of anti-shrink grout in an attempt to reduce the anticipated vertical strain required to engage the lateral confining effect of the devices where it was postulated that shrinkage could result in a small gap between the grout and the block concrete or in residual tension forces in the grout. Also, this exercise was, in part, introduced to try to take advantage of strength increases for grout filled masonry observed when effects of grout shrinkage were reduced (Steadman et al. 1995).

As a logical requirement, the ability to repair damaged construction after a major earthquake should be an important consideration in choosing the type of ductility producing system and the degree of damage that is acceptable. Documents such as FEMA 308 (ATC 1999) provide repair guides for concrete and masonry walls following earthquake induced damage. One applicable repair category in this publication is that of structural repairs which "address component damage directly with intent to restore structural properties" (ATC 1999). This includes specific guidelines for repair of structural spalling such as was the observed damage mode for prisms in this program. To fulfill guidelines such as these, three of the original prototype specimens were retrofitted after testing and retested in order to investigate the ease of repair around the confining devices and the effectiveness of repair in terms of capacity and ductility.

Table 2.1. Prism Test Program

Prism Series Reference	**Block Type**	**Grouting**	**Number of Specimens Tested**
UST	Standard Stretcher	Ungrouted	5
GST	Standard Stretcher	Standard Grout	4
USP	Standard Splitter	Ungrouted	4
GSP	Standard Splitter	Standard Grout	4
UPI	Prototype Block, Type I (no device)	Ungrouted	3
GPI	Prototype Block, Type I (no device)	Standard Grout	3
GPIR	Prototype Block, Type I with Confining Device	Standard Grout	3
UPII	Prototype Block, Type II (no device)	Ungrouted	5
GPII	Prototype Block, Type II (no device)	Standard Grout	5
GPIIR	Prototype Block, Type II with Confining Device	Standard Grout	5
GPIIR-A1	Prototype Block, Type II with Confining Device	Anti-Shrink Grout 1 (A1)	5
GPIIR-A2	Prototype Block, Type II with Confining Device	Anti-Shrink Grout 2 (A2)	2
GPR-R	GPIIR – Retrofit		3
LABELLING CONVENTION: G = *Grouted,* U = *Ungrouted,* ST = *Stretcher Block,* SP = *Splitter Block,* PI = *Type I Prototype Block,* PII = *Type II Prototype Block,* R = *Reinforced with Confining Device*			

2.3.2. Prism Construction

Construction of the prisms for this study was performed in one work-day by an experienced mason. Prior to the arrival of the mason, some blocks were saw-cut into half blocks with a diamond blade as is standard in construction practices. As previously described, all prisms were constructed in running bond (using these half blocks) to a height of four courses in order to accurately simulate a wall section and

to avoid the end-confining effects of the loading platens of the test machine (specified in CSA S304.1-04 Annex D Table D.l (CSA 2004a)).

Standard prisms were built using a 10 mm thick face shell mortar joint and mortared end webs whereas for prisms constructed from prototype blocks, a full-mortared bed joint was used since these prototype blocks are not intended for ungrouted construction and have no equivalent face shell. The full-mortared bed joint also ensured a fully solid cross-section after grouting which could not be guaranteed with a partially mortared bed joint. Inspection of the prisms following construction indicated that joint widths appeared to be consistent within 1 mm and that all prisms were level and plumb.

Grouting of the specimens was also completed in one additional work-day, after a period of 12 days from construction. The exception to this was the anti-shrink grout prisms, which were grouted 42 days after initial construction due to delayed availability of materials. The high-slump grout was poured and thoroughly vibrated to ensure complete filling of the cells. In order to fill the exposed frogged ends of stretcher units in a manner consistent with in-wall conditions, prisms were arranged as shown in Figure 2.5 with the ends sealed in plastic and abutting against a solid face shell surface of another prism to allow continuous filling of the frogged ends at the first and third courses. All prisms were air-cured in a controlled laboratory environment with temperatures varying between 18 and 21˚C and relative humidity generally around 35%.

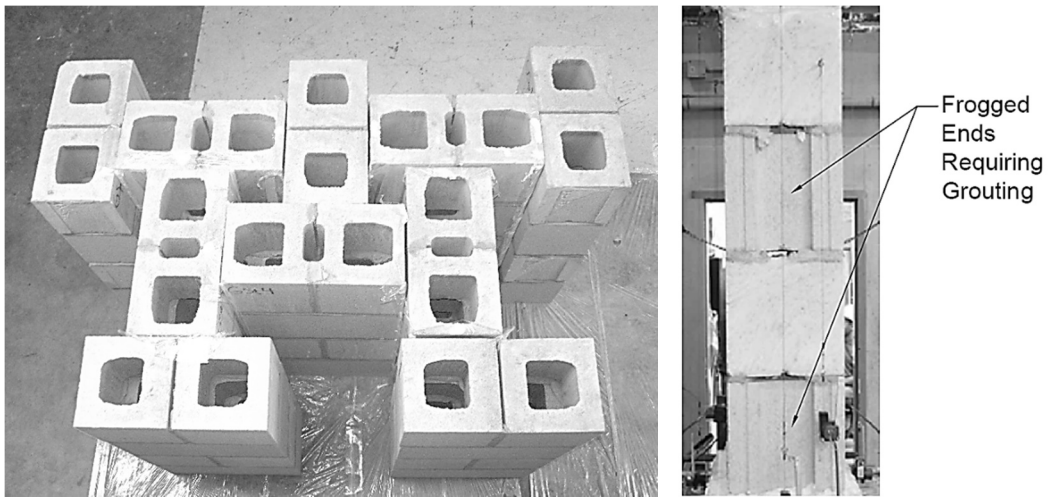

Figure 2.5. Prism Layout for Grouting of Frogged Ends of Stretcher Blocks in Prisms

Following grouting, continuing consolidation of the grout and absorption of water by the concrete blocks caused the level of the grout to drop as much as 10 mm

below the top of the prism. Therefore, at about one hour after initial grouting, additional grout was added to the prisms to increase the height of the grout column to be level with the top of the prism. This was necessary in order to provide a uniform bearing surface with uniform thickness of capping for loading.

2.4. Materials

Tests were performed on all of the materials involved in prism construction in order to both evaluate consistency of materials and determine specific material properties. The determined strength properties for all tested materials are presented in Table 2.2 and test procedures are described below. A complete record of material test results has been provided in Appendix A.

Table 2.2. Material Properties

Material Test		Average Strength (MPa)	C.O.V. (%)
Mortar		14.2	11.0
Standard Grout	Cylinder	24.5	8.5
	Cell Molded	31.7	7.2
Anti-Shrink Grout	Mix 1 (Type K cement)	22.2	0.3
	Mix 2	13.9	2.7
Block	Standard Stretcher	28.5	2.6
	Standard Splitter	30.0	6.7
	Type I Prototype	26.1	-
	Type II Prototype	26.4	4.5
Steel (Device)	Yield	485	-
	Ultimate	549	-

2.4.1. Mortar

The Type S mortar used for all specimens was mixed in a wheelbarrow in small, 50 kg batches according to the mix proportions outlined in Table 2.3. Mortar was batched by weight using oven-dried masonry sand for quality control. The batches were too small to be mixed in a mortar mixer but had the advantage of being used up within one half hour after mixing so that retempering was not required. A total of nine batches were mixed and for each batch, three 50 mm mortar cubes were taken in accordance with CSA A179 (CSA 2004c). A flow test was performed on each batch, also in accordance with CSA A179 (CSA 2004c) to ensure proper consistency, resulting in an average of 103% flow with a C.O.V. of 11.2%. The mortar cubes were tested in compression at the start, midpoint and conclusion of the prism testing period in order to obtain an average mortar strength and to indicate change in strength over the seven week test period. Mortar strength data presented in Table 2.2 was for an average age of 48 days.

Table 2.3. Mortar Mix Proportions

Constituent Material	**Parts by Weight**	**kg per 50 kg Batch**
Portland Cement (Type GUL)	1.0	7.6 kg
Dry Masonry Sand	4.39	33.5 kg
Hydrated Lime	0.21	1.6 kg
Water	0.95	7.3 kg

2.4.2. Grout

The fine grout mix presented in Table 2.4 was chosen to have relatively low compressive strength and was used as the standard grout in the grouted prisms. The intent of choosing a relatively low strength was to provide data that would closely represent construction practice and satisfy the minimum requirements for grout according to CSA A179 (CSA 2004c). For all prisms except those filled with anti-shrink grout, 420 kg batches were mixed in the laboratory and grouting was completed in one day. Slump tests performed on every batch to measure workability gave an average slump of 276 mm with a C.O.V. of 1.5%. Three 101.6 mm diameter cylinders were prepared from each batch for material tests according to CSA A179 (CSA 2004c). Additionally, block-molded specimens more representative of in-situ strength were prepared from every second batch and, following curing, were saw-cut to 80 mm by 80 mm by 160 mm prisms for testing. As was the case for the mortar samples, grout specimens were tested at the start, midpoint and conclusion of the prism testing period to obtain representative, average strengths and monitor any strength gain over time. No trend with respect to strength gain over time was observed within the complete grout data set as presented in Appendix A. As expected due to water absorption by the block, the block molded grout prisms had an average strength of 31.7 MPa, approximately 30% higher than the 24.5 MPa strength obtained from the traditional grout cylinders.

Table 2.4. Grout Mix Proportions

Constituent Material		**Parts By Weight**	**kg per Batch**		
			Standard Grout	**Anti-Shrink Grout 1**	**Anti-Shrink Grout 2***
Portland Cement	Type GUL	1.00	71.3 kg	-	11.9 kg
	Type K		-	71.3 kg	-
Dry Concrete Sand		4.00	285.2 kg	285.2 kg	47.5 kg
Hydrated Lime		0.04	2.9 kg	2.9 kg	0.5 kg
Water		0.85	60.6 kg	60.6 kg	10.1 kg
Sika Intraplast-N		(0.01)	-	0.71 kg	0.12 kg
Total			420 kg	421 kg	70 kg

*Smaller batch size was necessary as only two prisms were grouted using this type

The anti-shrink grout was mixed in a manner consistent with the standard grout and with identical mix proportions. The two anti-shrink grouts tested in this study were made using an expanding grout additive Sika Intraplast-N (at 1% by weight of cementitious material, according to manufacturer instructions) to reduce the effects of plastic shrinkage. Additionally, in the first anti-shrink mix (used for GPIIR-A1 specimens), Type GUL cement was replaced with Type K cement in order to counteract drying shrinkage. Batches were produced with and without the Type K cement in order to isolate the behaviour effected by each additive and to compare the effects of reducing plastic shrinkage and drying shrinkage, respectively.

2.4.3. Concrete Block

To limit material variability, all blocks used in this study were manufactured in the same production run using the same concrete batches. The dry mass of each type of block was measured to determine whether the prototype blocks would fall within the range to which the mason is accustomed. While the Type I prototype block was a relatively heavy unit (23.2 kg) the Type II prototype block mass (17.7 kg) fell between that of the standard stretcher (17.1 kg) and the standard splitter (18.3 kg) and was deemed reasonable by the mason during construction.

Tests were conducted on each block type to determine accurate values for dimensions and strength. Volume/density tests were conducted in accordance with ASTM C140M (ASTM 2013) and calculated according to Equations 2.1 to 2.3. The net cross-section areas for determination of unit strength as well as the densities of each block, calculated to ensure consistency of consolidation, are presented in Table 2.5. Three blocks of each type were tested in compression according to CSA A165.1 (CSA 2004d) which, when divided by the aforementioned areas, provided the average strengths presented in Table 2.2. All block tests were performed at 28 days following manufacture as significant additional block strength increase was not expected following the Autoclave curing process performed at the block plant.

$$\text{Net Volume } (V_n) = (M_s - M_i)/\rho_{H_2O} \times 10^6 \tag{2.1}$$

$$\text{Average Net Area } (A_n) = V_n/H \tag{2.2}$$

$$\text{Density } (\rho) = M_d/V_n \tag{2.3}$$

where M_s is the saturated block mass
M_i is the immersed (buoyant) block mass
ρ_{H_2O} is the density of water at room temperature
H is the block height
M_d is the oven-dried block mass

Table 2.5. Concrete Block Types - Physical Properties

Block Type	Average Cross-Section Area (mm^2)	C.O.V. (%)	Average Density (kg/m^3)	C.O.V. (%)
Standard Stretcher (ST)	41,800	0.73	2150	0.60
Standard Splitter (SP)	45,700	0.29	2110	0.42
Type I Prototype (PI)	58,900	-	2080	-
Type II Prototype (PII)	43,800	1.08	2120	1.76

2.4.4. Steel Used in Manufacture of Confining Devices

Tension tests were performed on the three steel samples obtained from the manufactured confining devices to confirm the values from coupon testing as provided by the manufacturer. The first sample was a vertical cut out from a confining device with tabs on either side where horizontal loops met the vertical member (see Figure 2.6). Strain readings for this test were taken using an extensometer over a 200 mm gauge length. The second test involved a similar sample, but was measured using a strain gauge bonded to the steel between tab sets. For the third test, a horizontal member from a flat section of the punched steel was used and all tabs from the connections of vertical members were ground off. This specimen was measured using an extensometer over the same 200 mm gauge length as the first test.

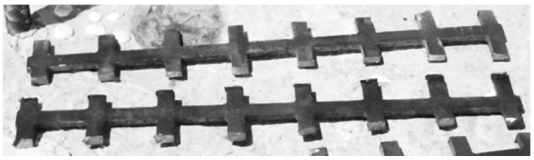

Figure 2.6. Steel Test Specimens (with connecting tabs)

These tests produced differing results due to the variations in cross-section area. The tabbed specimens tested to higher strengths than the ground sample due to the likely reduction of cross-section area in the ground zone of failure. Despite these explainable differences, the test results were all in excess of the yield strength of 400 MPa provided by the manufacturer and approached the ultimate strength of 560 MPa provided by the manufacturer. As these manufacturer properties did not appear to be reliable, results from a representative test have been presented. As stiffnesses were consistent through all three tests performed and the reduced strength observed for the ground sample was not reflective of the condition within the devices, the first test performed on the tabbed sample has been taken as representative and is presented in the form of a stress-strain curve in Figure 2.7. Yield stress was estimated to be 485 MPa from this test using the 0.2% offset method (as prescribed by ASTM A370 (ASTM 2012a)) and is presented in Table 2.2 along with the ultimate strength achieved in this test.

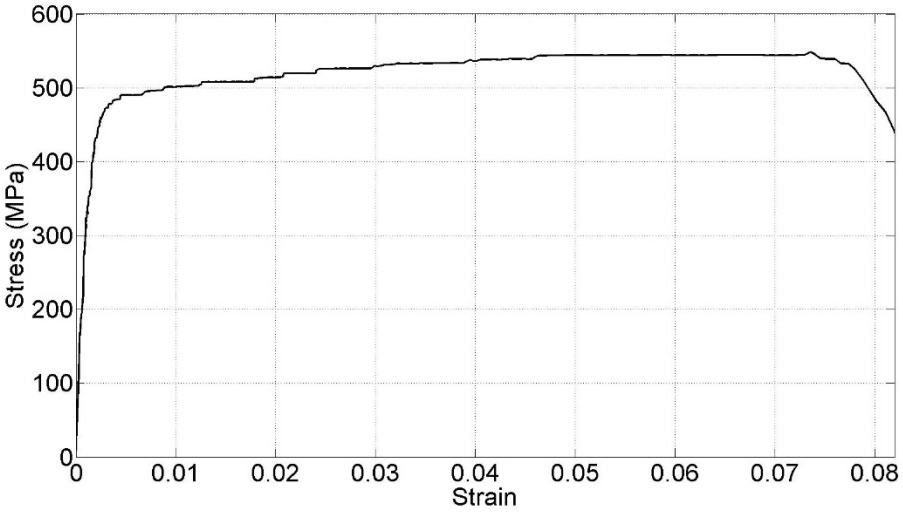

Figure 2.7. Representative Stress-Strain Curve for Steel used in the Manufacture of Confining Devices

2.5. Prism Test Configuration

2.5.1. Test Setup

All prisms in this study were tested under axial compressive load applied in a servo-hydraulically controlled testing machine (Rhiele) with a capacity of 2500 kN. The compressive force in this setup was generated by the upward motion of the rigid steel plate that forms the lower bound of the system. Prior to placing a prism into the test setup, 76.2 mm thick steel plates were levelled on the lab floor for capping. Each prism was crane-lifted, levelled with a spirit level and, in compliance with ASTM C1552 requirements (ASTM 2012b) for capping of standard masonry prisms, bonded to the plate with a thin layer (less than 5 mm) of high strength gypsum cement (Hydro-Stone). The procedure was repeated on the top bearing surface of each prism with a second 76 mm steel plate at least two hours prior to testing. Capped prisms were then lifted into the test machine and vertically centered beneath the spherically seated loading head to ensure concentric loading. To maintain a consistent centering procedure, in order to minimize variation between tests, all prisms were loaded in a consistent direction with the block ends facing east-west (see Figure 2.8).

2.5.2. Measurements

Once centered under the spherical head, each prism was instrumented with a series of eight 50 mm range, draw-wire potentiometers to measure average strains over segments of the height of the specimen. The first four potentiometers (one located on each side of the specimen) spanned a 600 mm gauge length from the mid-height of the top block to mid-height of the bottom block of the prism and were mounted

directly onto the block. These potentiometers gave representative strain readings up to the initiation of cracking and spalling of the outer shell of the blocks, without being influenced by the confining effects of the steel plates at the top and bottom of the specimen. The second set of four potentiometers spanned from the bottom capping plate to the top capping plate on each side of the specimen to read strain over the full height of the prism. Although likely influenced by confining effects of the capping plates, these potentiometers continued to provide relevant readings in the post-cracking stages of the test. Even though confining effects would be expected to result in reduced average strains over the prism height, readings from this latter group of potentiometers were found to be in agreement with results from those located directly on the block, with a minor offset being the only notable difference.

A second form of instrumentation provided validation of the readings obtained from the draw-wire potentiometers at low strains. One specimen in each series was also outfitted with gauge points for a demountable mechanical (Demec) strain gauge over a mid-height 200 mm gauge length. Manual measurements at regular intervals up to 50% of maximum load yielded results that closely agreed with the digital output from the draw-wire potentiometers. As use of a Demec gauge has been an accepted standard technique for measuring strain readings on concrete materials (Morice & Base 1953), these readings were used simply to verify that the results from the draw-wire potentiometers were sufficient for the remainder of the tests.

2.5.3. Test Procedure

Following instrumentation, prisms were subjected to vertical compression under displacement (strain) control in order to obtain a complete stress-strain curve including any post-peak descending branch The loading (bottom) head of the machine was set to travel at a constant rate of approximately 0.9 mm/min corresponding to an average strain rate of 0.0011 per minute. Output from three load cells, visible above the top head of the machine in Figure 2.8, were combined to obtain load readings throughout the test. Load cell and potentiometer outputs were recorded at a sampling frequency of 2 Hz. To obtain stress-strain curves for each specimen, load readings were divided by the appropriate area of the block prism and potentiometer readings were divided by their respective gauge lengths as measured prior to each test. An average of the strain readings from the potentiometers on each of the four sides of the prism provided average strain reading across the prism cross-section.

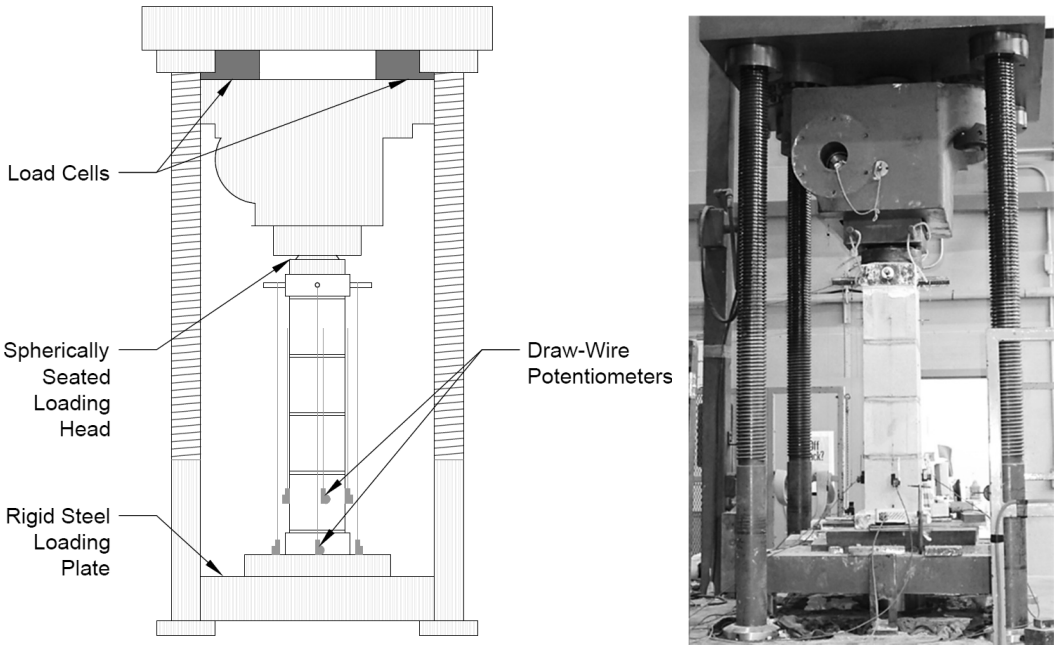

Figure 2.8. Prism in Test Machine

2.6. Closure

To simplify discussion of the test results in the following chapter, basic information regarding the component materials has been provided separately here for ease of reference. As an important part of the proof-of-concept, manufacturability of SR Block was confirmed. Also, it is noteworthy that block, mortar, and grout strengths were chosen to approximate the minimum conditions normally found in construction. While the strengths achieved (especially the block strengths which were controlled by the manufacturer) were above code minimums, they were near to the lower acceptable range of what is typically found in construction practices. Because the manufacture of the confining devices was found to be quite costly and time consuming, it was concluded that alternative designs would have to be investigated in subsequent phases of this research program.

CHAPTER 3

PROOF-OF-CONCEPT: PRISM RESULTS AND ANALYSIS

3.1. Introduction

This chapter contains the results and findings from the tests of the 51 prisms described in Chapter 2. As a proof-of-concept stage of the research, the main objective of these tests was to compare the compressive behaviours of prisms built with different block types in both ungrouted and grouted states. These included standard blocks and two types of prototype blocks as well as comparison of the performance of the self-reinforced block (SR Block) with similar unreinforced blocks. Comparisons of this nature were necessary to isolate the effects of this new method of confinement. Also examined are the effects of using anti-shrink grout mixes within the SR Block prisms and the effectiveness of repairing/retrofitting SR Block construction following damage under compressive loading.

3.2. Methodology For Presentation of Data

3.2.1. Stress-Strain Curves

To present the stress-strain results from this test program in a form that is straightforward to understand, compare, and utilize in subsequent analyses, all acquired data had to be analyzed and combined in a consistent way. As described in Chapter 2, the three sets of strain data obtained were from demountable mechanical (Demec) strain gauges over a 200 mm gauge length, draw-wire potentiometers mounted on the prisms over a 600 mm gauge length, and draw-wire potentiometers attached to the top and bottom capping plates which provided an 800 mm gauge length over the full height of the prism. In all cases, average values from the four measurements (one on each face of the prism) were used.

Through comparison with curves obtained from the Demec gauges, it was determined (as described in Chapter 2) that the draw-wire potentiometers mounted directly onto the faces of the prism (potentiometer set 1) provided the most accurate strain readings prior to cracking and spalling of the face shell concrete outside of the confining devices. Therefore, the direct average of the values obtained from each of the four prism faces was used to provide the ascending portion of the presented curves up to a value of 80% of f'_m (first peak compressive strength) beyond which it was expected that cracking and/or spalling could initiate and readings might become unreliable due to movement or loss of the anchor points of the potentiometers in set 1.

As can be seen in the raw data curves reproduced in Appendix B and in the sample data shown in Figure 3.1 a), some settling of equipment and some closing of the mortar bed joints in the very low stress range often resulted in an initially relatively flat part of the curve, particularly in the curves from the potentiometers spanning the full height of the prism (potentiometer set 2) (Drysdale & Hamid 2005). Alternatively, as shown in the curve for potentiometer set 1, there was often an initial delay in recording strain for those potentiometers mounted over only the mid-height of the prisms. As specified in CSA S304 (CSA 2004a) and ASTM C1314 (ASTM 2010) and correspondingly in ASTM E111 (ASTM 2004), it is considered to be appropriate to perform a linear regression (by method of least squares) in the elastic range of the curve between 5% and 33% of f'_m to determine the elastic modulus. Following a similar process, discrepancies in the initial shape of the stress-strain data below 5% of f'_m were removed by tangentially extending the regression line to the point of zero stress and then offsetting the entire curve to have zero stress coincide with zero strain (see Figure 3.1 b)).

Following face shell cracking and the initiation of spalling, when the potentiometers mounted directly on the prisms could no longer be relied upon, the strain values obtained from the set of potentiometers spanning the full height of the prism (potentiometer set 2) were used. Although the readings were very similar, to maintain a continuous, smooth curve, this second curve was shifted to match the strain of the first curve at a stress of 80% of f'_m as illustrated in Figure 3.1 c). The curve from the full-height potentiometers generally displayed a slightly different strain due to the uneven distribution of strains over the height of the prims due to end platen effects. Using this strain offset to match the strain of the directly-mounted potentiometers, the full-height potentiometers provided values for the remainder of the curve. This process allowed strain values to be extracted from the data sets for significant points such as that of maximum stress as well as the maximum strain. Figure 3.1 d) illustrates the completion of this process for an example GSP prism (grouted prism made with splitter block).

Curve averaging for each series of tests was achieved by interpolating between nearest values to a prescribed set of strain points within the data from each test. The stresses at these defined strains could then be averaged. Average curves were smoothed for presentation purposes using a Savitzky-Golay moving average smoothing filter (fits adjacent subsets of data points to a low degree polynomial using least-squares regression) in Matlab.

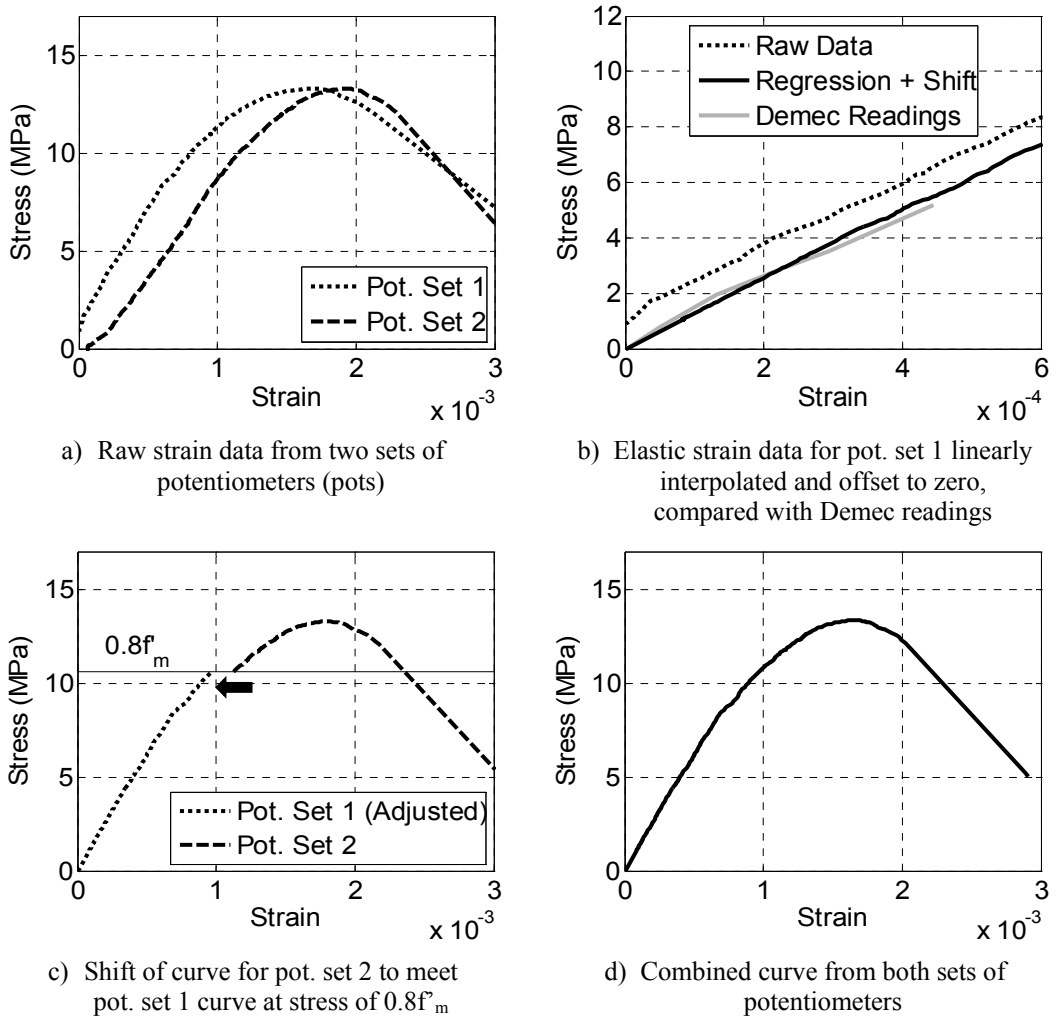

a) Raw strain data from two sets of potentiometers (pots)

b) Elastic strain data for pot. set 1 linearly interpolated and offset to zero, compared with Demec readings

c) Shift of curve for pot. set 2 to meet pot. set 1 curve at stress of $0.8f'_m$

d) Combined curve from both sets of potentiometers

Figure 3.1. Process for Representing Stress-Strain Test Data

3.2.2. Test Machine Calibration

A machine malfunction during the early stages of testing necessitated recalibration of the testing machine. The system had been used reliably in the past and had been calibrated on a regular basis by an external calibration company. However, during the 13th and 14th prism tests, erroneously high load values were displayed in a very unexpected and jagged pattern with no similarities to previous tests. This anomalous behaviour prompted an investigation into the machine setup and it was determined that the signal conditioner/indicator had failed and was no longer reporting accurate load values. Consequently, results from the two tests with clearly erroneous readings were discarded. To overcome this problem, the three load cells were wired directly into the data logging system and were calibrated using a hydraulic jack and a separately calibrated load cell.

This new calibration provided an accurate average load reading and was used in all subsequent testing. As there was no prior reason to doubt the earlier calibration of the signal conditioner (which unfortunately could not be rechecked after its failure), results from all tests were considered valid and have been included in the data presentation below. However, upon reviewing the results of the 12 prisms tested prior to the signal conditioner failure, it was observed that most of the results were slightly higher than the mean value but not the highest values in their prism series. Therefore, although this is statistically possible and the full data set is considered to be valid, an alternate set of data that would avoid any possible bias associated with the recalibration of the machine was provided for reference by the reader in Appendix B but has not been discussed further here. This alternate set of average data excludes the tests done prior to the recalibration. It is worth noting that the overall results and conclusions from this test program would not be affected in any way by the slight changes resulting from excluding the data from the first twelve prisms.

3.3. Prism Series Results

3.3.1. Summary of Key Data

Stress and strain results for all prism series are presented in detail in Appendix B. The averages of these results are summarized in Tables 3.1 to 3.4. Notes taken during testing and observations of behaviour during testing follow.

Table 3.1. Summary of Average Results for Ungrouted Prism Series

Series	**Average Peak Stress (MPa)**	**C.O.V. (%) / No. of Tests**	**Average Strain at Peak Stress**	**C.O.V. (%)**
UST (stretcher block)	18.8	5.4 / 5	0.0023	13.5
USP (splitter block)	19.0	16.2 / 4	0.0020	7.1
UPI (type I prototype)	15.6	3.9 / 3	0.0021	14.4
UPII (type II prototype)	21.0	5.2 / 5	0.0025	3.1

Table 3.2. Summary of Average Results for Grouted Prism Series

Series	**Average Peak Stress (MPa)**	**C.O.V. (%) / No. of Tests**	**Average Strain at Peak Stress**	**C.O.V. (%)**
GST (stretcher block)	12.4	5.9 / 4	0.0014	8.2
GSP (splitter block)	14.1	4.7 / 4	0.0017	7.9
GPI (type I prototype)	16.6	7.0 / 3	0.0018	5.9
GPII (type II prototype)	13.4	4.0 / 5	0.0017	15.1

Table 3.3. Summary of Average Peak Stress Results for Self-Reinforced Prism Series

Series	**Average Stress (MPa)**	**C.O.V. (%) / No. of Tests**	**Average Strain**	**C.O.V. (%)**
At Initial Peak Stress				
GPIR (type I prototype)	18.0	- * / 3	0.0022	-
GPIIR (type II prototype)	15.2	8.2 / 5	0.0017	13.0
GPIIR-A1 (grout mix A1)	15.2	8.4 / 5	0.0021	9.7
GPIIR-A2 (grout mix A2)	16.3	- / 2	0.0018	-
At Second Peak Stress				
GPIR	19.1	5.8	0.0104	18.6
GPIIR	18.0	5.3	0.0139	19.0
GPIIR-A1	16.0	4.1	0.0156	25.7
GPIIR-A2	14.9	-	0.0102	-

*C.O.V. not provided where less than 3 values were available (or where an outlier was omitted from the average; see explanation in test observations)

Table 3.4. Summary of Average Results at High Strains for Self-Reinforced Prism Series

Series	Average Stress (MPa)	% of Initial Peak Capacity	C.O.V. (%)
At 0.8% Strain			
GPIR	18.6	97	5.7
GPIIR	16.9	111	7.9
GPIIR-A1	15.4	101	5.1
GPIIR-A2	14.5	89	-
At 1% Strain			
GPIR	18.9	98	6.9
GPIIR	17.4	114	6.5
GPIIR-A1	15.5	102	5.8
GPIIR-A2	14.5	89	
At 1.5% Strain			
GPIR	18.4	96	3.7
GPIIR	17.7	116	5.4
GPIIR-A1	15.7	103	6.0
GPIIR-A2	13.6	83	
At 2% Strain			
GPIR	17.2	94	2.2
GPIIR	17.0	112	3.5
GPIIR-A1	15.3	100	5.0
GPIIR-A2	13.9	85	-
At 3% Strain			
GPIR	15.2	83	9.0
GPIIR	14.1	93	-
GPIIR-A1	13.3	87	-
GPIIR-A2	12.8	78	-

3.3.2. Ungrouted Standard Stretcher (UST)

The detailed results for the five prisms constructed from ungrouted standard stretcher units are presented in Appendix B and the averages of key values are summarized in Table 3.1. In accordance with CSA S304 (CSA 2004a) and as plotted in Figure 3.2 (a), stress values were calculated based on an effective mortar bedded area of 31090 mm^2 corresponding to an average face shell thickness of 31090/(2 x 390) = 40 mm. Effective mortar bedded area was determined for all block types by overlaying the cross-section profiles of the units in a running bond pattern. The average calculated compressive stress capacity of 18.8 MPa is typical of values obtained for similar strength standard block in an ungrouted state. Figure 3.2 (b) shows the typical failure pattern for the UST prisms. Failure was initiated by vertical splitting of the webs in the middle two courses, which propagated and resulted in a complete loss of capacity between 0.0025 and 0.003 strain. This failure is characterized as very brittle, which is typical for concrete and is the expected

mode of failure for ungrouted concrete block assemblages (Drysdale & Hamid 2005).

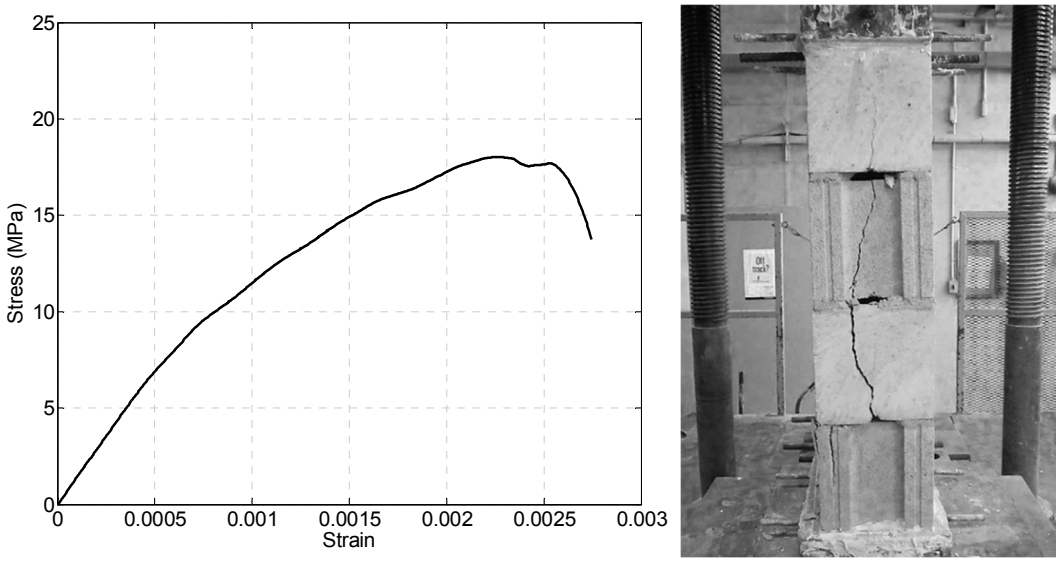

a) Average Stress-Strain Curve b) Typical Failure Pattern

Figure 3.2. Failure of UST Prisms

3.3.3. Ungrouted Standard Splitter (USP)

The detailed results of the four prisms constructed from ungrouted standard splitter (end) units are presented in Appendix B and average values are summarized in Table 3.1. Stress values including those plotted in Figure 3.4 (a) were calculated based on an effective mortar bedded area of 42150 mm^2. With a full-mortared bed joint as was used in construction of these prisms, the effective mortar bedded area is much higher for splitter blocks, due to some overlapping of the block webs, than for standard stretcher blocks where the webs do not align vertically in running bond. This phenomenon is illustrated in Figure 3.3 in which the hatched areas represent the overlapping mortar bedded area for each block type.

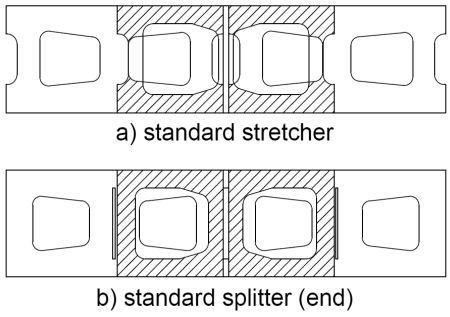

Figure 3.3. Comparison of Mortar Bedded Areas

The average calculated compressive stress capacity of 19.0 MPa is similar to that of the UST prisms. Figure 3.4 b) shows the typical failure pattern for the USP prisms. As was the case with the UST prisms, failure was initiated by vertical splitting of the webs and face shells in the middle two courses, which propagated and resulted in a complete loss of capacity between 0.0025 and 0.003 strain. This failure is also characterized as very brittle and is the expected mode of failure for ungrouted concrete block assemblages (Drysdale & Hamid 2005).

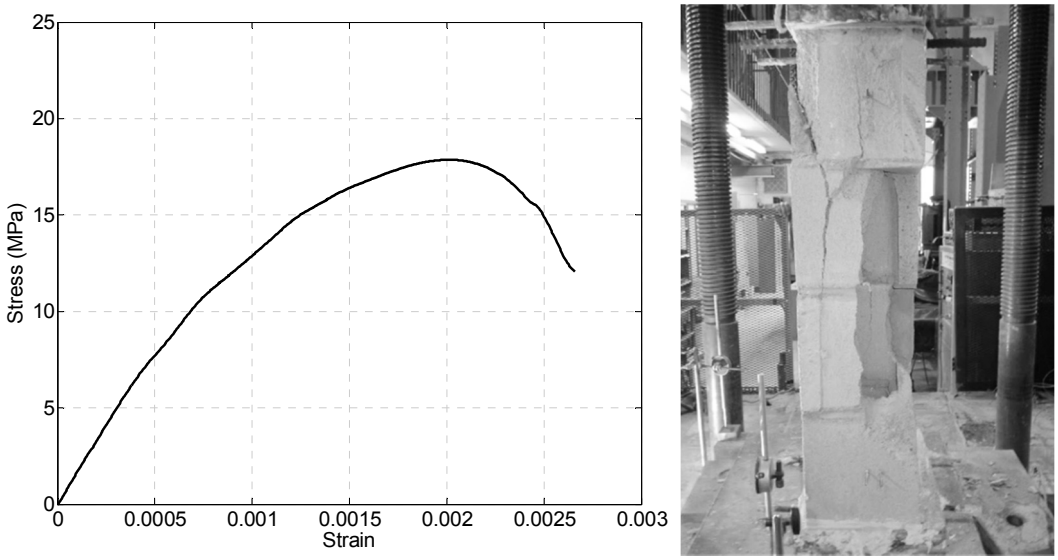

a) Average Stress-Strain Curve b) Typical Failure Pattern

Figure 3.4. Failure of USP Prisms

3.3.4. Ungrouted Type I Prototype (UPI)

The detailed results of the three prisms constructed from ungrouted Type I prototype units are presented in Appendix B and the average values are listed in Table 3.1. Stress values including those plotted in Figure 3.5 (a) were calculated based on an effective mortar bedded area of 53820 mm^2. As was the case with the splitter blocks, the overlapping of web areas contributed significantly to the increased mortar bedded area. Although the objective at the start of block plant trials was to have the cells perfectly aligned form course to course, some adjustments made to the mold during trials resulted in an offset of nearly 5 mm between the cells. This, in combination with the presence of a 10 mm head joint between cut blocks, resulted in a mortar bedded area smaller than the net block area.

The average calculated compressive stress capacity of 15.6 MPa is lower than that of the UST or USP prisms as is typically found to occur in prism tests with solid and 75% solid block units (Chahine 1989; CSA 2004a). Figure 3.5 b) shows the

typical failure pattern for the UPI prisms. Unlike the UST and USP prisms, failure was caused by a combination of vertical splitting of the webs and more local spalling of the face shells near the bed joints in the middle two blocks, which resulted in a complete loss of capacity between 0.002 and 0.003 strain. This failure is also characterized as very brittle but differs slightly from the expected failure of hollow ungrouted prisms. Instead, this failure type is very similar to that expected for solid and semi-solid block prisms. At 78% solid this Type II prototype block is more comparable to semi-solid units (generally 75% solid) than to standard hollow units (generally about 50% solid) (Chahine 1989).

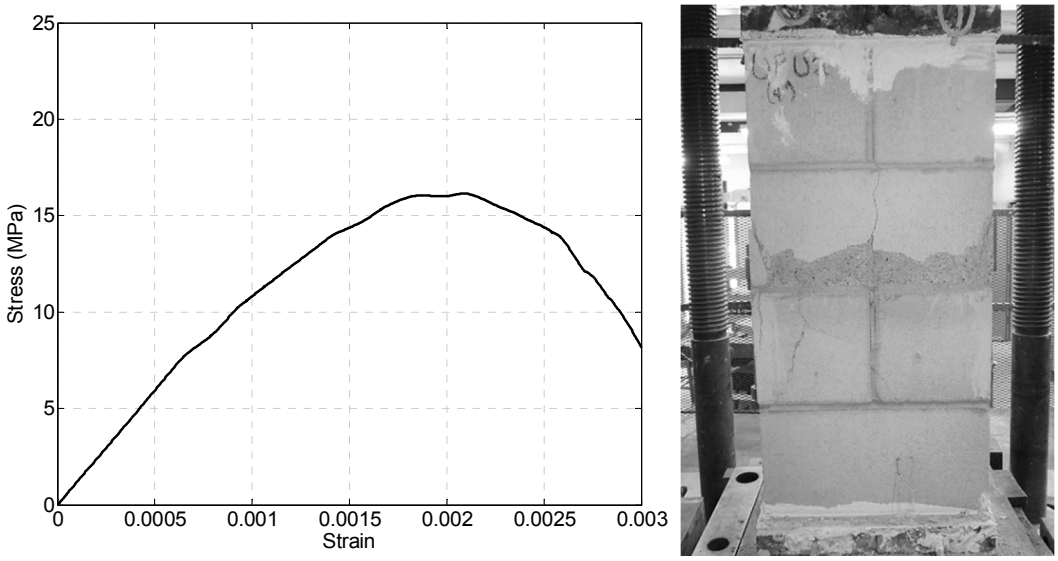

a) Average Stress-Strain Curve b) Typical Failure Pattern

Figure 3.5. Failure of UPI Prisms

3.3.5. Ungrouted Type II Prototype (UPII)

The detailed results of the five prisms constructed from ungrouted Type II prototype units are presented in Appendix B and the average values are summarized in Table 3.1. Stress values for all UST prisms including those plotted in Figure 3.6 a) were calculated based on an effective mortar bedded area of 39110 mm^2. As was the case with the Type I prototype blocks, adjustments made to the mold during manufacturing trials resulted in an offset of slightly less than 5 mm between the cells and, in combination with the presence of a 10 mm head joint between cut blocks, resulted in a mortar bedded area smaller than the net block area.

The average calculated compressive stress capacity of 21.0 MPa is higher than measured for the UST or USP prisms. This may be attributable to the better alignment of the face shells and webs from top to bottom of the prism, which allowed the stresses to be better distributed throughout the volume of each block

compared to the situation with standard blocks. Figure 3.6 b) shows the typical failure pattern for the UPII prisms. Similar to the UST and USP prisms, failure was initiated by vertical splitting of the webs and face shells in the middle two courses, which propagated and resulted in a complete loss of capacity between 0.0025 and 0.003 strain. This failure is also characterized as very brittle and is the expected mode of failure for ungrouted concrete block assemblages (Drysdale & Hamid 2005).

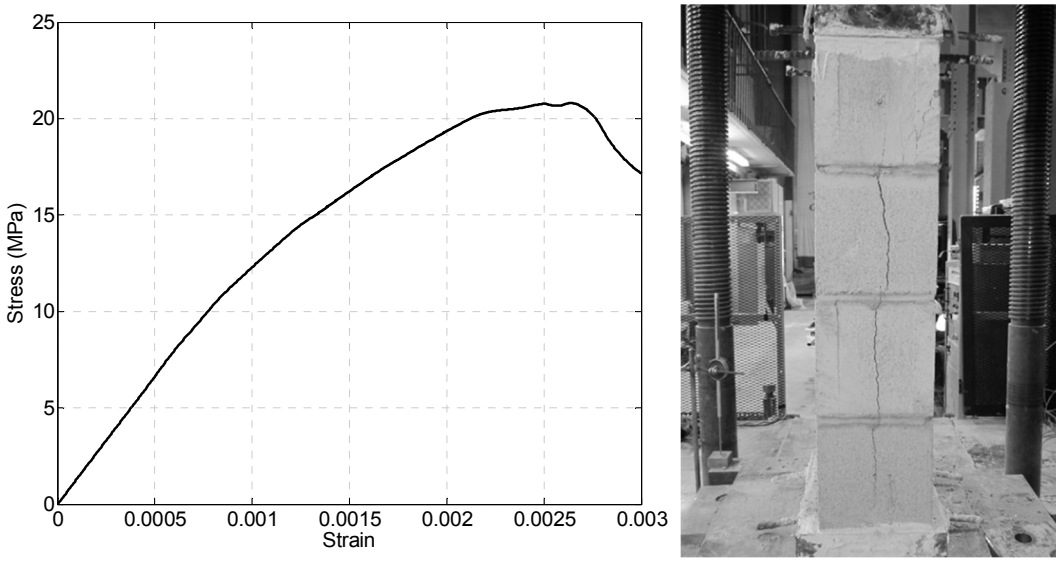

a) Average Stress-Strain Curve b) Typical Failure Pattern

Figure 3.6. Failure of UPII Prisms

3.3.6. Grouted Standard Stretcher (GST)

The detailed results of the fully grouted prisms constructed from standard stretcher units are presented in Appendix B and the average results are summarized in Table 3.2 and in the stress-strain curve plotted in Figure 3.7 a). In accordance with CSA S304 (CSA 2004a), stress values for all grouted prisms were calculated based on an area of 74100 mm^2 which is the calculated gross area of a standard 190 mm by 390 mm fully grouted block. The average calculated compressive stress capacity of 12.4 MPa is typical of values obtained for similar strength standard block prisms in a grouted state. As expected (CSA 2004a), this strength is approximately 35% lower than that of the corresponding ungrouted series (UST) based on effective area. Figure 3.7 b) shows the typical failure pattern for the GST prisms. Failure was initiated by vertical cracking of the block web and face shells due to the lateral expansion of mortar and grout within the block and concluded with a final conical shaped splitting as a result of restricted lateral expansion at the top and bottom of the prism due to end platen restraint effects (Chahine 1989; Liu 2012) for the long

(face) direction of the section. Final vertical splitting was more pronounced in the short (end) direction of the cross section. The initial decrease in capacity coinciding with block failure was followed by a somewhat more gradual splitting of the grout cores and then complete loss of capacity at strains slightly higher than 0.003.

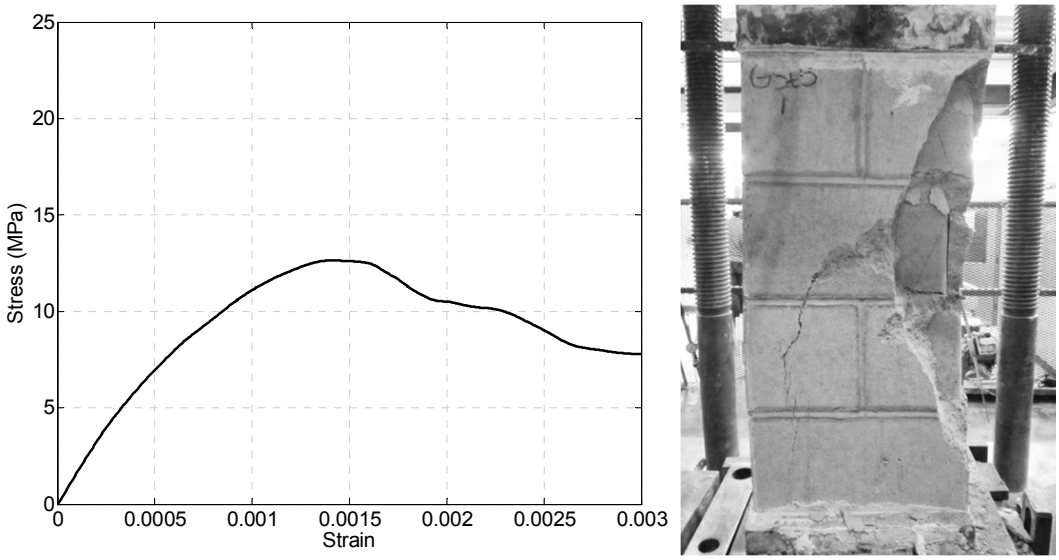

a) Average Stress-Strain Curve b) Typical Failure Pattern

Figure 3.7. Failure of GST Prisms

3.3.7. Grouted Standard Splitter (GSP)

The detailed results of the four fully grouted prisms constructed from standard splitter (end) units are presented in Appendix B and average results are summarized in Table 3.2 and in the stress-strain curve plotted in Figure 3.8 a). The average calculated compressive stress capacity of 14.1 MPa is typical of values obtained for similar strength standard block in a fully grouted state. As expected (CSA 2004a), this strength is approximately 25% lower than that of the corresponding ungrouted series (USP). Figure 3.8 b) shows the typical failure pattern for the GSP prisms. As with the GST series, failure was initiated by vertical cracking of the block through the web and face shells due to the lateral expansion of mortar and grout within the block. The initial post-peak decrease in capacity coinciding with block failure was followed by a somewhat more gradual splitting of the grout cores and a complete loss of capacity at strains slightly higher than 0.003.

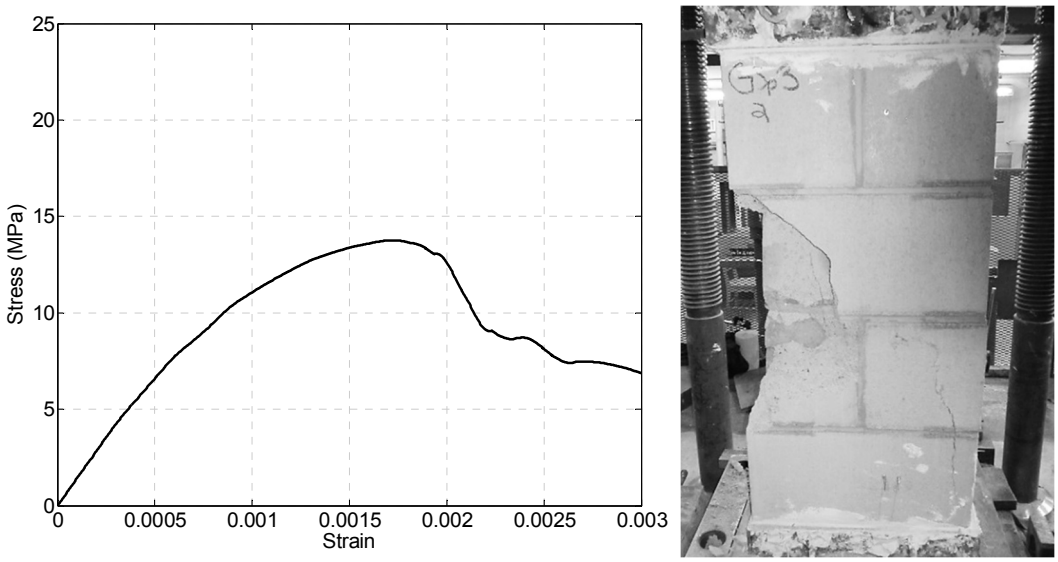

a) Average Stress-Strain Curve b) Typical Failure Pattern

Figure 3.8. Failure of GSP Prisms

3.3.8. Grouted Type I Prototype (GPI)

The detailed results of the three fully grouted prisms constructed from unreinforced Type I prototype units are presented in Appendix B and average results are summarized in Table 3.2 and in the stress-strain curve plotted in Figure 3.9 a). The average calculated compressive stress capacity of 16.6 MPa is approximately 5% higher than that of the corresponding ungrouted series (UPI) and generally supports the CSA (2004a) approach where semi-solid, fully solid and grout filled block masonry are considered to have the same compressive capacity. Figure 3.9 b) shows the typical failure pattern for the GPI prisms. Failure was initiated by vertical cracking of the block at the web and face shells due to the lateral expansion of mortar and grout within the block. This was followed by the spalling of the cracked concrete away from any lateral support of the end platen. Much less damage, however, was present in failed specimens compared to the GSP and GST series. This failure was more brittle than the previous grouted series and the prisms experienced a rapid loss of capacity at strains slightly lower than 0.003. This slightly more rapid failure can be attributed to the smaller volume of grout present to carry the load following the cracking/spalling of face shell concrete (approximately 20% of the total area compared to approximately 50% with the standard units).

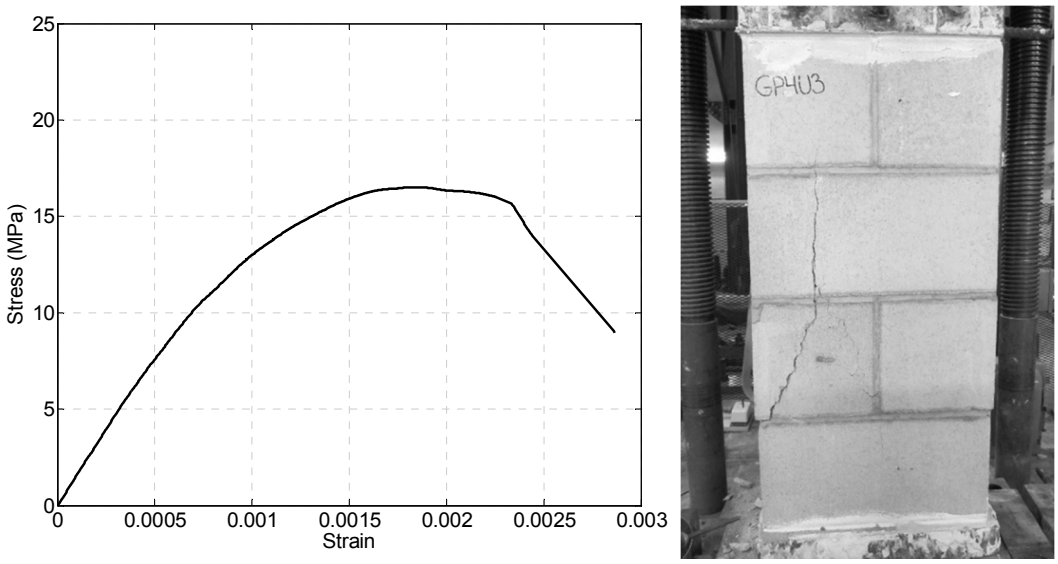

a) Average Stress-Strain Curve b) Typical Failure Pattern

Figure 3.9. Failure of GPI Prism

3.3.9. Grouted Type II Prototype (GPII)

The detailed results of the five fully grouted prisms constructed from unreinforced Type II prototype units are presented in Appendix B and average results are summarized in Table 3.2 and in the stress-strain curve plotted in Figure 3.10 a). The average calculated compressive stress capacity of 13.4 MPa is similar to that of the GST and GSP series. This strength is approximately 36% lower than that of the corresponding ungrouted series (UPII). Figure 3.10 b) shows the typical failure pattern for the GPII prisms. As with the GST and GSP series, failure was initiated by vertical cracking of the block at the web and face shells due to the lateral expansion of mortar and grout within the block. This was followed by the spalling of the cracked concrete away from any lateral support of the end platen. The initial post-peak decrease in capacity coinciding with block failure was followed by a somewhat more gradual splitting of the grout cores and a complete loss of capacity at strains slightly higher than 0.003.

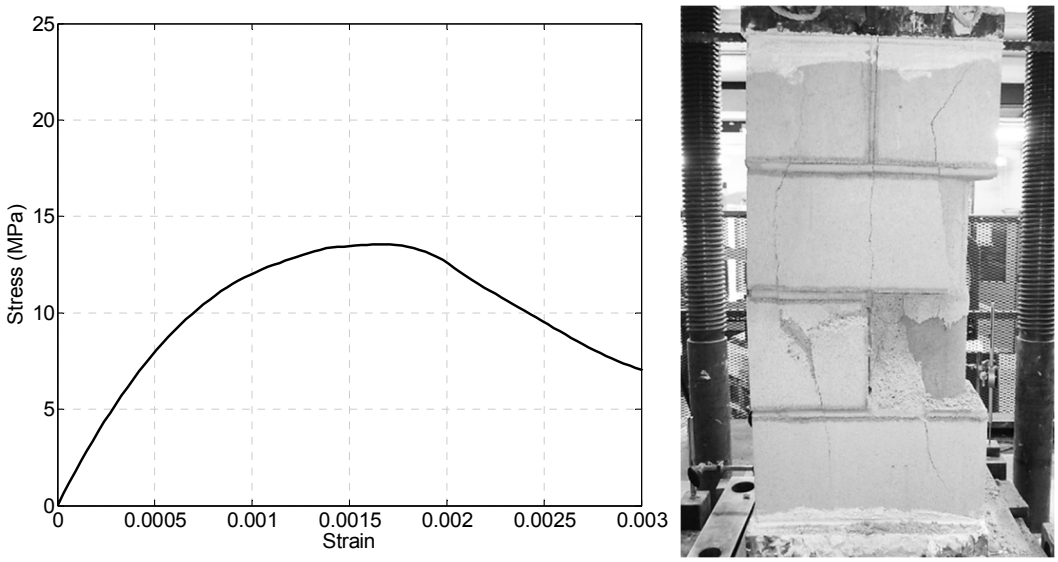

a) Average Stress-Strain Curve b) Typical Failure Pattern

Figure 3.10. Failure of GPII Prisms

3.3.10. Type I Prototype with Confining Device (GPIR)

The detailed results of the three fully grouted prisms constructed from Self-Reinforced Type I prototype units for this series are presented in Appendix B and average results are summarized in Tables 3.3 and 3.4 and in the stress-strain curve plotted in Figure 3.11. Two anomalies associated with this test series have been accounted for in the presentation of data. First, an error during the testing of the first prism in the series resulted in a very rapid loading rate up to the initial point of face shell spalling. Although the issue was resolved and the prescribed loading rate was resumed for the remainder of the test, the initial rapid loading resulted in a higher-than-expected initial peak loading value. The average initial peak stress presented in Table 3.3 for this series omits this high value but all test values are presented in Appendix B. The second anomaly was observed in the post-elastic shape of the stress-strain curve for the second prism in this series. Unlike all other SR Block prisms tested in this program, the stress-strain curve for this prism lacked an initial peak at the expected strain and instead, followed a gradual transition up to a post-spalling peak at a similar strain to the other prisms (see Appendix B). For this reason, values for initial peak stress and strain at initial peak stress for this series have been omitted from the averages presented in Table 3.3. Additionally, because of the aforementioned discrepancies at different points during these tests, rather than presenting an average curve, a smoothed plot of the third prism tested in this series has been presented in Figure 3.11 as a representative stress-strain curve that more accurately embodies the shape of the first and third tests and the

stress values of the second and third tests. The first part of the stress-strain curve is also replotted to a larger strain scale to better show this part of the behaviour.

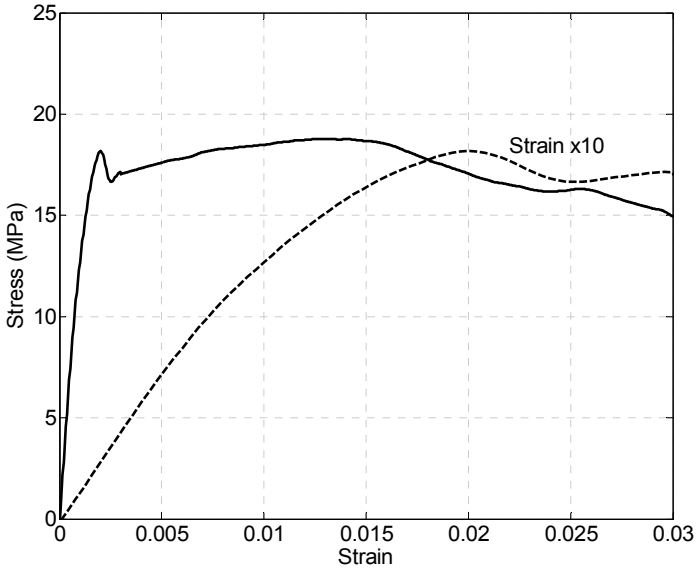

Figure 3.11. Representative Stress-Strain Curve for GPIR Prism Series

The observed failure patterns for this series were consistent, following a pattern similar to that of the unreinforced series (GPI) up to an initial peak compressive stress capacity of 18.0 MPa. This peak capacity is approximately 10% greater and was achieved at an approximately 20% higher strain than that of the unreinforced series (GPI). Figure 3.12 shows the typical splitting and spalling pattern for the GPIR prisms that occurred as the initial peak load was attained. As observed with the unreinforced series (GPI), failure was initiated by vertical compression splitting of the face shell concrete allowing the outer concrete to spall off. The vertical steel present in the confining devices provided increased vertical stiffness and additional material to laterally restrain the enclosed material to minimize the capacity decrease expected following the spalling of the unconfined portions of the prism.

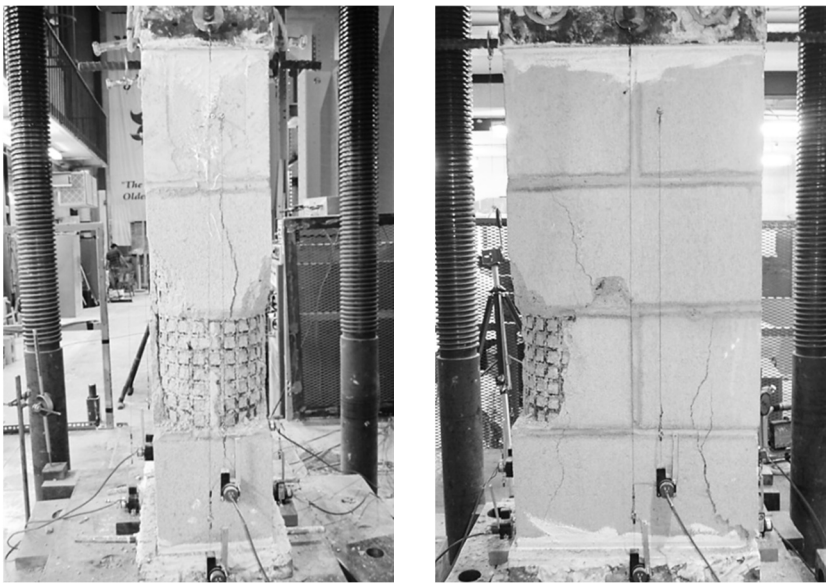

a) End View b) Face View

Figure 3.12. Typical Initial Splitting/Spalling of GPIR Prisms at 0.3% Strain

At strains greater than that corresponding to the initial peak stress (average strain of 0.0022), the spalling of the block concrete external to the confining devices resulted in a slight decrease in capacity (5% to 10%). As the prism continued to undergo increasing strain, the prisms regained strength up to and surpassing the original peak capacity. This second peak at an average stress of 19.1 MPa, occurred at an average of about 1% strain and exceeded the initial peak capacity by 6%. This stress was calculated based on the gross area of the original prism. However, since the load was being carried by only the remaining confined material (57% of the original area), this indicates that the true stress carried by this remaining area was almost double the reported value, peaking at a stress of 33.5 MPa. This peak was followed by a gradual decrease in capacity as the specimen continued to undergo increasing strain, resulting in a very ductile failure of the prism. At the very large average strain of 2%, the prisms still retained a capacity equal to the peak capacity of the unreinforced prisms. The photographs in Figure 3.13 provide evidence of the significant damage present around the confining devices and the limited damage to the confined concrete at 2% strain. Even at strains of over 3%, the confined volume of grout and concrete block remained intact with significant reserve compressive capacity. Although drift limitations in shear wall buildings may make it unlikely that strains above 2% can be utilized in seismic design, to observe ultimate failure patterns, loading of the GPIR prisms was continued until the prism capacity decreased to 50% of the initial peak load. The decrease in capacity at this point was accompanied by local distortion of the steel confining devices and a sliding-like failure of the enclosed materials.

a) End View b) Face View

Figure 3.13. Typical Condition of a GPIR Prism at 2% Strain

3.3.11.Type II Prototype with Confining Device (GPIIR)

The detailed results of the five fully grouted prisms constructed from Self-Reinforced Type II prototype units are presented in Appendix B and average results are summarized in Tables 3.3 and 3.4 and in the stress-strain curve plotted in Figure 3.14.

The observed failure patterns for this series were consistent, following a pattern similar to that of the unreinforced series (GPII) up to an initial peak compressive stress capacity of 15.2 MPa. This peak capacity is approximately 15% greater at an approximately 5% higher strain than that of the unreinforced series (GPII). Figure 3.12 shows the typical splitting and spalling pattern for the GPIIR prisms that occurred as the initial peak load was attained. As observed with the unreinforced series (GPII), failure was initiated by vertical compression splitting of the face shell concrete allowing the outer block concrete to spall.

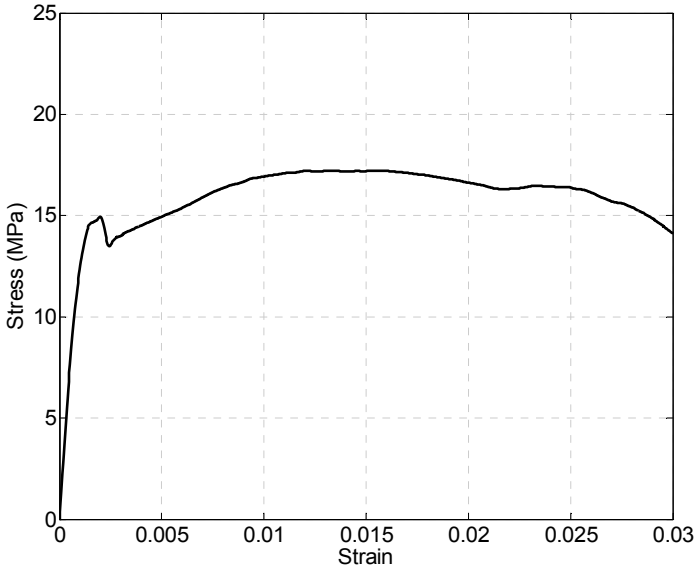

Figure 3.14. Average Stress-Strain Curve for GPIIR Prism Series

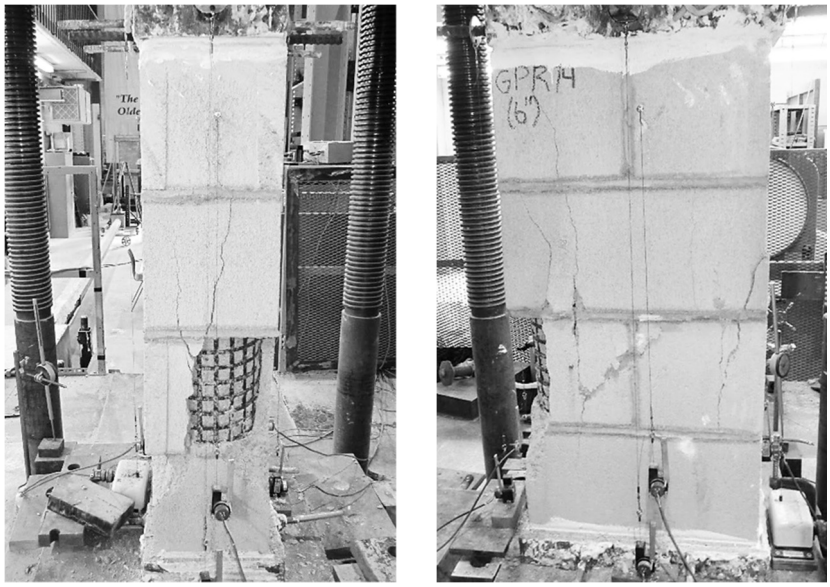

a) End View b) Face View

Figure 3.15. Typical Initial Splitting/Spalling of GPIIR Prisms at 0.3% Strain

Following the initial peak stress at an average strain of 0.0017, the spalling of the block concrete external to the confining devices resulted in a slight decrease in capacity (5% to 10%). With increasing strain, the prisms regained strength up to and surpassing the original peak capacity. This average second peak of 18.0 MPa, occurred at an average strain of about 1.4%. This stress was calculated based on the gross area of the original prism and exceeded the initial peak capacity by 18%. However, since the load was being carried by only the remaining confined materials

(57% of the original area), the true stress carried by this reduced area (31.6 MPa) was almost double the reported value. This second peak strength was followed by a gradual decrease in capacity with increasing strain, resulting in a very ductile failure of the prism. At the very large average strain of 2%, the prisms still retained a capacity considerably higher than the peak capacity of the unreinforced prisms. Figure 3.16 shows the significant damage present around the confining devices and the limited damage to the confined materials at 2% strain.

In order to preserve three of the GPIIR prisms in an acceptable condition for retrofitting, loading of the second, third and fifth specimens in the series was stopped as the stress of each prism began to decrease from the second peak (between 1.5% and 2.2% strain). Loading of the first and fourth specimens was continued until the prism capacity decreased to 50% of the peak load. The decrease in capacity to this point was accompanied by distortion of the steel confining devices and a sliding-like failure of the enclosed materials. As was the case with the GPIR prisms, at strains of up to and even beyond 3%, the confined volume of grout and concrete block in the GPIIR prisms remained intact with significant reserve compressive capacity.

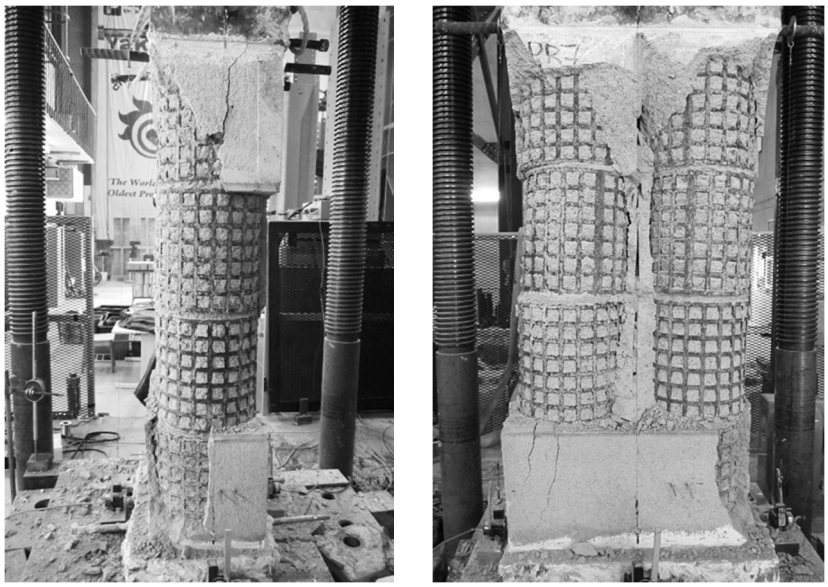

a) End View b) Face View

Figure 3.16. Typical Condition of a GPIIR Prism at 2% Strain

3.3.12. Type II Prototype with Confining Device – Anti-Shrink Grouts (GPIIR-A1 and GPIIR-A2)

Five prisms constructed from Self-Reinforced Type II prototype units and fully grouted with anti-shrink grout mix A1 were tested in series GPIIR-A1.

Additionally, two prisms constructed from Self-Reinforced Type II prototype units and fully grouted with anti-shrink grout mix A2 were tested in series GPIIR-A2. The complete results of these tests are presented in Appendix B. Average values are presented in Tables 3.3 and 3.4 and in the stress-strain plots in Figure 3.17. As the observed failure patterns for this series did not differ from the GPIIR series, test photos have not been presented.

Prisms in the GPIIR-A1 series achieved an initial peak stress of 15.2 MPa. The second peak stress of 16.0 MPa occurred at an average strain of 1.56% and exceeded the initial peak stress by 5%. Prisms in the GPIIR-A2 series achieved an initial peak stress of 16.3 MPa. The second peak stress of 14.9 MPa occurred at an average strain of 0.0102 and was almost 10% lower than the initial peak stress. These somewhat lower post-initial peak results can be attributed to the differences in strength between the anti-shrink grouts and the standard grout used in other prisms series and will be discussed in the following analysis. However, despite this lower second peak, over 80% of the initial peak capacity was maintained beyond 2% strain for both anti-shrink grout series.

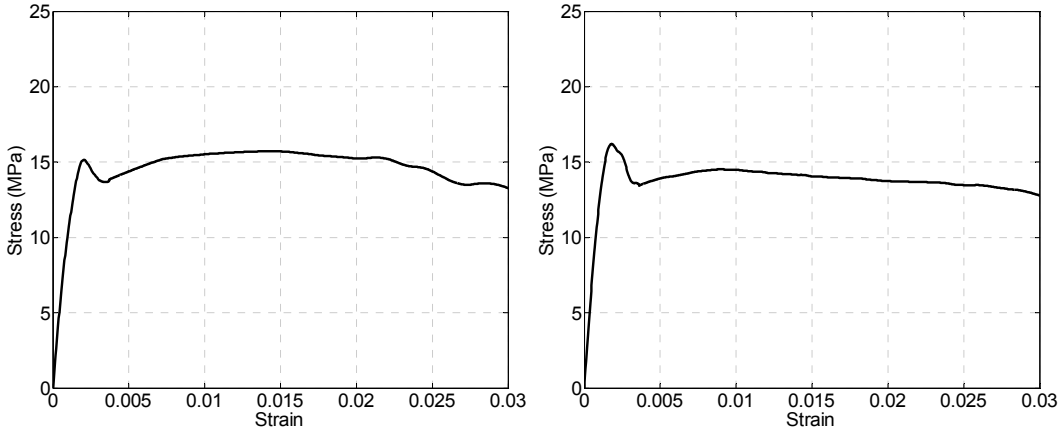

a) GPIIR-A1 Series b) GPIIR-A2 Series

Figure 3.17. Average Stress-Strain Curves for the Anti-Shrink Grout Prism Series

3.4. Analysis

3.4.1. Properties of the Different Block Types

As this study introduced not only a new confinement technique, but also new block configurations, it was important to first compare the performance of the prototype blocks to that of industry standard blocks in an unconfined state. It was concluded that compaction of concrete was the same for all block types as they were produced for the same batch of concrete in the same manufacturing run and had equivalent densities as presented in Chapter 2. This allowed direct comparison of the performance of each block shape without having to account for other variables. As

was previously stated, the mass of the Type II prototype block fell between that of a standard stretcher and standard splitter (end) block while the mass of the Type I prototype block was approximately 25% higher than that of a standard splitter (end) block. The average block strengths for the two prototypes were similar and both were slightly below that calculated for the standard blocks (see Chapter 2).

3.4.1.1. Ungrouted Prisms

The average stress-strain curves for all ungrouted prism series are presented together in Figure 3.18. In an ungrouted state, prisms constructed from standard stretcher and standard splitter blocks achieved almost identical average peak stresses. In comparison, the Type I prototype block prism stress-strain curve followed a similar shape to that of the standard splitter prisms, but had a lower peak stress, which can be associated with the different type of failure experienced by these specimens. While all other ungrouted series displayed typical in-plane tension splitting of web concrete to initiate failure, the Type I prototype series also experienced some local spalling of face shell concrete.

The decrease in strength and change in failure mode is thought to be due to the large volume of mortar causing larger lateral tension in the block (Chahine 1989). This is considered to outweigh the benefit of having increased thickness of webs and face shells to resist in-plane splitting at the top and bottom of the blocks. The increased out-of-plane lateral tension in the face shells and webs resulted in a local failure under tension-compression conditions. This type of failure is common in solid and semi-solid units, and is the origin of the approximately 25% lower masonry strength (f'_m) values in Table 4 of CSA S304 (CSA 2004a) for this type of block compared to that of hollow units. Previous work by Chahine (1989) concluded that, as the volume of block increases from 50% to 75% to 100% solid, the failure mechanism changes from web cracking to a combination of face shell and web cracking and then to local face shell cracking alone. As the Type I prototype blocks were approximately 78% solid, this failure type, could be expected to be dominated by face shell cracking. Conversely, the Type II prototype block prism stress-strain curve, which also followed the shape of the standard splitter prisms, reached a peak stress approximately 10% higher than either of the standard block prisms, despite having a much larger mortar bedding area over which the applied load was divided. This could be explained by better alignment of the prototype blocks in running bond construction allowing for the development of nearly uniform stress throughout the block.

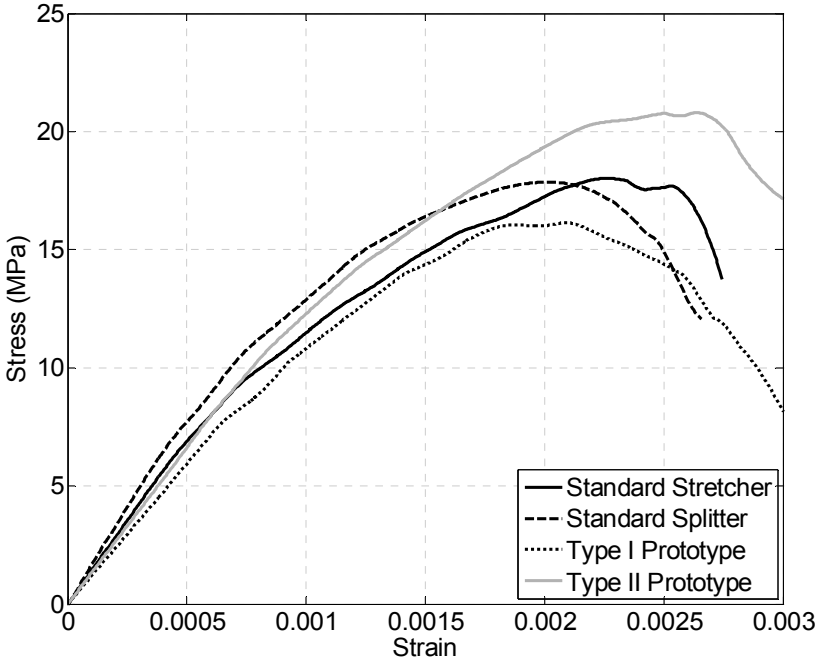

Figure 3.18. Comparison of Average Stress-Strain Curves for the Ungrouted Prism Series

3.4.1.2. Grouted Prisms

The stress-strain curves for all grouted test series are presented together in Figure 3.19. In a grouted state, the standard stretcher, standard splitter and Type II prototype block prisms performed in an almost identical manner, followed the same observed failure patterns and achieved similar peak stresses. The Type II prototype prism capacity fell between those of the standard stretcher and splitter prisms. The Type I prototype block prisms, however, attained a capacity approximately 20% higher on average than the other series. This could be attributed to the combination of the larger volume of block concrete in the prism resulting in increased thickness of webs and face shells to resist splitting, and the smaller volume of grout in the cells resulting in reduced lateral pressure to produce lateral tension in the block and subsequent splitting. This effect has been observed in previous testing (Wong & Drysdale 1985) and is accounted for in Table 4 of CSA S304 (CSA 2004a), which treats grout filled block that is 75% or more solid in the same way as solid block.

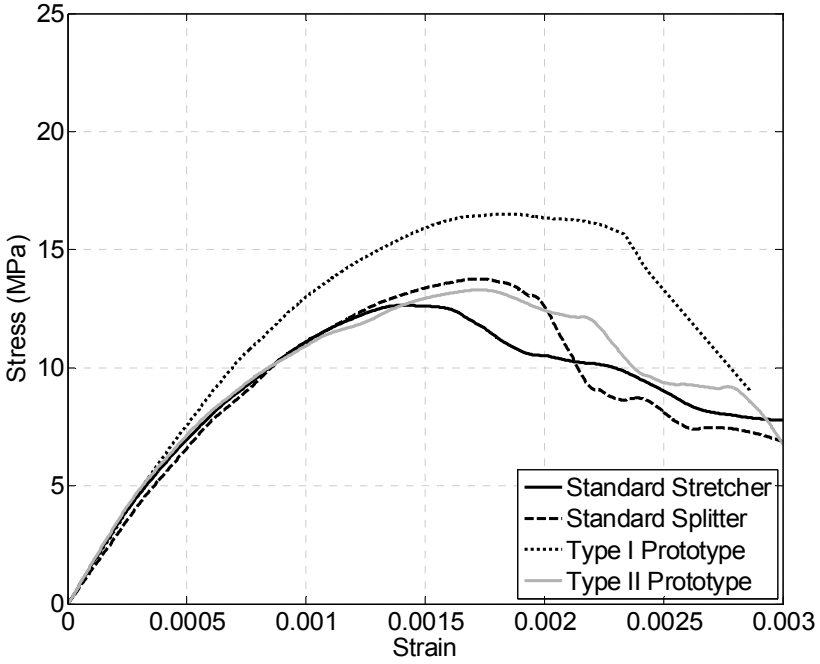

Figure 3.19. Comparison of Average Stress-Strain Curves for the Grouted Prism Series

3.4.2. Comparison of Self-Reinforced and Unreinforced, Grouted Prisms Constructed with Type I and II Prototype Blocks

Stress-strain curves for the unreinforced and SR Block prisms are presented together for the Type I prototype block series and for the Type II prototype block series in Figure 3.20. These curves indicate that, within the elastic loading range of the prisms (prior to cracking of the face shell concrete), the presence of the confining device has little influence on the stress-strain response of the prism. At the initial peak stress, the approximately 10% increase in SR Block prism strength can be attributed to the presence of the vertical steel strips within the confining devices acting as vertical reinforcement. Otherwise both sets of prisms followed the same pattern up to the initial peak capacity. Following the initial peak, both curves show a decline in capacity but, while the unreinforced specimens rapidly lost all capacity at a strain of approximately 0.3%, the self-reinforced specimens regained strength. As the enclosed concrete and grout underwent vertical strain, the resulting lateral expansion against the confining device created a triaxial compression state of stress in the confined concrete and grout that enhanced the vertical compressive strength of this remaining 57% of the original cross-section. This beneficial effect was sufficient to allow full load capacity to be regained and exceeded up to very high strain levels.

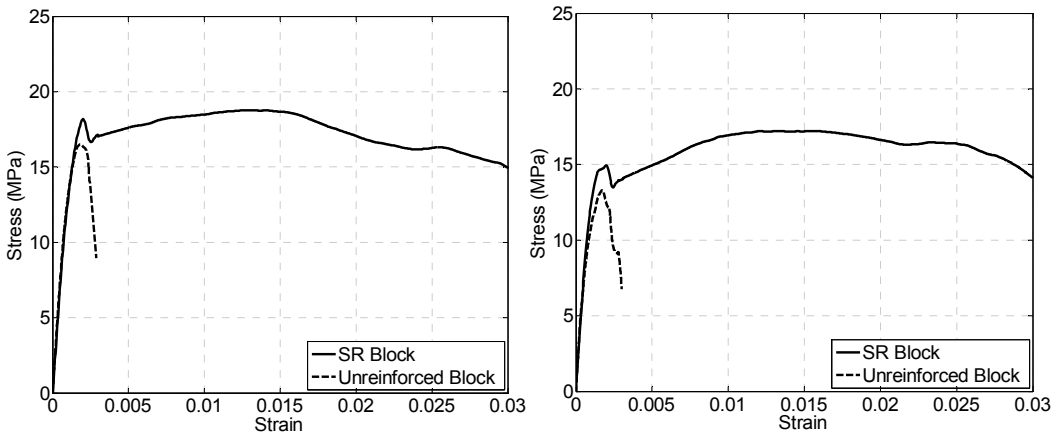

a) Type I Prototype Block b) Type II Prototype Block

Figure 3.20. Comparison of Stress-Strain Curves for Self-Reinforced and Unreinforced, Grouted Prisms

3.4.3. Comparison of SR Block Prisms Constructed with Type I and Type II Prototype Blocks

Stress-strain curves for the SR Block prisms for Type I prototype and Type II prototype block are presented together in Figure 3.21. As previously noted, compared to results for Type II prototype series, the increased volume of block concrete (and decreased volume of grout) in the Type I prototype series resulted in higher initial peak capacities, and subsequently, higher secondary peak stresses. However, the second peak stress for the Type I prototype series represents only a 3% increase over the initial capacity while for the Type II prototype series, the second peak averaged 17% higher than the initial peak capacity. This indicates that, after the spalling of the external concrete at strains where the confining devices become effective, there is little difference between the two prototype blocks. In fact, at strains of approximately 2%, the stress-strain curves for the two block types converged and followed a similar trend for the remainder of loading.

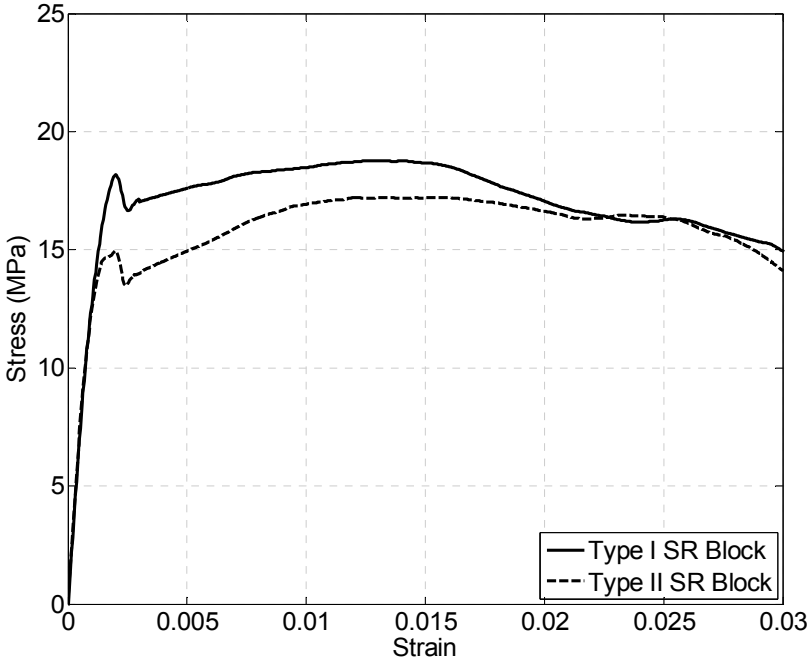

Figure 3.21. Comparison of Stress-Strain Curves for Type I and Type II Self-Reinforced Block (Grouted)

3.4.4. Comparison of Use of Standard Versus Anti-Shrink Grouts in SR Block Prisms

The observed failure patterns for the anti-shrink grout prism series (GPIIR-A1 and GPIIR-A2) were consistent with those observed for the GPIIR series. Stress-strain curves for all three of these series are presented together for comparison purposes in Figure 3.22. Contrary to initial expectations, the use of anti-shrink grout did not significantly reduce the stress decrease that followed the initial peak capacity. A certain amount of lateral expansion of the core concrete was still required to engage the effects of the confining device and during this expansion, a decrease in capacity similar to that of the standard grout series was observed. However, in all cases with and without the anti-shrink grouts, the lowest stress experienced during this capacity decrease remained above the capacity (f'_m) of the corresponding unconfined series (GPII), indicating that the SR Block was effective in maintaining a capacity above the intended strength throughout the loading history.

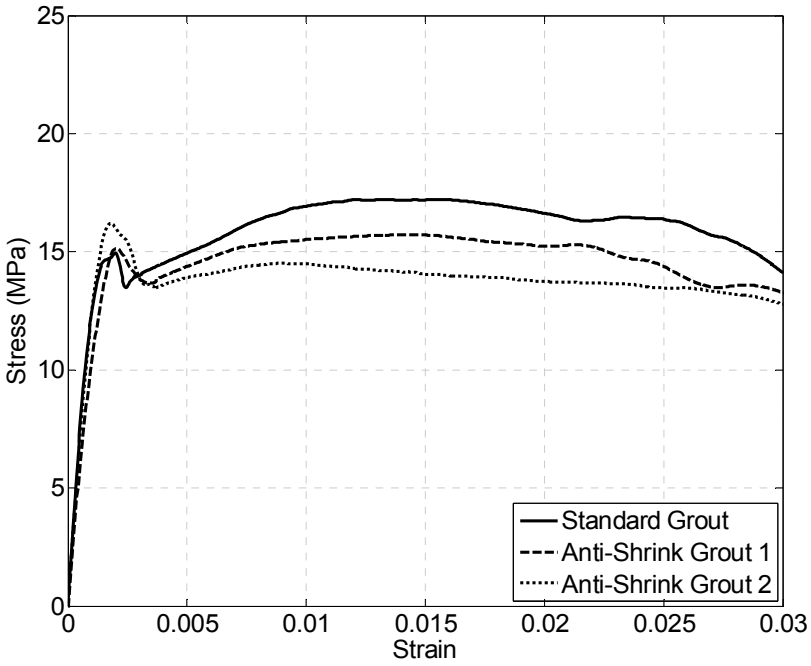

Figure 3.22. Comparison of Stress-Strain Curves for Type II Self-Reinforced Block with Standard and Anti-Shrink Grouts

The initial peak stresses for prism series GPIIR-A1 (15.2 MPa) and GPIIR-A2 (16.3 MPa) were comparable to those obtained with the standard grout (GPIIR). However, it seemed that the slightly (9%) lower strength of the anti-shrink grout mix A1 and the much (43%) lower strength of the anti-shrink grout mix A2 (see Chapter 2) resulted in lower secondary peak stresses for these prism series compared to SR Block prisms with standard grout. Nonetheless, it is worth noting that, even with much lower strength grouts, the confining devices remained effective in maintaining over 80% of the initial peak capacity beyond 2% strain. The ability of the specimens with a lower grout strength to reach equivalent peak stresses to specimens with standard grout is not unexpected as assemblage strength (f'_m) has been shown to be much more dependent on block strengths (compressive and tensile) than on the strength of the grout (Chahine 1989). The secondary peak strengths, however, appear to be more dependent on the grout strength as 73% of the confined area is composed of grout, resulting in a weaker overall confined material.

3.5. Retrofitting Procedure and Results of Retested Prisms

A subset of prisms from the GPIIR series were preserved during testing in order to be repaired to investigate the efficacy of a retrofitting procedure on damaged SR Block construction.

3.5.1. Retrofitting Procedure

As was previously stated, loading of the second, third and fifth specimens in the GPIIR series was stopped as the load resistance of each prism began to decrease from its second peak stress (between 1.5% and 2.2% strain). This termination point for original testing was adopted to maintain the prisms in a condition that may be considered appropriate for retrofit in the field where it is unlikely that strains above this range could be experienced during an earthquake. Following testing, each of these prisms was carefully removed from the test setup and separated from the steel capping plates. Any concrete that could be easily pried loose from the parts of the prisms external to the confining devices was removed; the material located within the confining devices was found to be very sound and none was removed. The specimens were then placed horizontally in wood forms conforming to original dimensions of the prisms except that the height was adjusted to preserve the displaced prism height after the first test (see Figure 3.23).

Figure 3.23. Tested SR Block Prisms Positioned in Forms in Preparation for Repair

It is worth noting that upon close inspection of these and other tested SR Block prisms, it was observed that the position of the confining devices varied from the intended, centred position by up to 10 mm, but generally by less than half that amount. (It may be recalled that the confining devices were hand positioned on the bottom plates of the block mold during manufacturing without any restraining device to keep them in place during filling the molds and compaction of the concrete.) These issues related to both potential misplacement and displacement within the block molds were addressed in subsequent manufacturing runs as described in Chapter 4.

Previous research by Atkinson and Schuller (1993) documented the use of expansive admixtures to ensure minimal plastic shrinkage of repair grout.

Consequently, the anti-shrink grout mix 1 containing both Type K cement and Sika Intraplast-N admixture which was used to grout the GPIIR-A1 series was also used in the repair of these prisms. The admixture also contained fluidizing agents, which helped to ensure complete filling of the forms and around the spalled specimens. After pouring and vibrating the fluid grout around the existing specimens, they were moist-cured for a 28-day period under wetted burlap. Upon removal of the formwork, no voids were visible and, as confirmed by inspecting the specimens again during and after retesting, full compaction had been achieved. Figure 3.24 shows the repaired prisms immediately following grouting and after removal of formwork. The repaired prisms were tested in the same manner as the original prisms, except that loading was continued until a 50% reduction below peak capacity was reached.

a) Prisms in Horizontal Formwork b) Prism Removed from Form

Figure 3.24. Retrofit Prisms Following Completion of Repair Grouting

3.5.2. Retrofit Prism Test (GPIIR-R) Results

The observations for the three initial (original) tests of these specimens were presented with the GPRII series above. The specific stress values for each test are presented again in Table 3.5 to facilitate direct comparison with the retrofit results. The repaired prisms consistently exceeded the capacity of the original prisms and exhibited equally large strains at stresses exceeding the peak stresses in the original tests. This improved strength behaviour was not a necessary or sought after result but is easily explained. The average strength of the repaired prisms was approximately 50% greater at the initial peak capacity than that of the original prisms at their initial peak capacity. Considering the 22.2 MPa strength of the repair grout versus the 13.4 MPa (original grouted f'_m) or the 21.0 MPa (ungrouted f'_m)

strength of the original mortared block outside of the confining device, an increase of this magnitude could be predicted. As this unconfined material gradually began to spall, the behaviour of the prisms gradually reverted to the observed behaviour recorded at the end of the original tests. For this reason, no second peak capacity was either expected or observed. The grout strength was in the range of what would normally be considered as in the lower range of what is encountered in construction. The results for the retrofit tests are also presented in Table 3.5.

Table 3.5. Peak Stress Results for Original and Retrofit Prism Tests

Prism No.	Original Test (GPIIR Series)		Retrofit Test (GRIIR-R Series)
	Initial Peak Stress (MPa)	Secondary Peak Stress (MPa)	Initial Peak Stress (MPa)
2	13.2	17.9	24.3
3	15.0	16.9	21.3
5	15.7	17.5	20.5
Average	14.6	17.4	22.0
C.O.V. (%)	8.7	3.0	9.0

Observed failure patterns for the three repaired prisms were consistent, initiating with vertical cracks in the centre courses, followed by propagation along the full height of the prism at increased vertical strains. As shown in Figure 3.25 a), spalling at the ends of the prisms over the middle courses occurred first at a strain of 0.003 to 0.004. The exposed confining devices began to noticeably bulge at high strains of 0.015, coinciding with spalling across the faces of the prisms as shown in Figure 3.25 b). However, even at strains of 0.015 to 0.025, some areas of repair concrete remained intact between the two columns of confined material.

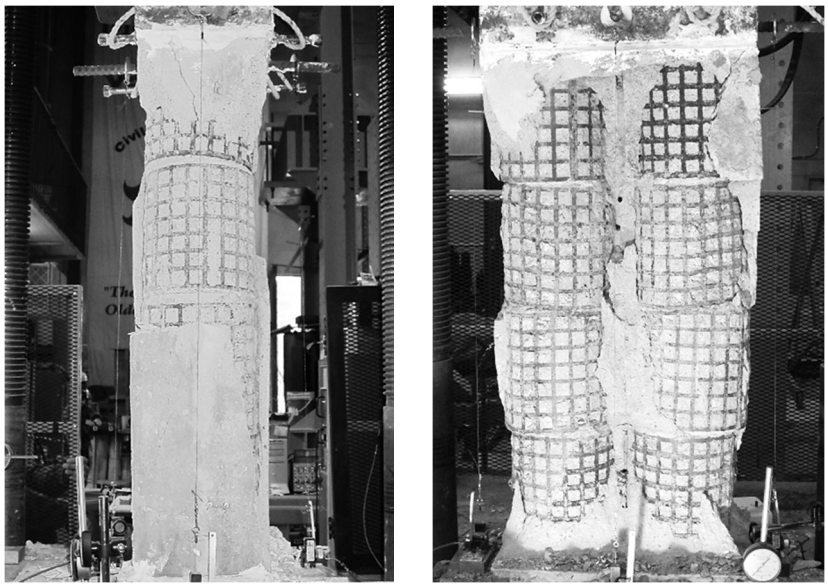

a) End Spalling at 0.4% Strain b) Device Bulging at 1.5% Strain

Figure 3.25. Progressive Failure Patterns Observed for GPIIR-R Series

3.5.3. Analysis of Retrofit Prisms

The stress-strain curves from tests before and after repair of each prism are presented in Figures 3.26 to 3.28. Inspection of the unloading curves from the original specimen tests confirmed that the reloading up to the initial peak capacity followed a similar slope/stiffness to that of the unloading during the original tests. Consequently, in order to present an accumulated compression strain for each specimen, the retrofit stress-strain plots have been shifted to account for the residual strains in these prisms. (The incremental strain recorded during the tests of the retrofit prisms is indicated at the top of each plot.)

As can be seen in all cases, the repairs effectively restored the initial high stiffness of the grouted concrete block prisms under compression loading. The repaired prisms exhibited two distinct failure modes. Two of the prisms reached peak strength at the time of failure of the repair concrete with no subsequent load gain. The third repaired prism (GPIIR5) behaved in a pattern similar to the original prisms with two distinct peaks. However, unlike the original prism tests, the second peak did not reach the initial repaired peak capacity.

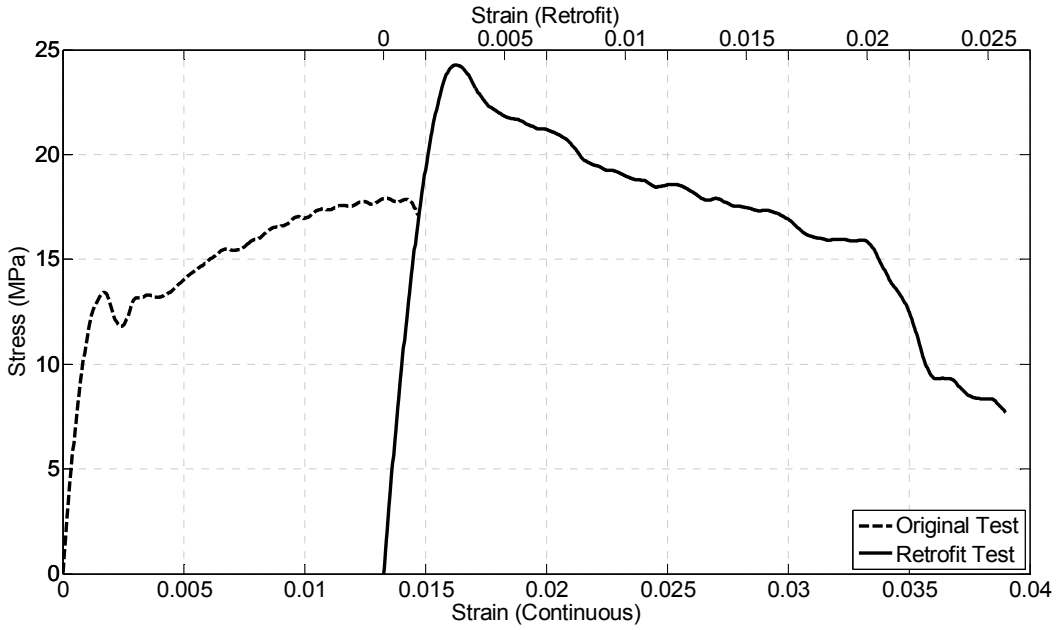

Figure 3.26. Stress-Strain Curves for Prism GPIIR2 Before and After Repair

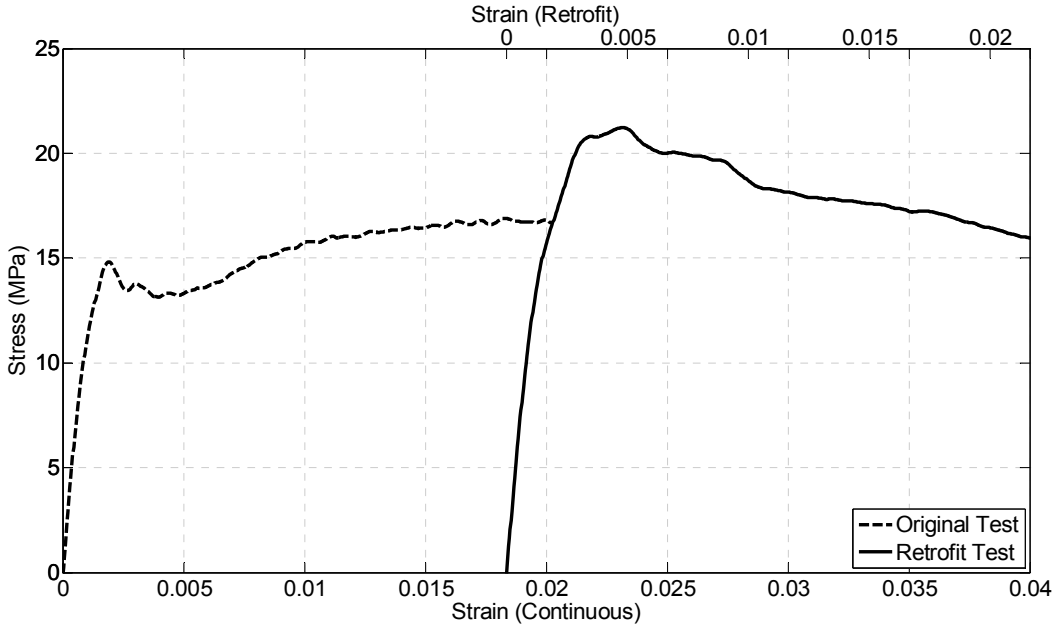

Figure 3.27. Stress-Strain Curves for Prism GPIIR3 Before and After Repair

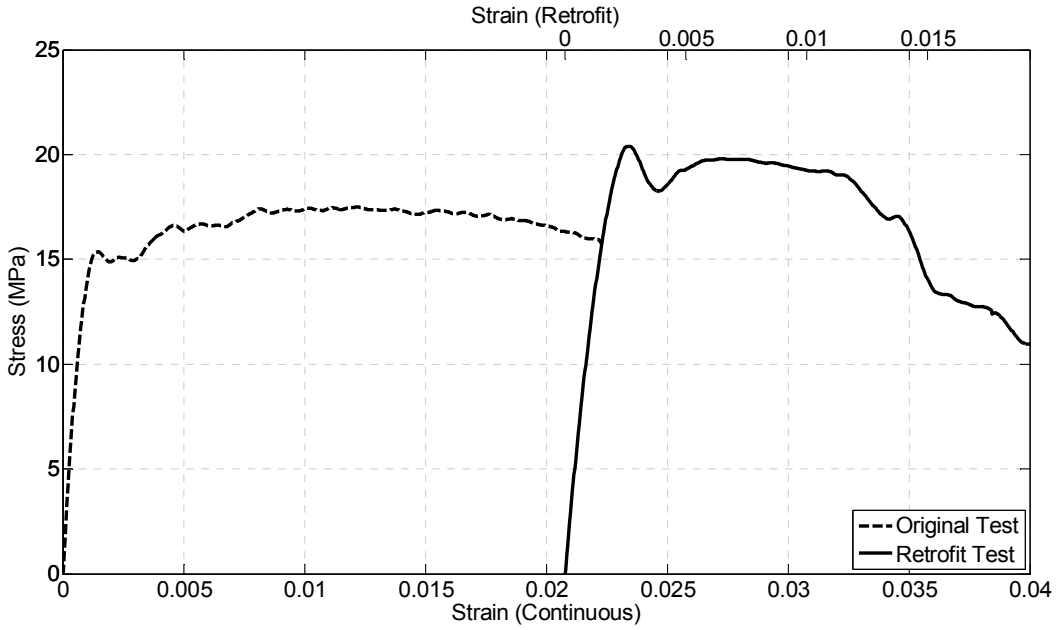

Figure 3.28. Stress-Strain Curves for Prism GPIIR5 Before and After Repair

As could be seen more easily if the original and retrofit test strains were plotted from the same origin (overlapping), the strengths of the repaired prisms gradually decreased until they converged with the stress-strain curves of the original prisms. This occurred at an average stress corresponding to the point at which original testing of the prisms was terminated. The fact that this intersecting phenomenon coincided with the very high spalling strains indicates that the repaired prisms had returned to the original damaged condition sustained at termination of the original tests. The plotted results in Figures 3.26 to 3.28 illustrate the continued effectiveness of the confinement following repair and the ability of the prisms to reach cumulative strains of over 3% without significant decreases in capacity. This is the same as was the case with prisms GPIIIR1 and GPIIR4, which were tested monotonically to failure. The ability of the prisms to be repaired and remain stable following application of new high compression strains is attributed to the lateral confining devices within the blocks continuing to effectively confine the enclosed parts of the cross-section.

3.6. Conclusions

The proof-of-concept prism data presented in this chapter clearly showed that the inclusion of steel confining devices within the body of concrete blocks works very well as a method of permitting the confined block and grout material to reach compressive strains that are an order of magnitude larger than achievable in standard block. This was achieved with only a temporary, small decrease in capacity followed by an increase in capacity to levels significantly higher than the

initial peak values. The following specific conclusions were drawn from these test series regarding the new prototype block designs:

a) Prisms made with (unreinforced) Type I prototype blocks (with small cells) had higher initial capacities than standard blocks in a grouted state. While this was a satisfactory result, when the negative effect for construction due to the increased mass of each unit was considered, it was concluded that this prototype block was not an ideal solution. It had previously been seen that the larger body of concrete was not necessary to achieve compaction around the confining devices during block manufacture.

b) Prisms made with (unreinforced) Type II prototype blocks performed equivalently to standard blocks in a grouted state. These results along with consideration that the mass of each unit was similar to standard block led to the decision that this was a more suitable block shape, having the minimum face shell and web thicknesses equal to 30 mm which satisfied the minimum requirements of CSA A165 (CSA 2004d) for hollow concrete block geometry.

c) The Type I prototype blocks provided little benefit over the Type II prototype blocks in a grouted, self-reinforced state. While both were technically feasible, the Type II prototype is a more economical design and provides a higher level of constructability with more space for grout consolidation and placement of vertical reinforcement. This further supports the decision to adopt this design in subsequent tests.

Additionally, from the test data reported and analyzed above, the following more detailed observations were made:

d) All SR Block prisms initially reached load carrying capacity in excess of the peak capacity of their unreinforced counterparts. After undergoing spalling of the block and mortar material outside of the confining devices and a small decrease in load resistance, all SR Block prisms reached second peak capacities considerably in excess of the initial peak capacities.

e) All SR Block prisms retained at least the capacity of their unreinforced counterparts up to strains of at least 2%, an increase of over sixfold (compared to the failure strain of 0.3% observed for equivalent unconfined prisms) and a tenfold increase compared to the 0.2% strain at peak stress in the unconfined prisms.

f) No discernible benefit was observed for grouting SR Block prisms with anti-shrink mixes compared to use of standard grout.

g) Retrofit tests of SR Block prisms demonstrated that initial stiffness and strength of the concrete block masonry can be fully restored using a simple and economical repair technique.

h) Repaired prisms remained stable following application of new high compression strains due to the lateral confining devices within the blocks continuing to effectively confine the enclosed parts of the cross-section.

While this test program satisfied all proof-of-concept objectives with very encouraging results, observations during this preliminary testing led to the following suggested improvements for further testing and eventual application:

i) A process is required to ensure accurate positioning of the confining devices in the block mold and to hold those devices in place during filling and consolidating the concrete in the mold.

j) Although the 30 mm minimum thickness of the face shell in the prototype block satisfies CSA A165 requirements (CSA 2004d), it remains slightly lower than the 32 mm minimum face shell thickness presently used by block producers in Canada. Acceptability of the thinner face shell should be investigated.

k) Beyond the minimum face shell thickness consideration, the desire to maximize the size of the confined section led to an embedment cover of the confining devices within the block concrete of only 11.5 mm, leaving the steel susceptible to corrosion. This issue could be addressed by using corrosion resistant material to make the devices or by providing a form of corrosion resistance on the steel after manufacture of the devices.

In terms of future application of this method of developing high ductility and energy dissipation in reinforced concrete block construction, the following potential savings and benefits are suggested based on the observed behaviour:

l) If design codes only permit reliance on comparatively low increased compression strains such as the 0.8% proposed for masonry in the next edition of CSA S304 (CSA 2014) or the 1.4% currently allowed in CSA A23.3 (CSA 2004b) for concrete, a reduction in the amount of confinement required would be justified. Similarly, if retention of 80% of peak compressive capacity at high strains is deemed to be satisfactory, there will be less need for high confining pressures. For either or both of these reasons, the reduced amount of required confinement would result in reducing the cost of confining devices.

m) The confined material was observed to remain able to resist high stresses at repeated cycles of very high strain. The apparent soundness of this confined

material indicates that it should be able to support and prevent buckling of compression reinforcement. This would add significantly to the calculated capacity of reinforced masonry where, currently, reinforced bars in compression are not allowed to be included in strength calculations because of the concern that buckling could occur. This change would improve efficiency of masonry design.

CHAPTER 4

MATERIAL AND PRISM TESTING ASSOCIATED WITH THE SHEAR WALL TEST PROGRAM

4.1. Introduction

Following the initial proof-of-concept prism test program, a second program of prism tests was developed to serve two main purposes. Firstly, the program was to investigate the effectiveness of a second confining device design for the SR Block that used spiralled wire to replace the punched steel tube design. Secondly, the tests served as companion material testing for two shear walls constructed in parallel with these prisms. For this reason, all material strength and prism test results presented in this chapter are applicable as material tests for the shear wall test program presented in Chapter 5. These tests were performed using identical test configuration and procedures described in Chapter 3.

4.2. Procedure

4.2.1. Design of Confining Device

As an alternative to the punched steel tube design of the confining device tested in the proof-of-concept program, a device design more like standard transverse reinforcement in ductile reinforced concrete columns was tested for this program. The aim was to provide a similar amount of steel with similar spacing as was found to be effective in the initial proof-of-concept tests.

The spiral devices were produced by a manufacturer of coils and mechanical springs with existing equipment. Adopting a spring shape, a 4.76 mm ($^{3}/_{16}$”) diameter wire was coiled at a pitch of 22.2 mm ($^{7}/_{8}$”) to a centre-to-centre diameter of 165.1 mm (6½”). The coil was cut so that, with the ends squared (closed), it would stand level at a height of 184.2 mm (7¼”) to provide confinement for the complete block height. In order to provide vertical stiffness during block manufacturing and to maintain consistent spacing between turns of the spiral, four 3.2 mm ($^{1}/_{8}$”) diameter steel wire members were welded vertically to the inside of the device at each turn. An additional weld was made at the top and at the bottom of each device along where the coil was squared off to sit level in the mold. This was to prevent unravelling of the coil due to lateral expansion. A photograph of a completed device is shown in Figure 4.1 a).

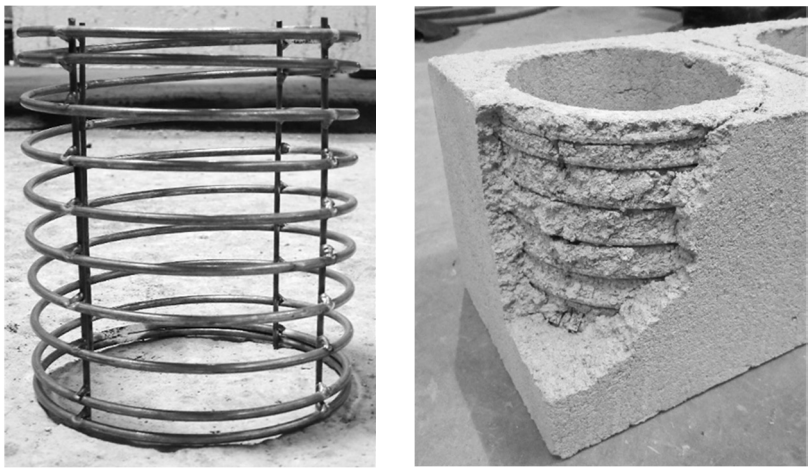

a) Complete Spiralled Wire Device b) Embedment of Device in Block

Figure 4.1. Spiralled Wire Device

Due to time constraints and the limited availability of highly deformable (ductile) steel wire, several different wire types were tested prior to manufacture of these devices. Although wire Type B (WB) was determined to be the most suitable option based on the lower yield strength and higher elongation at failure, limited availability of this steel meant that some of the devices had to be produced using Type A (WA) and Type C (WC) steel wires. (As will be detailed in Chapter 5, care was taken to position the blocks containing these latter devices in less critical areas of the walls.)

Unlike the previous block-manufacturing trial in which the devices were placed on the bottom plate of the mold, hand-centred and raised into place around the cores, a different technique was implemented during block manufacture with these spiral confining devices. Clips made from steel strapping were bent to fit between spirals and notched to fit around the vertical steel rods. With one clip placed along each of the four vertical rod members (see Figure 4.2), they served to accurately position the confining devices around the core of the block mold. Also, the stiffness of these clips was sufficient to hold the weight of the device around the core bars of the form until the base of the form was raised into place. Hence, the devices were not placed on the bases but rather were initially placed around the cores used to mold the block cells. After the mold had been filled with concrete, the friction between the core and the clips was sufficiently low as not to impede demolding and the device remained embedded within the fully compacted concrete as can be seen in Figure 4.1 b).

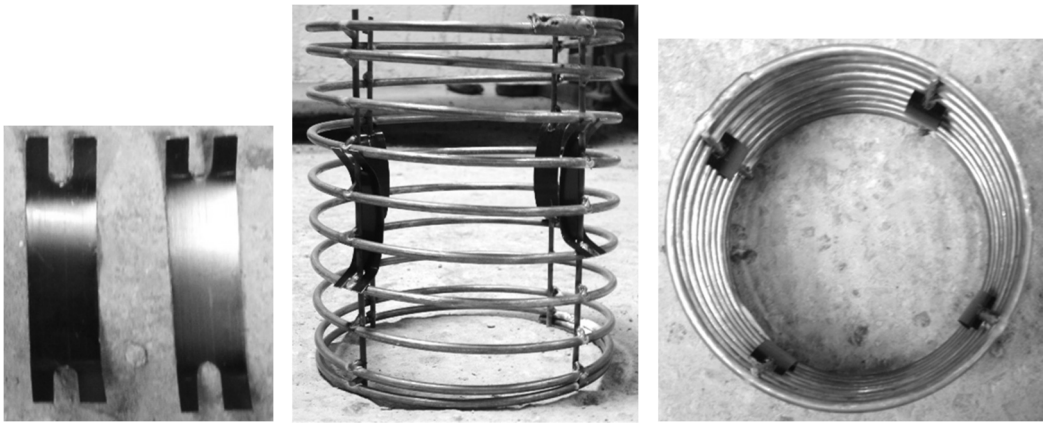

a) Bent Steel Clips

b) Side View of Clips Fit to Vertical Rods

c) Top View of Clip Placement around Perimeter

Figure 4.2. Use of Steel Clips for Positioning Confining Device in Block Mold

4.2.2. Test Program

Based on the results of the previous test program, the Type II prototype block configuration was selected for subsequent SR Block and unreinforced prototype block manufacturing and is henceforth referred to simply as Prototype block. As this program was designed both to investigate the performance of the different style of device and as a material test program for the shear walls, it was necessary to test a total of 18 prisms comprising six different series of three prisms each as summarized in Table 4.1.

For the purpose of material testing, it was important to test grouted prisms constructed from both standard stretcher and SR Block units which made up the majority of the wall construction. As standard splitter (end) blocks were only present at the ends of the walls well above the critical compression zone, and the behaviour of splitter block prisms had previously been compared to that of stretcher block prisms and prototype block prisms, tests of standard stretcher block were deemed sufficient to confirm material properties and no standard splitter (end) block prisms were tested for this program.

Grouted, unreinforced prototype block prisms were also tested in this program in order that the behaviour of the spiral SR Block could be quantified without needing to account for possible influences of variations in material properties of these tests compared to the proof-of-concept tests. To be able to relate results of this program to results from the previous test program, tests were also performed on ungrouted prisms constructed from both standard stretchers and prototype block as an indicator of the assemblage (mortar and block) strengths.

Within the SR Block prism series, prisms containing confining devices produced from two different types of steel were tested. In testing of the device steel, Type WA steel and Type WB steel performed quite differently and provided bounds for the performance of Type WC steel. For this reason, it was deemed unnecessary to test prisms with Type WC steel devices.

Table 4.1. Prism Test Series

Series Reference	Block Type	Grouting
UST	Standard Stretcher	Ungrouted
GST	Standard Stretcher	Standard Grout
UP	Prototype Block	Ungrouted
GP	Prototype Block	Standard Grout
GPR-WA	Prototype Block with Confining Device (Type WA Steel)	Standard Grout
GPR-WB	Prototype Block with Confining Device (Type WB Steel)	Standard Grout

4.2.3. Procedure Notes

Procedures for construction and testing of these prisms followed those outlined for the proof-of-concept test program. Construction of the prisms for this program occurred over a one-week period in parallel with construction of the shear walls by an experienced mason. All construction specifications outlined in Chapter 2 were also followed for this program.

4.3. Material Properties

Tests were performed on all of the materials involved in construction of both the prisms in this program and the shear walls presented in Chapter 5. The strength properties for all tested materials are presented in Table 4.2 and the corresponding test procedures are described below. A complete record of material test results has been provided in Appendix A.

Table 4.2. Material Properties (for Prisms and Shear Walls)

Material Test		**Average Strength (MPa)**	**C.O.V. (%)**
Mortar		16.5	11.1
Grout	Cylinder	22.9	7.1
	Cell Molded	29.3	10.8
Block	Standard Stretcher	29.7	0.8
	Standard Splitter	25.9	3.7
	Prototype Block	28.3	2.5
Spiral Steel – WA	Yield (0.5% elongation)	620	1.5
	Ultimate	730	0.7
Spiral Steel – WB	Yield (0.5% elongation)	573	1.9
	Ultimate	692	2.0
Spiral Steel – WC	Yield (0.5% elongation)	608	3.7
	Ultimate	673	2.0
Shear Wall Base Beam Concrete		27.0	17.1
Wall Horizontal Reinforcement (10M)	Yield	491	2.4
	Peak (elongation strain at fracture)	688 (0.163)	3.2 (4.3)
Wall Vertical Reinforcement (25M)	Yield	423	0.8
	Peak (elongation strain at fracture)	628 (0.227)	0.2 (5.0)

4.3.1. Mortar

Type S mortar for all specimens was mixed in a wheelbarrow in 25 kg batches according to the mix proportions previously outlined in Table 2.2. A total of 20 batches were mixed for the construction of the two shear walls and 18 prisms. For each batch, a flow test was performed to ensure proper consistency; retempering was not permitted. Flow tests resulted in an average flow of 121% with a C.O.V. of 4.8%. Three mortar cubes were taken from each batch and tested in compression at the conclusion of the prism testing to obtain the average mortar strength for the prisms and walls presented above in Table 4.2. For the purpose of comparing prisms in this program with prisms from the proof-of-concept test program, it is noted that the average measured strength for mortar used in these series exceeded that of the previous series by 16%.

4.3.2. Grout

The fine grout used for all grouted prisms and the two shear walls was mixed in the horizontal drum type laboratory concrete mixer in 420 kg batches with proportions equal to the typical grout mix presented in Table 2.3. For the nine batches required, three 101.6 mm diameter cylinders were cast from each batch for material tests. Additionally, block-molded specimens more representative of in-situ strength were made from every second batch and, following curing, were saw-cut to 90 mm by 90 mm by 180 mm prisms for testing. Finally, one 152.4 mm cylinder was poured from every second batch so that Demec gauge points requiring a 200 mm gauge

length could be used to obtain representative stress-strain behaviour for the grout. As expected, the block molded prism strengths were approximately 30% higher than those obtained from the grout cylinders. The average elastic modulus obtained from the four cylinders with Demec instrumentation was 18.9 GPa (C.O.V. of 22.8%). Grout strength values were presented at the start of this section in Table 4.2. For the purpose of comparing prisms in this program with prisms from the initial test program, it is noted that the average strengths for grout used in these series were 7% less than that of the previous series.

4.3.3. Concrete Block

To limit material variability, all blocks used in this study were manufactured in the same production run using the same concrete batches. Tests were conducted on each block type to determine accurate values for dimensions and strength. Volume and density tests were conducted in accordance with ASTM C140M (ASTM 2013a) and the values were calculated according to Equations 2.1 to 2.3. The average net cross-section areas for determination of unit strength as well as the densities of each block, calculated to ensure consistency of compaction, are presented in Table 2.5. These properties varied very little from those obtained during the proof-of-concept testing. Three blocks of each type were tested in compression according to CSA A165.1 (CSA 2004d), which provided the average strength for each block type as presented in Table 4.2 using the appropriate cross-sectional areas. Four draw-wire potentiometers were situated within the test setup spanning from the loading plate to the top cap of each block during testing so that stress-strain behaviour for each block type could also be obtained. The elastic modulus results from these tests are also presented in Table 2.5 for each block type. For the purpose of comparing prisms in this program with prisms from the proof-of-concept test program, it is noted that the average strengths for blocks used in these series exceeded those of the previous series by an average of 5%.

Table 4.3. Concrete Block Types - Physical Properties

Block Type	**Average Cross-Section Area (mm^2)**	**C.O.V. (%)**	**Average Density (kg/m^3)**	**C.O.V. (%)**	**Average Elastic Modulus (GPa)**	**C.O.V. (%)**
Standard Stretcher (ST)	41,400	0.3	2170	0.5	9280	10.0
Standard Splitter (SP)	46,600	0.7	2140	1.2	8400	4.6
Prototype Block (P)	43,700	0.3	2160	0.2	9850	6.7

4.3.4. Steel Wire Used in Manufacture of Confining Devices

Several tension tests were performed on each of the three types of steel used to produce the spiralled wire confining devices in order to obtain stress and elongation characteristics. Tests were performed in a standard compression-tension machine and specimens were instrumented with an extensometer. Because of the curved nature of the coiled wire test specimens received from the manufacturer, an apparent softness was present in the initial portion of the raw stress-strain curves as the wires straightened under tension. In order to straighten specimens without damaging them and obtain a more accurate modulus of elasticity, specimens were loaded to approximately 60% of expected ultimate load and then unloaded to within 10% of ultimate load. In all cases, the reloading of specimens following this procedure occurred along an initially linear path identical to the linear unloading path. The validity of this loading path was checked for each test using the slope (elastic modulus), which was near to the expected 200 GPa in all cases. This path was considered to be an accurate representation of the material modulus and was extrapolated to zero load to eliminate the initial softness due to the initial bend in the steel specimens. Representative stress-strain curves for each type of steel are presented in Figure 4.3.

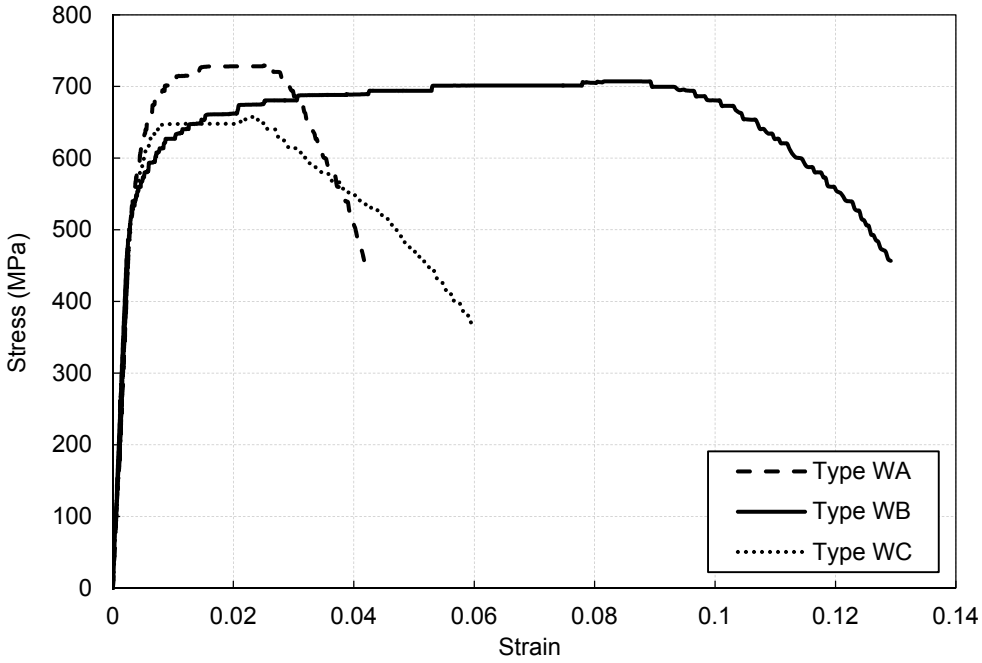

Figure 4.3. Stress-Strain Curves for Spiralled Wire Device Steel

These stress-strain curves illustrate the differences in properties between the three types of steel. Type WB is the most ductile steel, having the lowest yield strength and achieving over 10% elongation at fracture (according to ASTM A370 (ASTM 2012a)) and was the preferred material for producing all of the confining devices. However, due to limitations in quantity availability, other steel types were also utilized. Type WA was the most brittle steel, having the highest yield strength and the lowest elongation at fracture of approximately 3%. Type WC steel exhibited similar elongation characteristics to Type WA, while only attaining yield strengths in the range of Type WB. Yield strength values for these tests were determined in accordance with ASTM A1064 (ASTM 2013b) for wire reinforcement in concrete, as the stress corresponding to 0.5% elongation. The average yield strength and ultimate strength values for each type of steel were presented in Table 4.2.

4.3.5. Shear Wall Base Beam Concrete

The beams forming the base of each wall were cast from one batch of concrete provided by a ready-mix manufacturer. The concrete was ordered to a specified strength of 25 MPa to ensure sufficient strength for bond development of the vertical reinforcement and to withstand the axial forces expected at the base of the wall. During pouring of the beams, three 152.4 mm (6”) cylinders were also poured. These cylinders were tested in compression at the mid-point of wall testing and

results have been presented in Table 4.2. The average compressive strength of 27.0 MPa is within the range of what is likely to be used in footings in construction.

4.3.6. Shear Wall Reinforcement

Horizontal reinforcement was provided in both walls in the form of 10M deformed steel bars. Steel for this purpose was ordered from a reinforcement supplier and bent in the laboratory to have 180˚ hooks at each end. To obtain properties for this steel, three samples were selected at random and tested in tension using a compression-tension machine in the laboratory. Samples were instrumented with extensometers to measure elongation. Yield points of this steel were well-defined at an average of 491 MPa and have been presented in Table 4.2 along with peak strengths and total elongation at fracture.

Vertical 25M deformed reinforcement was provided in both walls. This reinforcement was ordered from a reinforcement supplier with a 90˚ bend at one end to provide anchorage in the base beam. To obtain properties for this steel, three samples were selected at random and were tested in tension using a compression-tension machine in the laboratory. A fourth sample was tested in which the deformations of the bar were ground to a smooth finish at the midpoint. As grinding in this manner was performed to mount strain gauges on the steel at some locations within the wall, this sample was tested to determine whether this grinding action would affect the strength and elongation characteristics of the material. As results from this specimen were similar to the other three test specimens, results from all four tests were averaged and presented in Table 4.2. Representative stress-strain curves for both types of wall reinforcement are presented in Figure 4.4, which show the yield strengths of 423 MPa and 491 MPa for the vertical and horizontal reinforcement, respectively.

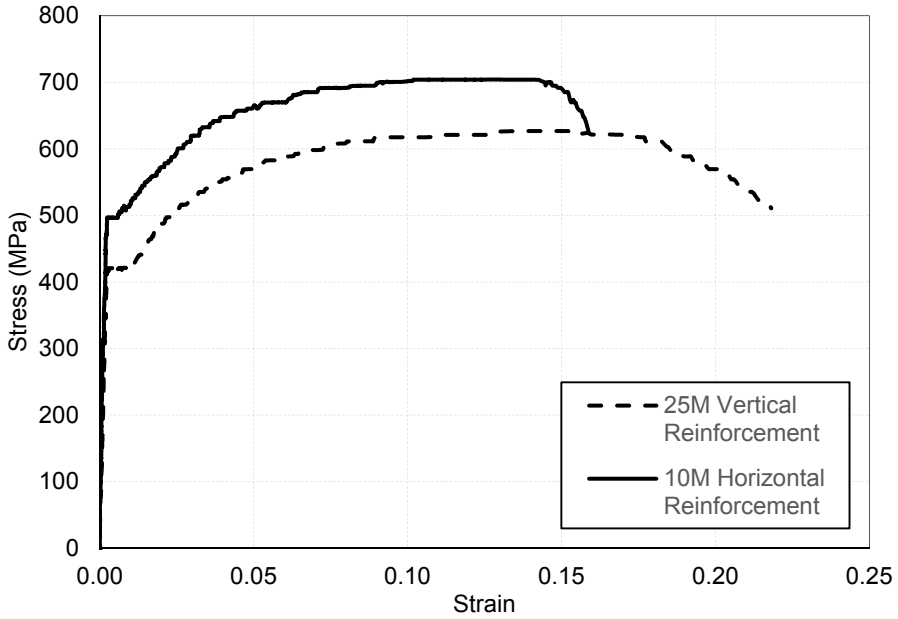

Figure 4.4. Stress-Strain Curves for Wall Reinforcement

4.4. Prism Test Results

Stress and strain results for all of the prism series for this phase of the research program are presented in detail in Appendix B and are summarized in Tables 4.4 to 4.6. Testing notes and observations follow. Stress-strain curves presented in this section represent the average results for each series and were constructed in a manner consistent with that described previously in Chapter 3.

Table 4.4. Summary of Results for Unreinforced Prism Series

Series	Average Peak Stress (MPa)	C.O.V. (%)	Average Strain at Peak Stress	C.O.V. (%)
UST (ungrouted stretcher)	18.3	7.7	0.0025	12.9
UP (ungrouted prototype)	17.6	16.7	0.0025	10.9
GST (grouted stretcher)	11.6	4.2	0.0013	5.8
GP (grouted prototype)	13.5	5.8	0.0016	6.1

Table 4.5. Summary of Peak Stress Results for Self-Reinforced Prisms

Series	Average Peak Stress (MPa)	C.O.V. (%)	Average Strain at Peak Stress	C.O.V. (%)
At Initial Peak Stress				
GPR-WA (Steel Wire A)	13.9	5.6	0.0016	6.1
GPR-WB (Steel Wire B)	12.6	2.7	0.0016	5.6
At Second Peak Stress				
GPR-WA	17.8	4.6	0.0239	1.3
GPR-WB	19.3	3.5	0.0238	5.7

Table 4.6. Summary of Results at High Strains for Self-Reinforced Prisms

Series	Average Stress (MPa)	% of Initial Peak Capacity	C.O.V. (%)
At 0.8% Strain			
GPR-WA	13.4	96	11.7
GPR-WB	13.0	103	1.6
At 1% Strain			
GPR-WA	14.5	104	7.9
GPR-WB	14.7	117	3.9
At 1.5% Strain			
GPR-WA	16.5	119	4.6
GPR-WB	17.5	139	3.3
At 2% Strain			
GPR-WA	17.6	127	4.6
GPR-WB	19.0	150	3.5
At 3% Strain			
GPR-WA	-	-	-
GPR-WB	16.4	130	3.0

4.4.1. Ungrouted Block Prisms

In this program, three ungrouted prisms in the UST series were constructed with standard stretcher blocks and three in the UP series were constructed with prototype block. The complete results of these tests are presented in Appendix B and are summarized in Table 4.4 and in the average stress-strain plots in Figure 4.5. In accordance with CSA S304 (CSA 2004a), stress values for all UST prisms were calculated based on an effective mortar bedded area of 31090 mm^2 while stress values for UP prisms were based on an effective mortar bedded area of 39110 mm^2, as determined for the proof-of-concept test program. The significant difference in mortar bedded area is due to the alignment of the four webs in the prototype block that is not present with the frogged ends of the stretcher block. The average peak stresses of 18.3 MPa for the UST series and 17.6 MPa for the UP series are similar and occurred at the same average strain. These values are comparable to results

from the proof-of-concept test program and test observations indicated identical failure patterns to those described for the corresponding series in Chapter 3.

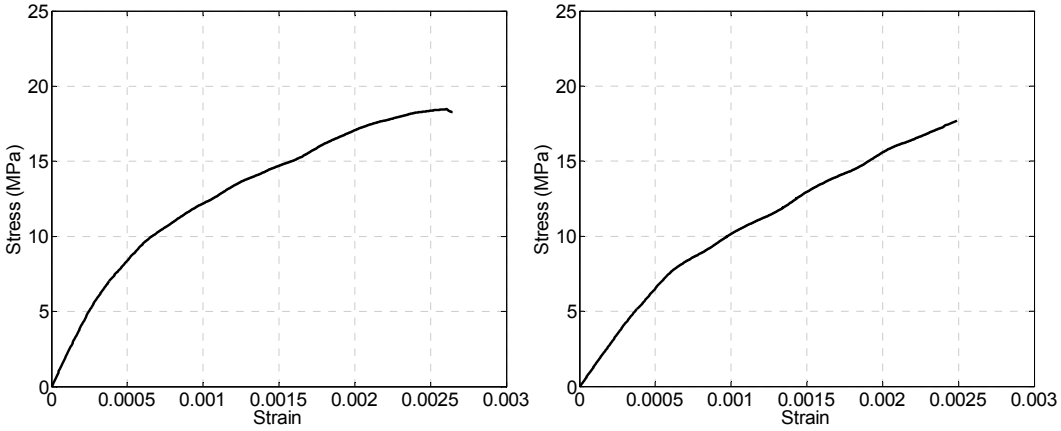

a) UST Series b) UP Series

Figure 4.5. Average Stress-Strain Curves for Ungrouted Prisms Series

4.4.2. Grouted Block Prisms

In this program, three fully grouted prisms in the GST series were constructed with standard stretcher blocks and three in the GP series were constructed with prototype block. The results of these tests are presented in Appendix B and are summarized in Table 4.4 and in the average stress-strain plots in Figure 4.6. Stress values for all grouted prisms were calculated based on a gross area of 74100 mm^2 as determined for the proof-of-concept test program. The average peak stresses of 11.4 MPa for the GST series and 13.5 MPa for the GP series are similar and occurred within the same range of average strains. The values for the grouted state are 37% and 23% lower than for the ungrouted state for the stretcher and prototype block prisms, respectively. These values are comparable to results from the proof-of-concept test program and test observations indicated identical failure patterns to those described for the corresponding series in Chapter 3.

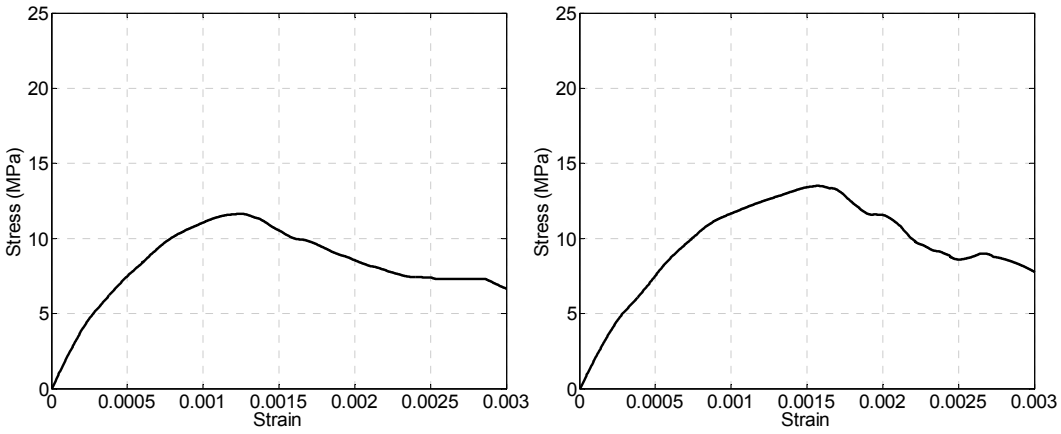

a) GST Series b) GP Series

Figure 4.6. Average Stress-Strain Curves for Grouted Prisms Series

4.4.3. SR Block Prisms

In this program, three fully grouted, self-reinforced prisms in the GPR-WA series were constructed with SR Blocks containing spiralled wire devices made from Type WA steel and three in the GPR-WB series were constructed with SR Blocks containing spiralled wire devices made from Type WB steel. The results of these tests are presented in Appendix B and are summarized in Tables 4.5 and 4.6 and in the average stress-strain plots in Figure 4.7.

The observed failure patterns for these series were consistent and followed a pattern similar to that of the unreinforced grouted series (GP) up to initial peak compressive stress of 13.9 MPa for the GPR-WA series and 12.6 MPa for the GPR-WB series. These peak capacities are within 6% of the peak capacity of the unreinforced series (GP) and occurred at exactly the same average strain, indicating that no additional compressive strength was provided by this type of confining device at the point of the initial peak strength. Figure 4.8 shows the typical splitting and spalling pattern for the spiral GPR prisms that occurred as the initial peak load was attained. As observed with the unreinforced series (GP), failure was initiated by splitting of the face shell concrete, allowing the outer concrete to spall off.

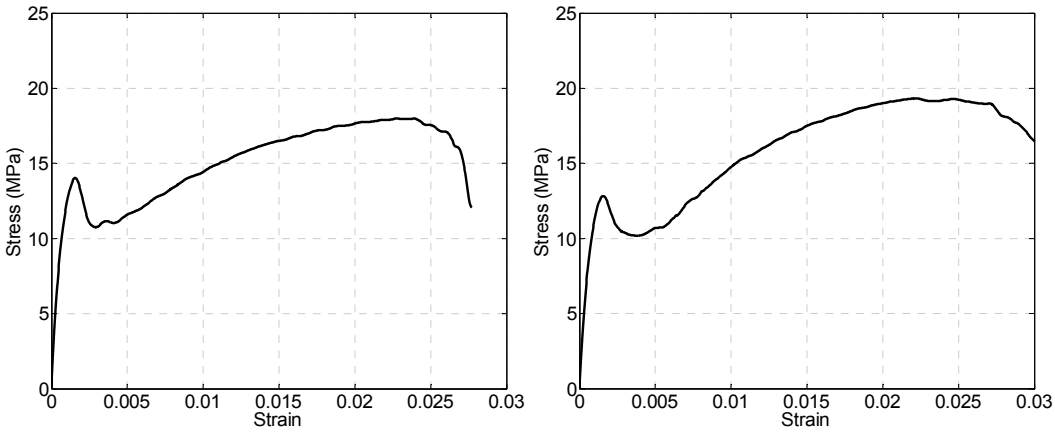

a) GPR-WA Series b) GPR-WB Series

Figure 4.7. Average Stress-Strain Curves for Spiralled Wire SR Block Prism Series

a) End View b) Face View

Figure 4.8. Typical Initial Splitting/Spalling Patterns of Spiralled Wire SR Block Prisms

Following the initial peak stress at an average strain of 0.0016, the spalling of the block concrete external to the confining devices resulted in a drop in load resistance of approximately 25%. As the specimens continued to undergo increasing strain, they regained strength up to and surpassing the initial peak.

In the GPR-WA series, the second peak capacity of 17.8 MPa, occurred at an average strain of approximately 2.4% and exceeded the initial peak capacity by 28%. Figure 4.9 shows the significant damage present around the confining devices and the limited damage to the confined concrete at 2% strain. The second peak

capacity was followed by a rapid decrease in capacity under increasing strain such that each specimen experienced a complete failure (capacity reduced by 50%) at very high strains between 2.5% and 3.5%.

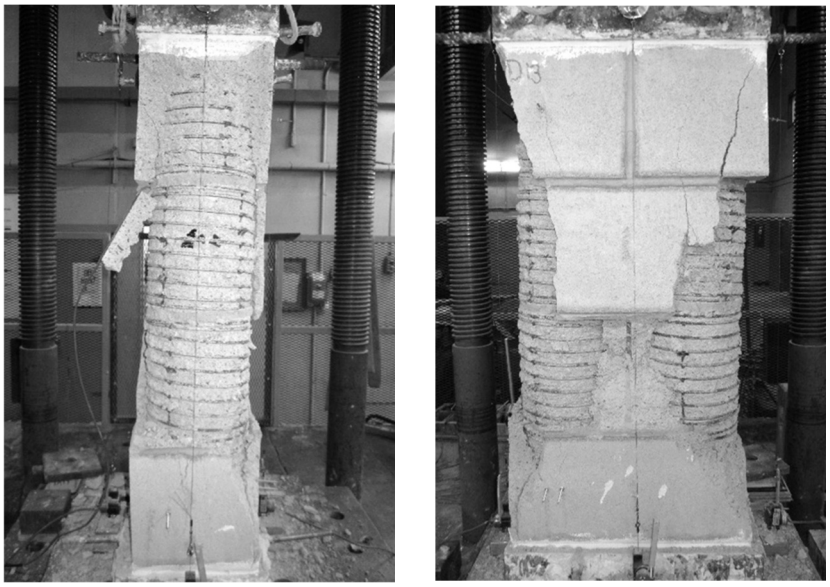

a) End View b) Face View

Figure 4.9. Typical Spiralled Wire GPR Prism at 2% Strain

The GPR-WB series exhibited even more desirable behaviour, reaching a second peak capacity of 19.3 MPa, which exceeded the initial peak capacity by 39% and occurred at an average strain of about 2.4%. This second peak capacity was followed by a more gradual decrease in capacity as the specimen continued to undergo increasing strain, resulting in an even more ductile failure of the prism. At an average strain of 2%, the prisms had reached capacities considerably higher than the initial peak capacity and at strains of over 3%, the confined volume of grout and concrete block in the GPR-WB prisms remained intact with reserve compressive capacity exceeding the initial peak. Damage patterns for this series at 2% strain were consistent with those observed in the GPR-WA series and have therefore not been presented independently. Loading of the GPR-WB prisms was continued until the prism capacity dropped to 50% of the initial peak load. The drop in capacity to this point occurred due to distortion and fracturing of the steel confining devices followed by crushing of the interior concrete materials.

4.5. Interpretation of Results

4.5.1. Spiralled-Wire Device Design

Stress-strain curves for the unreinforced and SR Block prisms are presented together for the Type WA steel spiralled wire series and for the Type WB steel

spiralled wire SR Block series in Figure 4.10. These curves indicate that, within the elastic loading range of the prisms (prior to cracking of the face shell concrete), the presence of the confining device has no influence on the characteristics of the prism. Following the initial peak, all curves show a decline in capacity, but while the unreinforced specimens rapidly lost all capacity at a strain of approximately 0.3%, the self-reinforced specimens regained strength. As the enclosed concrete and grout underwent vertical strain, the resulting lateral expansion against the confining device created a triaxial compression state of stress in the confined concrete and grout which enhanced the vertical compressive strength of this remaining 58% of the original cross-section. This beneficial effect was sufficient to allow full load capacity to be regained at a strain of about 0.8% with the capacity continuing to increase up to strains in excess of 2.0%.

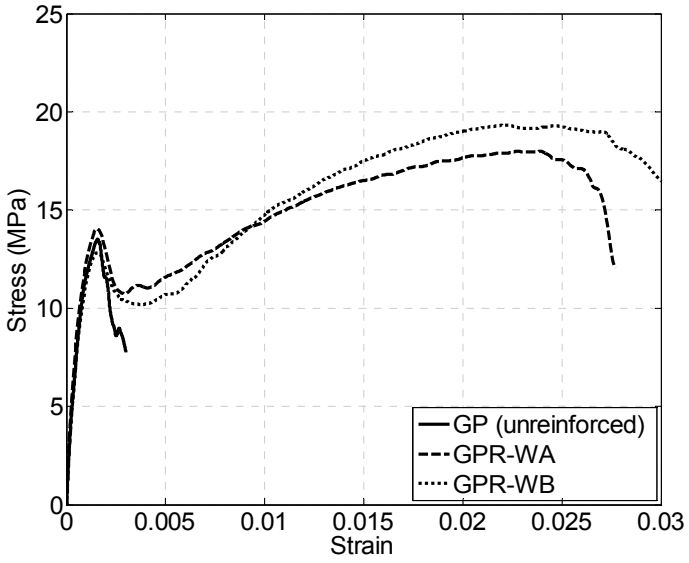

Figure 4.10. Stress-Strain Curves for Unreinforced and Self-Reinforced Prisms Containing Type WA and Type WB Steel Spiralled Wire Devices

While both Self-Reinforced series in this program followed the same basic pattern of initial peak followed by an approximately 25% capacity drop and regain of strength with increasing strain to a second peak strength at an average of 2.4% strain, there were some differences that may be attributed to the use of the two different types of steel to manufacture the confining devices. Use of the less ductile Type WA steel resulted in fracture of steel spirals at prism strains between 2.5 and 3%; this may be attributed to the limited post-yield deformability in this steel. Use of the more ductile, Type WB steel resulted in a more gradual ductile failure mechanism in which prisms experienced capacity loss at a more gradual rate with increasing strain beyond 2.5%. It is worth noting that in these tests, despite all other factors being constant, the higher strength confining steel (Type WA) did not result

in a higher ultimate prism capacity. It is noted that the prisms with the more ductile but slightly lower strength confining steel (Type WB) achieved a higher ultimate prism capacity where the only definable difference was the ability of the confining steel to maintain strength at higher strains.

4.5.2. Comparison of Device Type Behaviour

To evaluate whether SR Block prism results from this test program could be directly compared to those from the proof-of-concept program, a comparison of the corresponding unreinforced specimens was required. Comparison of the average stress-strain curves and capacity values for the grouted, unreinforced prototype block prisms tested in this program with those tested in the initial program reveal almost identical performance of the two series (see Figure 4.11).

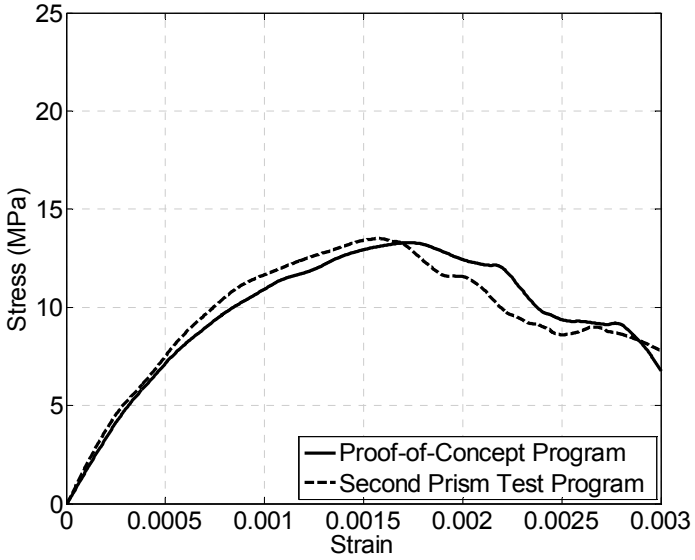

Figure 4.11. Comparison of Average Stress-Strain Curves for Grouted Prototype Block Prisms from Proof-of-Concept and Second Prism Test Programs

This very similar unreinforced behaviour provides support for directly comparing the results for self-reinforced prisms with the two types of confining devices without having to make adjustments to allow for differences in properties of the constituent materials. As it was determined that the behaviour of the spiralled wire devices produced from Type WB steel is more desirable, comparison of the performance of the two device designs is carried out using the GPR-WB series with spiralled wire devices described here and the GPIIR series with punched steel devices described in Chapter 3. Stress-strain curves for these series are presented together for comparison in Figure 4.12.

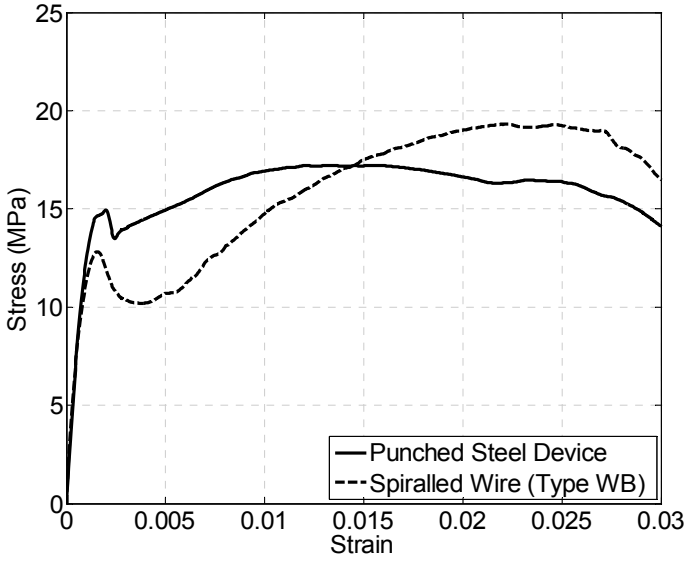

Figure 4.12. Comparison of Average Stress-Strain Curves for the Punched Steel and Spiralled Wire Device Designs

The first notable difference between the above two series is in the initial (first) peak stress. SR Block prisms with the punched steel confining device achieved a 13% increase in the initial peak capacity over the unreinforced counterpart while the prisms with the spiralled wire device experienced no capacity increase at this point. This evidence would seem to suggest that this difference could be attributed to the difference in vertical steel present and its contribution to resisting vertical load as well as perhaps improving the confinement of the enclosed concrete materials. Calculations and further analysis to this effect is presented in Chapter 6 of this dissertation. The second difference between the behaviours of the reinforced prisms is in the amount that the capacities decreased following reaching the initial peak capacities. For the series with the punched steel confining devices, this decrease in strength never exceeded 10% of the initial peak capacity. However, for the series with spiralled wire confining devices, the decrease averaged 25% of the initial peak capacity. This difference may have been affected by both the shape of the devices and the properties of the grout and is discussed in detail in the analysis presented in Chapter 6.

Both confining device designs enabled the prisms to regain their initial peak capacity following the aforementioned decreases in strength. Because the decrease experienced by the prisms containing the spiralled wire confining devices was more significant than that experienced by the prisms containing the punched steel confining devices, it could be expected that a greater strain increase would be necessary before the initial strength could be regained. While the prisms with the punched steel confining devices, which first peaked at a strain of 0.0017 regained

this strength by an additional increase in strain of 0.0033, prisms with the spiralled wire confining devices, which first peaked at a strain of 0.0016 required an additional strain increase on average of 0.0062 before the full initial peak strength was regained.

Prisms in both series continued to gain strength after regaining their initial peak strength. The prisms with the punched steel confining devices achieved a second peak strength of 18.0 MPa (corresponding to a true stress of 31.6 MPa) at a strain of 1.4% and held this capacity at a plateau with very little strength degradation up to and well beyond 2% strain. The prisms with the spiralled wire confining devices continued to gain strength until a higher second peak of 19.3 MPa (corresponding to a true stress of 33.3 MPa over the remaining area) at a very large strain of 2.4%. In this case, there was very little plateau in the capacity, but rather the strength decreased immediately following reaching the second peak capacity. While these prisms also continued to maintain a capacity above the initial peak to beyond 3% strain, the shape of the curve and visual test observations indicate a less ductile failure mechanism. The differences in capacity increase between the two prism series is discussed in detail in Chapter 6 of this dissertation.

4.6. Conclusions

The prism test program presented in this chapter provided material and assemblage properties relevant to the shear wall specimens. Tests of the individual materials provide documentation of their properties for reference as components in the walls. These material test results indicated that the lower strength values targeted to approximate minimum values typically encountered in the field were achieved with the mortar and grout mixes. As the strength of the vertical reinforcing steel in the wall is an important factor in the overall wall capacity, it was important also to use steel with strength representative of the lower range expected to be encountered in the field. The strength values for the vertical reinforcing were near to the nominal code lower limit.

The prisms test results reported in this chapter also served to investigate the performance of a second, spiralled wire confining device design leading to the following observations and conclusions:

a) Although wire with appropriate properties was difficult to procure, the spiralled-wire devices were easily manufactured using existing facilities and, using the developed steel clips, were effectively and efficiently placed within the SR Blocks on an existing manufacturing line.

b) The new spiralled wire confining device enabled prisms to regain and exceed initial peak strength and maintain high strength capacity above strains of 2% and up to 3% strain.
c) In comparing the prisms reinforced with spiralled wire confining devices produced from two different types of steel, those made from a lower strength, more ductile steel produced more desirable prism performance.
d) Prism tests results for the unreinforced specimens in this program were consistent with those obtained from the proof-of-concept test program, allowing direct comparison of the SR Block prism results for the two device designs.

CHAPTER 5

SHEAR WALL EXPERIMENTAL PROGRAM AND RESULTS

5.1. Introduction

A shear wall test program was designed as part of this study to provide direct evidence of the effectiveness of using SR Block construction to improve the ductility and overall performance of concrete masonry shear walls. Details of two wall specimens designed and constructed for this purpose are presented. Following the outline of the test program and test setup, results and observations from three full scale shear wall tests are presented. The effects of including SR Block within compression zones to improve the seismic performance (ductility) of concrete masonry shear walls under lateral loading are discussed in the interpretation of the experimental data presented in Chapter 6.

5.2. Wall Design

5.2.1. Program Development

The shear wall experimental program was designed to obtain direct evidence of enhanced ductility of reinforced concrete block shear walls through use of SR Block to increase compressive strain capacity. In order to document the effect of the SR Block within shear walls, it was important to be able to compare the results from walls containing SR Blocks with those from walls constructed from only conventional block. To accomplish this without having to construct conventional shear walls, it was planned to use results from walls previously tested with the same configuration at McMaster University (Shedid 2006). For meaningful comparisons between results, the dimensions of the walls in this SR Block program were based on those previously tested. One storey walls with a height-to-length ratio of two ($A_R = 2$), measuring 3600 mm high by 1800 mm long were recently tested, full-scale masonry walls that were suitable for comparison. Additionally, as these unconfined walls were tested at McMaster University, it was possible to closely match block type, grout, and mortar.

The high vertical reinforcement ratios presented in Table 5.1 were anticipated to provide a large enough compression zone to make it possible to examine the compression strain enhancing effects of the SR Block and, in this respect, be comparable to the previous research. Additionally, to increase the size of the compression zone, an axial stress of 0.75 MPa was chosen to be applied to both walls to simulate dead load. Axial loading and overall dimensions were kept constant in order that the effect of reinforcement ratio could be isolated. Following testing of the two constructed shear walls, it was decided that one of the tested

specimens would be retrofitted in place to examine the effects of economical repair on the restored stiffness and strength in addition to ductility of the wall.

Table 5.1. Wall Design Details

Wall	Height (mm)	Length (mm)	Vertical Reinf. (bars)	Vertical Reinf. Ratio (%)	Horizontal Reinf. (bars)	Horizontal Reinf. Ratio (%)	Axial Stress (MPa)
1	3600	1800	5 x 25M	0.73	9 x 10M	0.13	0.75
2	3600	1800	9 x 25M	1.32	18 x 10M	0.26	0.75

The reinforcement details for these shear walls are shown in Figure 5.1. Horizontal reinforcement consisted of 10M bars (A_s = 100 mm^2) in both walls, continuous along the length of the wall and bent into 180˚ hooks around the end vertical bars at each end of the wall. Vertical reinforcement was provided in both walls in the form of 25M bars (A_s = 500 mm^2), continuous over the height of the wall. In Wall 1, every second course contained a horizontal bar and every second cell contained a vertical bar. In Wall 2, every course and every cell contained a horizontal and vertical bar, respectively.

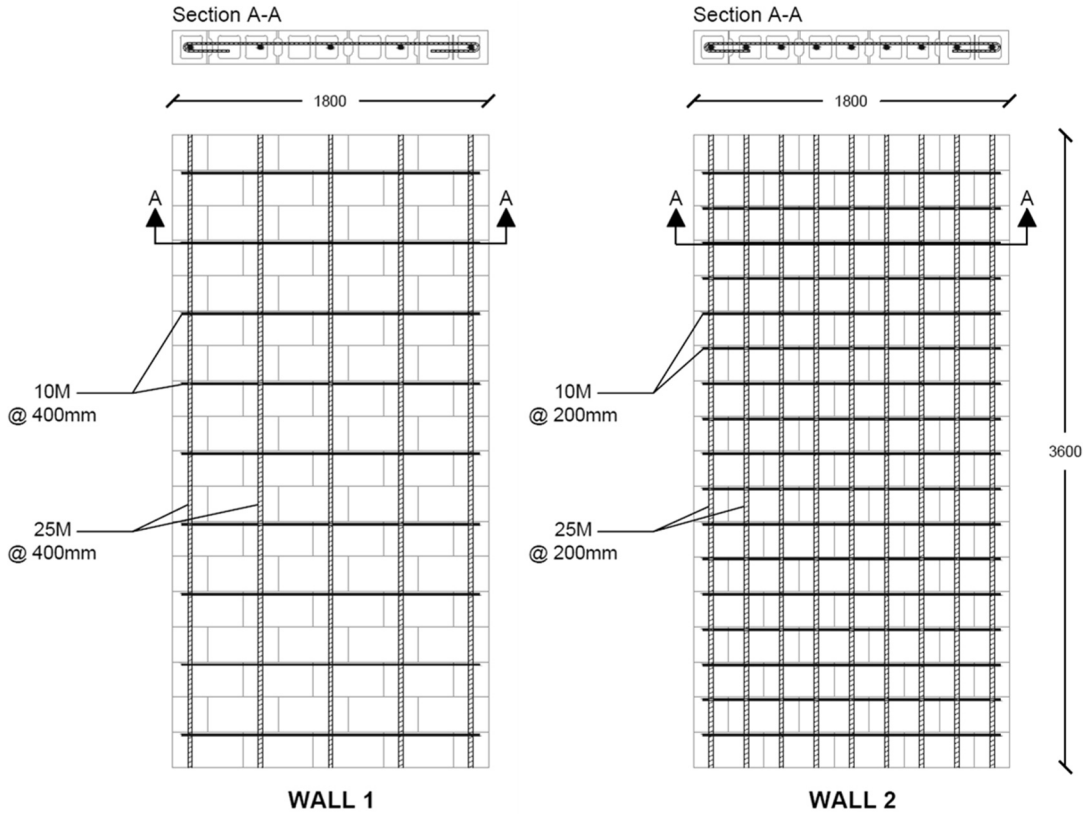

Figure 5.1. Wall Details (dimensions in mm)

5.2.2. SR Block Use

As stated in Chapter 4, the shear walls for this program were constructed in parallel with a set of prism series built with SR Blocks containing the same spiralled wire confining devices. To provide symmetrical confinement in the 4 ½ block long walls without placing cut blocks in the middle of a course, some SR Blocks were manufactured with only one confining device, leaving the second cell unconfined. Additionally, for consistency between the two shear walls, the placement of SR Block within the two wall specimens was identical. The pattern of placing SR Block and other block is shown in Figure 5.2.

The SR Block was specifically designed to increase the axial compressive strain capability of a shear wall to increase the curvature ductility while maintaining full load capacity. As such, it was necessary that the regions constructed with SR Block be sufficiently large to occupy the critical compression zones of the wall required to balance tension forces provided by the vertical reinforcement and resist externally applied axial load. Given that the walls were constructed before prism testing could provide an accurate stress-strain profile for use in a pushover analysis, conservative estimates were made as to the probable location of the neutral axis and therefore, as to where to place the SR Block within the wall.

With respect to the cross-section at the base of the wall, it was assumed that four confined cells (44% of the length of the wall) on each end of the wall would exceed the length of the compression zone and would, therefore, be a conservative arrangement of the SR Block. In the second course of the wall, use of three confined cells at each end of the wall (33% of the length of the wall) was likewise expected to be more than sufficient as the moment due to applied lateral load as well as the axial compression forces due to self-weight decreased with wall height. The three-cell confinement pattern was maintained up to the seventh course of the wall, above which two cells on each end were confined to a height exceeding the mid-height of the wall. Given that the most conservative estimations of equivalent plastic hinge length place the top of the hinging region at mid-height of the wall (CSA 2004a), above this height, it was expected that confinement would no longer provide any benefit and the remainder of the wall was constructed with conventional fully grouted hollow blocks.

Due to the need to use devices produced from three different types of steel wire within the available SR Blocks, decisions also had to be made as to where to place blocks containing each steel type within the wall. Following tension tests of the wire specimens, the most ductile Type WB steel wire was expected to exhibit the most desirable performance within the block and was therefore placed in the critical

zones of each wall: that is within the bottom four courses. As Type WA and Type WC steels performed similarly, blocks containing the higher strength Type WA steel wire were placed next, followed by blocks containing Type WC steel wire placed closer to the mid-height of the wall, where very little confinement demand was expected. A full layout of SR Block layout within the shear walls is shown in Figure 5.2.

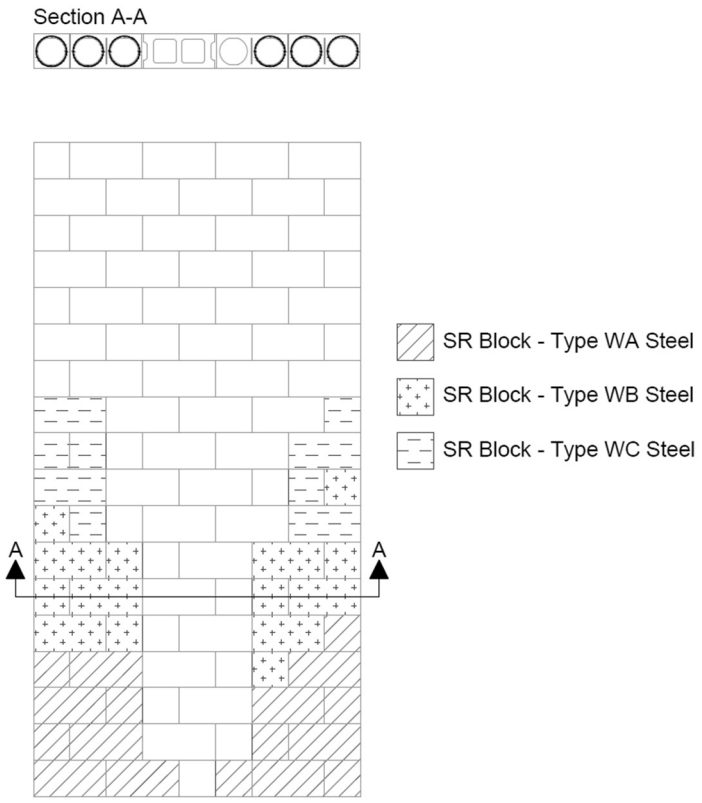

Figure 5.2. Placement of SR Block in Wall Construction

5.3. Wall Construction

Properties of all materials used in the construction of the two shear walls described above and the associated prism series were presented in Chapter 4.

5.3.1. Base Beam

A base beam was constructed for each wall to provide a fixed end condition at the bottom of the walls and facilitate centering and securing of the wall within the test setup. These beams were designed to remain uncracked throughout loading and to have sufficient depth to provide development length for the vertical wall reinforcement. The vertical reinforcing bars were set into the base concrete to a depth of 500 mm and terminated in a 400 mm length beyond a 90˚ bend.

Reinforcing cages for these beams consisted of 15M longitudinal reinforcement and 10M shear stirrups as shown in Figure 5.3. These cages were lowered into wooden forms with dimensions of 2300 mm long by 500 mm wide by 600 mm deep. The vertical wall reinforcement was tied into place at the bottom of the reinforcing cage as well as to a temporary support frame at a height of approximately 1700 mm above the top of the beam form. This ensured that proper alignment and spacing of the bars was maintained during concrete placement (see Figure 5.4).

a) Base Beam Reinforcing Cage

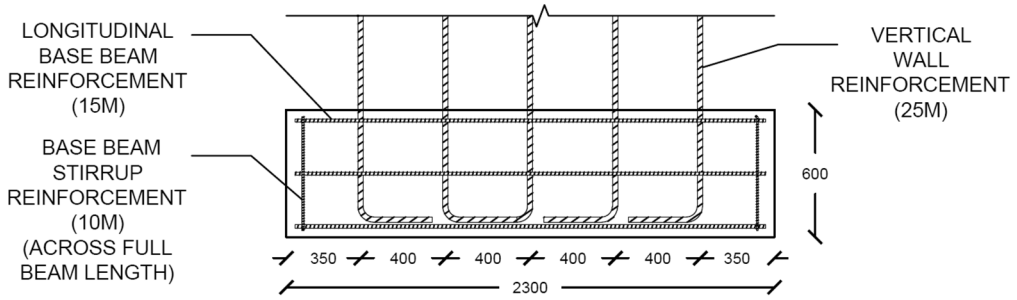

b) Complete Base Beam Form (dimensions in mm)

Figure 5.3. Details of Reinforcement in Base Beam

Ten lengths of 32 mm diameter PVC pipe were also secured vertically within the base beam formwork. These pipes were positioned to coincide with locations of post-tensioning hold down rods within the test setup, which allowed the base to be fastened to a reusable concrete floor slab for testing. The pipes were removed with the formwork following curing of the concrete.

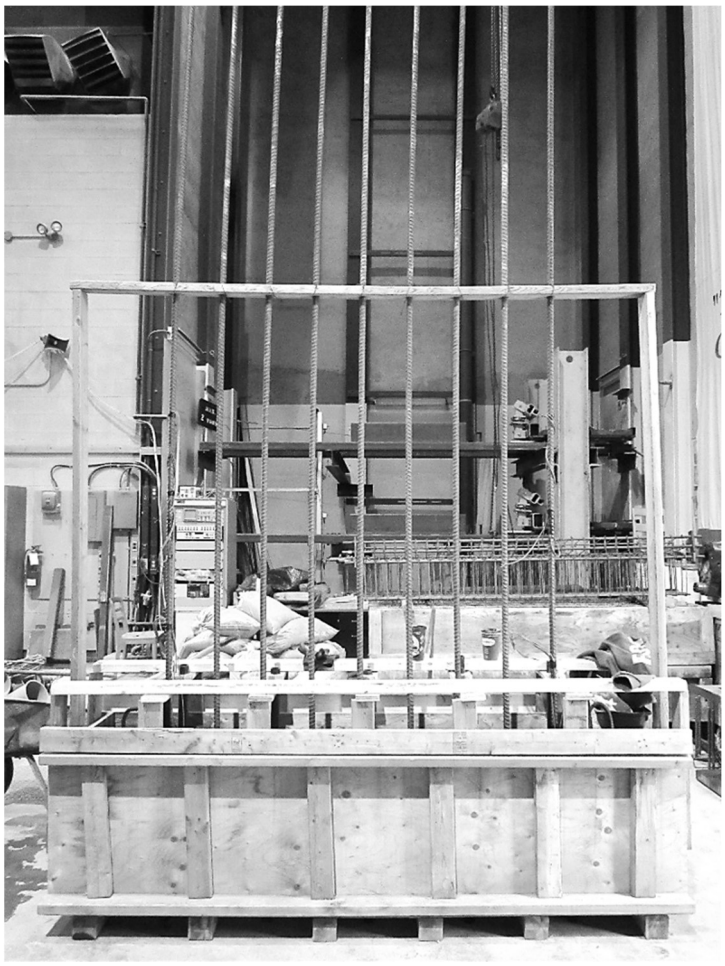

Figure 5.4. Base Beam Formwork with Support for Vertical Wall Reinforcement

5.3.2. Masonry Construction

Following curing of the concrete base beams which secured the vertical reinforcement in place, construction of the two shear walls was performed by an experienced mason over a four-day period. Blocks were threaded down over the vertical reinforcing bars allowing the mason to lay them into place (Figure 5.5). Prior to construction, notches had been ground to a depth of 6 mm into the block webs corresponding to the 6 mm of block concrete above the confining devices in each SR block; correspondingly all other block types were ground similarly to accommodate the placement of the 10M horizontal reinforcement into this thickened mortar bed joint. The horizontal reinforcement was threaded over the vertical reinforcing bars following the completion of a course by the mason and set into the notches and mortar joint. The walls were constructed in two halves: the lower nine courses of both walls were constructed on the first day and the upper nine courses on a separate day to allow time for grouting in lifts of nine courses.

Figure 5.5. Wall Construction: Blocks Being Lowered Over Vertical Reinforcement

5.3.3. Grouting

Following mixing (in the laboratory) of the high slump grout, each 420 kg batch of grout was loaded into a bucket fitted with a chute and crane-lifted to permit grout filling to take place in a cell by cell pattern since sideways flow of the grout was not possible with the full mortar bedding and alignment of the SR Blocks. Following construction of the lower half of the two walls, grouting was performed up to 8.5 courses and vibrated thoroughly to ensure complete filling around reinforcement. The level was kept one half block below the top of the course to facilitate formation of a shear key to avoid a weak shear sliding plane at the bed joint at mid-height of the wall. Once construction up to the full height of each wall was complete, the remaining 9.5 courses were fully grouted in a similar manner.

5.4. Shear Wall Test Details

5.4.1. Test Setup

Following a curing period of a minimum of 28 days, each wall specimen was loaded into the test setup on top of a reusable concrete floor slab with dimensions of 4200 mm long by 1100 mm wide by 600 mm deep. This slab had been previously secured to the strong floor of the McMaster University Applied Dynamics Laboratory with ten 63 mm diameter, post-tensioned steel bolts at 920 mm spacing. Anchored into

this reusable slab were 25.4 mm diameter high-strength steel rods at 400 mm intervals in two rows spaced 320 mm apart. The base beam of each wall was lowered over ten of these prestressing rods and levelled onto the reusable floor slab with a layer of stiff mortar. Following curing of the mortar, these bars were post-tensioned to provide a clamping stress of 250 MPa per bar on the base beam in order to prevent slipping or rotating of the wall base during testing.

5.4.1.1. Lateral Loading System

Cyclic lateral load was applied to each wall using an MTS hydraulic actuator with a capacity of $\pm$500 kN and 500 mm of total stroke. In order to evenly apply load along the top of the wall and create a zero moment condition, the actuator was mounted on a stiff reaction frame and aligned so that the loading plate was centered in line with the top plane of the wall. It was attached by four high-strength, threaded steel rods to a stiff loading beam constructed for each wall.

The original loading beam design utilized for testing of Wall 1 and the start of Wall 2 consisted of two steel angles running the full length of the wall and capped by a welded plate at the loading end. The channels were levelled into place on a mortar bed along the full length of the top of the wall. A series of drilled steel plates were then threaded over the vertical reinforcing bars protruding directly from the wall and welded into place between the channels. Finally, a pair of steel W-section elements were welded to the beam and the back of the loading plate to provide additional stiffness and load transfer when attached to the actuator. This configuration, shown in Figure 5.6, allowed the lateral load to be transmitted to the wall evenly through the vertical reinforcing bars of the wall.

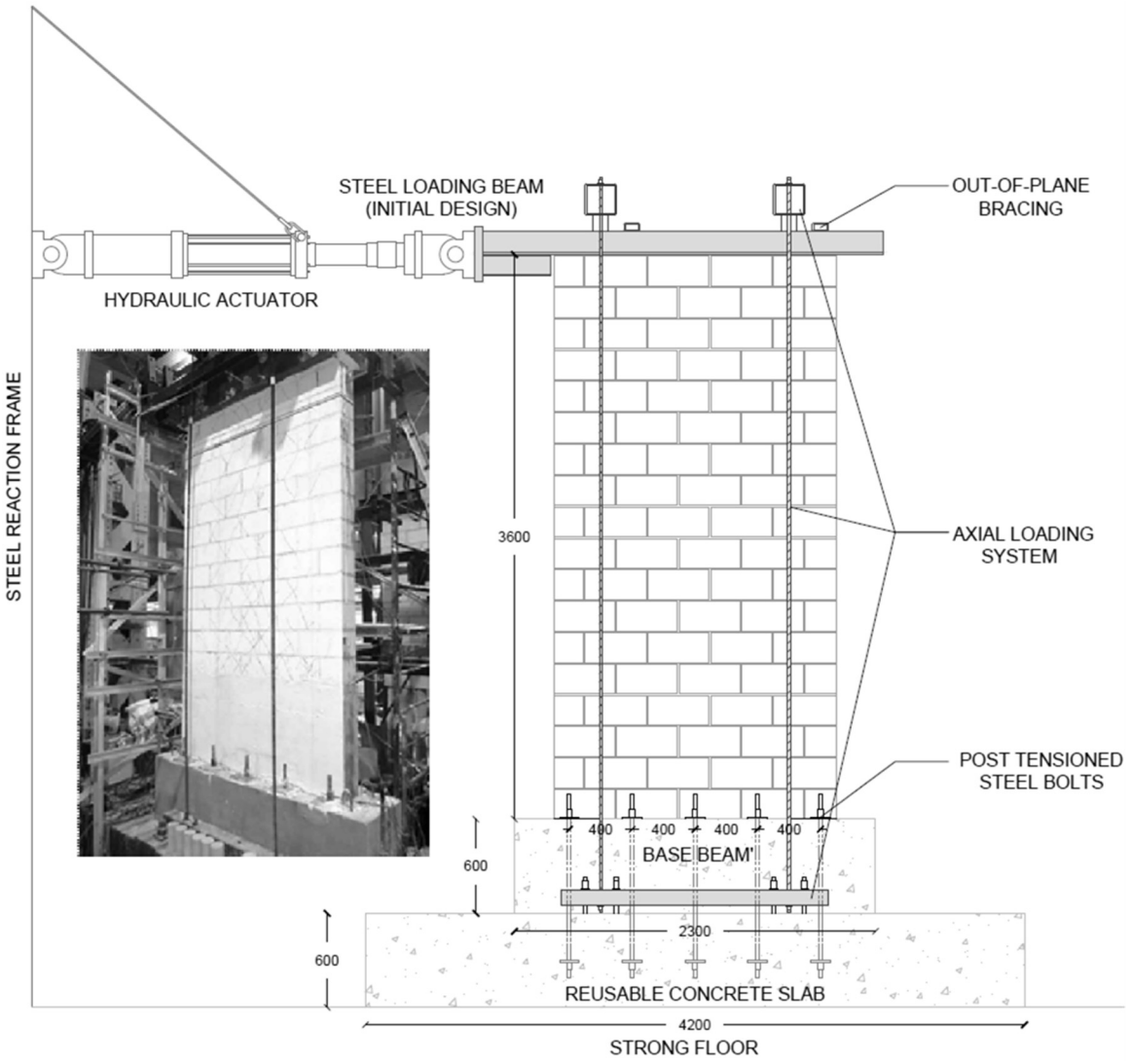

Figure 5.6. Wall Test Setup: Lateral Loading System (dimensions in mm)

5.4.1.2. Axial Loading System

An automated system was developed for this test program to allow a constant axial load to be applied uniformly along the top of the wall as it was displaced laterally. The system consisted, mechanically, of a series of four, 16 mm diameter, high strength, threaded steel rods which spanned from the top of the wall to the base where they were connected to an HSS section bolted on either side of the wall to the reusable concrete slab (see Figures 5.6 and 5.7). At the top of the wall, these rods were connected through a pair of larger, laterally spanning HSS sections resting on steel rollers on top of the loading beam. Tension on these threaded rods, along with the inclusion of the rollers, ensured that pure axial force could be applied without an out-of-plane moment component.

Tension in the system was provided by a pair of hydraulic actuators connected to the threaded steel rods on one side of the wall as illustrated in Figure 5.7. Load in the system was measured by a pair of 100 kN capacity load cells mounted at the intersection of the HSS sections and the threaded rods at the top of the wall. At each end of the wall, one of these load cells was paired with the corresponding actuator and wired to an MTS 406 Controller. The two controllers were set to the desired axial load prior to testing and used feedback from the load cell to control extension and retraction of the actuators to maintain constant axial load (within 1%) during testing. A drawing of the complete axial loading setup is provided in Figure 5.7.

5.4.1.3. Out-Of-Plane Support System

To ensure that the lateral in-plane capacity of the wall was determined without any influence of applied torsion or out-of-plane deflection at the top of the wall, a system was placed within the test setup to limit out-of-plane movement of the wall along the length of the wall at the top (mimicking the effect of a rigid diaphragm joining a system of shear walls). In order to accomplish this while still allowing free range of motion for in-plane lateral translation, the setup utilized a system of bearings running parallel to the wall.

A pair of rigid steel HSS sections positioned parallel to each other were welded to the top of the stiff loading beam near each end of the wall and connected to one another by a channel member to ensure rigid, simultaneous displacement of these support arms. The far end of each arm was bolted to a box containing two sets of four, 25.4 mm diameter, 375 kg load capacity bearings in contact with each side of a smooth HSS section. This HSS section was bolted, in parallel with the wall, to a rigid frame attached to the laboratory floor.

The bearing setup in this system, illustrated in Figure 5.7, ensured that wall movement was directed in line with the supporting HSS section, positioned parallel to the wall, without the presence of friction. The absence of friction and effectiveness of the bearings was inspected visually during loading, confirming that even at very high lateral in-plane loads, the bearings moved smoothly and were not transferring in-plane force to the supporting frame.

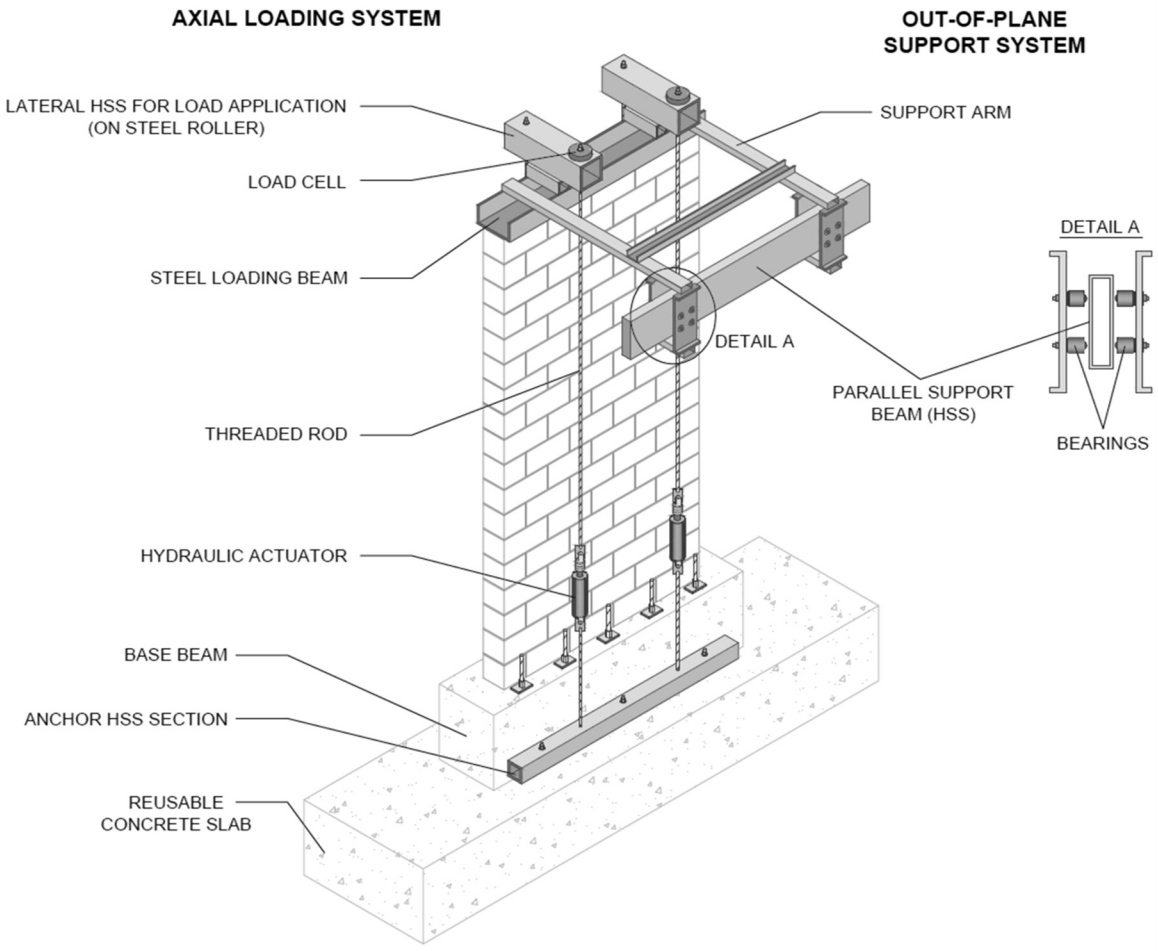

Figure 5.7. Axial Loading and Out-of-Plane Support Systems

5.4.2. Measurements

The instrumentation utilized to measure the performance of the wall specimens is illustrated in Figure 5.8. A 60-channel data acquisition system was used to record deformation readings at four-second intervals.

Lateral displacement of the wall was measured from an independent, rigid aluminum frame constructed adjacent to the loading end of the wall (henceforth referred to as the "near" end of the wall). At the top of this frame were mounted two parallel MTS Temposonics Linear-Position Sensors (L8 and L9), each connected to the end block of the wall at a height of 3500 mm from the base (100 mm from the top plane of the wall). An average of the readings from these sensors was used to represent the total displacement of the wall and was the data output used in the control of displacement testing cycles. An additional seven horizontally positioned potentiometers (both linear and draw-wire) (L1-L7) were attached to the

wall and the independent reference frame to measure the lateral displacement at various intervals over the height of the wall.

A set of seven linear potentiometers were mounted vertically along the height of the wall on both the near (N1-N7) and far (F1-F7) ends and were used to determine the average curvatures over various segments of wall height. An additional four linear potentiometers (N8-N9 and F8-F9) were mounted vertically on the face of the wall across its length to show average strain profiles for wall segments up to 300 mm and 700 mm above the base. Two further linear potentiometers (ND and FD) were mounted diagonally to measure corner-to-corner deformation across the wall in each direction.

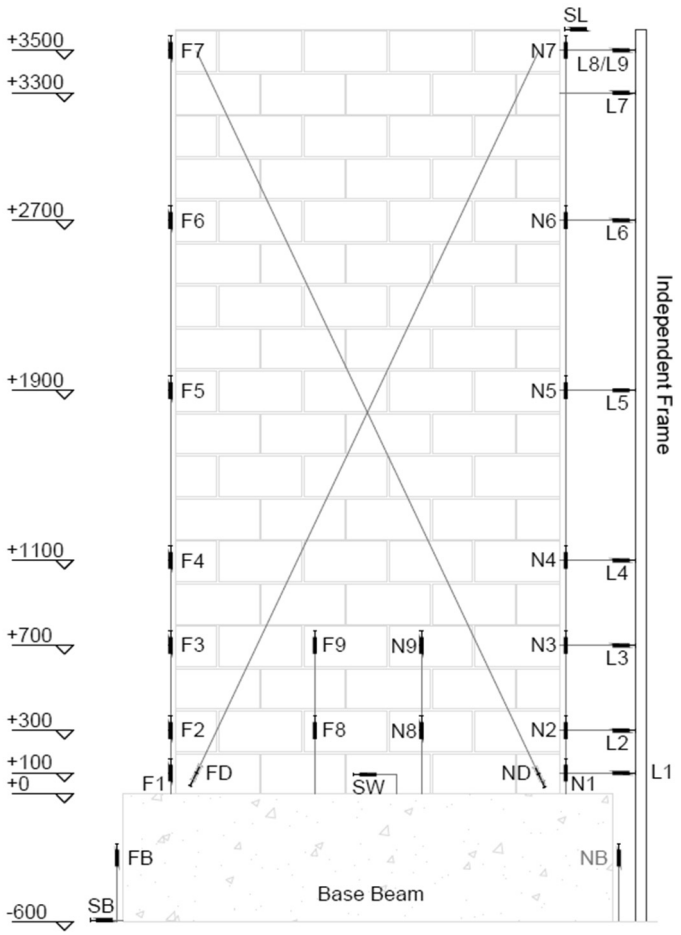

Figure 5.8. Wall Instrumentation Layout (dimensions in mm)

A final set of five linear potentiometers were used to monitor movements around the loading beam and the base of the wall. This included potentiometers NB and FB mounted vertically on either side to measure possible uplift of the base, as well as three horizontally mounted potentiometers (SL, SW and SB) to measure any

sliding of the loading beam relative to the wall, sliding of the wall relative to the base beam, and sliding of the base beam relative to the concrete slab, respectively.

To supplement the external instrumentation, a series of strain gauges were mounted on the vertical reinforcement within the wall and base to measure the extent of steel elongation and to define the experimental point of yielding to be used in the cyclic loading of each wall. Twelve 5 mm long, linear, foil strain gauges were used in each wall, mounted in pairs on opposite sides of each end bar at three different heights. These were used to measure the steel strain occurring in the base, at the interface between the wall and base, and in the wall at a height of 900 mm above the base.

To install these electronic gauges, the rib deformations on the reinforcing bars were ground down to provide a smooth mounting surface at the site of each gauge (see Figure 5.9). The foil gauges were then bonded directly to the steel using an epoxy and were layered with a sealer coating for waterproofing as well as a layer of butyl rubber and electrical tape for protection from physical damage during construction. The use of a pair of gauges at each location, provided opportunity to confirm the measurements for improved reliability and afforded the opportunity for averaging to maximize accuracy.

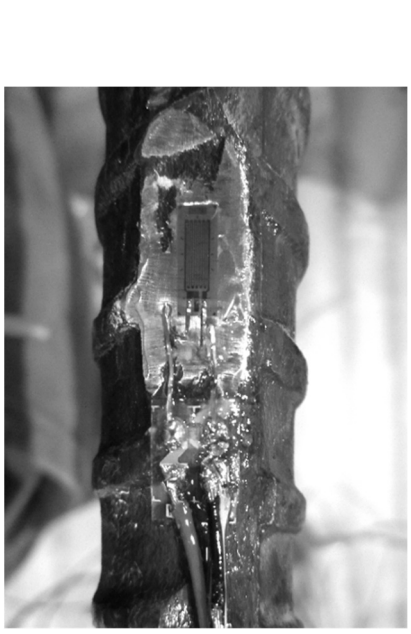

a) Gauge mounted to ground portion of bar

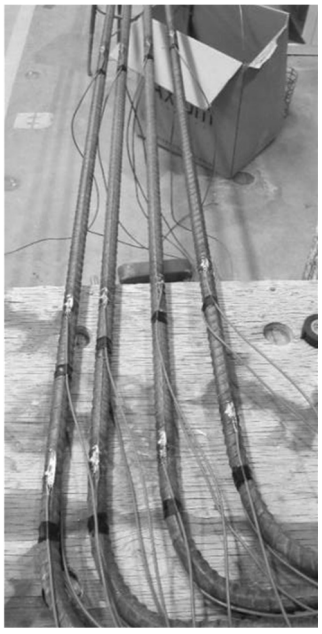

b) Gauges mounted at three heights along each bar

Figure 5.9. Installation of Electronic Strain Gauge Instrumentation

Load readings during testing were recorded by three load cells. The first cell, internal to the MTS hydraulic actuator, measured the lateral force applied to the wall. The remaining two cells, as described in Section 5.4.1.2 within the axial load system, provided axial load readings throughout testing.

5.4.3. Test Procedure

The shear walls were tested under reversing cyclic lateral loading using displacement-control. Loading patterns for each wall were determined based on a combination of the ISO 16670 Protocol (Test Method B) and the Sequential Phased Displacement (SPD) Loading Protocol (Test Method A) as outlined in ASTM E2126-11 (ASTM 2011a). This document states that the ISO Protocol is conservative for most practical cases and "is intended to produce data that sufficiently describe elastic and inelastic cyclic properties and typical failure mode[s] that [are] expected in earthquake loading" (ASTM 2011a). As such, this was the prescribed method most suited to the purposes of the test program and was used to define the number and pattern of cycle repetitions performed at each displacement step. However, as shear walls containing SR Block had not been previously tested, rather than using the cycle displacement definitions defined for the ISO Protocol, which are dependent on the ultimate displacement as obtained from monotonic loading, cycle definitions based on the wall yield point as defined in the SPD Loading Protocol were adopted.

At the outset of testing and from the experience (Shedid 2006) of previous test programs, it was anticipated that many displacement levels for loading cycles would be required to reach failure. Given this expectation and a desire to reduce the chance of low cycle fatigue failure of the reinforcing steel bars (known to occur at high plastic strains) as a failure mechanism in later tests, the number of cycles performed at each displacement step was reduced from three (in the ISO Protocol) to two. Since the number of high strain cycles would be significant compared to possible seismic load cycling, fatigue failure under these conditions would not be a relevant failure condition. Additionally, any reinforcement failure would have reduced the value of post-test retrofitting of the walls.

The final loading patterns applied to each of the three wall tests are shown in Table 5.2 and illustrated in Figure 5.10. Loading was terminated when capacity degradation of 20% from ultimate was reached except in the case of Wall 2 which, in order to be preserved for retrofitting, was loaded only until a full cycle was completed at the first displacement level when a reduction in resistance to lateral load was observed.

Table 5.2. Final Wall Loading Patterns

Step	Disp. (mm)	No. of Cycles	% of Yield
Wall 1			
1	2	2	17
2	5	2	43
3	8	2	70
4	11.5	2	100
5	23	2	200
6	34.5	2	300
7	46	2	400
8	69	2	600
9	92	2	800
Wall 2			
1	2	2	11
2	5	2	28
3	10	2	56
4	18	2	100
5	27	2	150
6*	18	1	100
7	36	2	200
8	45	2	250
9	54	2	300
10	72	2	400
11	90	2	500
Repaired Wall			
1	6	2	33
2	12	2	67
3	18	2	100
4	36	2	200
5	54	2	300
6	72	2	400
7	90	2	500
8	108	2	600

*cycle to reach zero load/displacement condition for loading beam adjustment

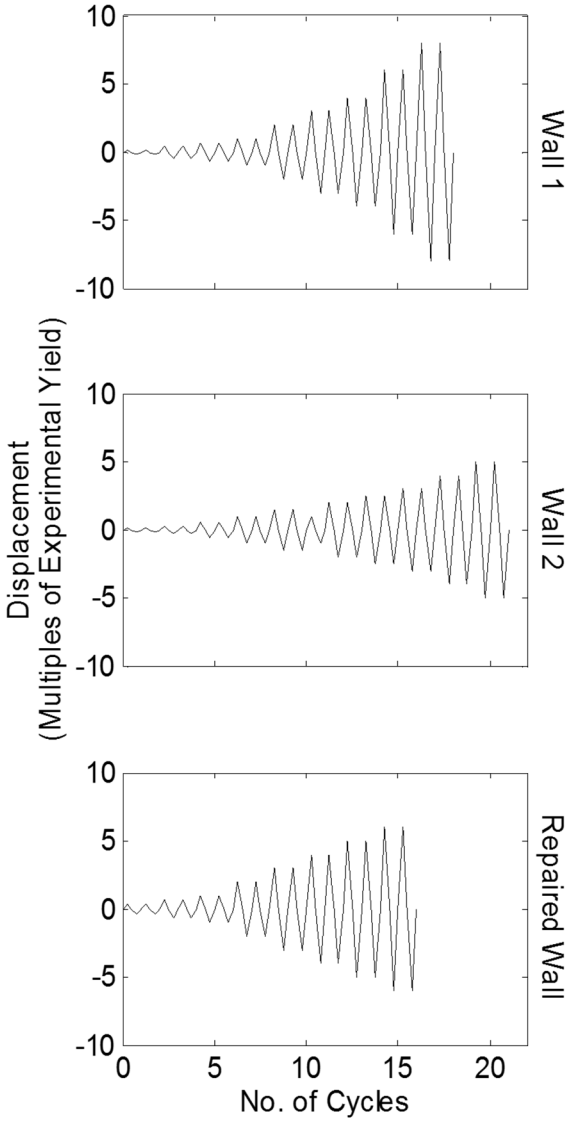

Figure 5.10. Wall Loading Patterns

For all loading cycles which occurred prior to reaching the experimental yield displacement of the wall, loading intervals were calculated as fractions of the predicted yield displacement for the wall. The experimental yield displacement was identified as the point at which the reinforcing bar in the outermost cell of the wall reached an average strain at the base of the wall of 0.21% corresponding to the yield strain determined from the reinforcing steel test results. After the yield

displacement had been reached, displacement values for subsequent cycles were defined as multiples of this yield displacement. The intervals between steps were designed so that approximately 10 steps (20 complete cycles) would be required for testing of each wall.

Other procedures adopted during testing included the application of axial load to the wall at the beginning of each test day with the wall in a position of zero lateral force. Frequent visual checks were made to ensure that the out-of-plane bracing system was running smoothly. Cracks were traced during each load cycle and the wall face was photographed in order to monitor crack propagation and identify failure patterns.

5.5. Wall 1

5.5.1. Load-Displacement Hysteresis Loops

The load-displacement hysteresis loops for Wall 1 under reversed-cyclic loading have been reproduced in Figure 5.11. These loops indicate a very stable and very symmetrical behaviour in the push (positive) and pull (negative) loading directions.

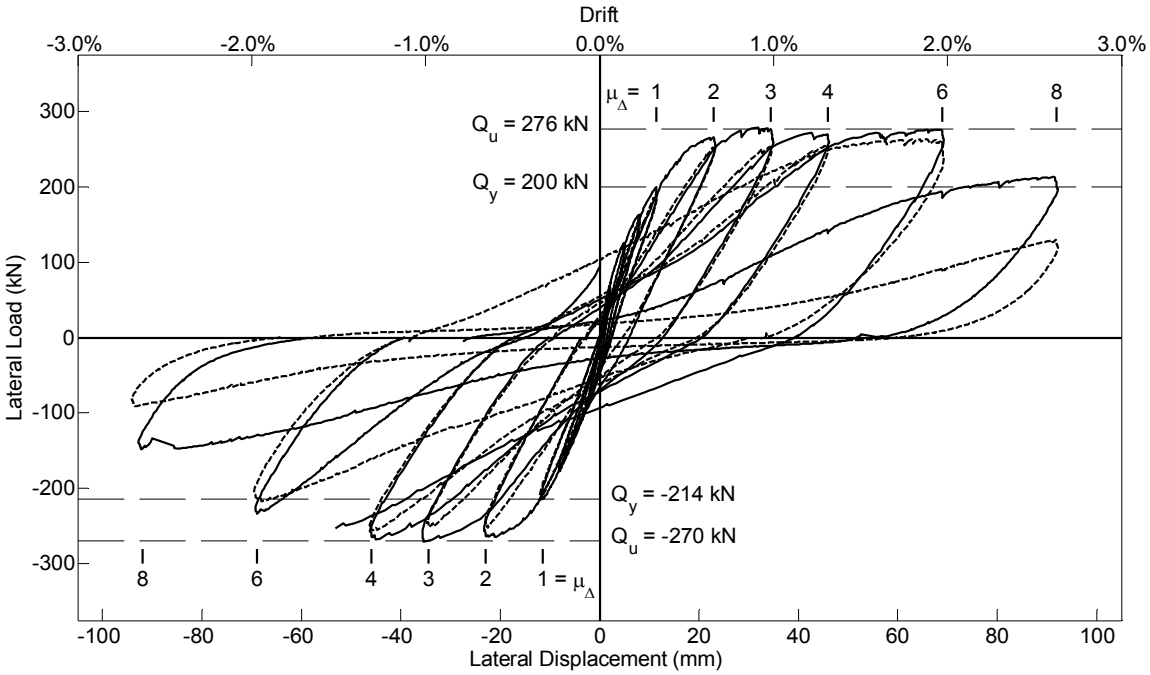

Figure 5.11. Hysteretic Load-Displacement Response of Wall 1

5.5.2. Test Observations

Observed crack propagation in this wall followed expected patterns up to the point of yield. Initially only horizontal flexural cracks were present in the bed joints between courses of block, up to approximately mid-height of the wall. At the point

of experimental yield (Δ_y), vertical cracking in the head joints of the masonry accompanied the horizontal cracking, forming a stepped crack pattern up to a height of approximately 14 courses as shown in Figure 5.12 a). Shear cracking in the form of approximately 45˚ diagonal cracks through the blocks began to appear during the 23 mm displacement ($2\Delta_y$) cycles as shown in Figure 5.12 b). These and additional cracks continued to propagate throughout all further cycles.

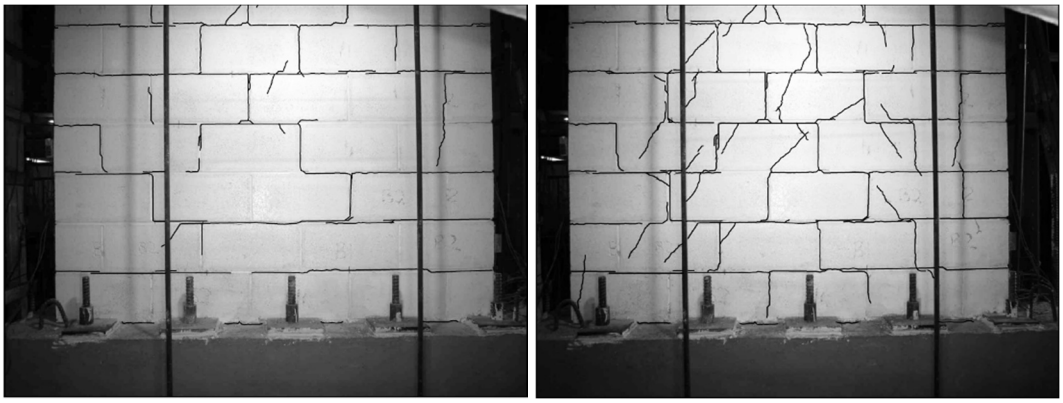

a) Stepped Flexural Cracking at Yield Cycle

b) Propagation of Shear Cracking at 34.5 mm Deflection Cycle

Figure 5.12. Flexural and Shear Cracking in the Lower Half of Wall 1

The first vertical compression related cracks at the toes of the wall were observed during the second cycle at 23 mm displacement ($2\Delta_y$) and extended up into the second course during the 34.5 mm displacement ($3\Delta_y$) cycles. As the first 46 mm displacement ($4\Delta_y$) cycle was reached, the face shell of the outermost cell at the bottom corners of the wall spalled to expose one confining device on each end of the wall. Toe cracking and spalling are shown in Figure 5.13.

Due to extreme shear cracking to be discussed later and the corresponding reduced stiffness of the wall in the large displacement cycles, the out-of-plane bracing system was unable to fully restrain the wall and some twisting was observed during the second 69 mm ($6\Delta_y$) push cycle. Adjustments to the support system were made to remedy the situation and the wall was straightened. Shear cracking continued to develop into the 92 mm ($8\Delta_y$) cycle. During this cycle, very extensive spalling exposed all columns of confined masonry within the bottom four courses of the wall and vertical sliding occurred between these confined columns. As a result of these large shear distortions, these columns began to act in a largely independent manner, linked only by the horizontal reinforcement acting as very flexible coupling at every second course. This shear failure mechanism, shown in Figure 5.14, caused a significant degradation of the capacity of the wall.

a) Vertical Toe Crack at 34.5 mm Cycle

b) First Spalling to Reveal Confining Device at 46 mm Cycle

Figure 5.13. Toe Cracking and Spalling in Wall 1

Inspection of the wall following testing revealed that an unforeseen weakness was present in the form of the slot used to divide splitter blocks into two parts. The location of these at the centre of every SR Block created a void similar to an empty head joint when the solid face shell regions outside of the confining devices spalled (Figure 5.14 a)). Following spalling of the block face-shells, very little connection existed between adjacent columns of confined grout and block. Along the vertical planes through head joints and empty splitter slots in alternating courses, there was only some mortar in the head joints present to provide friction resistance against vertical sliding shear between these columns. The independent bending of the individual confined regions could be clearly seen with double curvature between the base of the wall and the relatively undamaged wall section above the fourth course. The only coupling over the four-course height was the small amount created by the horizontal 10M bars at the first and third courses above the base. The photo in Figure 5.14 b) shows the deformation that occurred in the horizontal shear reinforcing bars where little concrete material was present to provide friction against sliding shear forces. Fortunately this unanticipated limiting factor occurred only after large ductility had already been recorded, but it did result in an underestimation of the full ductility that may have been available if sliding due to shear had been avoided.

a) Extent of Spalling at Test Completion

b) Shear Sliding and Reinforcement Deformation between Confined Columns

Figure 5.14. Extreme Spalling and Shear Sliding in 92 mm Cycle (Wall 1)

5.5.3. Response

Referring back to the hysteresis response in Figure 5.11, behaviour of the wall up to the point of experimental yield was initially linear-elastic. Nonlinear behaviour began at higher displacements indicating the effects of increased cracking as well as yielding of the reinforcement. The yield point of the wall (first yield of reinforcement) was identified (by strain readings on the extreme reinforcing bar as previously described) at a displacement of 11.5 mm and at load capacities of 200 kN in the push direction and 214 kN in the pull direction. Following yielding of the reinforcement, the slopes of the hysteresis loops decreased, indicating reductions in stiffness, and the width of the loops increased significantly, indicating increased energy dissipation. These observations correspond to the plastic behaviour expected in the post-yield phase of loading of a ductile shear wall.

Maximum lateral loads of 276 kN in the push direction and 270 kN in the pull direction were reached at the 34.5 mm ($3\Delta_y$) cycle and were maintained (within 1%) at cycles of 46 mm ($4\Delta_y$) and 69 mm ($6\Delta_y$) in the push direction. During the first 69 mm ($6\Delta_y$) cycle in the pull phase, a weld broke in the loading beam connection at a displacement of -55 mm resulting in an abrupt return to zero load. After repairing this break, the pull to -69 mm was repeated before continuing on to the second cycle. This doubled pull cycle produced a lower load capacity in the pull direction at this displacement; however, given the slope of the load-displacement response prior to the break and the earlier symmetry between loading directions, it is expected that the push direction results better represent the wall behaviour following the interruption. It is not known what damage might have been caused

during the fracture and abrupt load change but subsequent loadings suggested that it had an effect on the wall strength in the pull direction only.

The loading cycles at 92 mm ($8\Delta_y$) illustrate the rapid capacity loss that the wall experienced as the sliding shear mechanism began to govern behaviour. At this point, the first cycle indicated a sudden 23% drop from the peak load capacity. Additionally, whereas a capacity loss between first and second cycles of less than 10% was consistent in all previous cycle repetitions, the second load cycle at 92 mm ($8\Delta_y$) indicated an additional 30% capacity decrease for a total load capacity loss of 53% by the completion of the two 92 mm ($8\Delta_y$) cycles. At this point, the specimen was considered to have failed and testing was terminated.

The decrease in resistance to lateral load at this high displacement corresponded to the occurrence of vertical slip along the head joint/splitter block slot plane. Even when the confined columns were acting essentially as separate four-course high elements with ends fixed against rotation as shown in Figure 5.14 a), the wall still had significant resistance to lateral load and was stable under the applied axial compression; the confined block and grout material and the enclosed vertical reinforcement continued to function effectively.

5.5.4. Behaviour Profiles

The in-plane lateral displacements over the height of the wall were measured by a series of eight potentiometers and are presented in Figure 5.15 for the push and pull loading cycles up to the 69 mm ($6\Delta_y$) cycle. Instrumentation nearest the base was ineffective at high displacement cycles due to face shell spalling which accounts for the missing data points. These profiles give an indication of the extent of plasticity over the height of the wall and indicate where bending behaviour was concentrated. Slopes of the deflection profiles remained relatively constant above a height of 1100 mm for all cycles, indicating that comparatively little bending was present in this zone. Changes in slope below 1100 mm and especially below 700 mm indicated a concentration of bending and therefore plastic behaviour in this lower region.

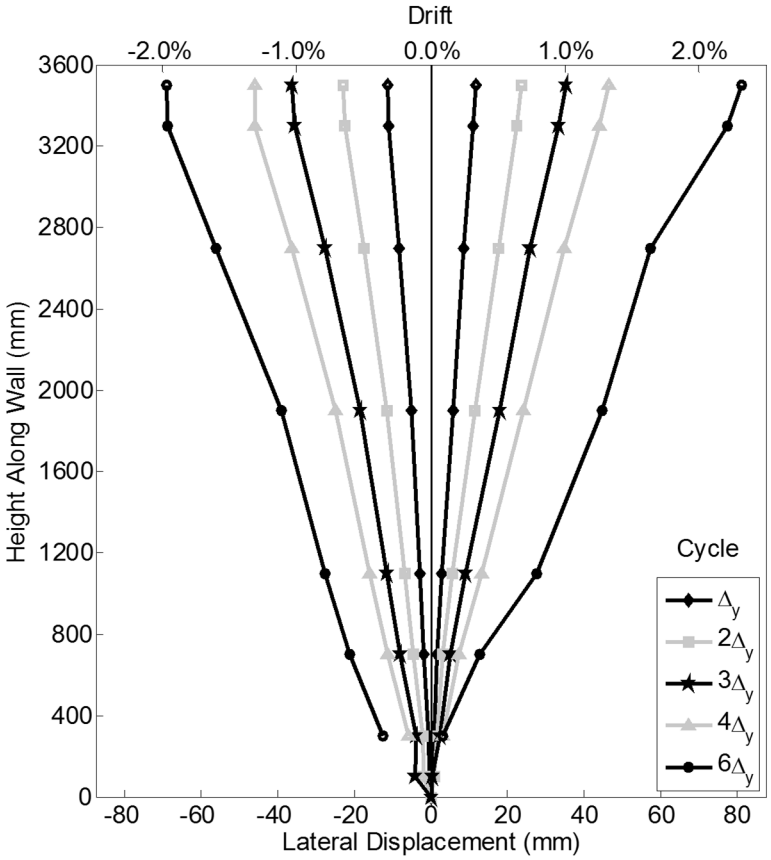

Figure 5.15. Lateral in-Plane Deflection (Wall 1)

Average curvatures were calculated at seven points corresponding to seven increments of wall height over the total height of the wall to display the curvature profile throughout the loading cycles. Average curvature data points represent curvature at the mid-point of respective segments of wall height and were calculated using vertical displacement readings from the opposing ends of the wall according to the parameters described in Figure 5.16 and in Equation 5.1.

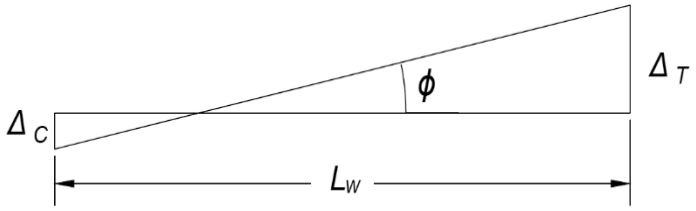

Figure 5.16. Strain Profile for Curvature Calculation

$$\phi = \frac{\frac{\Delta_C}{h} + \frac{\Delta_T}{h}}{L_w} \tag{5.1}$$

Where Δ_C or Δ_T is the increment of vertical displacement
h is the height of the segment (measured as the distance between the potentiometers attached at the top and bottom of the segment)
L_w is the length of the wall

During very high displacement cycles, instrumentation attached near the base of the wall became ineffective due to spalling of the face shell concrete in these regions. This explains the lack of curvature profiles for wall segments near the base of the wall as shown in Figure 5.17. This curvature profile corresponds with the behaviour observed in the lateral deflection profile, indicating a concentration of bending in the lower region of the wall, below a height of 1100 mm from the base. Above this point, the curvatures were much smaller and decreased gradually toward the top of the wall. Much higher curvatures were observed near the base of the wall and increased significantly with each loading cycle, approaching 0.03 rad/m in the 46 mm ($4\Delta_y$) cycle.

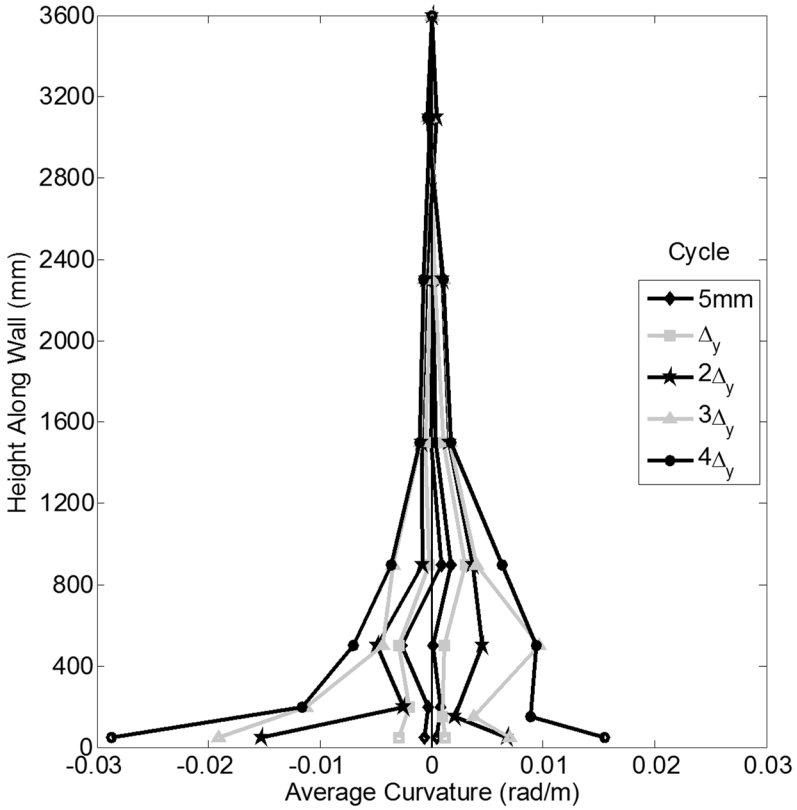

Figure 5.17. Average Curvatures over Wall Height (Wall 1)

To analyze the profile of masonry strain along the length of the wall, readings from four potentiometers along the wall face at two heights (300 mm and 700 mm) from the base were plotted. Figure 5.18 shows these results as an average strain over the

bottom 300 mm and then the next 400 mm of the wall (up to a total height of 700 mm) in both the push and pull directions. These plots suggest that the wall strain was essentially symmetric in the two directions of loading and indicate that, while the wall plane remained essentially linear when averaged over the segment of the wall height between 300 and 700 mm, some nonlinearity was present in strains averaged over the bottom 300 mm of the wall, in the region of highest bending/curvature.

These plots serve the additional purpose of identifying the length of the compression zone of the wall under lateral loading. As could be anticipated, in small part due to reduced self-weight of the wall and largely due to much smaller applied moment, the compression zone was smaller at higher points on the wall. The compression zone length interpreted from the plots averaged 250 mm in the push direction and 320 mm in the pull direction when considered between a height of 300 mm and 700 mm from the base while the lengths from the plots at a height of 300 mm from the base averaged approximately 330 mm and 460 mm in the push and pull directions, respectively. Up to the 46 mm ($4\Delta_y$) displacement cycle, the lengths of the compression zones appeared to remain nearly constant during the post-yield cyclic loading of the wall.

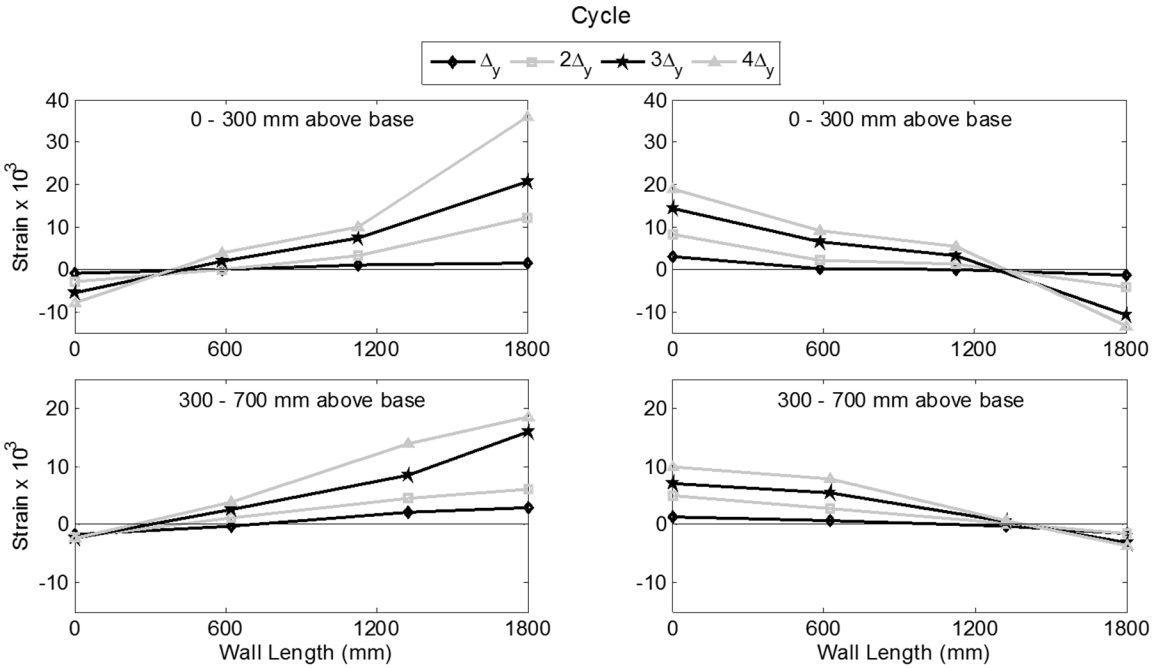

a) Push Direction b) Pull Direction

Figure 5.18. Profile of Average Strain along Wall Length (Wall 1)

5.6. Wall 2

5.6.1. Modifications Undertaken for Wall 2 Test

5.6.1.1. Addressing the Unanticipated Sliding Shear Mechanism

As was discussed for Wall 1, an unexpected sliding shear mechanism began to occur at a displacement of $6\Delta_y$. Since this was undesirable and prevented the full flexural ductility of the wall from being investigated, adjustments were made to increase the resistance to sliding prior to testing of Wall 2. It seemed apparent that the reduction in resistance to sliding was due, at least in part, to the presence of the 6 mm wide splitter slots in the SR Block (a feature not present in the stretcher blocks), which became a gap in the block concrete similar to an open head joint following face-shell spalling. The resulting weak vertical plane along head joints and these gaps in alternating courses resulted in low resistance to vertical sliding similar to that of a stack-pattern configuration. Without the presence of these voids (as could be easily achieved with SR Blocks made with an adjusted mold not containing the splitter slot for subsequent rounds of manufacturing), more friction strength would be available to resist vertical sliding shear displacement between the columns of confined material remaining after the unconfined concrete face shells had spalled.

In an attempt to delay this mechanism and more accurately represent a wall without this built-in weakness, the simplest course of action was to fill these empty slots prior to testing of Wall 2 (see Figure 5.19 a)). In this regard, it was desirable for the filling material to form a full bond with the block concrete and provide enough strength that cracking and sliding, if it occurred, would take place in the block concrete adjacent to the joint, rather than through the joint itself.

Two different materials were tested to achieve the desired failure mechanism. For both materials, filling was achieved by drilling a hole at the base of the slot, large enough to accommodate the nozzle of a tube of material, and a second hole near the top of the joint to allow air to escape. The material was pumped in through the bottom hole until it exited through the top hole as shown in Figure 5.19 b) which visibly indicated when the slot was filled. The effectiveness of this filling method was also verified by sealing the top and bottom of a test block with a transparent fibre-glass sheet to observe the filling process.

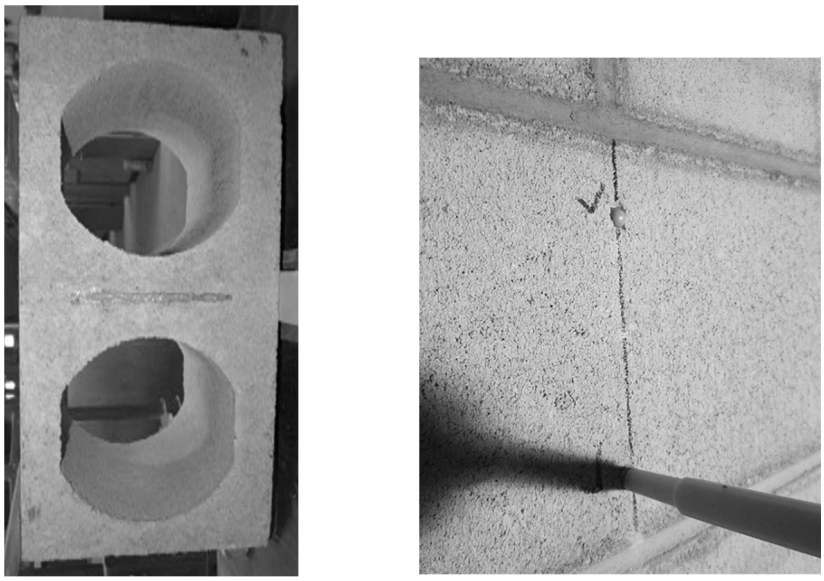

a) Test Specimen with Filled Splitter Slot b) Filling Process in Wall

Figure 5.19. Filling of Splitter Slots

Splitting tests (Figure 5.20 a)) were performed on prototype block specimens with filled splitter slots in a manner similar to the split cylinder test for concrete (ASTM 2011b). In these tests, the first material assessed, Rockite, was similar in composition to a Portland cement grout and splitting tension failure of the specimen occurred at the bond between the block and the fill material. The second filler material, Quikrete FastSet Anchoring Epoxy, proved to be a simple and effective method of filling the voids. In all splitting tension tests, the failure occurred as a splitting crack in the concrete block material adjacent to the filled section as shown in Figure 5.20 b). This indicated that the tensile strength of the bond exceeded the tensile strength of the block material. These test results led to the selection of the anchoring epoxy as the filling material for all slots in the SR Block in the second wall. It is worth noting that, due to some grout and mortar presence in these slots, not all voids could be completely filled with the epoxy and, based on the volume of epoxy used, an estimated average of 70% of each slot contained epoxy following this filling process.

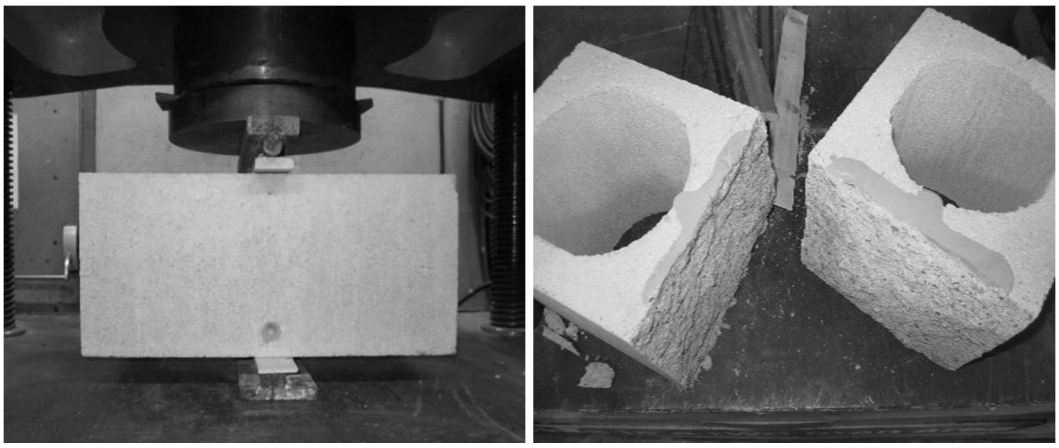

a) Block Splitting Test b) Typical Failure Pattern for Epoxy-Filled Slot

Figure 5.20. Splitting Tests for Epoxy Filled Slots

While it was not anticipated that this retrofit would fully replicate a slot-less block condition, it was expected to remain sufficiently intact to avoid development of the open "head joint" type of condition experienced in the testing of Wall 1. The filled slots were expected to provide direct resistance to vertical sliding at early stages of loading and, when vertical cracking had commenced, allowing friction to be developed between the confined grout columns clamped together by the horizontal reinforcement. This was expected to delay the onset of any sliding which might limit the ability of the wall to resist lateral load at very high displacements.

5.6.1.2. Adjustments to Loading Beam

The original loading beam design was effective until very high loads were reached during testing of the second wall. At this point the load transferred through the vertical bars in the end cells of the wall provided sufficient bearing force on the adjacent grout that vertical splitting of grout cells and block began to occur in the top courses of the wall. When this phenomenon was observed, testing was paused in a zero-load position so that the loading beam could be strengthened. Angles were welded to the beam at each end and mortared into place against the wall to simulate a floor slab condition. Additionally, 350 mm deep channel sections spanning the full length of the wall were welded to the underside of the loading beam on either side of the wall, directly against the block, and drilled to allow eight threaded steel rods to be epoxied into place through holes drilled in the wall. These rods created additional loading planes to further distribute the high lateral forces along the full length of the wall. This modified loading beam setup, shown in Figure 5.21, was effective in transferring the higher lateral loads experienced during remaining test cycles.

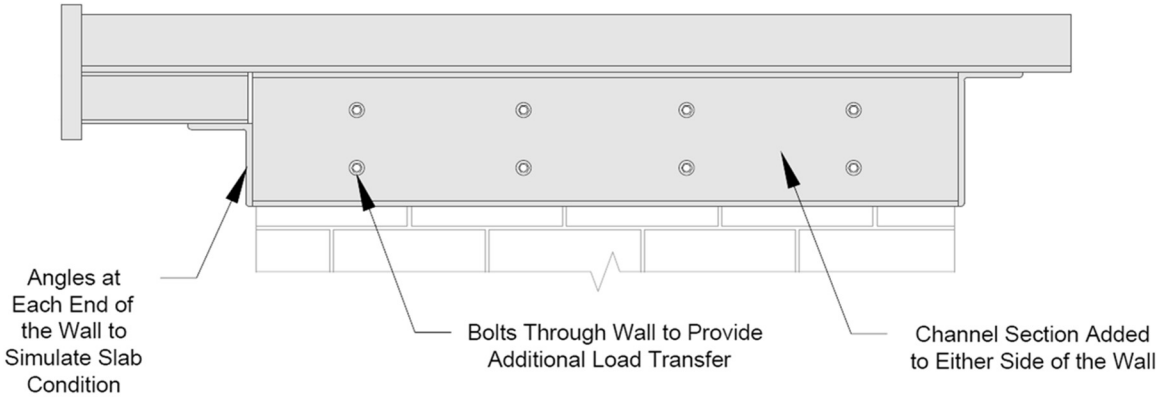

Figure 5.21. Modified Loading Beam for Wall 2

5.6.2. Load-Displacement Hysteresis Loops

The Wall 2 load-displacement hysteresis loops under reversed-cyclic loading have been reproduced in Figure 5.22. These loops indicate very stable and symmetrical behaviour in the push (positive) and pull (negative) loading directions.

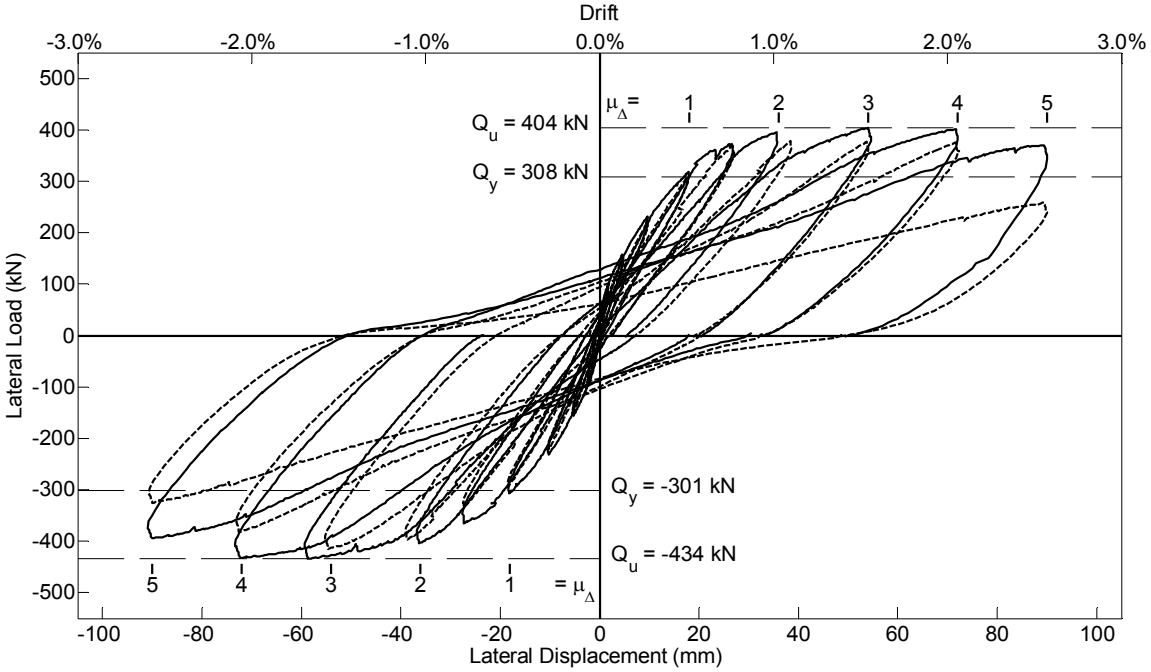

Figure 5.22. Hysteretic Load-Displacement Response of Wall 2

5.6.3. Test Observations

As was the case with Wall 1, cracking in Wall 2 began in the first displacement cycle with horizontal flexural cracks in the bed joints to above mid-height of the wall and the full length of the wall in the cycle prior to yielding of the wall (10 mm) as shown in Figure 5.23 a). At the point of first yield of the flexural steel, rather

than the formation of vertical cracking in the head joints of the masonry to form a stepped-crack pattern as was the case with Wall 1, this more heavily reinforced wall experienced 45˚ diagonal shear cracking passing through blocks as shown in Figure 5.23 b).

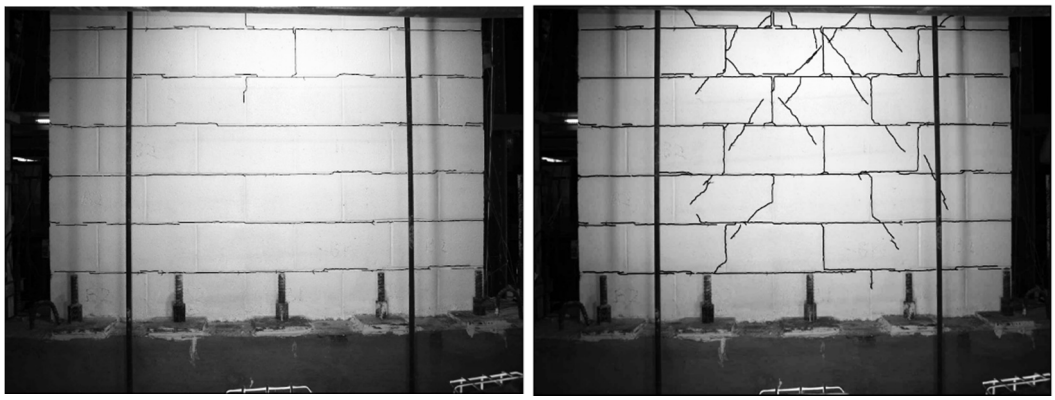

a) Horizontal Flexural Cracking at 10 mm Cycle

b) Formation of Shear Cracking at Δ_y = 18 mm Cycle

Figure 5.23. Flexural and Shear Crack Progression in Wall 2

Diagonal shear cracking continued to develop during all subsequent load cycles, but remained contained within the centre portion of the wall without propagating into the outermost block length (400 mm) on each end of the wall, as can be seen in Figure 5.23 b). In the 36 mm ($2\Delta_y$) cycles, vertical compression related cracks at the toes of the wall initiated and propagated into the second course. During the 54 mm ($3\Delta_y$) cycle, these cracks were sufficiently substantial to cause the first spalling of face shell concrete to expose one confining device at each end of the wall. Also beginning in the 54 mm ($3\Delta_y$) cycles, clusters of short cracks began to appear in a vertical line along the centre of confined regions at the location of the second and third cells from each end. Through the 54 mm ($3\Delta_y$) and the 72 mm ($4\Delta_y$) cycles, the horizontal flexural cracks between courses of block up to a height of four courses (800 mm) widened up to 5 mm at the tension end of the wall as can be clearly seen in Figure 5.24 b). During the 72 mm ($4\Delta_y$) loading cycles, toe spalling continued to expose confining devices on the ends of the second course of block and face shell cracking in a web-like pattern along the next-to-end cells became more prominent as shown in Figure 5.24.

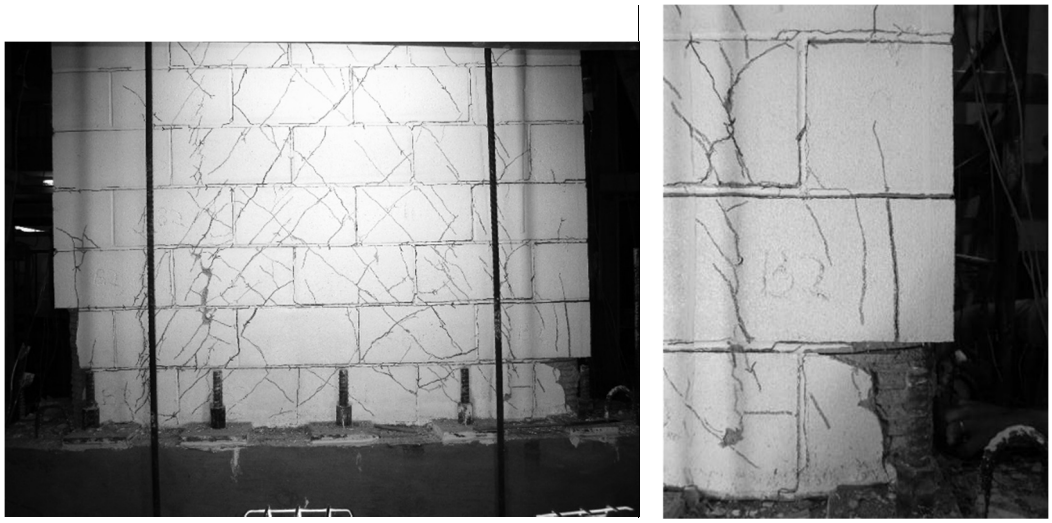

a) Propagation of Cracking and Spalling Across Wall

b) Exposure of Confining Device and Widening of Flexural Cracks

Figure 5.24. Spalling and Crack Progression at 72 mm Cycle (Wall 2)

By the completion of the 90 mm ($5\Delta_y$) loading cycles, the combination of cracking and compressive forces had led to complete face shell spalling to a height of four courses of block (800 mm) across the full length of the wall, as well as widening diagonal shear cracks throughout the centre portion of the wall. In order to preserve the wall in reasonable condition to carry out a retrofitting procedure, loading was terminated following completion of the 90 mm ($5\Delta_y$) loading cycles. It is worth noting that, unlike with Wall 1, a substantial amount of block concrete and grout remained intact in the mid-length portion of the wall not containing confining devices at the completion of testing. Additionally, following face shell spalling, the splitter slots that had been filled with epoxy were visible and could be seen as remaining effective in maintaining a bond between the confined grout columns as shown in Figure 5.25 b). This observation indicated that the onset of vertical shear-slip along a combination head joints and splitter block slots, as occurred for Wall 1, was avoided.

Due to the toe crushing and bar buckling failure mechanisms observed in standard reinforced block construction subjected to this type of loading, spalling damage does not usually propagate far beyond the original compression zone on the ends of the wall. This typical behaviour provided the original reasoning behind locating the SR Block/confining devices in cells only near the ends of the wall. However, tests of Walls 1 and 2 brought to light the propagation of damage that results when toe crushing and bar buckling are delayed. As is evident in Figure 5.25 a), face shell spalling and damage well beyond the zone containing the SR Block contributed to the eventual capacity degradation of Wall 2 at very high strains. This mechanism

was similar to the behaviour of Wall 1 and indicated an altered compression zone which, near failure, encompassed an area beyond that which contained the SR Block. This issue was addressed in the wall retrofit that was performed following testing of Wall 2.

a) Extensive Spalling across the Bottom of the Wall

b) Retained Material Between Columns of Confined Material

Figure 5.25. Wall 2 at Completion of Testing

A procedural incident that occurred during the testing of Wall 2 was noted earlier. During loading cycles at 36 mm ($2\Delta_y$) and 54 mm ($3\Delta_y$), as loads began to exceed what had been experienced by Wall 1, diagonal block cracking observed in the top course of the wall led to the loading beam being modified as described in Section 5.6.1.2. Since this local cracking was isolated from the zone of plastic behaviour, it was considered not to have had any influence on the ductility of the wall.

5.6.4. Response

Referring back to the hysteresis response in Figure 5.22, as observed with Wall 1, behaviour of Wall 2 up to the point of experimental yield was essentially linear-elastic, characterized by thin loops. The yield point of the wall (first yield of reinforcement) was identified (by strain readings on the extreme reinforcing bar as previously described) at a displacement of 18 mm (Δ_y) and at lateral loads of 308 kN in the push direction and 301 kN in the pull direction. At displacements higher than the yield displacement, the slopes of the hysteresis loops decreased, indicating reductions in stiffness, and the width of the loops increased significantly, indicating an increase in energy dissipation. These observations correspond to the plastic behaviour expected in the post-yield loading phase of a ductile shear wall and were similar to the observed behaviour of Wall 1.

Maximum lateral loads of 404 kN in the push direction and 434 kN in the pull direction were reached at the 54 mm ($3\Delta_y$) displacement cycle and were maintained at cycles of 72 mm ($4\Delta_y$). At the first cycle at 90 mm ($5\Delta_y$), loads of 370 kN in the push direction and 394 kN in the pull direction were achieved, representing capacity losses of 8% from the peak load capacity in the push direction and 9% in the pull direction. At the second 90 mm ($5\Delta_y$) displacement cycle, decreases in the loads represented losses greater than 20% from the peak load. The test was terminated following this cycle so that the wall could be repaired and retested. It was apparent from visual inspection at the 90 mm ($5\Delta_y$) displacement that some preliminary signs of shear failure contributed to the decrease in capacity of this wall. However, as a result of the higher horizontal reinforcement ratio in this wall and the modifications made to strengthen the potential sliding planes in the splitter slots in the SR Block, the concrete between the confined columns and in the unconfined region at mid-length of the wall remained more intact than in Wall 1 and more resistant to sliding. Therefore, the decrease in lateral capacity at the same displacement (approximately 90 mm) was much less than had been experienced in Wall 1. The wall was in sufficiently sound condition that it was deemed appropriate to return the wall to a zero load/zero displacement condition for retrofitting.

5.6.5. Behaviour Profiles

Using the same instrumentation as described for Wall 1, in-plane lateral displacement readings were recorded for the push and pull loading cycles up to the 90 mm ($5\Delta_y$) loading cycle. The instrumentation nearest the base was ineffective at high displacement cycles due to face shell spalling. The deflection profiles plotted in Figure 5.26 help to visualize the extent of plasticity achieved over the height of the wall and clearly indicate the bending behaviour concentration at the base of the wall. As was observed with Wall 1, the slope of Wall 2 remained essentially constant above a height of about 1100 mm for all cycles, indicating that comparatively little bending was present in this zone. It is worth noting that some distortion of the lateral profile was present near the top of the wall due to the previously described loading beam issues which caused cracking in this location and, consequently, affected the instrumentation anchored in this area. Changes in slope below 1100 mm and especially below 700 mm height were significant, indicating a concentration of bending and, therefore, plasticity in this lower region.

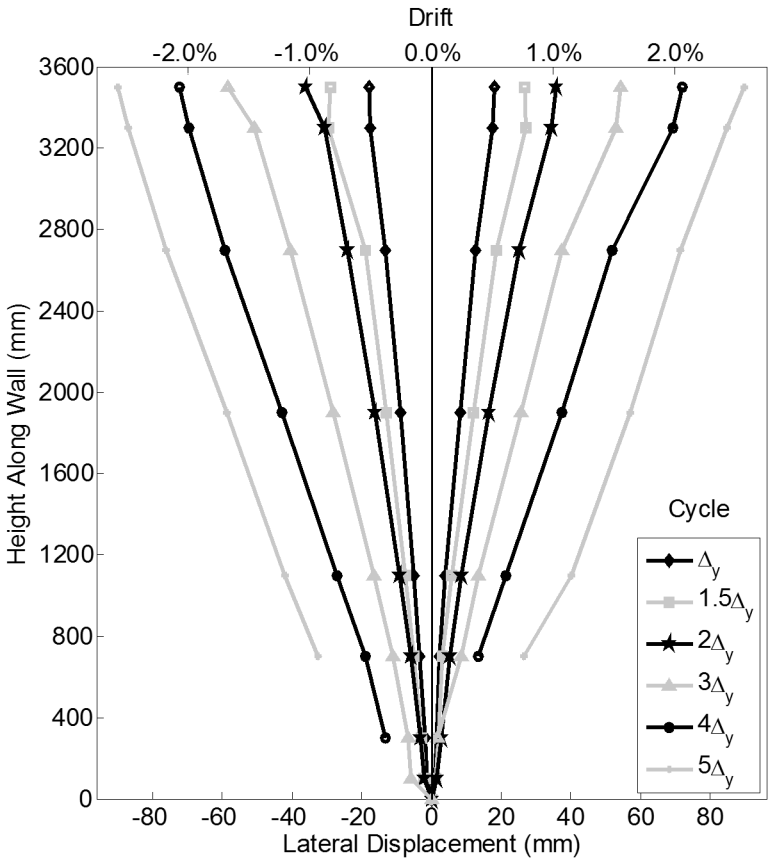

Figure 5.26. Lateral in-Plane Deflection (Wall 2)

Average curvatures for seven segments of wall height were calculated in the manner described in Section 5.5.4 to display the curvature profiles throughout the loading cycles. During cycles at very high displacement, instrumentation attached and anchored near the base of the wall became ineffective due to spalling of the face shell concrete in these regions. Additionally, due to significant cracking in the top course, vertical potentiometers attached near the top of the wall were compromised and were no longer effective following the modifications to the loading beam. The curvature profiles presented in Figure 5.27 correspond to the behaviour observed in the lateral deflection profile, indicating a concentration of bending in the lower region of the wall, below a height of 1100 mm above the base. Above this point, the curvatures remained relatively unchanging with increased deflection prior to the 54 mm ($3\Delta_y$) cycle. Much higher curvatures were observed near the base of the wall; these increased significantly with each loading cycle and approached 0.02 rad/m in the 54 mm ($3\Delta_y$) loading cycle.

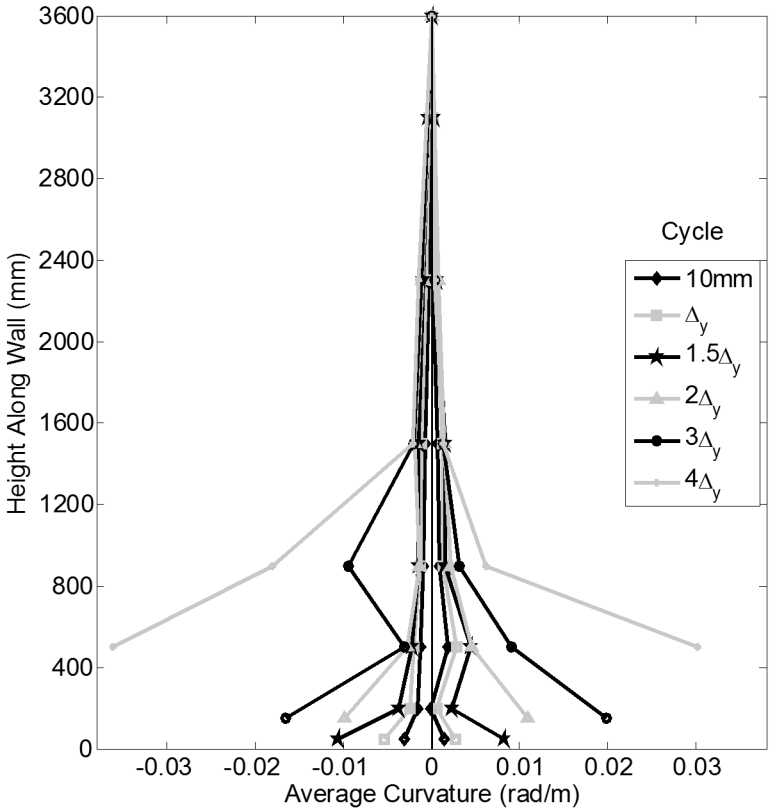

Figure 5.27. Average Curvature over Wall Height (Wall 2)

Similar to Wall 1, average strains along the wall length were plotted in Figure 5.28 for the first 300 mm wall segment and the next 400 mm wall segment above the base. These plots suggest that the wall strain was approximately symmetrical in the two directions of loading and indicate that, while the wall plane remained essentially linear when averaged over the 300 mm to 700 mm segment of the wall height through cycles up to 36 mm ($2\Delta_y$), some nonlinearity was evident in strains averaged over the bottom 300 mm of the wall. When displacement cycles exceeded 36 mm ($2\Delta_y$), this nonlinearity was observed over both of the wall segments.

As was the case with Wall 1, using these plots to identify the average lengths of the compression zones of the wall under lateral loading showed that they were smaller at the higher segment of the wall. The compression zone length interpreted from the plots averaged at a height between 300 and 700 mm from the base was approximately 260 mm at both wall ends while the lengths from the plots averaged over a height of 300 mm from the base were approximately 450 mm at both ends. Up to at least the 54 mm ($3\Delta_y$) displacement cycle, the average lengths of the compression zones remained almost constant in the post-yield cyclic loading of the wall.

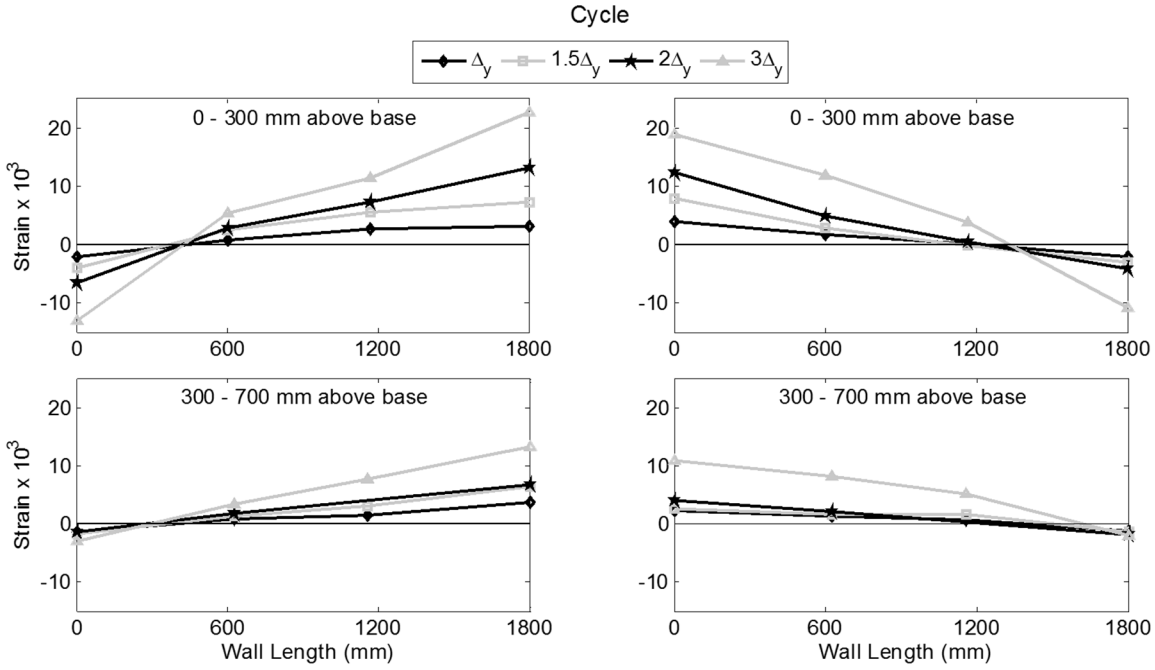

a) Push Direction b) Pull Direction

Figure 5.28. Profile of Average Strain along Wall Length (Wall 2)

5.7. Retrofit Wall

The final wall tested in this program was a retrofitted Wall 2, which was augmented with additional reinforcement and repaired to investigate the feasibility of retrofitting following heavy damage to a wall containing SR Block. Because of the lessons learned regarding potential for vertical sliding shear failure and potential for increased lengths of compression zones to occur at very large strains, additional shear reinforcement and additional confining devices were included to observe the effect that their presence would have on the ductility, failure mechanisms, and overall behaviour of the wall.

5.7.1. Retrofitting Procedure

All retrofitting steps for this wall were performed with the wall in place within the test setup in order to replicate a practical situation. After Wall 2 was returned to a zero load/zero displacement condition at the completion of testing, the following modifications were made to prepare the wall for the pouring of repair concrete to replace the spalled regions of concrete block.

1. All grout and block concrete within the bottom four courses of the wall which was not contained within the confining devices (between the confined columns and in the centre, unconfined region of the wall) was chipped out to provide as much space as possible for the flow of repair concrete. This process was

extensive as can be seen by comparing the post-test Wall 2 specimen shown in Figure 5.25 a) to the pre-pour retrofit specimen shown in Figure 5.29 a).

2. To provide increased resistance to the type of undesirable shear sliding mechanism observed in both previous wall tests, horizontal reinforcement was doubled in the damaged region up to the top of the fourth course. To accomplish this, the first four mortar joints above the bottom of the wall were chiseled out to the location of the vertical bar on the side of the wall opposite to the existing horizontal reinforcement. (The original 10M bars had been placed on alternating sides of the wall in successive courses.) A second horizontal bar was then fitted into place in each mortar joint (see Figure 5.29 b)) and secured with the same anchoring epoxy used previously in filling the splitter slots in the SR Block. This was to ensure bonding in the tight space around the bar where it was thought that repair grout might not penetrate.
3. These new, straight horizontal bars were welded to the 180˚ bends on either end of the existing reinforcement within the end cells to ensure that the new horizontal reinforcement was effectively anchored.
4. As damage levels extended into the central, unconfined portion of the wall in the Wall 2 test, nine confining devices, similar to those contained in the SR Blocks, were produced and threaded into place around the vertical reinforcing bars in this previously unconfined region as shown in Figure 5.29. These additional devices were expected to replicate the behaviour that would be expected if SR Block had been present across the full length of the critical zone of the wall.

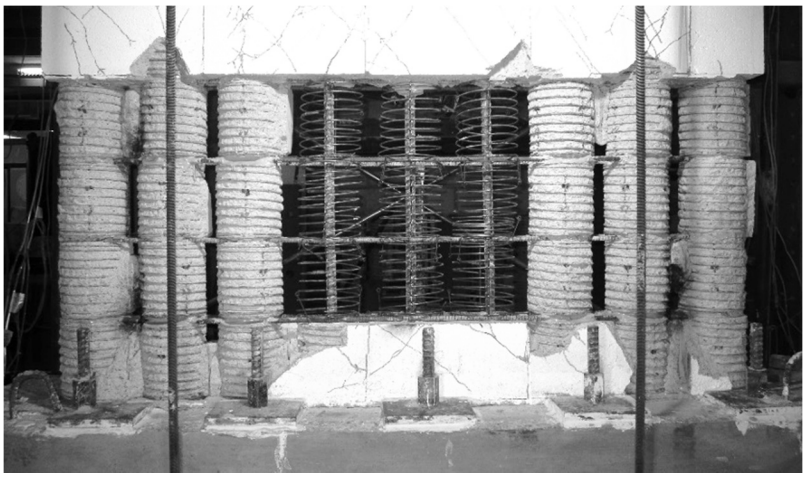

a) Wall Prepared for Retrofit Following Chiseling of Concrete between Confined Grout Columns

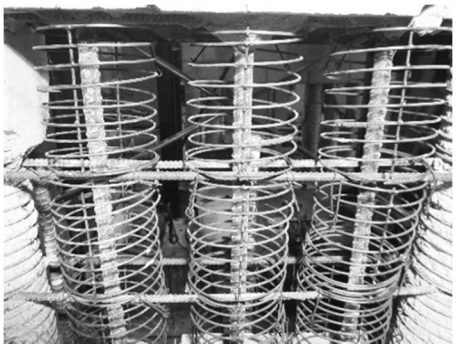

b) Additional Confining Devices and Horizontal Reinforcement

Figure 5.29. Modifications for Wall Retrofit

Following these modifications, the bottom of the wall was formed to the original cross sectional dimensions of 190 mm x 1800 mm using wood forms, sealed to prevent leaking. The two stage form allowed direct pouring of a fluid grout into the centre of the wall through the open fourth course on one face of the wall as shown in Figure 5.30 a). Following this, a second level of plywood was added to cover the fourth course and the remaining grouting was accomplished by pumping grout into the ends of the wall to ensure complete filling. The grout was thoroughly vibrated to ensure complete consolidation throughout the repair area. The grout used for the repair of this wall was identical in mix proportions to the grout used in the original wall construction. Sample cylinders taken from the grout mix and tested after a 28-day curing period had an average compressive strength of 24.8 MPa (C.O.V. of 5.5%).

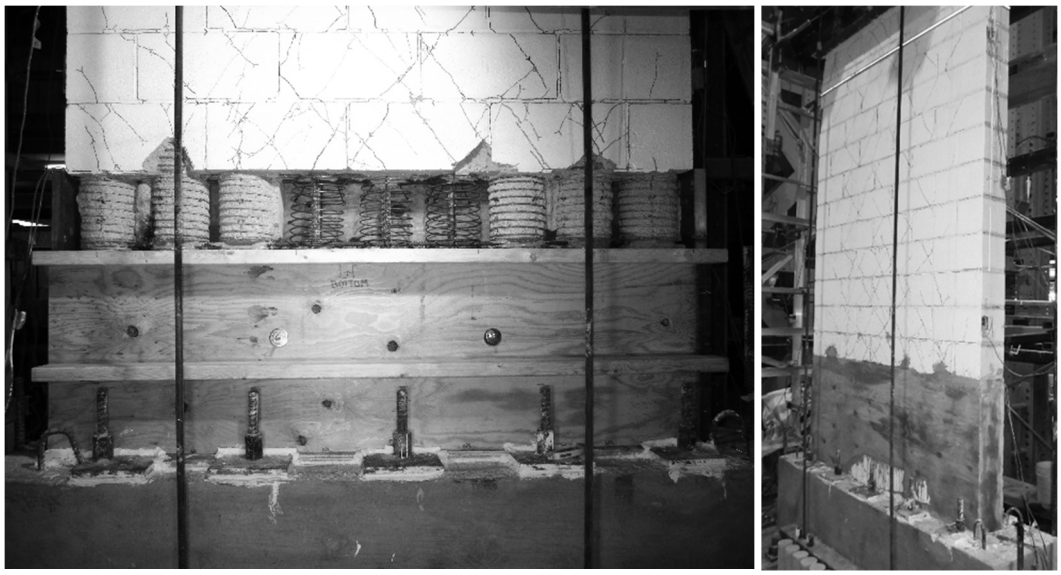

a) Formwork for Repair Grout Pour, Showing Open Fourth Course for Initial Pouring

b) Repair Grout Following Removal of Formwork

Figure 5.30. Grout Pour for Retrofit Wall

5.7.2. Load-Displacement Hysteresis Loops

The Retrofit Wall load-displacement hysteresis loops under reversed-cyclic loading have been reproduced in Figure 5.31. These loops indicate a very stable and very symmetrical behaviour in the push (positive) and pull (negative) loading directions.

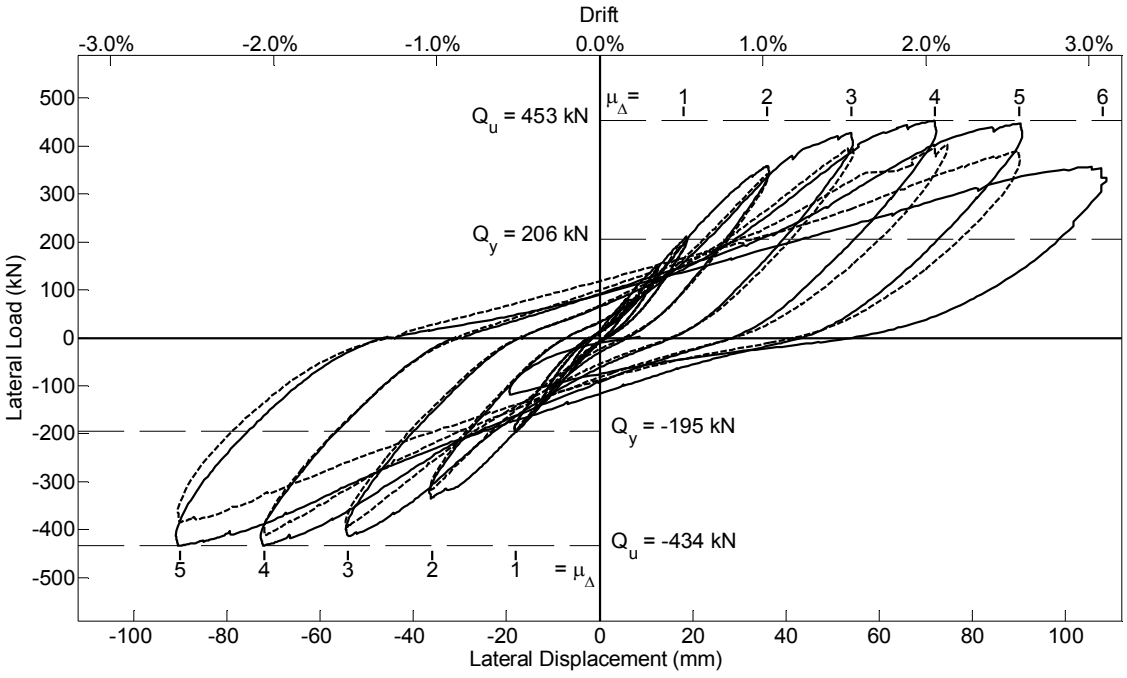

Figure 5.31. Hysteretic Load-Displacement Response of Retrofit Wall

5.7.3. Test Observations

Observations of crack formation and propagation during this test were significantly different from previous tests due to the existing cracks in the unrepaired regions and the fact that the stronger repair grout did not contain weak planes along mortar joints. Prior to the start of this test, extensive shear cracking was already present above the location of the repair, extending well above the mid-height of the wall. As the extreme tension steel in the retrofit wall had already been elongated well beyond its original yield strain, an independent yield displacement for the purpose of establishing displacement increments for cyclic testing could not be easily defined during testing. Therefore, as a reasonable displacement for increments for cyclic testing, a nominal Δ_y was set as equal to the yield value of 18 mm observed during the first testing of Wall 2.

Two cycles at each of two intermediate deflections were completed prior to reaching the nominal yield cycles for this wall. Only minor flexural cracking was observed in the repaired zone of the wall during these four cycles of deflection. Following this, during the cycle at nominal yield deflection (18 mm), shear cracks formed in both directions across the mid-length of the repaired zone as is shown in Figure 5.32 a). Beginning in the yield cycle and increasingly in the 36 mm ($2\Delta_y$) cycles, cracks in the course of masonry above the repair zone also propagated upward to the mid-height of the wall and downward toward the repair zone, while new diagonal cracks continued to form in this region. By the end of the 54 mm ($3\Delta_y$) displacement cycle, spalling was observed at the ends of the wall both in the repair zone and in the course of masonry above the repair zone as shown in the photograph in Figure 5.32 b).

a) Shear Cracks in Repair Zone at Yield Cycle

b) Spalling and Cracking in and above Repair Zone at 54 ($3\Delta_y$) mm Cycle

Figure 5.32. Crack Propagation in and Above Repair Zone (Retrofit Wall)

During the first of the 72 mm ($4\Delta_y$) displacement cycles, cracking above the retrofit area propagated to beyond mid-height of the wall. Additionally, flexural cracking in the repair had become significant, reaching widths of approximately 3 mm at a height of 400 mm from the base of the wall. During the 90 mm ($5\Delta_y$) cycle, face shell spalling was occurring along both the top and ends of the repaired zone and extended into the two courses of block above the repaired zone. The push cycle at 108 mm displacement was the final loading cycle performed with this wall. During this cycle, a large amount of damage was apparent in the two courses above the repaired zone as is shown in Figure 5.33 a). This damage allowed the wall to deflect out-of plane which caused the wall to begin to interfere with the surrounding test setup. At this point testing was terminated as a precaution for protection of equipment. At the termination of the test, the wall had already reached 3% drift and more than five times the nominal Δ_y so that the behaviour of the retrofitted wall had already surpassed that of the original Wall 2. The final deflected shape of the wall is shown in Figure 5.33 b), in which a line representing the position of the original straight wall has been drawn for comparison purposes. Inspection of the damage region in the two courses of block above the repair zone showed that significant shear cracking and spalling had developed in the region which, because it had not been sufficiently damaged in the Wall 2 test, had not been strengthened with additional shear reinforcement and confining devices. Therefore, in the end, the termination of testing was due to the original underestimation of the need for shear reinforcement to resist most of the shear force as the spalling and cracking of the masonry became significant. Similarly, the extension of the compression zone into regions not containing confining devices pointed to the need for more extensive use of these devices if the intent is to maintain full capacity at extremely high ductilities.

a) Spalling Damage at Wall Ends and at Interface above Repaired Zone

b) Final Deflected Profile

Figure 5.33. Retrofit Wall after Completion of Testing

5.7.4. Response

Referring back to the shape of the hysteresis response in Figure 5.31, it is apparent that the retrofitted wall was not as stiff as the original, uncracked Wall 2 but that it exhibited greater stiffness than recorded in the final displacement cycles for Wall 2. As a result, the load resistance at a displacement of 18 mm (representing nominal Δ_y) for this retrofit wall was 206 kN in the push direction and 195 kN in the pull direction, both over 100 kN lower than the initial values found in the test of Wall 2. Clearly, existing cracking and damage above the fourth course had a large effect on overall stiffness during reloading of the wall. Despite this, however, behaviour within this range of displacement appeared to remain initially linear-elastic, characterized by thin loops. At displacements between nominal yield displacement (Δ_y) and $2\Delta_y$, the slopes of the hysteresis loops decreased only slightly, and significant reductions in stiffness did not occur until the 54 mm ($3\Delta_y$) displacement cycles.

Maximum lateral load capacities of 453 kN in the push direction and 434 kN in the pull direction were reached at the 72 mm ($4\Delta_y$) displacement cycle and maintained at the displacement cycles of 90 mm ($5\Delta_y$). This peak was, on average, slightly

higher than that achieved by Wall 2, and was reached at a higher displacement than was the case with Wall 2. Second cycles at each displacement larger than 36 mm ($2\Delta_y$) produced a slightly greater decrease in capacity than was observed in Wall 2. The final cycle at 108 mm ($6\Delta_y$) displacement reached a lateral load resistance of 357 kN representing a drop of 21% from the peak capacity for loading in the push direction. Visual inspection of the wall showed that the vertical shear slip mechanism had begun in the two to three courses above the repaired zone (see Figure 5.33 a)) where there had not been any addition of horizontal reinforcing bars as had been done in the repaired region. The decrease in lateral load resistance was likely due to this weakening effect as the confined columns began to function independently at this location, similar to the effect observed in the lower region in Wall 1. Similar to Wall 1, this sliding shear distortion was accompanied by increased cracking and spalling in the mid-length zone of the wall where there were no confining devices present to improve behaviour as the compression zone expanded into this region.

It is postulated that the beginning of out-of-plane deflection of the wall above the repaired zone was due to the weakening effect described above and, in hindsight, was a reminder that increasing the strength of damaged areas results in higher forces being developed outside of the repaired zone that may cause these areas to become the critical regions.

5.7.5. Behaviour Profiles

The deflection profiles observed for this retrofitted wall indicate a significantly different behaviour pattern than was observed for Walls 1 and 2. The in-plane lateral displacements, measured by eight potentiometers over the height of the wall, have been presented in Figure 5.34 for the push and pull loading cycles up to the 90 mm ($5\Delta_y$) displacement cycle. These profiles provide some indication of the extent of plasticity over the height of the wall. As was the case with the previously tested walls, no significant change in slope was observed above a height of about 1100 mm at any displacement, indicating that relatively little bending deformation was present in this zone. However, whereas the most significant change in slope in the other walls occurred at the base of the wall, with the change decreasing steadily with height up to 1100 mm, in this Retrofit Wall, a change of slope equally as significant as that at the bottom of the wall occurred between heights of 700 mm and 1100 mm from the base. This segment encompassed the height of 800 mm where the repair interface was located and indicated a concentration of bending and therefore plasticity in this region, in addition to that at the base of the wall.

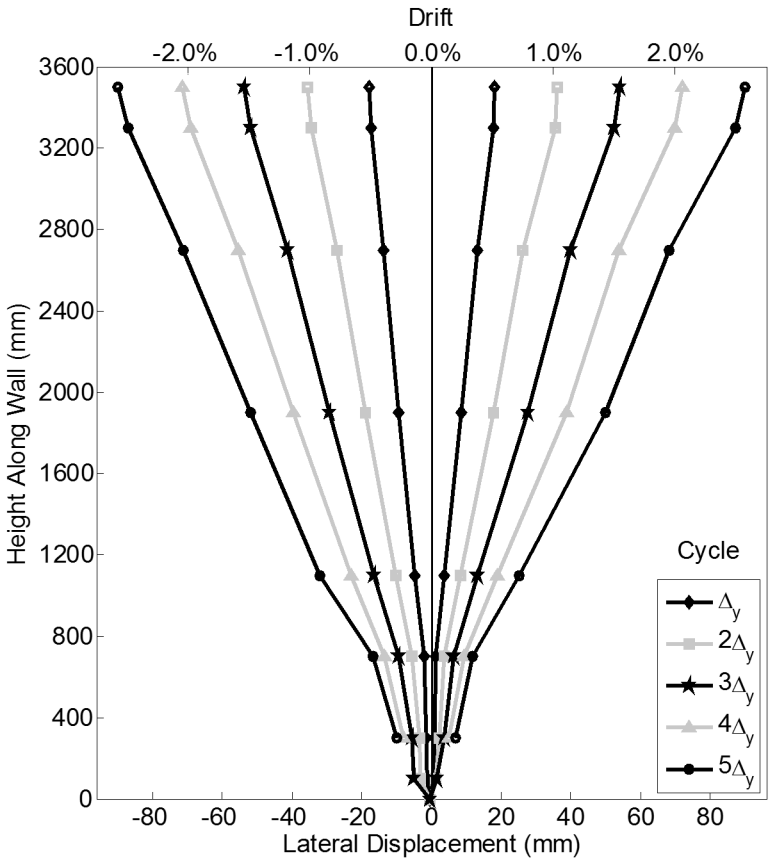

Figure 5.34. Lateral in-Plane Deflection (Retrofit Wall)

Average curvature was calculated as described previously in Section 5.5.4 at seven points over the height of the wall to display the curvature profile throughout the loading cycles. During loading cycles at very high displacements, instrumentation attached and anchored near the base of the wall was ineffective due to spalling of the face shell concrete in these regions. Additionally, due to the modified shape of the loading beam, instrumentation could not be placed at the very top of the wall. Therefore, these factors resulted in no data being available for some wall segments as presented in Figure 5.35. These curvature profiles are compatible with the behaviour observed in the lateral deflection profile, indicating a concentration of bending in the region of the wall above the repaired zone, below a height of 1100 mm and above a height of 700 mm from the base, as well as at the base of the wall. The highest curvatures were observed near the base of the wall and increased significantly with each loading cycle. They exceeded 0.02 rad/m in the 54 mm ($3\Delta_y$) displacement cycle. Additionally, curvatures in the segment from 700 mm to 1100 mm (averaged at a height of 900 mm) from the base exceeded 0.01 rad/m in the 54 mm ($3\Delta_y$) cycle: more than double what was observed at the same displacement during the initial testing of the wall (Wall 2).

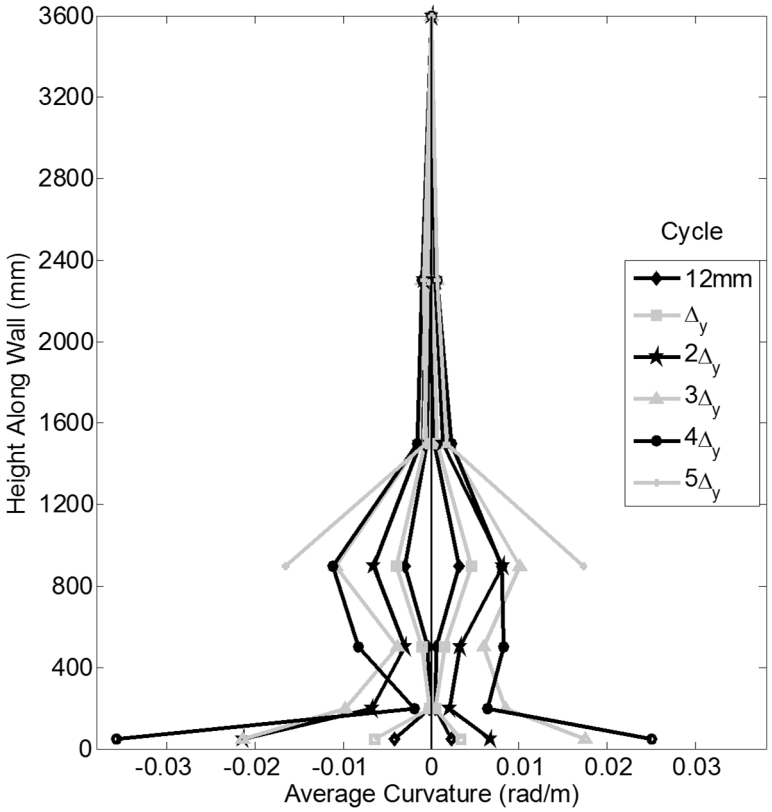

Figure 5.35. Average Curvature over Wall Height (Retrofit Wall)

To analyze the profiles of masonry strain across the length of the wall, readings from four potentiometers across the wall face at two heights (300 mm and 700 mm) above the base were plotted in Figure 5.36 as average strains over the bottom 300 mm and the next 400 mm of the wall (up to a total height of 700 mm) in both the push and pull directions. These plots suggest that the wall strain was approximately symmetric in the two directions of loading and indicate that significant nonlinearity (non-planar behaviour) was present in strains averaged over the length of the wall. The wall strain profiles over the bottom 300 mm for this retrofit wall were approximately the same as those observed for Wall 2 at the same loading cycles.

In using these plots to identify the length of the compression zone of the wall under lateral loading, unlike with the previous walls, the average compression zone was larger at a higher point on the wall. The average compression zone length interpreted from the plots in the push direction was approximately 400 mm over the bottom 300 mm of the wall and approximately 600 mm between heights of 300 mm and 700 mm from the base of the wall. This was a significantly different result from the previous two wall tests in which the length of the compression zone decreased with height. This observation is in line with previous observations of this wall suggesting that more deformation was taking place at greater distances from

the base of the wall than had been the case with the previous two wall tests. At least up to the 72 mm ($4\Delta_y$) displacement cycle, the lengths of the compression zones appeared to remain reasonably constant in the post-yield cycling of the wall.

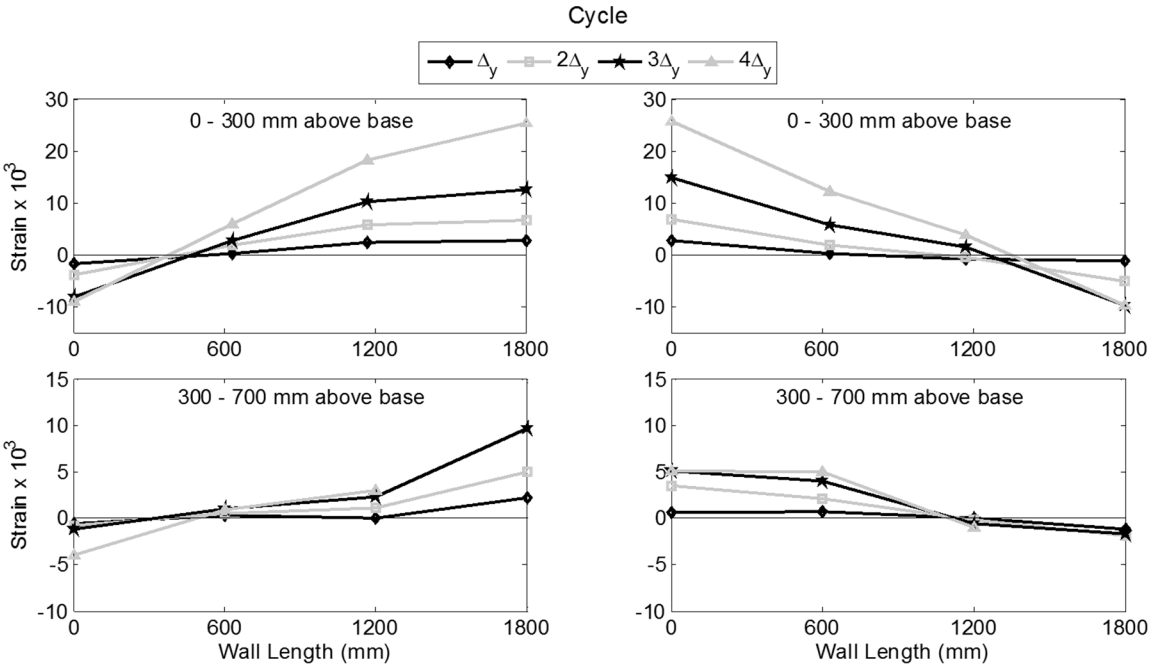

a) Push Direction b) Pull Direction

Figure 5.36. Profile of Average Strain along Wall Length (Retrofit Wall)

5.8. Closure

The unrefined data from the tests of Walls 1 and 2 clearly show the development of very ductile behaviour and the ability of these walls to sustain large amounts of damage while retaining their initial peak capacity. The ability to develop extremely high compressive strains in the plastic hinging regions of these walls was attributable to the presence of the confining devices and was consistent with the performance observed in the prism tests presented in Chapters 3 and 4. A more extensive study of the ductilities achieved is included in Chapter 6. In hindsight, the inclusion of splitter slots in the SR Block and the effect that these would have was an oversight in the original block design and is easily corrected in future block manufacture.

Additionally, although related to the presence of the splitter slot in the SR Block, the observed tendency for sliding shear to develop as the masonry reached high levels of damage at very high strains, served as a reminder that at high ductility levels, the shear reinforcement in reinforced masonry should be designed to resist most if not all of the shear force rather than relying on the damaged masonry. Also,

as a result of the very high levels of ductility reached, the related damage in the compression zones was shown to result in a greatly increased compression zone length which had the effect of requiring that confining devices be included not only in the originally intended compression zone but also in the expanded zone.

The retrofit of Wall 2 was easily and quickly achieved and the test results show that full capacity and displacement capability were restored. This indicates that the use of SR Block has the added benefit that buildings damaged in the process of resisting earthquakes can be quickly and economically repaired to restore the originally designed ability to resist the effects of large earthquakes.

CHAPTER 6

INTERPRETATION AND ANALYSIS OF RESULTS

6.1. Introduction

In this chapter, test results from each of the reported experimental programs have been briefly analyzed. Prism test results were used to compare the effectiveness of the different trial block and confining device designs and to evaluate possible methods for calculating the strength of the confined masonry materials based on existing methods for confined concrete. Additionally, prism and material test results were used to calculate expected shear and flexural strengths for the shear walls tested in this program, which were then compared to the experimental results from wall testing.

Wall test results were used to calculate both idealized and experimental values for displacement ductility as an indication of the ability of buildings constructed with these types of walls to dissipate energy from earthquakes and to modify their structural response to this dynamic loading. Wall test results were also compared to experimental results for similar, unconfined walls tested previously at McMaster University by Shedid (2006). From these results, conclusions could be drawn with respect to the effects of including SR Block in masonry shear wall construction.

6.2. Confining Strength

It is desirable for future research on SR Block, to be able to predict the compressive capacity of confined material without the need to test all potential loading conditions. As a start on this work, the two established methods of calculating the effect of confinement of concrete presented in the literature review in Chapter 1 have been used to calculate expected capacities for comparison with the experimental test results. The first method (Equation 1.2) is an empirical equation found frequently in literature (MacGregor & Wight 2004; Paulay & Priestley 1992) and calculates the confined strength, f'_{cc}, as an increase over the unconfined strength, f'_c, of 4.1 times the confining pressure, f_1. To directly apply this equation to concrete masonry would yield:

$$f'_{cm} = f'_m + 4.1 f_1 \tag{6.1}$$

Where f'_{cm} is the strength of the confined masonry (MPa)
f'_m is the corresponding unconfined strength of masonry (MPa)
f_1 is the lateral confining stress on the confined volume of masonry (MPa)

For the purposes of this analysis, f'_m was taken as the strength of the grouted, unconfined prisms corresponding to each SR Block series. It is worth noting that this value is not necessarily closely representative of the confined material, given that the core of material confined by the devices was composed of a different grout/mortar/block ratio than the fully grouted prisms tested. However, unconfined columns of the identical composition to that which existed within the confinement were not tested, so the best available assemblage strengths were utilized.

A second method of calculating confined strength of concrete (Equation 1.6) was presented by Paulay and Priestley (1992). This series of equations, based on the same parameters as the above equation and adjusted to directly apply to masonry yields:

$$f'_{cm} = -1.254f'_m + 2.254\sqrt{f'^2_m + 7.94f'_m f'_1} - 2f'_1 \quad (6.2)$$

Values used in these two calculations have been determined according to Equations 1.4 and 1.5 and have been presented together with the experimental test results in Table 6.1 and results of the calculations have been presented in Table 6.2. Experimental test results presented (stress) have been calculated as force over confined area directly without making any allowance for some added capacity due to the presence of the vertical steel members in the confining devices.

As explained below in Section 6.3.1, while it seems clear that the presence of significant vertical steel has an impact on the initial peak capacity and subsequent capacities of the prisms, no attempt to theoretically predict the magnitude of this effect was made. At the point of reaching the second peak stress, when spalling around the outside of the devices and some degradation of the mortar joints between the non-continuous vertical members of the confining devices had occurred, compression strains would be much larger than yield strains for the steel in the confining devices. However, the absence of vertical members across the mortar bed joint and the need for stress to build up from the top and bottom of the device would likely limit their effectiveness in providing vertical load capacity. For these reasons, it was expected that the following predicted confined capacities would represent a lower bound for the true prism strengths which would increase in some proportion with the amount of vertical steel present in the confining devices.

Table 6.1. Test Values Relating to Confined Strength

Type	f'_m (MPa)	f_l (MPa)	Experimental f'_{cm} (MPa)
Punched Steel Prototype I	15.9	4.26	32.5
Punched Steel Prototype II	13.4	4.26	30.9
Spiral Steel (Type WB)	13.5	5.56	33.3

Table 6.2. Confined Strength Predictions

Type	Confined Strength, f'_{cm}			
	From Eqn 6.1 (MPa)	% of Experimental	From Eqn 6.2 (MPa)	% of Experimental
Punched Steel Prototype I	33.4	(103%)	34.3	(106%)
Punched Steel Prototype II	30.9	(100%)	30.8	(100%)
Spiral Steel (Type WB)	36.3	(109%)	34.2	(103%)

It seems, in comparing the predicted confined strength values to those achieved during prism testing, that both of the equations presented above, which originate from confined concrete literature, led to a reasonable estimate of the peak strength of the remaining confined area of the SR Block assemblage following the spalling of outer block concrete. However, according to the values calculated for this research program, these methods of estimation do not provide any level of conservatism and involve a series of assumptions including the use of grouted f'_m as a strength representative of the enclosed material. As such, as more experimental data becomes available with further testing of SR Block, it is suggested that these methods provide a basis for further analysis and perhaps be modified to more accurately and/or conservatively represent the strength of the confined masonry that results from the use of SR Block.

6.3. SR Block Design

6.3.1. Comparison of Trial Confining Device Designs

A comparison of the two different confining devices tested in this program was presented in Chapter 4. Some of the differences between behaviours of the prisms containing the confining devices have been discussed further here.

Although the behaviours of the grouted prism series corresponding to the two different confining devices were almost identical, as noted in Section 4.5.2, the prisms containing the punched steel device achieved a 13% increase in the initial peak capacity over the unreinforced counterpart while the prisms with the spiralled wire device experienced no capacity increase at this point. It was initially postulated

that this difference could be attributed to the difference in vertical steel present and its contribution to resisting vertical load, as well as perhaps improving the confinement of the enclosed concrete materials.

The punched steel cage contained 6.35 mm (¼") wide by 2.9 mm thick vertical strips at 25.4 mm (1") spacing all around the perimeter of the device, providing a much higher volume of vertical steel and therefore the potential for a more significant capacity increase than the four, 3.18 mm ($^1/_8$") diameter vertical wires welded within the spiralled wire device. The cross-sectional area of steel provided in the punched-steel devices consisting of 21 vertical members was 389.8 mm^2 while the four supporting vertical rods in the spiralled wire devices provided a total area of only 31.8 mm^2. Given that the initial peak capacity was achieved in both prism sets at a strain of approximately 0.002 and that the elastic modulus of steel is 200 GPa, the maximum stress that could be developed in the steel at the initial peak load would be about 400 MPa. (This is below the known yield stress of both steel types.) Translating to force, the vertical steel members in the two punched steel confining devices per prism could contribute a maximum capacity of 311.8 kN while the vertical steel rods in the two spiralled wire devices could contribute only a maximum force of 25.4 kN.

When the initial peak capacity of the prisms containing the punched steel confining devices was compared to the capacity of the unreinforced prototype Type II prisms, the punched steel vertical members could be thought to have accounted for 133.4 kN of the total average first peak capacity of 1126 kN for the GPIIR prisms. Since this value is about half of the maximum possible increase in capacity noted above, it is clear that the idea of superimposing the separate strengths of the unreinforced prism and the vertical members of the confining device is not valid. Although the increase in first peak capacity was quite significant, this finding was not surprising as the vertical members of the confining devices do not cross the mortar bed joints and it is reasonable to expect that the built-up in force in these vertical members would be gradual from the top and the bottom of the devices toward the mid height of the device. Alternatively, the vertical wire rods in the spiralled wire devices did not affect any significant change on the total average load supported by the prisms. This further confirmed that superposition of the capacity of vertical steel members onto the load capacity of the unconfined prisms to predict initial peak strength was not appropriate. Despite this rejection of direct superposition, comparison of the difference in initial peak strength relative to the presence of vertical steel still suggests that the vertical members had some effect on the pre-spalling capacity of the prisms and it is possible that some benefit remained during loading to higher strains.

A second difference between the stress-strain behaviours of prisms containing the two devices that may have been due, in part, to the presence of the vertical steel members was the magnitude of the capacity decrease that followed the initial peak strength. As noted in Section 4.5.2, for the prisms with the punched steel confining devices, this decrease in strength never exceeded 10% of the initial peak capacity. The vertical steel appears to have provided sufficient stiffness and strength to minimize the compressive capacity decrease that occurred at the onset of the external block spalling. Conversely, without the presence of the high volume of vertical steel, the prisms containing the spiralled wire devices experienced a much greater (25%) decrease in capacity during spalling and consequently required a much higher compressive strain to regain the initial peak load capacity.

Differences in the second peak strength achieved by each prism series can be easily explained by the properties inherent to the device shapes, and the properties of the steels from which the devices were manufactured. Even with slightly lower grout strengths, the higher strength, less ductile steel used for the spiralled wire devices allowed prisms to reach higher ultimate capacities, but reduced the presence of a strength plateau when compared to the lower strength, more ductile steel used in the punched steel design. Also, as previously reported in concrete research (Sheikh & Toklucu 1993), yield or fracture at one location in the confining device, while not detrimental in a cylindrical structure such as the punched steel design which has other lateral members present to share the total load, can lead to more rapid failure in the spiral devices because the integrity of the entire, continuous confining loops is compromised.

6.4. Shear Wall Test Result Calculations

6.4.1. Strength Predictions

6.4.1.1. Flexural Strength

The stress-strain relationship exhibited by the SR Block in prism testing differed greatly from that of conventional construction. For this reason, it was not logical to predict the high strain behaviour of a wall containing SR Block under lateral loading using existing code parameters and assumptions. Instead, in order to predict the strength and deflection performance of the walls in this test series, pushover analyses were performed based on a revised set of assumptions and material behaviours determined by tests.

The following results from the pushover analyses were calculated based on the set of equations presented in Appendix C using an iteration method to determine position of the neutral axis to satisfy compatibility of axial load for a selected extreme fibre compression strain. Then the corresponding moment resistance was

calculated. The two stress-strain curves presented in Figure 6.1 were used to obtain all stress values for both the masonry and steel for this analysis. In this way, the results account for the strain hardening of both materials. The prism results for the GPR-WB prism series were used as blocks containing devices made from Type WB steel made up the critical compression zones at the base of each wall.

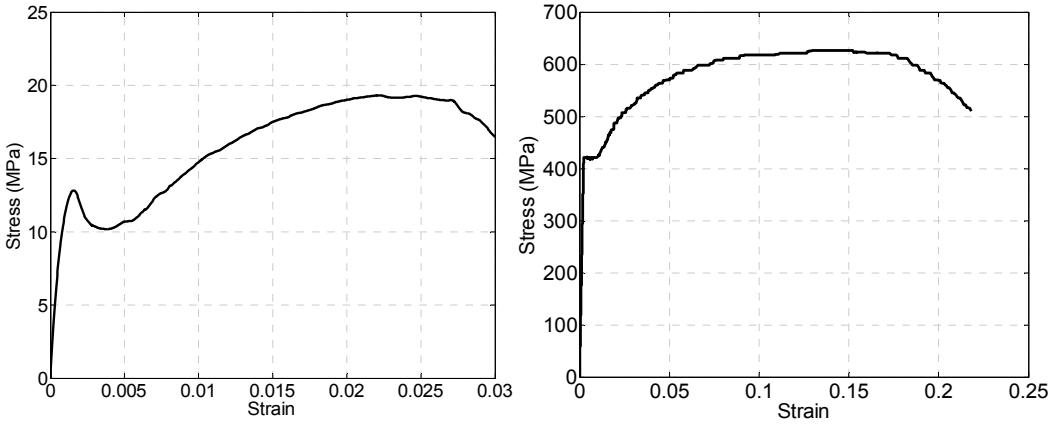

a) Average Curve for GPR-WB Prism Series b) Representative Curve for Vertical Steel

Figure 6.1. Material Stress-Strain Properties Utilized in Wall Performance Predictions

The yield displacement of each wall was established as the point at which the outermost reinforcing bar reached the yield strain as identified in the material testing. Following yield, although spalling of concrete material around the devices was expected, it was assumed that the behaviour of the material in the compression zone of the wall would be identical to that of the corresponding prisms under compression. As stresses from the prism tests used in this analysis were based on the original gross area of the prism rather than calculating a post-spalling area, the gross area of the compression zone in the wall was also retained in the strength calculations. This was expected to be more accurate than attempting to identify/predict the extent of area lost due to spalling in both the prism tests and wall tests.

As detailed material properties were available, there was no need to utilize the typical assumptions of a linear stress distribution prior to yield of the vertical reinforcement and an equivalent rectangular masonry stress block under ultimate conditions. Assuming that plane sections remained plane, strain at several points throughout the compression zone were calculated and the corresponding stress values from the prism stress-strain curve were used to calculate the stress profile in the compression zone for both yield and ultimate conditions.

Other assumptions made throughout the course of this analysis included a conservative assumption of plastic hinge length for post-yield calculations according to the CSA S304 (2004a) prescription of:

$$h_p = the\ greater\ of\ \ h_w/6\ \ or\ l_w \tag{5.1}$$

which in this case yielded a plastic hinge length of 1800 mm. Additionally, self-weight of the wall was calculated to be 4 kN/m^2 contributing an axial load of 26 kN at the base of the wall which, when combined with the applied axial load of 260 kN, resulted in total axial load for analysis purposes of 286 kN. Finally, compression steel was accounted for in all calculations as it was assumed that the confining devices and confined concrete material would provide sufficient lateral support to prevent buckling of these reinforcing bars.

The strengths presented in Table 6.3 were calculated according to five distinct criteria including first yield of tension reinforcement and six different definitions of ultimate compression strain in the masonry. The first ultimate condition represents a conservative estimate for non-confined masonry as a basis for comparison. A limiting strain of 0.2% was used for this base calculation, representing the point at which the prism test results displayed a strength loss of approximately 10% from the initial peak capacity. The current CSA S304 (CSA 2004a) code allows compressive masonry strains up to 0.3% for strength calculations, so wall capacities were also calculated for this condition, representing the generally expected behaviour of unconfined masonry. Following these ultimate conditions relating to unconfined masonry, the next ultimate condition presented was the limit allowed by the former Uniform Building Code (ICBO 1997) for confined masonry, defining ultimate conditions at a maximum masonry compressive strain of 0.6%. The fourth ultimate condition calculated represents the ultimate condition defined in the proposed seismic provisions in the draft of the 2014 edition of CSA S304 (CSA 2014). Clause 16.10.2 of the revised draft limits compressive strain in adequately confined masonry to 0.8%. A fifth ultimate condition calculated represents the ultimate condition defined by the CSA A23.3 (CSA 2004b) for confined concrete, using a maximum concrete compressive strain of 1.4%. Finally, although it might be considered unlikely that the compression zone of a wall would reach the ultimate strains achieved in prism testing because of drift limitations and other considerations, a failure condition for ultimate compressive masonry strain of 2%, representing the range in which prism specimens reached the secondary peak strength, has been presented.

Table 6.3. Wall Flexural Strength Predictions

	Lateral Force (kN)	
	Wall 1	**Wall 2**
Yield (FME) ε_s**= 0.0021**	205.1	283.9
Conservative Unconfined Limit ε_m**= 0.002**	258.0	352.1
CSA S304.1 Unconfined Limit ε_m**= 0.003**	263.9	371.3
Former UBC Criteria ε_m**= 0.006**	273.6	383.9
Proposed CSA Provisions ε_m**= 0.008**	285.6	398.9
CSA A23.3 Confined Concrete Limit ε_m**= 0.014**	319.4	448.6
Prism Test Peak ε_m**= 0.020**	345.3	485.8

6.4.1.2. Shear Strength

Shear-governed behaviour is generally thought to be a brittle and undesirable mode of failure in structural walls. Therefore, it was necessary to design the shear strength of each wall to ensure that sufficient shear strength would be available to allow the full flexural capacity to be developed. A shear analysis was performed according to two prescribed methods. The results of this analysis are presented in Table 6.4. Calculations for the purpose of this analysis were performed using the material strengths obtained from testing including a yield strength for the horizontal steel reinforcement of 490 MPa and a compressive strength for the grouted masonry of 13 MPa (representing the average strength from all grouted series within the corresponding prism test program).

The first shear capacity check was performed according to Clause 10.10 of CSA S304 (CSA 2004) for in-plane loading. As material strengths were established through testing, material resistance/reduction factors were left out of calculations; the resulting equation system is presented in Appendix C. The second set of criteria used to predict shear capacity were prescribed by Paulay and Priestley (1992) as a conservative approach for design. These equations have also been presented in Appendix C.

Both of the methods used to calculate shear capacities combine the strength provided by shear reinforcement (V_s) and the friction provided by axial loading and the masonry strength (V_m) to estimate an overall shear resistance (V_r). Both methods also require a significant reduction in the shear resistance provided by the masonry material within the potential hinge region. Capacities have been presented

for both the potential plastic hinging region and the region above this level for each calculation method.

Table 6.4. Wall Shear Strength Predictions

		S304.1 (2004)			Paulay and Priestley (1992)		
		V_s (kN)	V_m (kN)	V_r (kN)	V_s (kN)	V_m (kN)	V_r (kN)
Wall 1	above hinge region	105	220	325	175	230	405
	in potential hinge region		110	215		90	265
Wall 2	above hinge region	210	220	430	350	230	580
	in potential hinge region		110	320		90	440

Results from the analyses indicate that the CSA S304 method is a conservative approach for determining shear resistance when compared with the approach by Paulay and Priestley (1992). Additionally, Paulay and Priestley have suggested that the extent of their reduction required within the plastic hinge zone is a conservative approach. Taking these factors into account, it seemed reasonable to expect that the shear capacity provided by the walls in this test program would be sufficient to allow each wall to reach the desired flexural failure mechanisms outlined above, despite the fact that that the estimated shear strengths in the plastic hinge regions were lower than the shear forces required to reach the anticipated flexural strengths as shown in Table 6.3. This was especially true for Wall 2 in which the shear limits according to the definition by Paulay and Priestley (1992) would not be exceeded until a compressive masonry strain of 0.8% was surpassed.

6.4.1.3. Comparison to Test Results

The lateral load-displacement envelopes for all three tested walls have been presented in Figure 6.2 for comparison with the predicted lateral load capacities. Peak strengths of +276 kN/-270 kN were reached for Wall 1 and maintained up to a displacement of $6\Delta_y$, but at higher displacements and after significant damage, shear slip along the head joints began to govern. These peak capacities were in a range equal to the capacity of 274 kN predicted when allowing ε_m= 0.006 and were within 5% of the ultimate anticipated capacity predicted using ε_m= 0.008. The previously described unforeseen weak plane along the splitter block slots and mortar head joints that caused this shear weakness following spalling can be equated to the weakness that exists in stack pattern construction. CSA S304 has an alternate clause to address the shear strength under this condition, stating that "shear resistance in stack pattern walls shall not exceed that corresponding to the shear friction resistance of the continuous horizontal reinforcing used to tie the wall together at the continuous head joints" (CSA 2004a). This effect helps to explain

the rapid capacity decrease that followed the spalling damage as the strength of the wall began to be dependent on the horizontal reinforcement.

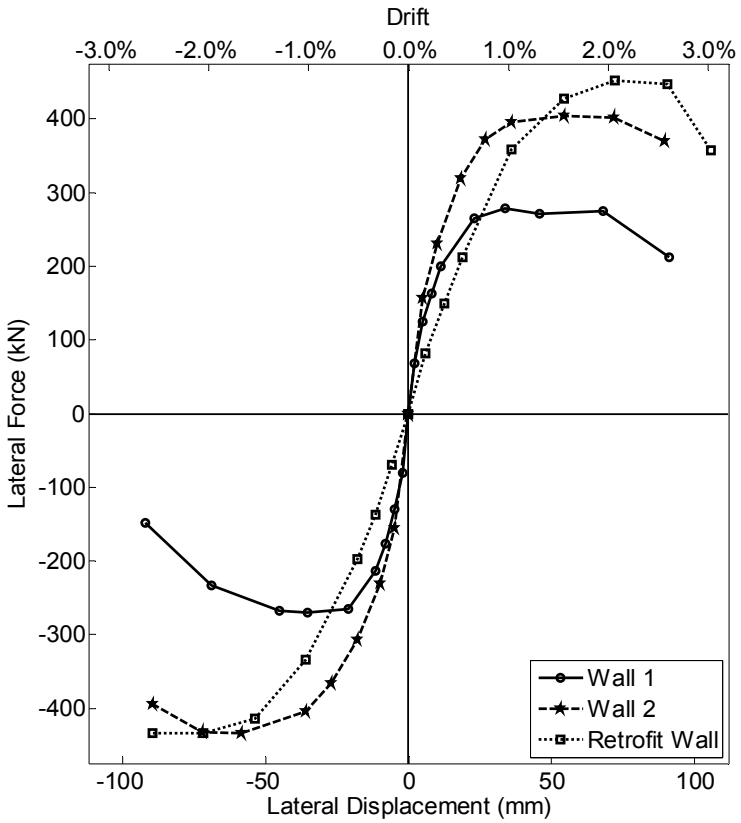

Figure 6.2. Load-Displacement Envelopes

Peak strengths of +404 kN/-434 kN were reached for Wall 2 and maintained until a displacement of $4\Delta_y$. These strengths exceed the anticipated flexural capacity predicted when allowing ε_m= 0.008 by 1% and 9%, respectively, but were still well below the shear limits predicted using the Paulay and Priestley equations both within and above the plastic hinge zone. No significant load degradation due to shear was observed in this wall as testing was stopped at high strains and displacements but before excessive spalling damage. In the Retrofit Wall, the shear reinforcement was doubled within the repair zone, increasing the theoretical shear resistance of the steel to V_s = 423 kN (CSA 2004a) or V_s = 706 kN (Paulay & Priestley 1992). This resistance alone exceeded all expected shear forces corresponding to the flexural capacities, indicating that the retrofit concrete did not have to be relied upon to resist shear. Shear slip began to occur, however, in courses above the repair zone following significant spalling as in Wall 1, causing load degradation below the peak of +453 kN/-434 kN at a displacement of $5\Delta_y$.

6.4.2. Ductility

Ductility is defined as the ability of a structural element to deform beyond elastic limits without significant strength degradation (Paulay & Priestley 1992). This is a beneficial property of the force resisting system in structures subjected to seismic loading (in this case, masonry shear walls). It indicates the capacity for energy dissipation through hysteretic behaviour and modification of the fundamental period of the structure to be less vulnerable to seismic excitation. Until recently, masonry construction was not considered to be capable of achieving comparable ductilities to other forms of construction.

While various methods have been documented, there is currently no codified method for calculating the ductility of a masonry shear wall (or similar elements of other materials) from experimental test data. Expressed in its most basic sense, ductility is equal to the ratio of the response at ultimate state to that when a condition of yield is first achieved. For the purposes of this study, ductility has been calculated and referred to in terms of displacement ductility (μ_Δ). Displacements at yield and ultimate conditions are simple to define in an elastic-perfectly-plastic material, but are less definitive in the context of a shear wall load-displacement envelope. For this reason, various approaches have been used to idealize this envelope into a bilinear elasto-plastic relationship in order to extract idealized yield and ultimate displacement values.

Although, as mentioned above, there is no officially recognized approach, there is a growing consensus that the equal energy approach described below provides a fair and least biased method to quantify ductility. The first estimation required for this idealization is of the stiffness of the elastic portion of the curve. In testing of the walls for this program, the experimental yield point (Δ_y) was established (for each of the originally constructed walls) as the first point of vertical steel yield. As this yield point was known from testing, it was selected to define the secant stiffness for the idealized elasto-plastic response for the purposes of this study. The method followed for this process was the same as that described by Shedid et al. (2009) so that results from this program could be compared to the tests of unconfined walls in his study. An alternative to this definition, for situations where the yield point is unknown, has been described by Paulay and Priestley (1992) where the effective secant stiffness is based on the experimental load-displacement curve at a load of 75% of ultimate load capacity. The loads achieved at yield and used for the secant stiffness for this study have been presented in Table 6.5 and shown in the final column as a ratio to the ultimate load for comparison to this estimation. It is clear from observing these ratios that the experimentally derived yield values were within

5% of this 75% estimation and can therefore be assumed to be reasonable for this idealization.

The second important estimation in the construction of the idealized elasto-plastic envelope is the point that is considered to represent ultimate displacement conditions. Paulay and Priestley (1992) define ultimate displacement conditions for the purpose of calculating displacement ductility as the displacement (beyond that at ultimate load) at which reduction of no more than 20% from the measured ultimate capacity is reached. Using this definition, linear interpolation between points on the load-displacement curve was used to define the ultimate displacement, $\Delta_{0.8Qu}$, as that corresponding to a decrease in load capacity to $0.8Q_u$. As loading of Wall 2 was terminated at high displacements but before significant damage had occurred which might hamper the retrofit, a 20% reduction in load was never achieved. As such, the maximum displacement reached during testing, Δ_u, corresponding to a decrease of approximately 10% of ultimate lateral load capacity was used to calculate an idealized ductility for each loading direction for this wall (and in the pull direction for the Retrofit Wall). Additionally, to provide an estimate of the displacement that could have been reached (if testing of Wall 2 had been continued) at the failure criterion defined by Paulay and Priestley, extrapolation was performed in both the push and pull direction using the minimum (conservative) displacement corresponding to $0.8Q_u$ as obtained from linear, quadratic, or cubic extrapolation of the post-peak portion of the load-displacement curve. An example of this extrapolation can be seen in the push direction idealization for Wall 2 in Figure 6.3 b).

Table 6.5. Summary of Measured Load/Displacement Values

Wall	Direction	Δ_y (mm)	Δ_{Qu} (mm)	$\Delta_{0.8Qu}$ (mm)	Δ_u (mm) (Wall 2)	Q_y (kN)	Q_u (kN)	Q_y / Q_u (%)
1	+	11.5	31.7	87.6		200	276	72
	-		35.4	73.6		214	270	79
2	+	18	54.4	104.1*	89.6	308	404	76
	-		58.1	101.4*	89.8	301	434	70
Retrofit	+	18	71.8	104.6		206	453	-
	-		72.3	n/a**		195	434	-

* Extrapolated using polynomial equation as 20% degradation was never reached

** Not available as no strength degradation was recorded in the push direction

Once the elastic stiffness and displacement at the limiting ultimate condition had been established, it was possible to draw the idealized bilinear curve. To best approximate the experimental loading curve (and to follow the procedure used by Shedid et al. (2009) for most accurate comparison with the unconfined walls), an equal area method was used to determine the point of ideal yield for the ductility

calculations. By setting the area from zero displacement to the ultimate displacement defined at $0.8Q_u$ under the experimental curve equal to the area beneath the ideal curve as presented in Figure 6.3, the ideal yield displacement (Δ'_y) values used in the calculation of the idealized (elasto-plastic) displacement ductility ($\mu^{ep}_{0.8Qu}$) presented in Table 6.6 could be determined.

Again, it is noted that, because no experimental data for displacement at $0.8Q_u$ was available for Wall 2 or for the pull direction of the Retrofit Wall, idealized ductilities in these cases have been presented using the ultimate displacement achieved. Additionally, as the Retrofit Wall had a much lower initial stiffness than the original Wall 2, the idealized elastic stiffness led to a significantly higher nominal yield displacement, consequently drastically reducing the calculated displacement ductility determined from this idealized relationship. As calculating the required ductility for a retrofit wall in a true situation would otherwise require a re-analysis of the entire building to re-determine the period/stiffness (to re-estimate the dynamic response) after the event that necessitated the repair, a second idealized ductility was calculated using the initial stiffness of the original Wall 2. It is well known that the dynamic response of the building will change during and after an event due to reduction in stiffness and energy dissipation. However, this is generally accounted for in design using a factor related to ductility (ie: R_d in NBCC (NBCC 2010) as discussed below).

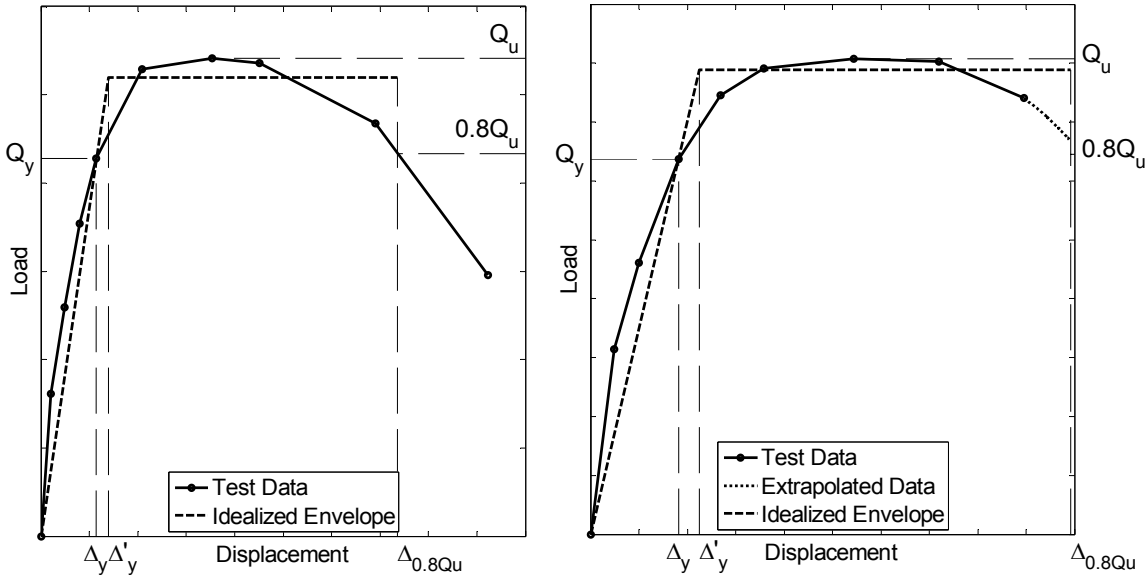

a) Wall 1 (Pull) b) Wall 2 (Push) with Extrapolation

Figure 6.3. Idealized Ductility Envelope Samples

In addition to this idealized method of calculating ductility, less conservative values for measured displacement ductility have been reported from the test data by simply taking ratios of ultimate displacement to the experimental yield displacement (Δ_y) with the ultimate displacements variously defined as that corresponding to ultimate load ($\mu_{\Delta Qu}$), 1% drift (the drift limit specified by the NBCC (2010) for post-disaster structures) ($\mu_{1\%}$), and the Paulay and Priestley ultimate criterion of $0.8Q_u$ ($\mu_{0.8Qu}$).

Table 6.6. Shear Wall Displacement Ductilities

Wall	**Direction**	*Simple Ratio*			*Idealized*		
		$\mu_{\Delta Qu}$	$\mu_{1\%}$	$\mu_{\Delta 0.8Qu}$	$\mu^{ep}_{\Delta 0.8Qu}$	$\mu^{ep}_{\Delta u}$	$\mu^{ep}_{\Delta 0.8Qu}$ **using original Wall 2 stiffness**
1	+	3.0	3.1	7.7	5.8		
	-	3.1	3.1	6.4	5.3		
2	+	3.0	1.9	5.5	4.4*	3.9	
	-	3.3	1.9	5.7	4.2*	3.6	
Retrofit	+	3.9	1.9	5.6	2.8		4.8
	-	4.0	1.9	n/a	n/a	2.4	n/a

***** Idealized ductility using the maximum achieved displacement is presented in cases where extrapolation was required to approximate the 0.8 Q_u criterion.

In the NBCC and CSA standards, a force reduction factor relating to ductility is applied in design. According to the National Building Code (NBCC 2010), this factor is calculated for these applications as $R_d = \mu_\Delta$ (Shedid et al. 2009). As such, R_d values for these walls can be taken as the $\mu^{ep}_{0.8Qu}$ values presented above. It is worth noting that current CSA S304.1 (CSA 2004a) code limits are 2.0 for moderately ductile shear walls (upper bound) and 1.5 for shear walls with limited ductility for masonry construction. The proposed seismic provisions in the draft of the 2014 edition of CSA S304 (CSA 2014) introduce a new category of ductile shear walls for masonry. Clause 16.9 of the revised draft (as accepted by the seismic committee (SCED)) will allow an $R_d = 3.0$ in cases where adequate ductility can be verified. Concrete code (CSA 2004b) limits allow up to $R_d = 3.5$ for ductile shear walls. It is clear that the ductilities of the shear walls tested in this program significantly exceed the expected values for moderately ductile shear walls and the proposed ductile shear wall category in the Canadian codes for masonry (NBCC 2010; CSA 2004a; CSA 2014).

6.5. Comparison of Behaviour of Confined Walls to Unconfined Walls

6.5.1. Presentation of Unconfined Wall Test Data

As described in the outline of the shear wall test program, no unconfined walls were tested as part of this study. However, the walls were constructed and tested to be comparable to standard concrete block walls that had been previously tested in the same test setup. Some of the results from an earlier test program by Shedid (2006)

at McMaster University have been presented here so that comparisons can be made to the results of the walls built with SR Block. All figures and values presented here have been extracted from two related papers (Shedid et al. 2008 and Shedid et al. 2009).

Results from four unconfined walls have been used for comparison and will be referred to henceforth as Walls 3-6. The details for these walls are presented in Table 6.7. Wall 3 has been included for comparison with Wall 1. Wall 1 was constructed to identical dimensions and reinforcement ratios to Wall 3 but Wall 3 was not subjected to an axial load whereas Wall 1 was subjected to 0.75 MPa total axial load. Walls 4 to 6 have been included for comparison with Wall 2 and had identical dimensions and reinforcement ratios but were subjected to different axial loads during testing. Wall 4 was not subject to any axial loading whereas Wall 5 was subject to the identical axial loading of 0.75 MPa applied on Wall 2. However, an equipment malfunction with the out-of-plane support system following the 38 mm cycle of Wall 5 was thought to have caused some premature degradation of resistance to lateral load, which makes use of this wall as the sole basis for comparison biased. Finally, Wall 6, which was subject to doubled axial loading of 1.5 MPa and was constructed with a 24% higher strength steel than the other walls provides a useful lower bound for ductility to accompany the upper bound provided by Wall 4. Although none of these walls provide an ideal comparison, observations may be made about the relative SR Block performance based on the combination of results from these walls. The hysteretic behaviour of the unconfined walls has been reproduced for reference in Figure 6.4.

Table 6.7. Unconfined Wall Details (Shedid et al. 2008)

Wall	Height (mm)	Length (mm)	Vertical Reinf. (bars)	Vertical Reinf. Ratio (%)	Horizontal Reinf. (bars)	Horizontal Reinf. Ratio (%)	Axial Load (MPa)
3	3600	1800	5 x 25M	0.73	9 x 10M	0.13	0
4	3600	1800	9 x 25M	1.32	18 x 10M	0.26	0
5	3600	1800	9 x 25M	1.32	18 x 10M	0.26	0.75
6	3600	1800	9 x 25M	1.32	18 x 10M	0.26	1.50

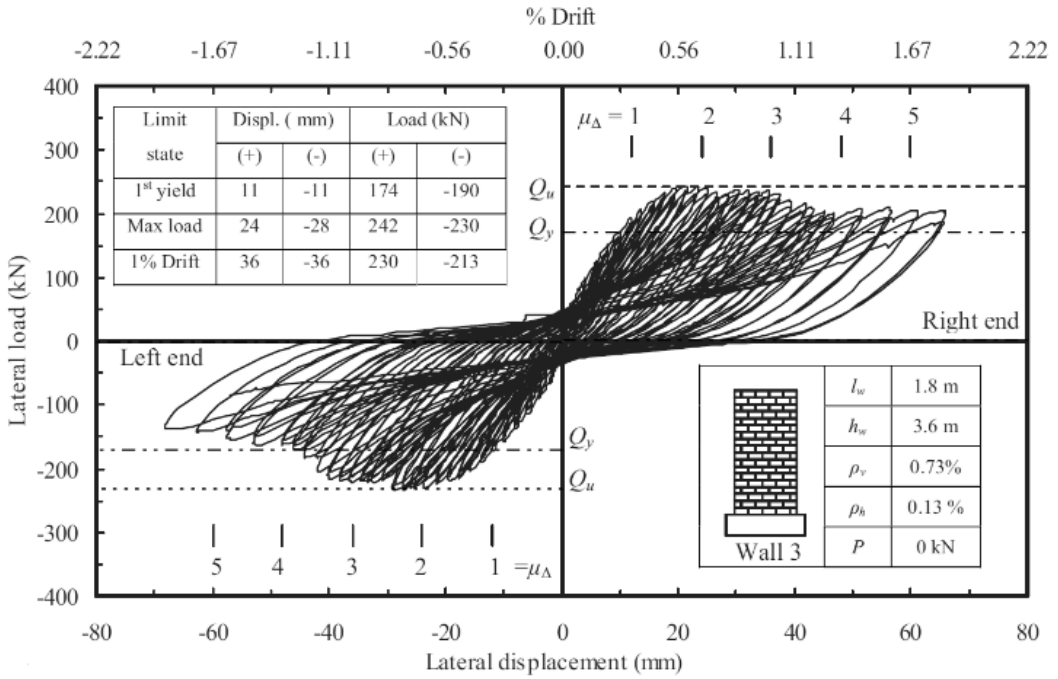

a) Wall 3

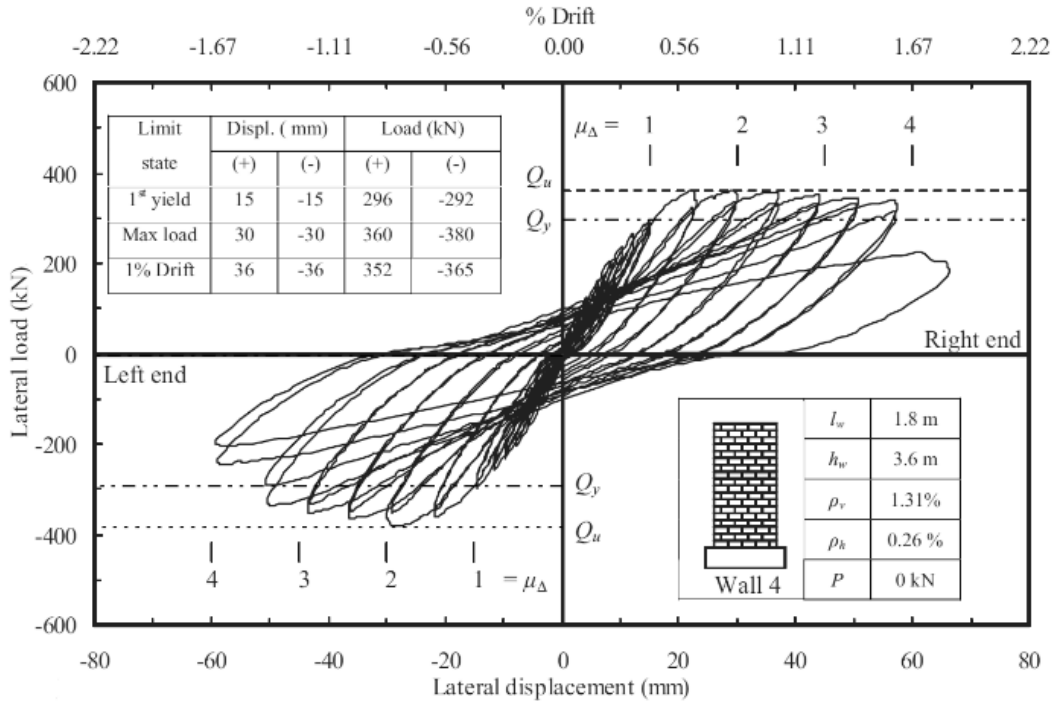

b) Wall 4

Figure 6.4. Hysteretic Load-Displacement Response of Unconfined Walls (reproduced from Shedid et al. 2008) (continued)

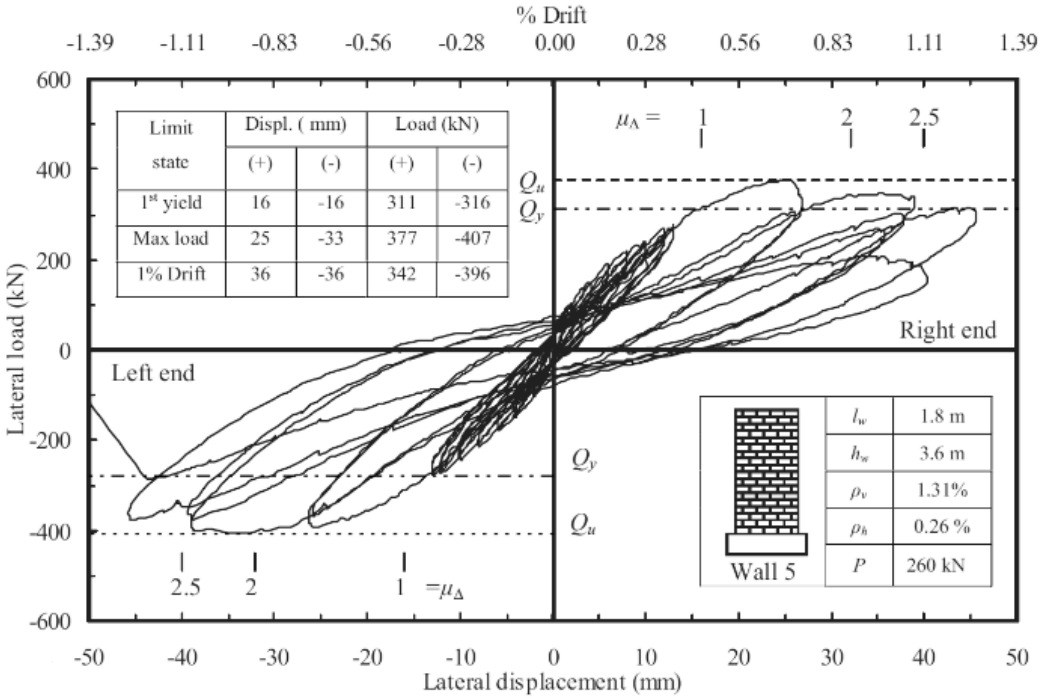

c) Wall 5

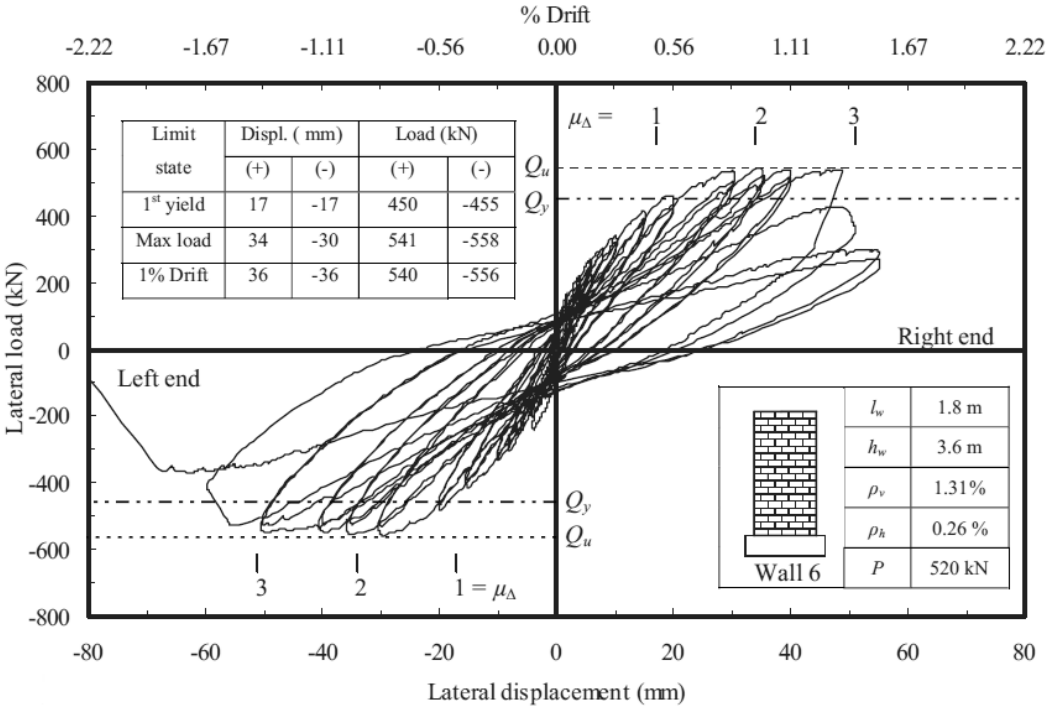

d) Wall 6

Figure 6.4. Hysteretic Load-Displacement Response of Unconfined Walls (reproduced from Shedid et al. 2008)

Behavioural observations noted with respect to these walls are related to the cracking and failure patterns. Walls 3 and 4 experienced strength degradation associated with cracking and splitting of grout columns at the toes of the walls followed by buckling of the outermost vertical bars under compression. Wall 5 displayed similar grout cracking and spalling corresponding to a moderate (10%) decrease in lateral load resistance prior to the malfunction of the out-of-plane support system. Further degradation following the malfunction was more rapid and was attributed to damage caused by the out-of-plane displacement. Finally, Wall 6 experienced horizontal cracking immediately followed by diagonal shear cracking rather than stepped cracks and experienced little strength degradation prior to the 50 mm displacement cycles. During the 50 mm cycles, spalling and bar buckling led to more rapid strength degradation, which was ultimately followed by shear compression failure at the ends of the wall in a subsequent pull cycle to 65 mm displacement.

6.5.2. Comparison of SR Block Walls to Unconfined Walls

A summary of the behaviour of each wall is presented in Table 6.8. A summary of the physical properties relevant to each comparison as discussed above has been presented for reference purposes in Table 6.9.

Table 6.8. Summary of Behaviour of All Walls

	Wall	**Direction**	**Δ_y (mm)**	**$\Delta_{@Qu}$ (mm)**	**Q_y (kN)**	**Q_u (kN)**	**$\mu_{\Delta 0.8u}$ (simple ratio)**	**$\mu^{ep}_{\Delta 0.8u}$ (idealized)**
SR Block	1	+	11.5	31.7	200	276	7.7	5.8
		-		35.4	214	270	6.4	5.3
	2	+	18.0	54.4	308	404	5.7	4.4
		-		58.1	301	434	5.7	4.2
	Retrofit	+	18.0	71.8	206*	453	5.6	4.8
		-		72.3	195*	434	5.8	-
Unconfined	3	+	11.3	24.2	174	242	4.1	3.2
		-		29.2	190	230	3.9	2.8
	4	+	14.8	29.8	296	360	4.2	3.5
		-		29.1	292	380	3.7	3.0
	5	+	16.2	25.3	311	377	2.8	2.3
		-		33.2	316	407	2.9	2.2
	6	+	16.9	29.9	450	541	3.0	2.3
		-		34.2	455	558	3.7	2.8

* It was suggested earlier that these are not truly the resistances to lateral load at initial yield and that the displacement and load recorded at the initial yield of Wall 2 is more appropriate to use in calculation of the ductility.

Table 6.9. Summary of Comparison of Wall Properties

	Compare				Compare				
Properties	**Wall 1**		**Wall 3**		**Wall 2**		**Wall 4**	**Wall 5**	**Wall 6**
SR Block Presence	Yes	to	No		Yes	to	No	No	No
Vertical Reinf. Ratio	0.73		0.73		1.32		1.32	1.32	1.32
Horizontal Reinf. Ratio	0.13		0.13		0.26		0.26	0.26	0.26
Axial Load (MPa)	0.75		0		0.75		0	0.75	1.5

In comparing the results shown in Table 6.8, the most significant difference that existed between the walls was in the level of applied axial load. In this regard, it is known (Priestley and Paulay 1992; Shedid et al. 2009) that application or increase of axial compression load affects the load-displacement behaviour of a shear wall. The initial compression state of the vertical reinforcing steel leads to an increase in the displacement required to reach the yield point (Δ_y) and, in a related manner for ductile walls, to an increase in the initial peak strength of the wall. However, as the ultimate displacement of a wall is more dependent on the properties of the concrete/masonry material than on the reinforcing steel, there is generally no increase in the ultimate displacement capacity of a wall corresponding to an increase in axial load. This, combined with the increase in yield displacement, leads to a decrease in the displacement ductility. These relationships were confirmed by Shedid et al. (2009) for shear walls similar to those tested in this program and can be clearly seen by comparing the results of Walls 4 to 6, which differed mainly in the total axial load applied. Wall strength tended to increase with axial load, as did the displacement at yielding of the extreme fibre reinforcement.

By acknowledging and accounting for the effects of applied axial load, comparisons may be drawn between Wall 3 (unconfined) and Wall 1 (confined), which had the same design as Wall 3 but was subjected to an axial load of 0.75 MPa while Wall 3 was not. The yield displacements of these two walls were comparable at 11.5 mm and 11.3 mm for Walls 1 and 3 respectively; the slightly higher value for Wall 1 can be attributed to the axial load. The peak load for Wall 1 exceeded that of Wall 3 by an average of 16%, some of which can be attributed to axial load. (For example, Wall 5 peak capacity exceeded Wall 4 peak capacity by 6% with the same change in axial load being the only difference.) It is suggested that the remainder of the difference was likely due to the presence of confinement in the compression zones. The most significant comparison that was drawn between these two walls is the difference between the ductility values. Wall 1 achieved an idealized displacement ductility that was 83% higher than for Wall 3 using the same method for idealization. This is an indication that the SR Block wall was able to maintain

load carrying capacity to much higher displacements than the unconfined wall with the only other difference between the wall tests, axial load, being one that would be expected to slightly reduce ductility of Wall 1.

The next comparison that was drawn was between the walls with the higher reinforcement ratios. The comparison of Wall 2 (confined) to Wall 4 (unconfined), is identical in nature to the previous situation in which the only difference between the wall tests other than the presence of SR Block was the axial load of 0.75 MPa applied only to the confined wall. As expected, higher yield displacement (22% increase) and higher load capacity (13% increase) were experienced by Wall 2 over that of Wall 4 and can be attributed, in part, to the application of axial load to Wall 2. However, as was the case in the comparison of the lower reinforced walls (Wall 1 and Wall 3), the confined wall in this case (Wall 2) was able to reach much higher displacements while maintaining load capacity, as can be seen by the 32% increase in idealized displacement ductility of the SR Block wall (Wall 2) over that of the unconfined wall (Wall 4). Again, this is particularly significant given that the only other difference between the test walls was axial loading which would normally cause a reduction in ductility. Considering that the yield displacement of the SR Block wall exceeded that of the unconfined wall by the significant margin of 22%, the difference in ductilities is even more impressive.

The only walls that were directly comparable between these two studies in terms of both reinforcement ratio and axial loading were Wall 2 (SR Block) and Wall 5 (unconfined). Unfortunately, due to the aforementioned out-of-plane displacement experienced by Wall 5 during testing, comparisons between these walls can only be made up to the 38 mm displacement cycle corresponding to degradation from the peak load of 10%. During further loading, the unrepresentative out-of-plane damage governed the wall behaviour. The peak load achieved by Wall 2 was 7% higher than that of Wall 5. Additionally, the displacement at yield was 11% higher for Wall 2 than Wall 5. Ductility comparisons could not be made between these walls, but it is evident that some increase in overall peak strength of the SR Block wall can be attributed to the presence of the confining devices.

The final unconfined wall presented for comparison to Wall 2 was Wall 6. Although the much higher yield strength of the reinforcement in Wall 6 and the higher axial load make numerical comparisons difficult, there is value in comparing the displacement ductilities as this wall provides a lower bound relative to Wall 2. Wall 6 and Wall 4 should demonstrate behaviours that would fall on either side of the behaviour expected for an unconfined wall like Wall 2 (and the existing Wall 5 that was not completely suitable because of the testing problem). The idealized displacement ductility of Wall 2 averaged 69% higher than that of Wall 6 indicating

that, with similar yield displacements, the SR Block wall was able to retain lateral capacity at much higher displacements than the unconfined wall.

In addition to the load-displacement characteristics of the SR Block walls and the unconfined walls, other comparisons can be made relating to wall behaviour. While the initial elastic behaviour was very comparable between the SR Block walls and the unconfined walls (as indicated by similar crack patterns and initial stiffnesses), the load degradation and failure patterns were very different. In all of the unconfined wall tests, failure was attributed to splitting of grout columns, toe crushing, and eventual buckling of the longitudinal reinforcement. As these modes of failure were protected against by the presence of the confining devices which both reduced the damage to the masonry in these regions and provided support for the reinforcement, other failure modes became more pronounced in the SR Block walls, but only at displacements much higher than those reached by the unconfined walls. The absence of the typical failure mechanism allowed the development of further damage across the faces of the walls which led to the shear weakness and eventual capacity degradation due to the previously described sliding mechanism. These limiting characteristics resulted from unforeseen effects of the splitter slot in the SR Block and the failure to design the shear reinforcement to resist most of the shear force as the block masonry became more damaged and unable to retain its original shear resisting capacity. Both of these effects can be easily avoided in future research and in application of SR Block in construction.

6.6. Closure

Results from both the prism test series and the shear wall test program have been analyzed to examine the behaviour of SR Block. The compressive loading of SR Block prisms provided a means for comparison of the different block and confining devices tested in this research program. The main differences observed between the confining devices related to the presence of significantly more vertical steel in the punched steel confining devices. This vertical steel provided some increase in the initial peak strengths of the prisms containing these devices and also seemed to provide enough stiffness to reduce the capacity decrease that followed the initial peak capacity. An additional difference between the confining devices was the higher ultimate peak capacity achieved by the prisms containing the spiralled-wire devices that was attributed to the higher strength steel used to manufacture these confining devices.

Presentation of data from a related unconfined shear wall test program from Shedid (2006) allowed direct comparison of the SR Block walls in this program with similar, unconfined walls. These comparisons indicated that the presence of SR

Block in the compression zones of shear walls had a positive effect on the achievable lateral strength and displacement ductility of each wall and also had a significant effect on the expected failure patterns of the shear walls under cyclic lateral loading. The idealized ductilities calculated for the SR Block walls exceeded those of the unconfined walls in all cases. Additionally, the displacement ductilities of the SR Block walls exceeded all code prescribed ductility factors (R_d) for masonry and concrete shear walls. The significant ductility capacities observed for the walls in this test program would lead to a significant reduction in the lateral load demand in seismic design, providing savings in the construction costs of reinforced masonry walls as a seismic force resisting system.

CHAPTER 7

CONCLUSIONS AND RECOMMENDATIONS

7.1. Summary

The focus of this research was to investigate the effectiveness and applicability of a new type of confinement in masonry construction in the form of Self-Reinforced Block (SR Block). Experimental testing for this research included an initial proof-of-concept study involving the testing of standard and SR Block prisms to quantify the behaviour of the SR Block under compressive loading. This was followed by a shear wall test program which included additional prism testing and the completion of three shear wall tests. These further prism tests provided data for the behaviour of a second confining device design to compare to that tested in the proof-of-concept program. The shear wall tests provided information on the load-displacement response of cyclically loaded masonry shear walls constructed with SR Block.

7.2. Conclusions

7.2.1. Manufacturability

An essential step in the proof-of-concept stage of testing was to ensure that SR Block could be mass-produced using existing facilities. Block plant trials demonstrated that it is possible to mold confining devices within concrete block without requiring adjustments to the mix design or the manufacturing equipment. Inspection of the blocks confirmed that full compaction of the concrete was achieved and the block strength was not impaired by the presence of the confining devices. As an improvement on the initial process of manually centering confining devices on the base plate of the block mold, during the second block manufacturing run for this program, steel clips were used to more effectively and efficiently place the confining devices within the SR Blocks on the existing manufacturing line. These multiple block plant trials confirmed the manufacturability of SR Block.

7.2.2. Block Design

Before manufacturability of SR Block was confirmed, two different prototype block molds were designed for production. Both of these block designs were tested in the proof-of-concept stage of this program. Prisms constructed with the Type I prototype blocks (with small cells) had comparable results to the Type II prototype blocks in both a grouted, unreinforced state, and in a self-reinforced state. However, when the negative effect for construction due to the increased mass of each unit was considered, it was concluded that the Type I prototype block was not ideal. It

was found that the larger body of concrete in the Type I prototype design was not necessary to achieve compaction around the confining devices during block manufacture. The Type II prototype blocks, which performed equivalently to standard blocks in a grouted, unreinforced state and comparably to the Type I prototype blocks in a self-reinforced state, were more economical and provided a higher level of constructability with more space for grout consolidation and placement of vertical reinforcement. As a result, the Type II prototype design was adopted for all subsequent manufacturing and testing.

7.2.3. Device Design

Two different confining device designs were tested in this study. Prisms in the proof-of-concept program contained confining devices manufactured from punched steel wrapped into a tubular shape. The shear walls and corresponding prisms contained spiralled wire confining devices manufactured from three different types of steel wire. In comparing the prisms reinforced with spiralled wire confining devices produced from different types of steel, those made from a lower strength, more ductile steel produced more desirable prism performance. Due to the overall high-strength, low-ductility steel used in the manufacture of the spiralled wire confining devices, all prisms containing these devices were able to achieve higher ultimate peak strengths than the punched steel counterparts. However, the prisms containing spiralled wire confining devices required the development of much higher strains to reach ultimate peak strengths and, while they effectively supported high loads to very high strains, did not maintain these ultimate peaks to the same extent as the prisms containing the punched steel confining devices.

The presence of substantial vertical steel in the punched steel confining devices provided benefit in the overall compressive performance, causing an increase in the initial peak load capacity and a reduction of the capacity decrease that occurred as the outer block concrete spalled. In comparing the results of SR Block prisms from both programs, it is clear that the combination of steel properties and geometric design of the devices leads to more desirable, ductile behaviour for prisms containing the original, punched steel confining devices than those containing the spiralled wire confining devices.

7.2.4. Enhanced Compressive Behaviour

All SR Block prisms initially reached load carrying capacity equal to or in excess of the peak capacity of their unreinforced counterparts. After undergoing spalling of the block and mortar material outside of the confining devices and a small decrease in load resistance, all SR Block prisms reached second peak capacities considerably in excess of the initial peak capacities. Additionally, all SR Block

prisms retained at least the capacity of their unreinforced counterparts up to strains of at least 2%, an increase of over sixfold (compared to the failure strain of 0.3% observed for equivalent unconfined prisms) and a tenfold increase compared to the 0.2% strain at peak stress in the unconfined prisms.

7.2.5. Application in Shear Walls

Application of the reported confining method of developing high ductility and energy dissipation in reinforced concrete block construction leads to potential savings and benefits in the design of reinforced masonry shear walls based on the observed behaviour. The confined material was observed to remain able to resist high stresses at repeated cycles of very high strain. The apparent soundness of this confined material indicated that it should be able to support and prevent buckling of compression reinforcement. The shear wall tests confirmed this characteristic which adds significantly to the calculated capacity of reinforced masonry where, currently, reinforced bars in compression are not allowed to be included in strength calculations because of the concern that buckling could occur. This change would improve efficiency of masonry design, consequently reducing the construction costs associated with reinforced masonry walls as a seismic force resisting system.

7.2.6. Enhanced Shear Wall Behaviour

The hysteretic load-displacement behaviour from the three SR Block shear wall tests demonstrated that the walls were able to sustain large amounts of damage while retaining the high initial peak load capacities achieved. The ability of the confined areas within the plastic hinging zone of each wall to develop very high strains was consistent with the observed prism performance and led to the development of highly ductile shear wall behaviour.

Unfortunately, the presence of the splitter slot in the SR Block led to an observed tendency for sliding shear to develop as the masonry reached high levels of damage at very high strains. This unanticipated weakness may have prevented the achievable ductility of the SR Block walls from being documented. As discussed in Chapter 5, the unforeseen consequence of leaving the splitter slot in the prototype SR Block is easily avoided by simply removing this part of the mold. The observation of the sliding mechanism served as a reminder that at high ductility levels, especially those that can be expected from SR Block walls, the shear reinforcement in reinforced masonry should be designed to resist most if not all of the shear force rather than relying on the damaged masonry.

Calculated displacement ductilities for all SR Block walls were very high, exceeding all ductility factors (R_d) present in current and proposed editions of CSA S304 (CSA 2004a; CSA 2014). Comparison of these ductilities and other overall

behaviours with results for similar, unconfined walls highlighted the benefits of including SR Block in the compression zones of shear walls. The ability to isolate the effect of SR Block through this comparison led to the conclusion that its presence in the shear walls led to an increase in the lateral capacity and a significant increase in the ductility capacity in all cases.

7.2.7. Strength Predictions

Two established methods for predicting the strength of confined concrete were applied to concrete masonry in the context of the SR Block and compared to prism results from three test series. The results of these calculations and comparisons ascertained that the equations originating from confined concrete literature led to a reasonable estimate of the peak strength of the remaining confined area of the SR Block assemblage following the spalling of outer block concrete. However, these methods of estimation do not provide any level of conservatism and involve a series of assumptions. As such, as more experimental data becomes available with further testing of SR Block, it is suggested that these methods provide a basis for further analysis and perhaps be modified to more accurately and/or conservatively represent the strength of the confined masonry that results from the use of SR Block.

Pushover analyses were performed to estimate the expected lateral load capacity of the shear walls in this research program. The calculations were made using a series of criteria for ultimate masonry compressive strain according to different code definitions. These analyses, using known material properties, provided reasonable strength estimates. A limiting masonry compressive strain of 0.8% from the proposed CSA S304 (CSA 2014) seismic provisions for adequately confined masonry provided the best estimate of expected lateral load capacity on average for the two walls.

7.2.8. Repair/Retrofit

Retrofits of three SR Block prisms and one SR Block shear wall were performed in this study to investigate the ease of repair and the effectiveness of retrofitting to regain strength and utilize remaining strain capacity of specimens. Retrofit tests of SR Block prisms demonstrated that initial stiffness and strength of the concrete block masonry can be fully restored with a simple and economical repair technique. Easily repaired prisms remained stable following application of new high compression strains due to the lateral confining devices within the blocks continuing to effectively confine the enclosed parts of the cross-section.

The shear wall retrofit was easily and quickly achieved and the retest results show that full capacity and displacement capability were restored. These results indicate

that the use of SR Block has the added benefit that buildings damaged in the process of resisting earthquakes can be quickly and economically repaired to restore the originally designed ability to resist the effects of large earthquakes.

7.3. Recommendations

Although two prototype block designs and two confining device designs were tested for this study, several more options with respect to SR Block are left to be investigated.

First, it was noted that ductile wire with a reasonable and defined yield strength was difficult to obtain and, as a result, several of the spiralled-wire confining devices for the described program were manufactured with relatively brittle steel. In the future, if more suitable steels cannot be located, heat-treating may be an option to improve desired properties in the steel used to manufacture these devices. An additional improvement to the steel that would be beneficial in both the punched-steel and the spiralled-wire device designs is the use of a coating (galvanization or other) to protect against corrosion. This may be especially important given that the concrete cover over the devices in the current block design was kept to a minimum in order to confine the largest possible volume of material.

Comparison of test results of the SR Block to similar unreinforced prisms show that despite spalling of the face shell concrete outside of the confining device, all SR Block prism specimens retained load carrying capacity in excess of the peak capacity of their unreinforced counterparts and were able to retain at least the capacity of the unreinforced counterparts up to strains well beyond 2%. In this regard, there are possible cost-saving refinements. If design codes only permit reliance on comparatively low increased compression strains such as the 0.8% proposed for masonry in the next edition of CSA S304 (CSA 2014) or the 1.4% currently allowed in CSA A23.3 (CSA 2004b) for concrete, a reduction in the amount of confinement required would be justified. Similarly, if retention of 80% of peak compressive capacity at high strains is deemed to be satisfactory, there will be less need for high confining pressures. For either or both of these reasons, the reduced amount of required confinement would result in reducing the cost of confining devices.

It was well established during testing of the shear walls that shear sliding between the confined columns led to high levels of damage and capacity degradation. It has already been suggested that in future manufacturing of SR Block, the splitter slot in the mold be omitted to help avoid this weakness. A possible additional improvement in this respect may be to provide ties between the cages, embedded within the concrete block during block making. This may provide additional

clamping force between the confined columns to reduce material loss and increase the resistance to shear sliding to prevent the columns from acting independently. Also, it is noted that reliance on the masonry component of shear resistance should be reduced where high levels of damage to the masonry are expected to occur. Such provisions have already been introduced to the proposed CSA S304 (CSA 2014) requirement for shear strength in ductile masonry walls

As the most standard block size for concrete masonry construction in Canada, only the 20 cm block size was tested in this program. While larger sizes are less common, sizes up to 25 cm and 30 cm are used in some construction practices and it would be beneficial to test larger SR Block for these purposes. The length-to-width ratio of the 20 cm block allowed two circular confining devices to be placed side by side in the block. In future manufacturing, larger block sizes may accommodate an overlapping of circular confining devices within the cover requirements (see Figure 7.1). This would have the benefit of further reinforcing the connection between the continuous confined columns and help to eliminate the potential for development of a vertical shear sliding mechanism.

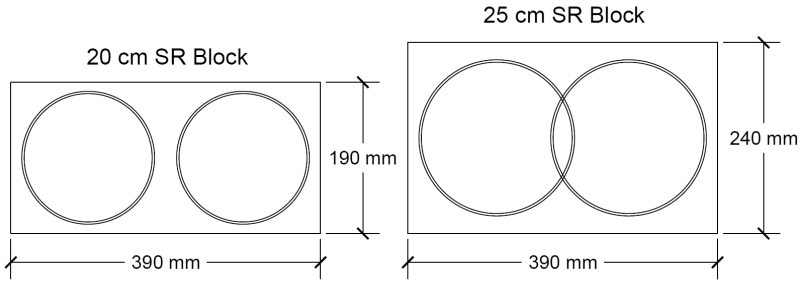

Figure 7.1. Possible Layout for Larger SR Block Sizes

7.4. Closure

It is evident from the results of this test program that use of Self-Reinforced Block (SR Block) is an effective method of producing the high compressive strains needed to create high ductility and of increasing the retained compressive capacity of concrete masonry. Although further testing is required to fully optimize the design for use of SR Block, the feasibility of mass-production of SR Block has been confirmed in this study. This new block type provides an easily constructible method for increasing the ductility capacity of shear walls.

REFERENCES

Ahmadi Koutalan, F. (2012). "Displacement-based Seismic Design and Tools for Reinforced Masonry Shear-Wall Structures." Ph. D. Thesis, The University of Texas at Austin, U.S.A.

American Society for Testing and Materials (ASTM). (2013a). "Standard Test Methods for Sampling and Testing Concrete Masonry Units and Related Units." *C140-13a*, ASTM International, West Conshohocken, PA.

American Society for Testing and Materials (ASTM). (2013b). "Standard Specification for Carbon-Steel Wire and Welded Wire Reinforcement, Plain and Deformed, for Concrete." *A1064M-13*, ASTM International, West Conshohocken, PA.

American Society for Testing and Materials (ASTM). (2012a). "Standard Test Methods and Definitions for Mechanical Testing of Steel Products." *A370-12a*, ASTM International, West Conshohocken, PA.

American Society for Testing and Materials (ASTM). (2012b). "Standard Practice for Capping Concrete Masonry Units, Related Units and Masonry Prisms for Compression Testing." *C1552-12*, ASTM International, West Conshohocken, Pa.

American Society for Testing and Materials (ASTM). (2010). "Standard Test Method for Compressive Strength of Masonry Prisms." *C1314-10*, ASTM International, West Conshohocken, Pa.

American Society for Testing and Materials (ASTM). (2004). "Standard Test Method for Young's Modulus, Tangent Modulus, and Chord Modulus." *E111-04*, ASTM International, West Conshohocken, Pa.

American Society for Testing and Materials (ASTM). (2011a). "Standard Test Methods for Cyclic (Reversed) Load Test for Shear Resistance of Vertical Elements of the Lateral Force Resisting Systems for Buildings." *E2126-11*, ASTM International, West Conshohocken, Pa.

American Society for Testing and Materials (ASTM). (2011b). "Standard Test Method for Splitting Tensile Strength of Cylindrical Concrete Specimens." *C496M-11*, ASTM International, West Conshohocken, Pa.

Applied Technology Council. (ATC). (1999). "Repair of Earthquake Damaged Concrete and Masonry Wall Buildings." *Federal Emergency Management Agency, FEMA-308*, Washington D.C., U.S.A.

Atkinson, R.H. and Schuller, M.P. (1993) "Evaluation of Injectable Cementitious Grouts for Repair and Retrofit of Masonry." *Masonry: Design and Construction, Problems and Repair, ASTM STP 1180*, 355-368.

Banting, B. R. (2013). "Seismic Performance Quantification of Concrete Block Masonry Structural Walls with Confined Boundary Elements and Development of the Normal Strain-Adjusted Shear Strength Expression (NSSSE)." Ph.D. Thesis, McMaster University, Hamilton, Canada.

Canadian Standards Association (CSA). (2004a). "Design of Masonry Structures." *CSA S304.1-04 (R2010),* CSA, Mississauga, Canada.

Canadian Standards Association (CSA). (2004b). "Design of Concrete Structures." *CSA A23.3-04 (R2010),* CSA, Mississauga, Canada.

Canadian Standards Association (CSA). (2004c). "Mortar and Grout for Unit Masonry." *CSA A179-04,* CSA, Mississauga, Canada.

Canadian Standards Association (CSA). (2004d). "Concrete Block Masonry Units." *CSA A165.1-04 (R2009),* CSA, Mississauga, Canada.

Canadian Standards Association (CSA). (2014). "Design of Masonry Structures (DRAFT)." *CSA S304-14*, CSA, Mississauga, Canada.

Department of the Army. (1992). "Military Soils Engineering." *Field Manual FM 5-410*, Field Manual Headquarters, Washington D.C., U.S.A.

Chahine, G.N. (1989). "Behaviour Characteristics of Face Shell Mortared Block Masonry under Axial Compression." M.Eng. Thesis, McMaster University, Hamilton, Canada.

Craig, R.F. (2004). *Craig's Soil Mechanics*. 7 ed. Taylor & Francis Group, London.

Drysdale, R.G. and Hamid, A. (2005). *Masonry Structures - Behaviour and Design*. 3 ed., Canada Masonry Design Centre, Mississauga, Canada.

Guo, Ping. (1991). "Investigation and Modeling of the Mechanical Properties of Masonry." Ph.D. Thesis, McMaster University, Hamilton, Canada.

Hart, G.C., Noland, J.L., Kingsley, G.R., Englekirk, R.E. and Sajjad, N.A. (1988). "The Use of Confinement Steel to Increase the Ductility in Reinforced Concrete Masonry Shear Walls." *The Masonry Society Journal*, 7(2), T19-T42.

Hervillard, T. P. C. (2005). "Effectiveness of Polymer Fibers for Improving the Ductility of Masonry Structures." M.S. Thesis, Washington State University, Washington, U.S.A.

International Code Consortium (ICC). (2000). International Building Code (IBC). International Code Council Inc., Falls Church, Virginia, USA.

International Council of Building Officials (ICBO). (1997). *Uniform Building Code (UBC)*. International Council of Building Officials, Whittier, California, U.S.A.

Joyal, M.P., Tait, M.J. and Drysdale R.G. (2013). "Feasibility of Self-Reinforced Concrete Block for Improved Ductility." 12th Canadian Masonry Symposium, Vancouver, Canada.

Kent, D.C. and Park, R. (1971). "Flexural Members with Confined Concrete." *Journal of the Structural Division*, 97(7), 1969-1990.

Liu, Jiaji. (2012). "The effect of Height-to-Thickness Ratio on the Compressive Strength of Concrete Masonry." M.A.Sc. Thesis, University of Windsor, Windsor, Canada.

MacGregor, J.G. and Wight, J.K. (2004). *Reinforced Concrete: Mechanics and Design*, 4 ed. Prentice Hall.

Malmquist, K.J. (2004). "Influence of Confinement Reinforcement on the Compressive Behavior of Concrete Block Masonry and Clay Brick Masonry Prisms." M.S. Thesis, Washington State University, Washington, U.S.A.

Mander, J.B., Priestley, M.J.N. and Park, R. (1988a). "Observed Stress-Strain Behaviour of Confined Concrete", *Journal of Structural Engineering*, 114(8), 1827-1849.

Mander, J.B., Priestley, M.J.N. and Park, R. (1988b). "Theoretical Stress-Strain Model for Confined Concrete", *Journal of Structural Engineering*, 114(8), 1804-1826.

Masonry Standards Joint Committee. (MSJC). (2011). "Building Code Requirements for Masonry Structures." *TMS 402/ASCE 5/ACI 530*, The Masonry Society, American Society of Civil Engineers, Boulder, New York/American Concrete Institute, and Detroit, USA.

Morice, P.B. and Base G.D. (1953). "The Design and Use of a Demountable Mechanical Strain Gauge for Concrete Structures." *Magazine of Concrete Research*, 13, 37-42.

National Building Code of Canada: Institute for Research in Construction (NBCC). (2010). *National Building Code of Canada 2010*. National Research Council of Canada, Ottawa, Canada.

Paturova, A. (2006). "The Influence of Vertical Reinforcement and Lateral Confinement on the Axial Capacity of Masonry Block Walls." M.S. Thesis, University of Saskatchewan, Saskatoon, Canada.

Paulay, T., and Priestley, M., J., N. (1992). *Seismic Design of Reinforced Concrete and Masonry Buildings*, John Wiley & Sons, Inc., New York and Toronto.

Priestley M.J.N. and Bridgeman, D.O. (1974). "Seismic Resistance of Brick Masonry Walls." *Bulletin of the New Zealand National Society for Earthquake Engineering*, 7(4), 167-187.

Priestley, M.J.N. (1981). "Ductility of Unconfined and Confined Concrete Masonry Shear Walls." *The Masonry Society Journal*, July-December, T28-T39.

Priestley, M. J. N. and Elder, D. M. (1983). "Stress-Strain Curves for Unconfined and Confined Concrete Masonry." *ACI Journal*, 80(3), 192-201.

Richart, F.E., Brandtzaeg, A. and Brown, R.L. (1929). "The Failure of Plain and Spirally Reinforced Concrete in Compression." *University of Illinois: Engineering Experiment Station*, Bulletin No. 190, Urbana, U.S.A.

Sajjad, N.A. (1990). "Confinement of Concrete Masonry." Ph.D. Thesis, University of California, Los Angeles, USA.

Sciascetti, A.N., Joyal, M.P., Tait, M.J. and Drysdale R.G. (2013). "Post Failure Repair of Self-Reinforced Concrete Block Prisms." 12th Canadian Masonry Symposium, Vancouver, Canada.

Scrivener, J.C. (1972). "Reinforced Masonry - Seismic Behaviour and Design." *Bulletin of the New Zealand National Society for Earthquake Engineering*, 5(4), 143-155.

Shedid, M.T. (2006). "Ductility of Reinforced Concrete Masonry Shear Walls." M.A.Sc. Thesis, McMaster University, Hamilton, Canada.

Shedid, M.T., Drysdale, R.G. and El-Dakhakhni, W.W. (2008). "Behavior of Fully Grouted Reinforced Concrete Masonry Shear Walls Failing in Flexure: Experimental Results." *Journal of Structural Engineering*, 134(11), 1754-1767.

Shedid, M.T. (2009). "Strategies to Enhance Seismic Performance of Reinforced Masonry Shear Walls." Ph.D. Thesis, McMaster University, Hamilton, Canada.

Shedid, M.T., Drysdale, R.G. and El-Dakhakhni, W.W. (2009). "Behavior of Fully Grouted Reinforced Concrete Masonry Shear Walls Failing in Flexure: Analysis." *Engineering Structures*, 31, 2032-2044.

Shedid, M. T., El-Dakhakhni, W. W. and Drysdale, R. G. (2010). "Alternative Strategies to Enhance the Seismic Performance of Reinforced Concrete-Block Shear Wall Systems." *J. Struct. Eng.*, 136(6), 676-689.

Sheikh, S.A. and Toklucu, M.T. (1993). "Reinforced Concrete Columns Confined by Circular Spirals and Hoops." *ACI Structural Journal*, 90(5), 542-553.

Standards Association of New Zealand (SANZ). (2004). "Design of reinforced concrete masonry structures." *New Zealand Standards Association* (*NZS) 4230:2004*, CEN, Wellington, New Zealand.

Steadman, M., Drysdale, R.G. and Khattab, M.M. (1995). "Influence of Block Geometry and Grout Type on Compressive Strength of Block Masonry." *Seventh Canadian Masonry Symposium*, Hamilton, Canada, 1116-1127.

Toopchi-Nezhad, H., Drysdale, R.G. and Tait, M.J. (2011a). "Compression Behavior of Grouted Concrete Block Prisms Using Laterally Confined (Self-Reinforced) Concrete Block." Research Report, Department of Civil Engineering, McMaster University, Hamilton, Canada.

Toopchi-Nezhad, H., Drysdale, R.G. and Tait, M.J.; McMaster University. (2011b). Self-Reinforced Masonry Blocks, Walls Made from Self-Reinforced Masonry Blocks, and Method for Making Self-Reinforced Masonry Blocks. *United States Patent Application PCT/CA2011/001043*.

Wong, H.E. and Drysdale R.G. (1985). "Compression Characteristics of Concrete Block Masonry Prisms." *Masonry: Research, Application, and Problems, ASTM STP 871*, 167-177.

APPENDIX A
MATERIAL TEST DATA

A.1. Mortar

Table A.1. Mortar Test Details for Proof-of-Concept Prism Program

Batch	Cube Strength (MPa)				Flow
	Testing Period			Average	
	Start	Mid	End		
1	10.9	11.1	10.7	10.9	84
2	12.9	14.1	14.2	13.7	93
3	14.8	14.8	15.4	15.0	87
4	13.8	13.8	13.5	13.7	111
5	13.2	15.7	14.8	14.6	119
6	13.5	14.9	12.5	13.6	113
7	15.1	16.3	14.5	15.3	114
8	13.0	15.2	14.4	14.2	112
9	16.2	16.2	13.6	15.3	104
10	16.1	16.8	14.8	15.9	99
11	15.6	13.2	12.5	13.8	104
Average	14.1	14.7	13.7	**14.2**	**103**
C.O.V.(%)	11.5	11.1	9.9	**11.0**	**11.2**

Table A.2. Mortar Test Details for Shear Walls and Corresponding Prism Program

Batch	Cube Strength (MPa)				Flow
	Specimen No.			Average	
	1	2	3		
1	13.8	14.0	12.96	13.6	110
2	13.7	15.2	13.9	14.3	134
3	15.8	17.8	16.8	16.8	126
4	16.2	18.1	14.7	16.3	124
5	15.8	17.2	14.5	15.8	114
6	16.7	17.9	15.7	16.8	125
7	14.6	16.1	14.5	15.1	124
8	16.5	16.8	15.5	16.3	134
9	17.1	17.2	14.7	16.6	132
10	16.0	17.4	15.8	16.4	119
11	16.4	16.8	16.7	16.7	120
12	14.1	13.0	12.8	13.3	109
13	17.7	17.6	17.4	17.6	110
14	18.3	16.3	17.8	17.5	108
15	18.4	19.1	18.8	18.8	98
16	16.8	18.4	17.8	17.7	114
17	16.9	16.8	16.9	16.9	135
18	17.3	17.1	17.9	17.4	126
19	14.3	17.3	16.9	16.2	131
20	21.1	19.5	21.4	20.7	130
Average	**16.5**				**121**
C.O.V.(%)	**11.1**				**4.8**

A.2. Grout

Table A.3. Grout Test Details for Proof-of-Concept Prism Program (Standard Grout)

Batch	Cylinder Strength (MPa)				Cell-Molded Prism Strength (MPa)			
	Testing Period			Average	Testing Period			Average
	Start	Mid	End		Start	Mid	End	
1	27.5	25.9	27.4	26.9	-	-	-	-
2	22.1	22.1	22.1	22.1	31.4	28.3	30.5	30.1
3	24.1	24.1	24	24.1	-	-	-	-
4	25.6	26.5	27.4	26.5	34.7	35.13	33.2	34.3
5	22.6	22.3	23.6	22.8	31.4	31	29.5	30.6
Average	24.4	24.2	24.9	24.5	32.5	31.5	31.1	31.7
C.O.V.(%)	9.1	8.3	9.6	8.5	5.9	10.9	6.2	7.2

Table A.4. Grout Test Details for Proof-of-Concept Prism Program (Anti-Shrink Grouts)

Batch	Cylinder Strength (MPa)				C.O.V. (%)
	Specimen No.			Mean	
	1	2	3		
A1	22.2	22.2	22.1	22.2	0.3
A2 – Batch 1	13.9	13.9	13.7	13.8	0.5
A2 – Batch 2	13.7	14.7	13.7	14.0	3.9
A2 - Average				13.9	2.7

Table A.5. Grout Test Details for Shear Walls and Corresponding Prism Program

Batch	Cylinder Strength (MPa)				Cell-Molded Prism Strength (MPa)				Elastic Modulus (GPa)
	Specimen No.			Average	Specimen No.			Average	
	1	2	3		1	2	3		
1	24.3	22.5	23.1	23.3	-	-	-	-	20.9
2	25.3	25.1	22.9	24.4	29.2	28.3	31.1	29.5	
3	22.0	23.6	19.3	21.6	-	-	-	-	15.7
4	23.3	22.7	20.0	22.0	22.3	30.3	32.4	28.3	
5	22.9	23.4	24.3	23.5	-	-	-	-	15.0
6	23.6	24.5	26.0	24.7	26.1	34.0	31.9	30.7	
7	21.4	21.1	22.6	21.7	-	-	-	-	24.0
8	21.7	22.6	21.5	21.9	30.4	26.7	29.4	28.9	
Average	22.9				29.3				18.9
C.O.V. (%)	7.1				10.8				22.8

A.3. Concrete Block

Table A.6. Block Test Details for Proof-of-Concept Prism Program

Block Type	Specimen No.	*Measured*				*Calculated*		
		Applied Force (kN)	M_d (kg)	M_i (kg)	M_s (kg)	ρ (kg/m^3)	A_n (mm^2)	Strength (MPa)
Standard Stretcher	1	1290	17.0	9.9	17.7	2150	41,500	31.1
	2	1160	17.2	10.0	17.9	2160	41,800	27.7
	3	1320	17.1	9.9	17.9	2130	42,100	31.3
	Average	1260	17.1	9.9	17.9	2150	41,800	30.0
	C.O.V. (%)	6.8	0.6	0.6	0.7	0.6	0.7	6.7
Standard Splitter	1	1280	18.3	10.7	19.4	2120	45,500	28.1
	2	1340	18.3	10.7	19.3	2100	45,700	29.3
	3	1280	18.3	10.7	19.4	2110	45,800	28.0
	Average	1300	18.3	10.7	19.4	2110	45,700	28.5
	C.O.V. (%)	2.7	0.2	0.4	0.2	0.4	0.29	2.6
Prototype I	1	1570	23.2	13.3	24.5	2080	58,900	26.7
	2	1500	-	-	-	-	-	25.5
	Average	1540	23.2	13.3	24.5	2080	58,900	26.1
Prototype II	1	1210	17.5	9.9	18.3	2080	44,400	27.3
	2	1170	17.8	10.1	18.4	2150	43,600	26.9
	3	1090	17.7	10.1	18.4	2140	43,500	25.0
	Average	1160	17.7	10.0	18.4	2120	43,800	26.4
	C.O.V. (%)	5.3	0.2	1.2	0.3	1.8	1.1	4.5

Table A.7. Block Test Details for Shear Walls and Corresponding Prism Program

Block Type	Specimen No.	*Measured*				*Calculated*			
		Applied Force (kN)	M_d (kg)	M_i (kg)	M_s (kg)	E (GPa)	ρ (kg/m^3)	A_n (mm^2)	Strength (MPa)
Standard Stretcher	1	1240	16.9	10.0	17.8	10,340	2160	41,300	30.0
	2	1230	17.2	10.2	18.1	8,640	2180	41,500	29.6
	3	1220	17.0	10.1	18.0	8,860	2160	41,300	29.5
	Average	1230	17.0	10.1	18.0	9,280	2170	41,400	29.7
	C.O.V. (%)	0.7	0.8	1.0	0.9	10.0	0.5	0.3	0.8
Standard Splitter	1	1250	18.5	10.9	19.6	8,080	2110	46,300	27.0
	2	1190	19.1	11.3	20.2	8,820	2140	47,500	25.3
	3	1190	19.1	11.4	20.2	8,300	2160	46,600	25.4
	Average	1210	18.9	11.2	20.0	8,400	2140	46,600	25.9
	C.O.V. (%)	3.0	1.8	2.4	1.7	4.6	1.2	0.7	3.7
Prototype	1	1270	17.9	10.6	18.9	10,580	2160	43,700	29.1
	2	1240	17.9	10.6	18.9	9,310	2150	43,800	28.2
	3	1200	17.9	10.7	19.0	9,650	2160	43,600	27.7
	Average	1240	17.9	10.6	18.9	9,850	2160	43,700	28.3
	C.O.V. (%)	2.6	0.1	0.6	0.2	6.7	0.2	0.3	2.5

A.4. Reinforcing/Confining Steels

Table A.8. Test Details for Steel Wire Used in the Manufacture of Spiralled Wire Confining Devices for Shear Walls and Corresponding Prism Program

Steel Wire Type	Specimen No.	Strength (MPa)	
		Yield	Ultimate
WA	1	627	732
	2	613	734
	3	609	725
	Average	620	730
	C.O.V. (%)	1.9	0.7
WB	1	573	707
	2	573	707
	3	588	683
	4	558	681
	5	568	682
	Average	573	692
	C.O.V. (%)	1.9	2.0
WC	1	595	672
	2	595	659
	3	634	685
	Average	608	673
	C.O.V. (%)	3.7	2.0

Table A.9. Test Details for Vertical Wall Reinforcement (25M)

Specimen No.	Strength (MPa)		Elongation Strain at Fracture
	Yield	Peak	
1	428	627	0.239
2	421	627	0.218
3	422	627	0.216
4	421	629	0.233
Average	423	628	0.227
C.O.V. (%)	0.8	0.2	5.0

Table A.10. Test Details for Horizontal Wall Reinforcement (10M)

Specimen No.	Strength (MPa)		Elongation Strain at Fracture
	Yield	Peak	
1	477	663	0.159
2	497	704	0.159
3	498	696	0.171
Average	491	688	0.163
C.O.V. (%)	2.4	3.2	4.3

APPENDIX B
DETAILED PRISM TEST DATA

B.1. Test Data: Proof-of-Concept Prism Program

Table B.1. Summary of Results for Ungrouted Prism Series (Proof-of-Concept Program)

Prism	Specimen No.		Peak Stress (MPa)	Strain at Peak Stress	Age of Specimen (Days)
UST (stretcher block)	1*		20.5	0.0025	54
	2		18.1	0.0024	62
	3		18.1	0.0025	64
	4		18.4	0.0022	70
	5		19.0	0.0018	83
	All Prisms	Average	18.8	0.0023	67
		C.O.V. (%)	5.4	13.5	
	Prisms Tested After Recalibration	Average	18.4	-	-
		C.O.V. (%)	2.4		
USP (splitter block)	1*		22.1	0.0021	43
	2		15.2	0.0019	70
	3		17.8	0.0020	77
	4		20.7	0.0022	83
	All Prisms	Average	19.0	0.0020	68
		C.O.V. (%)	16.2	7.1	
	Prisms Tested After Recalibration	Average	17.9	-	-
		C.O.V. (%)	15.4		
UPI (type I prototype block)	1*		15.8	0.0018	42
	2		16.0	0.0021	69
	3		14.9	0.0024	91
	All Prisms	Average	15.6	0.0021	67
		C.O.V. (%)	3.9	14.4	
	Prisms Tested After Recalibration	Average	15.4	-	-
UPII (type II prototype block)	1*		21.5	0.0024	47
	2		21.4	0.0025	61
	3		19.6	0.0025	65
	4		20.1	0.0026	76
	5		22.3	0.0026	91
	All Prisms	Average	21.0	0.0025	68
		C.O.V. (%)	5.2	3.1	
	Prisms Tested After Recalibration	Average	20.5	-	-
		C.O.V. (%)	5.8		

* indicates test before recalibration of test machine (affected stress only)

Table B.2. Summary of Results for Grouted Prism Series (Proof-of-Concept Program)

Prism	Specimen No.		Peak Stress (MPa)	Strain at Peak Stress	Age of Specimen (Days)
GST (stretcher block)	1*		11.4	0.0013	54
	2		12.7	0.0013	75
	3		13.1	0.0014	76
	4		12.3	0.0016	78
	All Prisms	Average	12.4	0.0014	71
		C.O.V. (%)	5.9	8.2	-
	Prisms Tested After Recalibration	Average	12.7	-	
		C.O.V. (%)	3.2		
GSP (splitter block)	1*		14.8	0.0019	42
	2*		14.6	0.0016	55
	3		13.9	0.0017	78
	4		13.3	0.0016	91
	All Prisms	Average	14.1	0.0017	67
		C.O.V. (%)	4.7	7.9	-
	Prisms Tested	Average	13.6	-	
GPI (type I prototype block)	1*		17.8	0.0019	47
	2		15.5	0.0018	65
	3		16.3	0.0017	91
	All Prisms	Average	16.6	0.0018	68
		C.O.V. (%)	7.0	5.9	-
	Prisms Tested	Average	15.9	-	
GPII (type II prototype block)	1*		14.2	0.0021	48
	2*		13.5	0.0021	50
	3		12.8	0.0018	70
	4		13.6	0.0015	79
	5		13.1	0.0016	79
	All Prisms	Average	13.4	0.0017	65
		C.O.V. (%)	4.0	15.1	-
	Prisms Tested After Recalibration	Average	13.2	-	
		C.O.V. (%)	3.4		

* indicates test before recalibration of test machine (affected stress only)

Table B.3. Summary of Peak Stress Results for Self-Reinforced Prism Series (Proof-of-Concept Program)

Prism	Specimen No.		Peak Stress (MPa)	Strain at Peak Stress	Second Peak Stress (MPa)	Strain at Second Peak Stress	Age of Specimen (Days)
GPIR (type I prototype SR block)	1*		20.5	0.0023	20.4	0.0106	48
	2		n/a	n/a	18.4	0.0084	71
	3		18.0	0.0020	18.6	0.0123	79
	All Prisms	Average	19.2	0.022	19.1	0.0104	66
		C.O.V. (%)	-	-	5.8	18.6	-
	Prisms Tested After Recalibration	Average	18.0	-	18.5	-	
GPIIR (type II prototype SR block)	1*		15.8	0.0018	19.5	0.0124	50
	2		13.2	0.0015	17.9	0.0134	61
	3		15.0	0.0020	16.9	0.0185	62
	4		16.5	0.0018	18.2	0.0128	77
	5		15.7	0.0014	17.5	0.0122	82
	All Prisms	Average	15.2	0.0017	18.0	0.0139	66
		C.O.V. (%)	8.2	13.0	5.3	19.0	-
	Prisms Tested After Recalibration	Average	15.1	-	17.6	-	
		C.O.V. (%)	9.2		3.3		
GPIIR-A1 (grout mix A1)	1		15.0	0.0020	15.5	0.0126	35
	2		15.8	0.0021	15.9	0.0161	40
	3		13.1	0.0024	15.7	0.0147	40
	4		16.1	0.0020	15.8	0.0223	43
	5		16.2	0.0019	17.1	0.0125	46
	Average		15.2	0.0021	16.0	0.0156	41
	C.O.V. (%)		8.4	9.7	4.1	25.7	-
GPIIR-A2 (grout mix A2)	1		15.5	0.0016	14.6	0.0095	54
	2		17.1	0.0019	15.3	0.0108	54
	Average		16.3	0.0018	14.9	0.0102	54

* indicates test before recalibration of test machine (affected stress only)

Table B.4. Summary of Results at High Strains for Self-Reinforced Prism Series (Proof-of-Concept Program)

Prism	**Specimen No.**		**Stress at 0.8% Strain (MPa)**	**Stress at 1% Strain (MPa)**	**Stress at 1.5% Strain (MPa)**	**Stress at 2% Strain (MPa)**	**Stress at 3% Strain (MPa)**
GPIR (type I prototype SR block)	1*		19.8	20.3	18.9	17.7	16.7
	2		17.9	17.8	17.7	17.0	14.0
	3		18.0	18.5	18.8	17.0	14.9
	All Prisms	Average	18.6	18.9	18.4	17.2	15.2
		C.O.V. (%)	5.7	6.9	3.7	2.2	9.0
	Prisms Tested After Recalibration	Average	18.0	18.2	18.2	17.0	14.5
GPIIR (type II prototype SR block)	1*		17.7	18.5	19.0	17.9	14.7
	2		16.1	17.0	17.5	-	-
	3		14.9	15.7	16.5	16.8	-
	4		18.2	18.4	18.3	16.8	13.6
	5		17.5	17.5	17.2	16.7	-
	All Prisms	Average	16.9	17.4	17.7	17.0	14.1
		C.O.V. (%)	7.9	6.5	5.4	3.5	-
	Prisms Tested After Recalibration	Average	16.6	17.2	17.4	16.8	13.6
		C.O.V. (%)	8.7	6.5	4.2	0.5	-
GPIIR-A1 (grout mix A1)	1		14.6	14.6	14.5	14.2	13.3
	2		15.4	15.8	15.8	15.7	-
	3		14.9	15.2	15.5	14.8	-
	4		15.4	15.0	15.8	15.4	-
	5		16.7	16.9	17.1	16.1	-
	Average		15.4	15.5	15.7	15.3	13.3
	C.O.V. (%)		5.1	5.8	6.0	5.0	-
GPIIR-A2 (grout mix A2)	1		14.5	14.5	13.9	13.8	13.1
	2		14.5	14.5	13.3	13.9	12.4
	Average		14.5	14.5	13.6	13.9	12.8

* indicates test before recalibration of test machine (affected stress only)

B.2. Detailed Data Plots: Proof-of-Concept Prism Program

The following figures contain individual stress-strain plots obtained directly from each prism test along with a final summary plot of the adjusted curves (according to the process described in Chapter 3) for each series.

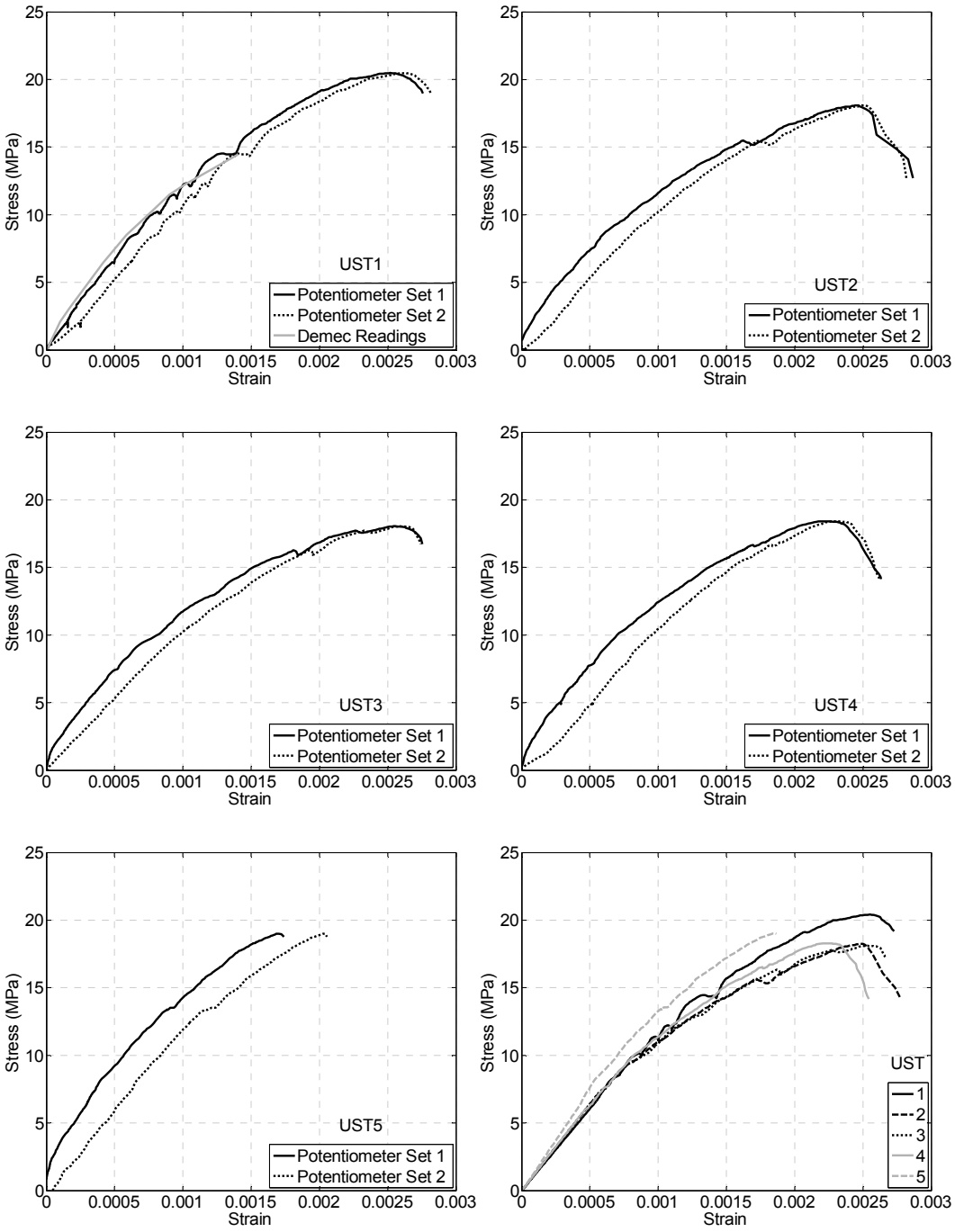

Figure B.1. Detailed Plots – Ungrouted, Stretcher Block (UST) Prisms

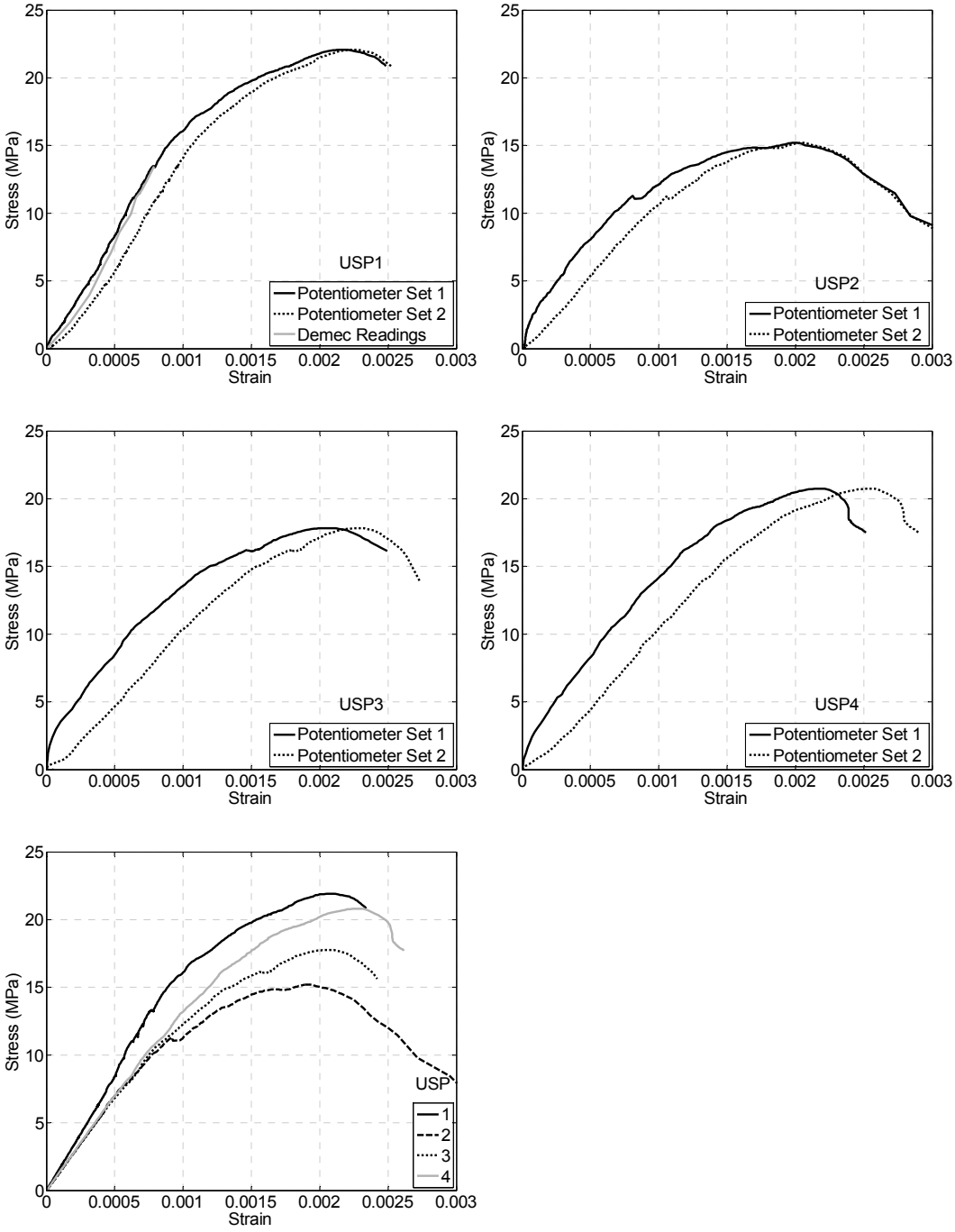

Figure B.2. Detailed Plots – Ungrouted, Splitter Block (USP) Prisms

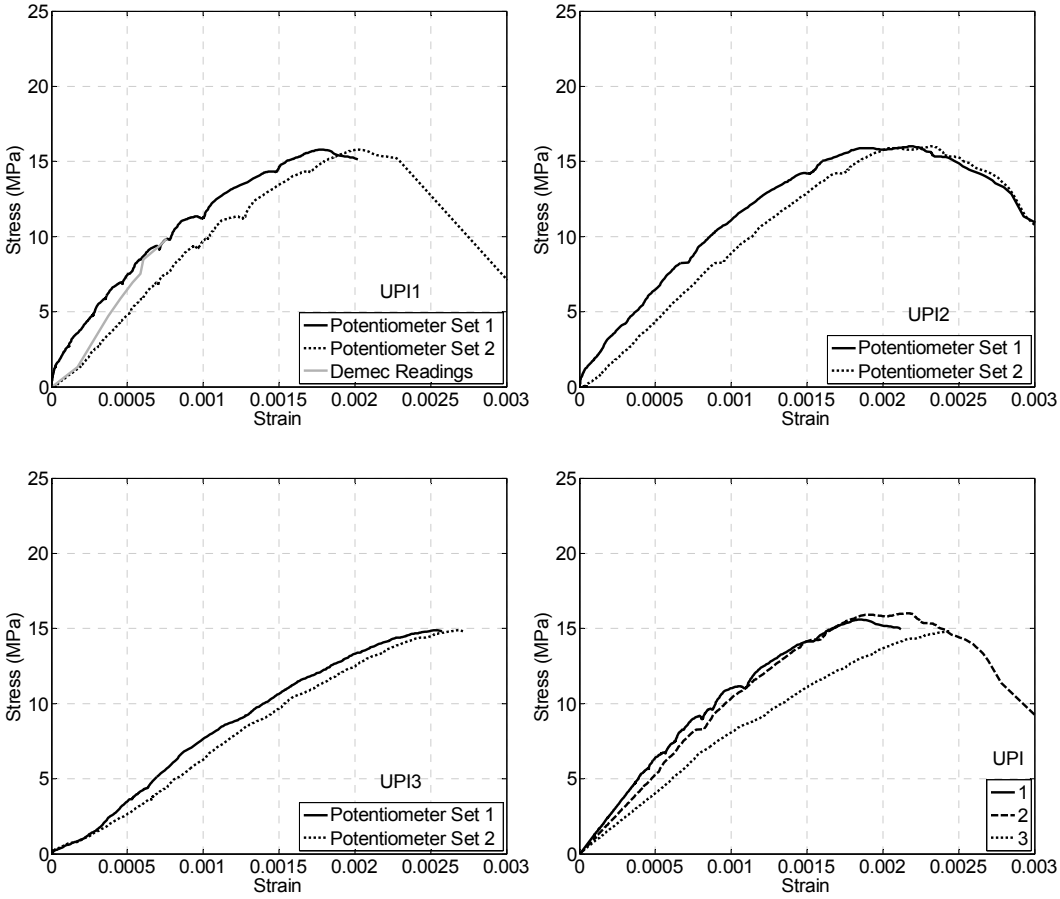

Figure B.3. Detailed Plots – Ungrouted, Type I Prototype Block (UPI) Prisms

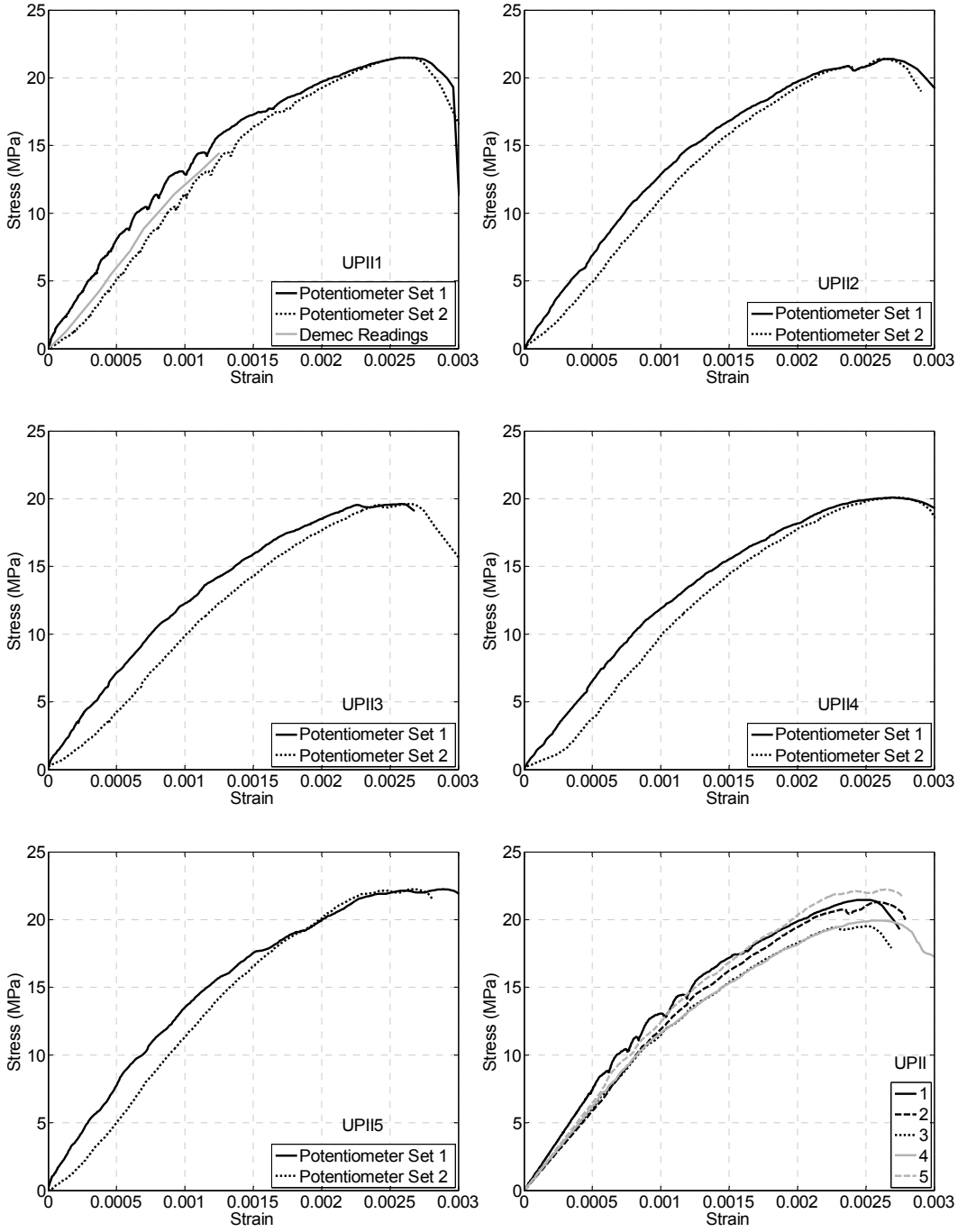

Figure B.4. Detailed Plots – Ungrouted, Type II Prototype Block (UPII) Prisms

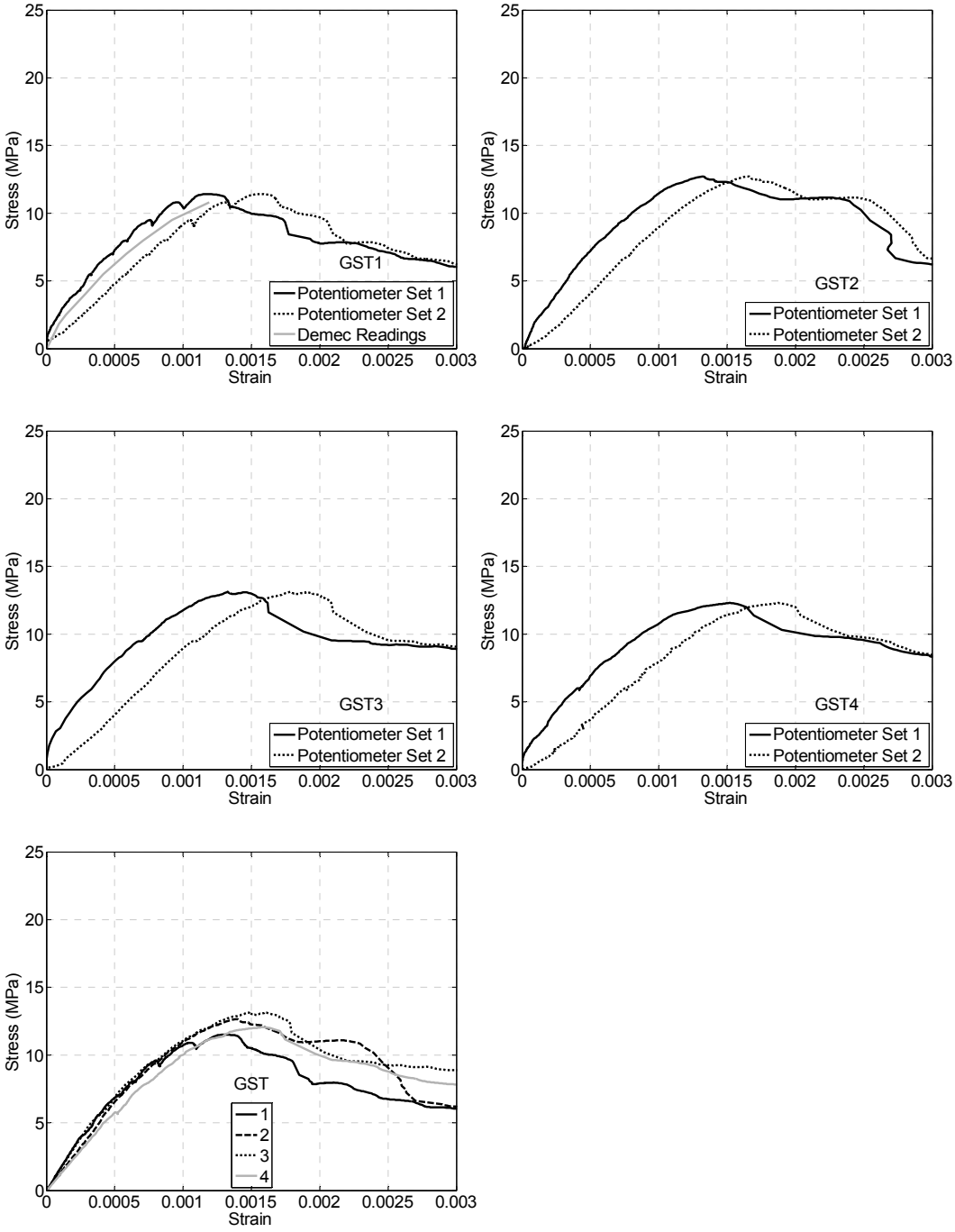

Figure B.5. Detailed Plots – Grouted, Stretcher Block (GST) Prisms

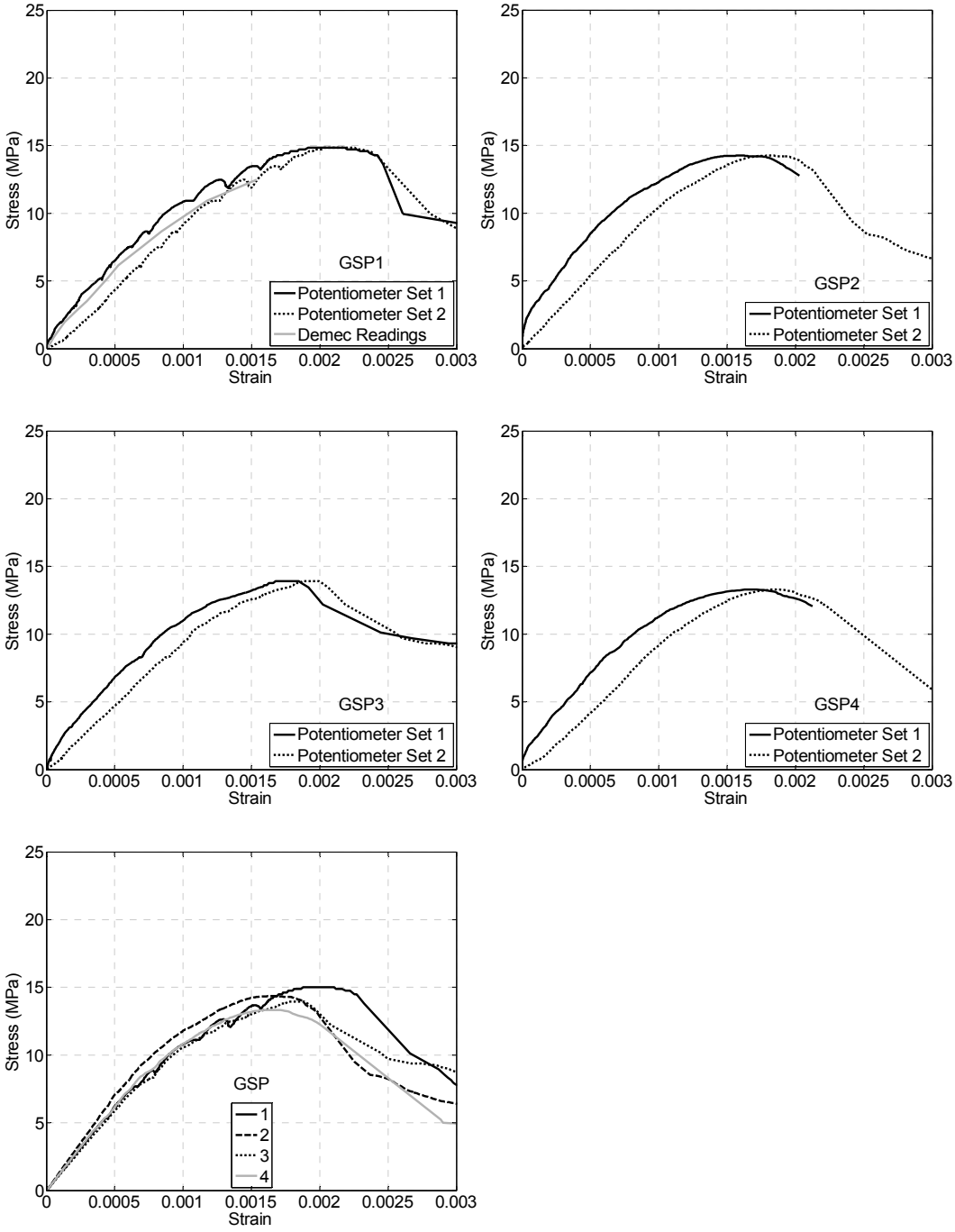

Figure B.6. Detailed Plots – Grouted, Splitter Block (GSP) Prisms

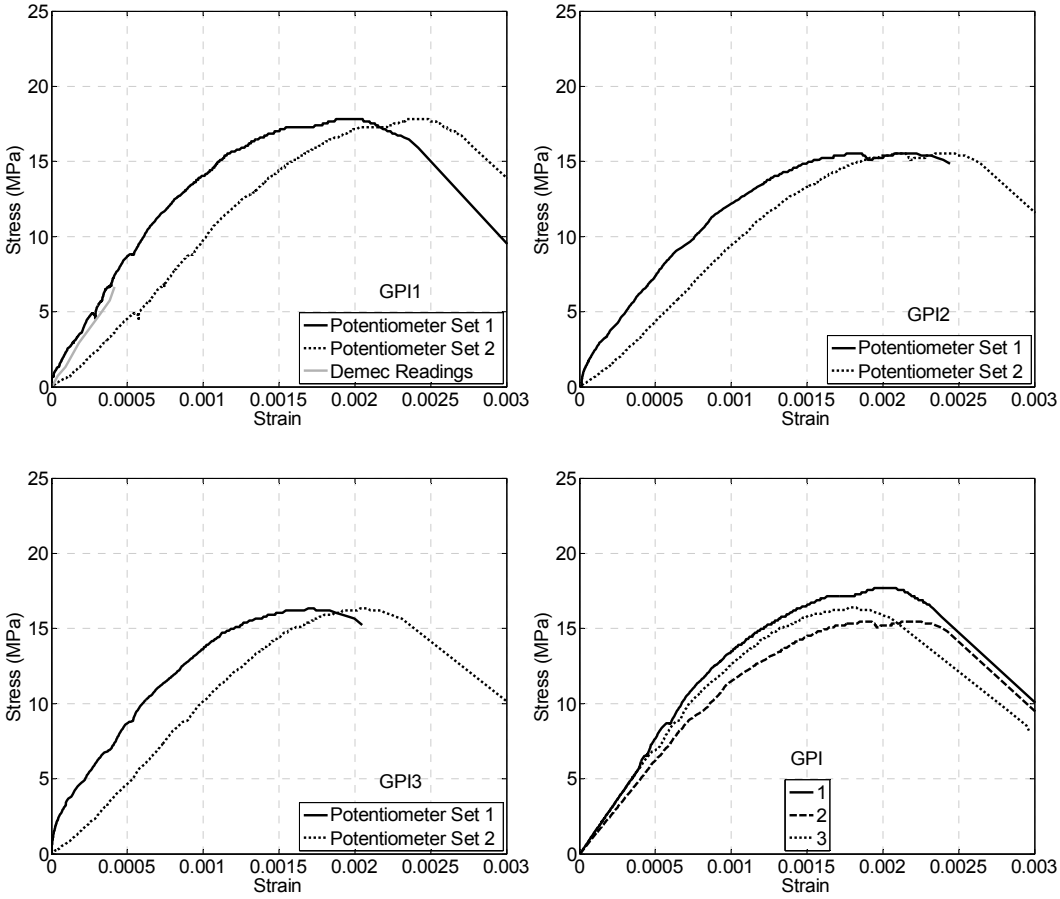

Figure B.7. Detailed Plots – Grouted, Type I Prototype Block (GPI) Prisms

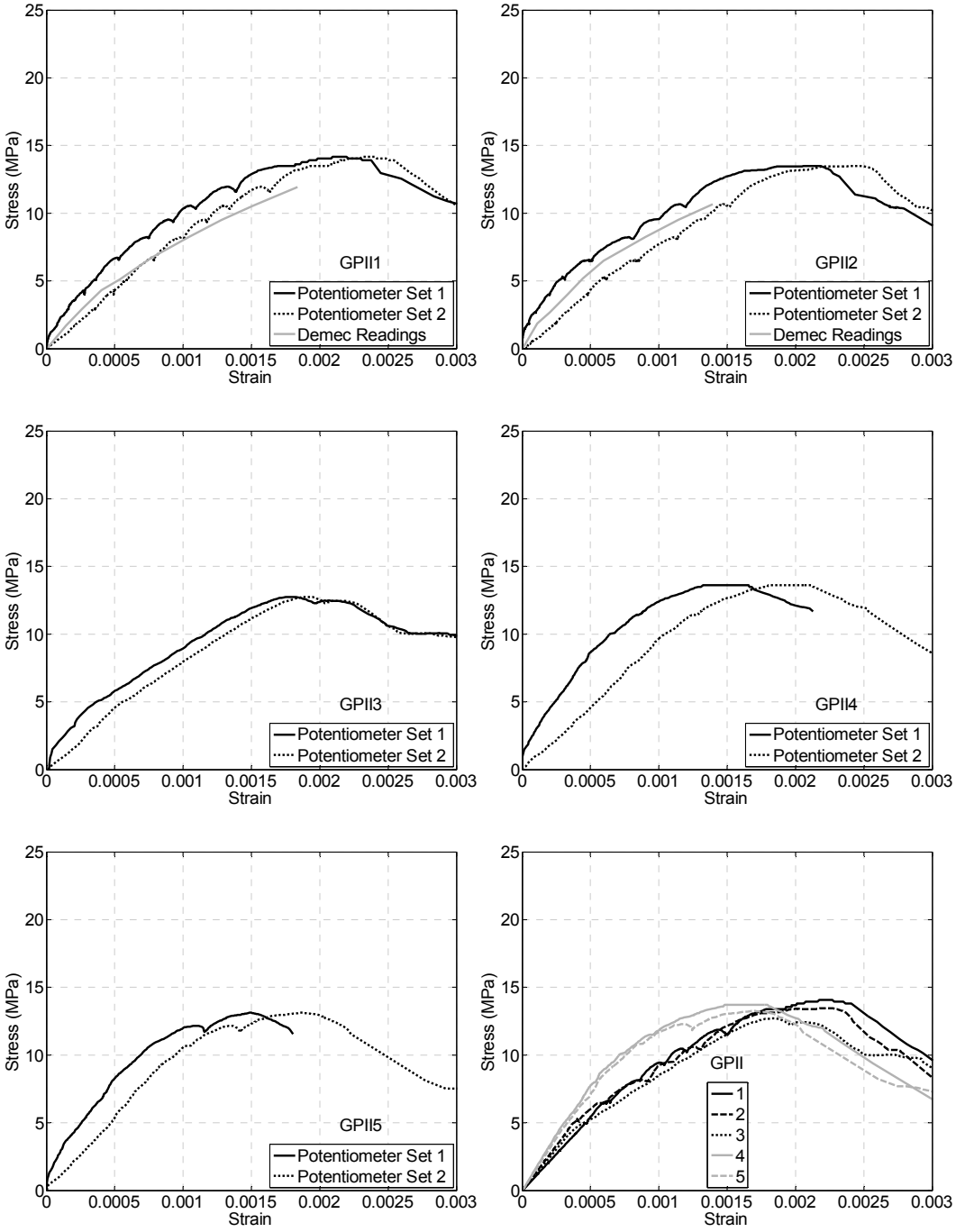

Figure B.8. Detailed Plots – Grouted, Type II Prototype Block (GPII) Prisms

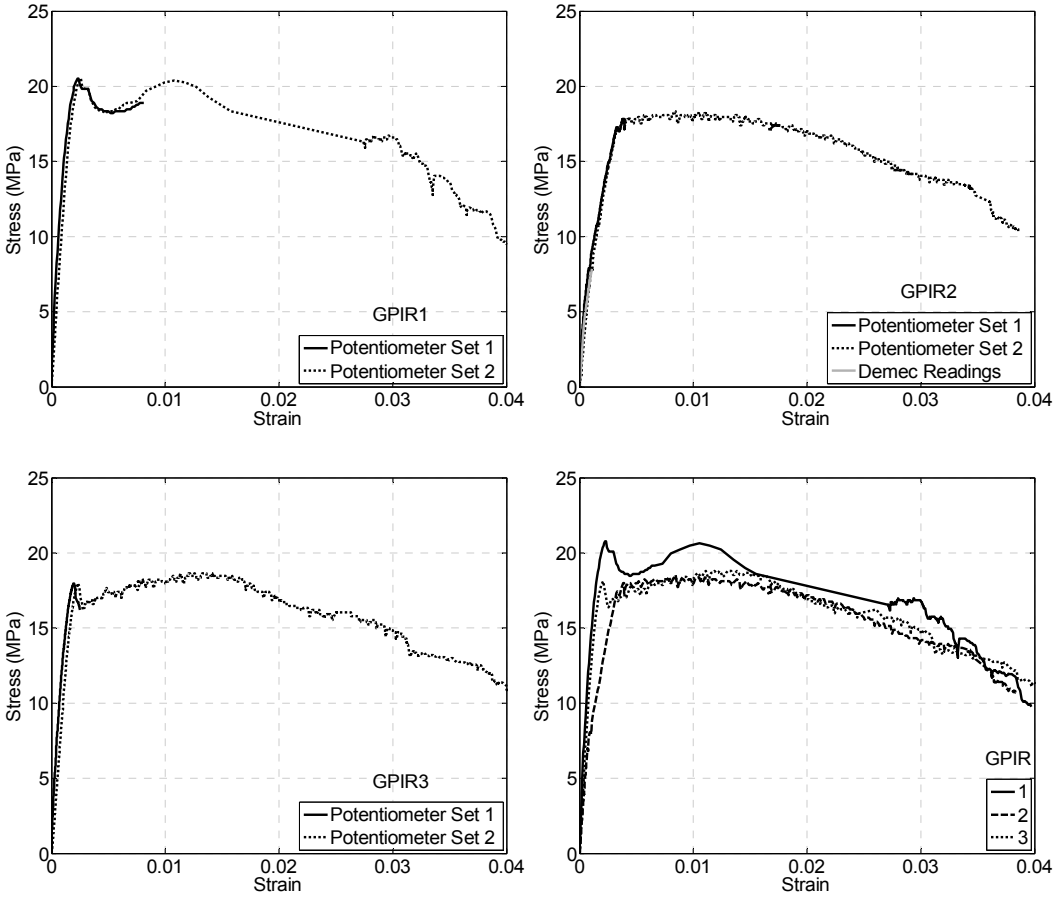

Figure B.9. Detailed Plots –Type I Self-Reinforced Block (GPIR) Prisms

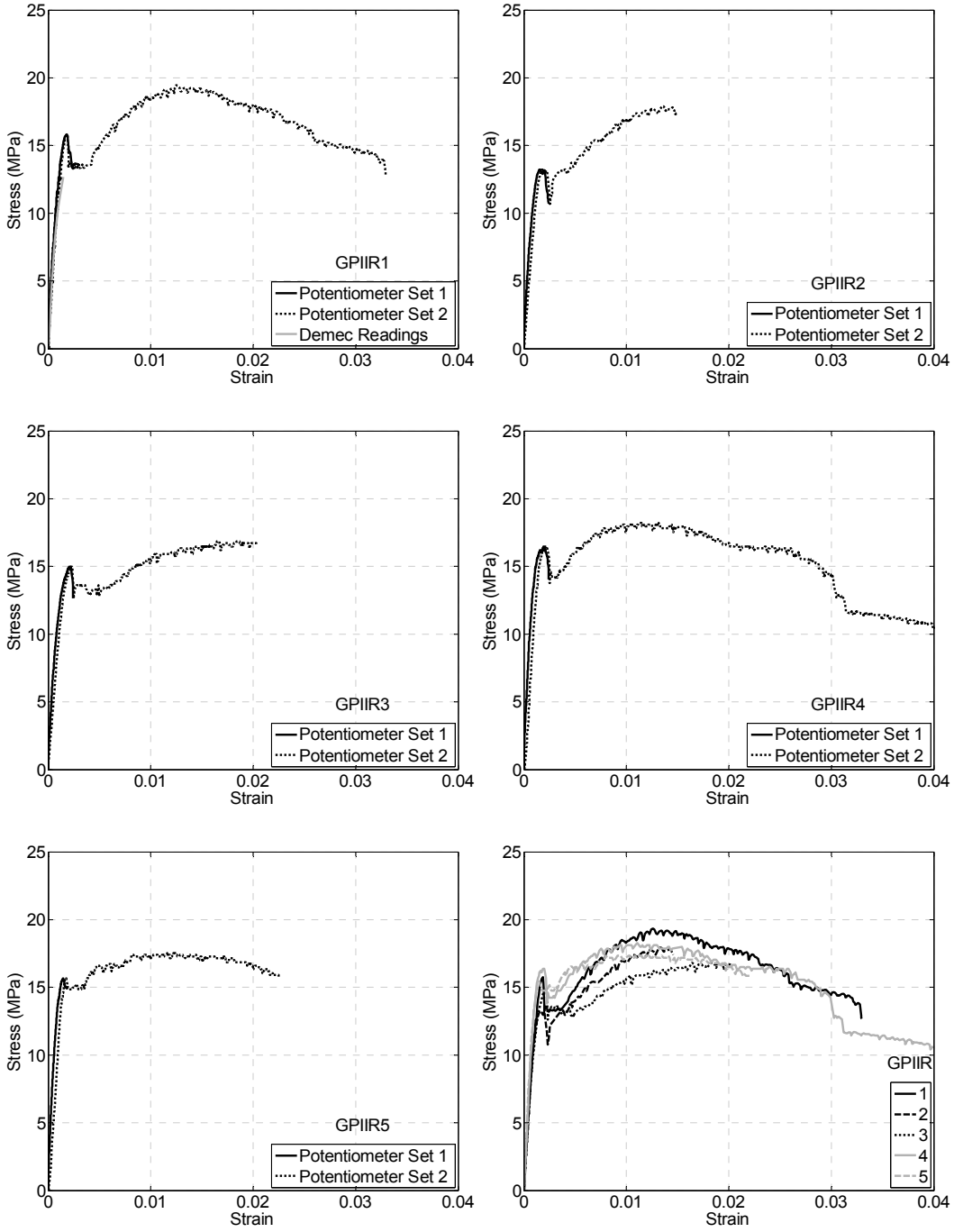

Figure B.10. Detailed Plots –Type II Self-Reinforced Block (GPIIR) Prisms

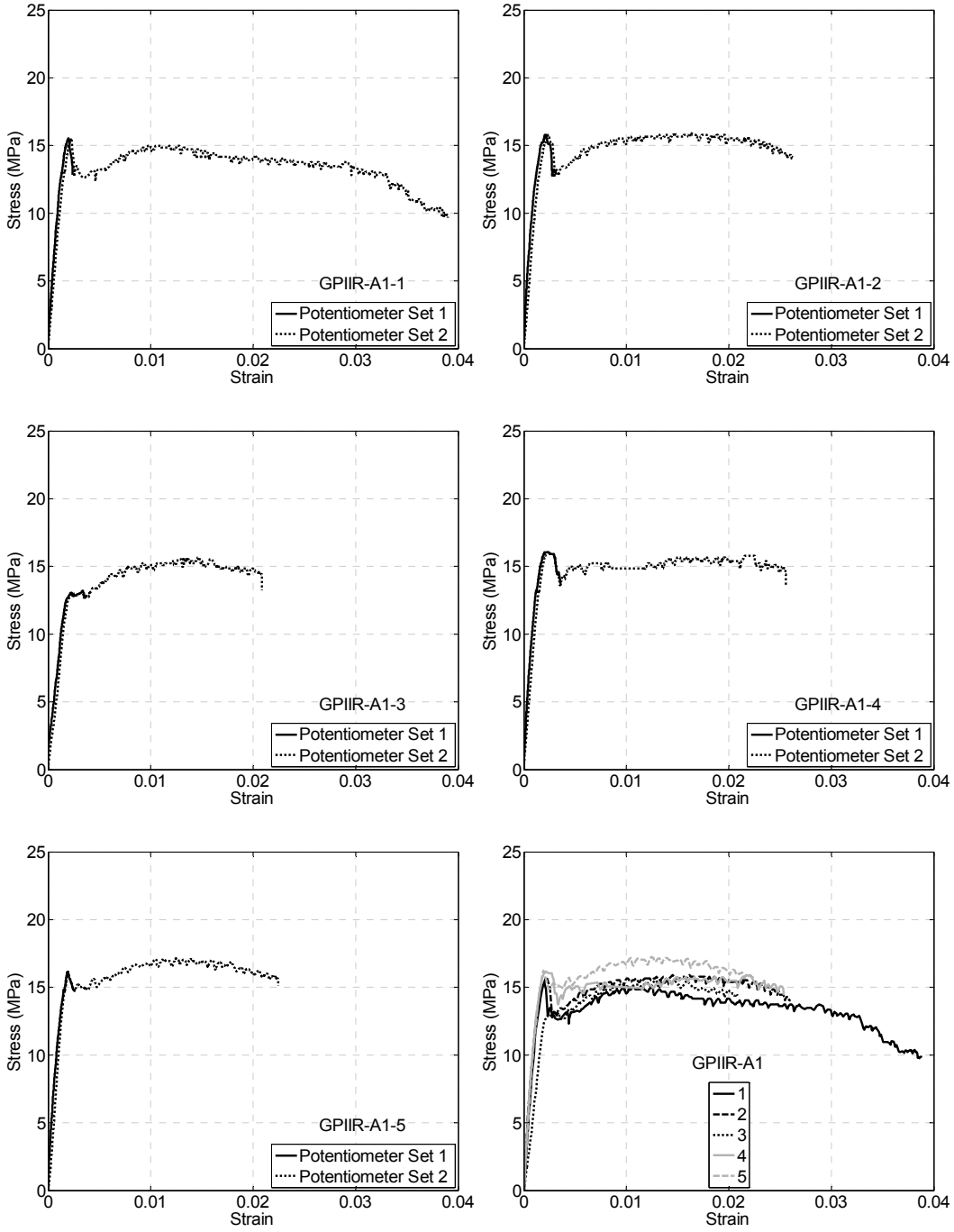

Figure B.11. Detailed Plots –Type II Self-Reinforced Block, Anti-Shrink Grout 1 (GPIR-A1) Prisms

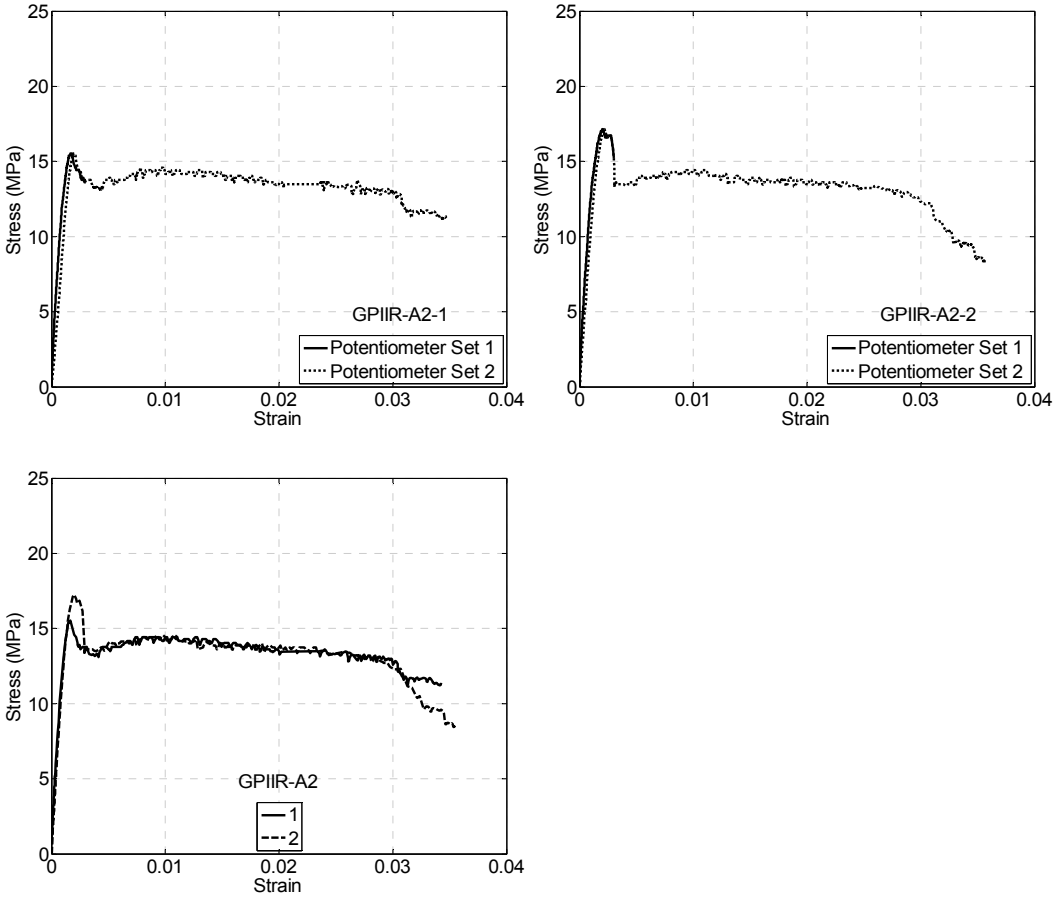

Figure B.12. Detailed Plots –Type II Self-Reinforced Block, Anti-Shrink Grout 2 (GPIR-A2) Prisms

B.3. Test Data: Prism Program Corresponding to Shear Walls

Table B.5. Summary of Results for Unreinforced Prism Series (Prism Program Corresponding to Shear Walls)

Prism	Specimen No.	Initial Peak Stress (MPa)	Strain at Peak Stress	Age of Specimen (Days)
UST (ungrouted, stretcher block)	1	16.86	0.0026	77
	2	18.51	0.0022	90
	3	19.65	0.0028	93
	Average	18.3	0.0025	87
	C.O.V. (%)	7.7	12.9	
UP (ungrouted, splitter block)	1	19.41	0.0025	83
	2	19.08	0.0028	86
	3	14.17	0.0023	93
	Average	17.6	0.0025	87
	C.O.V. (%)	16.7	10.9	
GST (grouted, stretcher block)	1	11.15	0.0013	83
	2	12.13	0.0013	89
	3	11.62	0.0012	93
	Average	11.6	0.0013	88
	C.O.V. (%)	4.2	5.8	
GP (grouted, splitter block)	1	14.31	0.0017	83
	2	12.77	0.0015	89
	3	13.33	0.0016	92
	Average	13.5	0.0016	88
	C.O.V. (%)	5.8	6.1	

Table B.6. Summary of Peak Stress Results for Self-Reinforced Prism Series (Prism Program Corresponding to Shear Walls)

Prism	Specimen No.	Initial Peak Stress (MPa)	Strain at Peak Stress	Second Peak Stress (MPa)	Strain at Second Peak Stress	Age of Specimen (Days)
GPR-WA (Steel Wire A)	1	13.0	0.0015	16.9	0.0240	85
	2	14.6	0.0015	18.2	0.0236	86
	3	14.0	0.0017	18.4	0.0242	91
	Average	13.9	0.0016	17.8	0.0239	87
	C.O.V. (%)	5.6	6.1	4.6	1.3	
GPR-WB (Steel Wire B)	1	12.3	0.0017	19.4	0.0244	84
	2	13.0	0.0016	20.0	0.0248	90
	3	12.7	0.0016	18.6	0.0223	91
	Average	12.6	0.0016	19.3	0.0238	88
	C.O.V. (%)	2.7	5.6	3.5	5.7	

Table B.7. Summary of Results at High Strains for Self-Reinforced Prism Series (Prism Program Corresponding to Shear Walls)

Prism	**Specimen No.**	**Stress at 0.8% Strain (MPa)**	**Stress at 1% Strain (MPa)**	**Stress at 1.5% Strain (MPa)**	**Stress at 2% Strain (MPa)**	**Stress at 3% Strain (MPa)**
GPR-WA (Steel Wire A)	1	11.6	13.2	15.7	16.7	12.0
	2	14.5	15.5	17.1	18.3	0 (failed)
	3	14.1	14.8	16.8	17.9	14.6
	Average	13.4	14.5	16.5	17.6	-
	C.O.V. (%)	11.7	7.9	4.6	4.6	-
GPR-WB (Steel Wire B)	1	13.0	15.2	18.0	19.3	15.8
	2	13.1	14.9	17.7	19.4	16.7
	3	12.7	14.0	16.9	18.2	16.6
	Average	13.0	14.7	17.5	19.0	16.4
	C.O.V. (%)	1.6	3.9	3.3	3.5	3.0

B.4. Detailed Data Plots: Prism Program Corresponding to Shear Walls

The following figures contain individual stress-strain plots obtained directly from each prism test along with a final summary plot of the adjusted curves (according to the process described in Chapter 3) for each series.

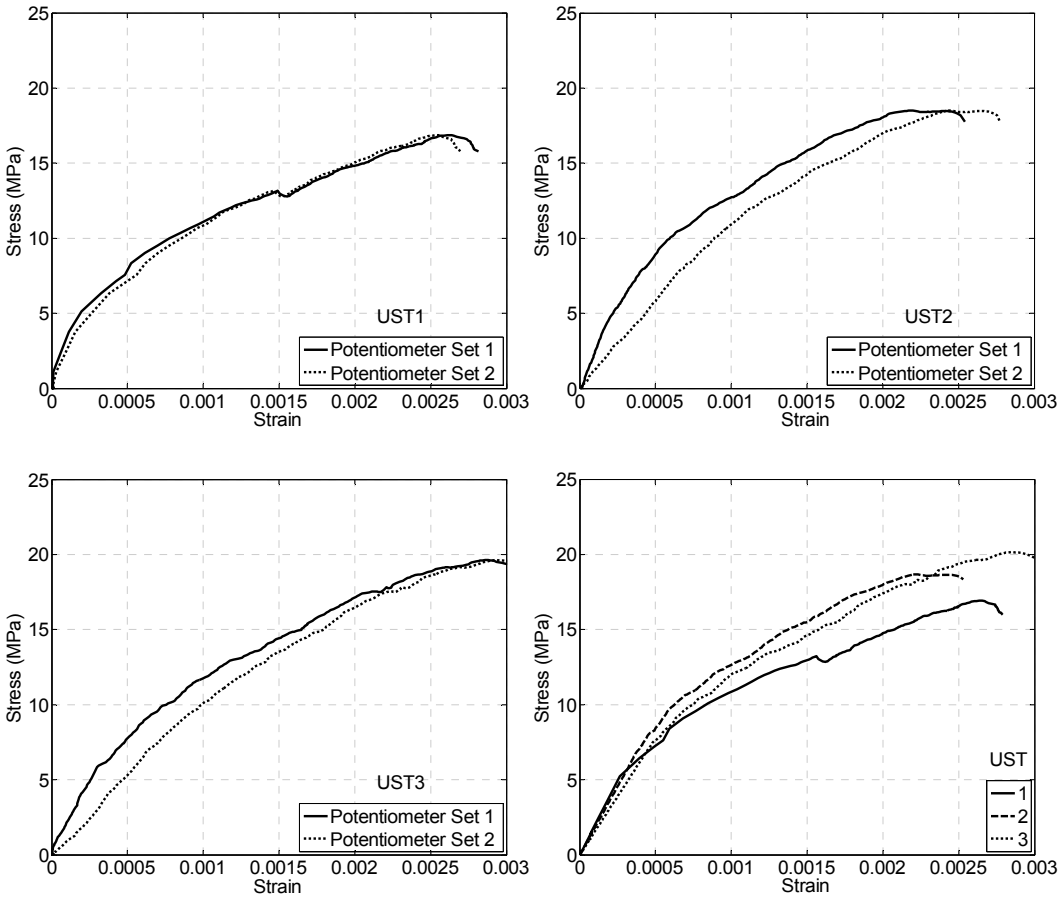

Figure B.13. Detailed Plots – Ungrouted, Stretcher Block (UST) Prisms

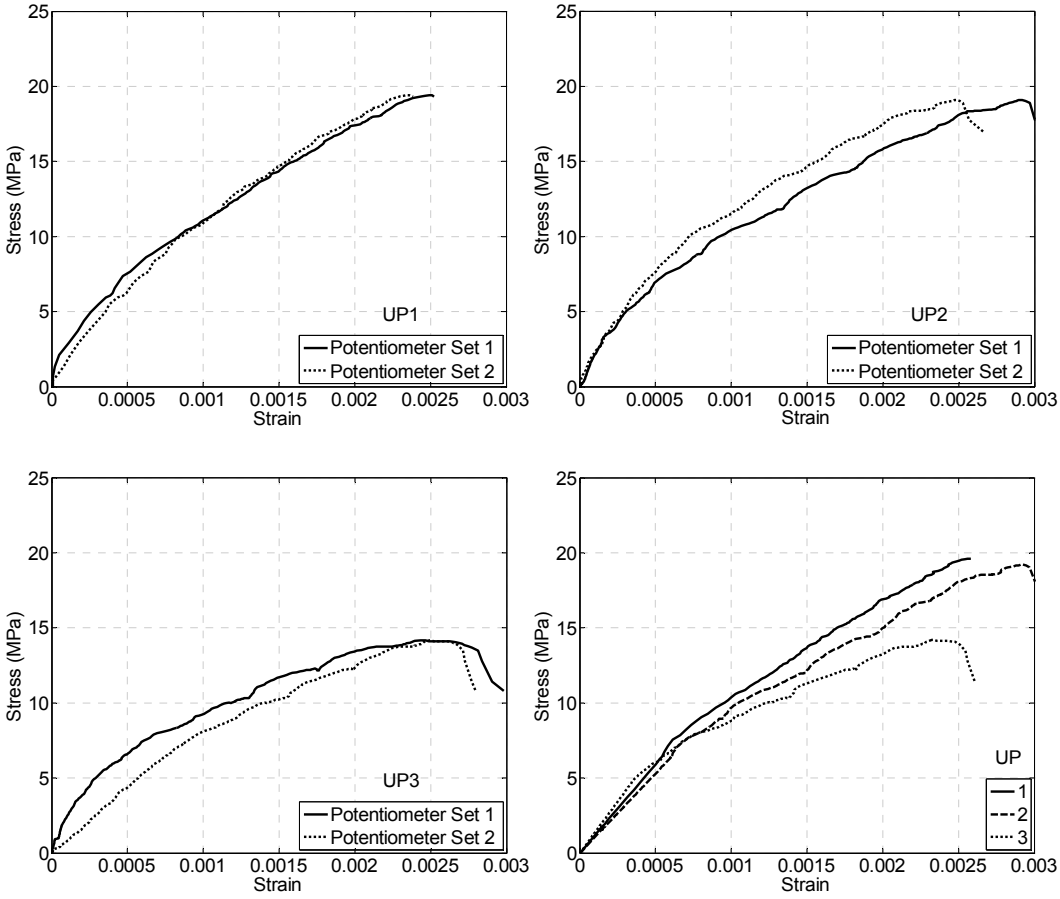

Figure B.14. Detailed Plots – Ungrouted, Prototype Block (UP) Prisms

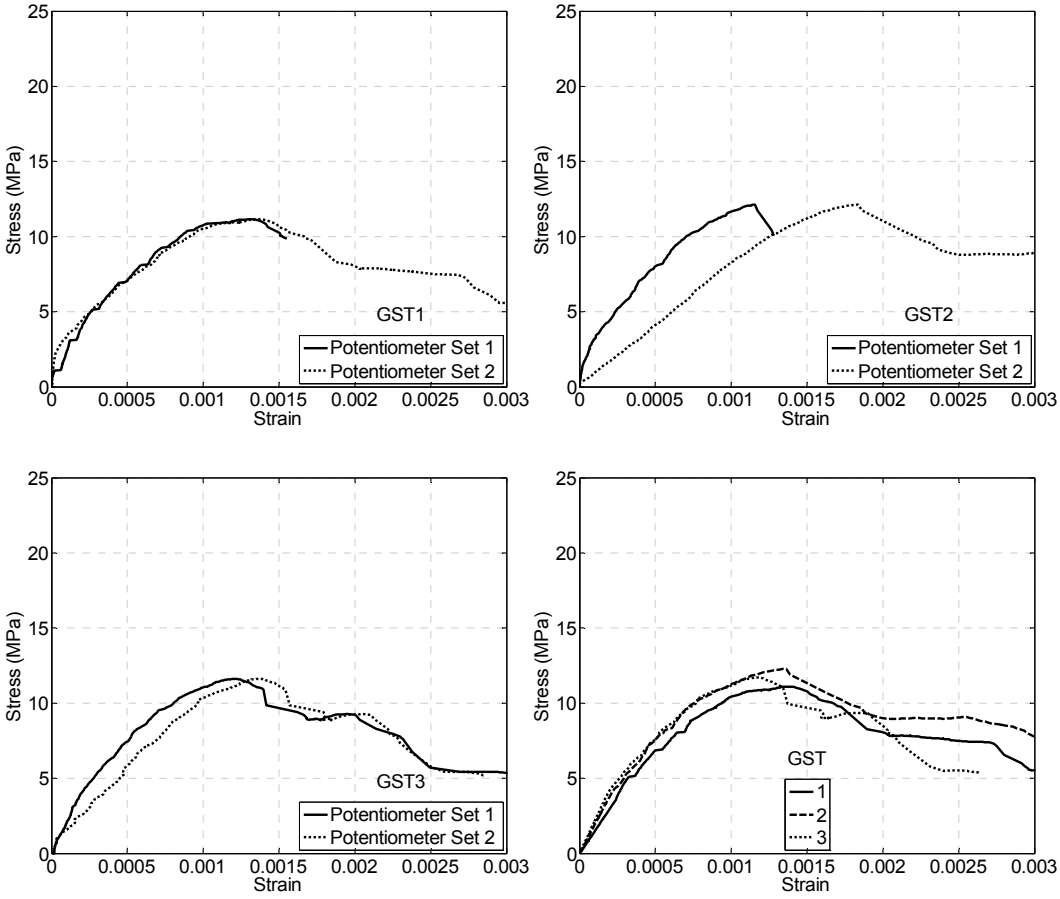

Figure B.15. Detailed Plots – Grouted, Stretcher Block (GST) Prisms

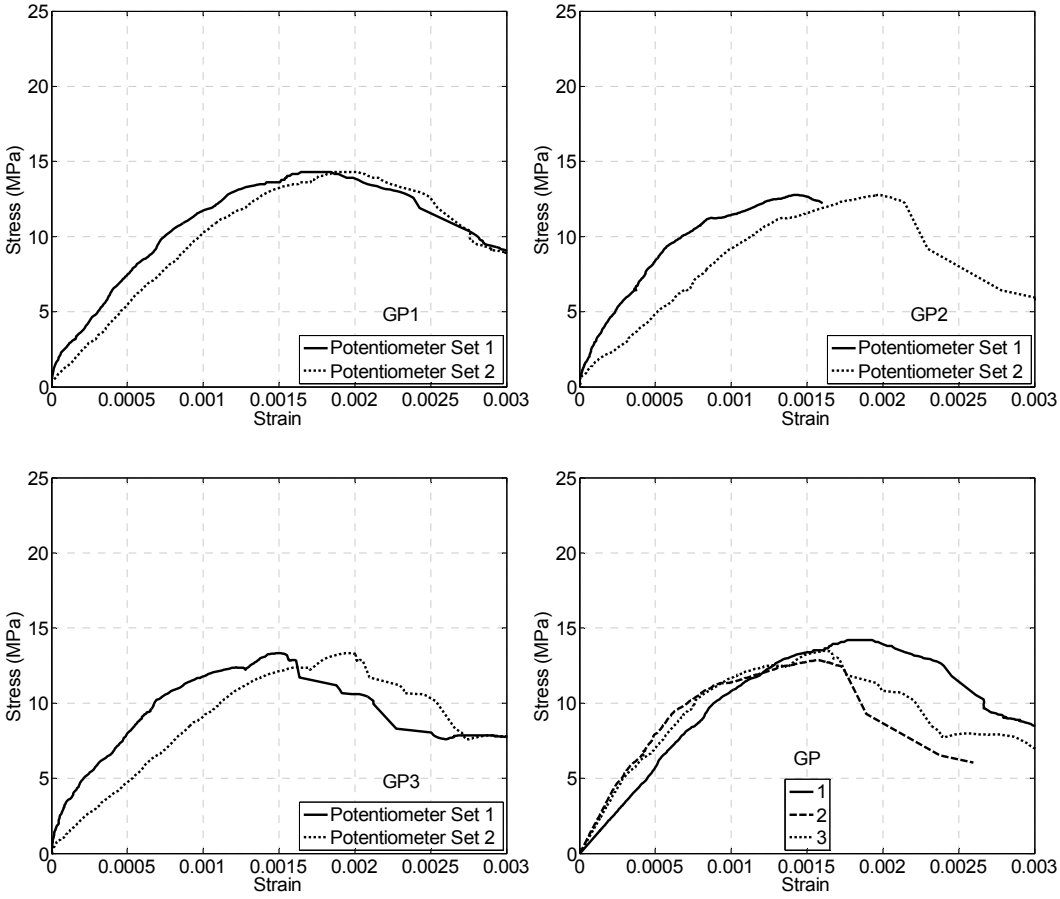

Figure B.16. Detailed Plots – Grouted, Prototype Block (GP) Prisms

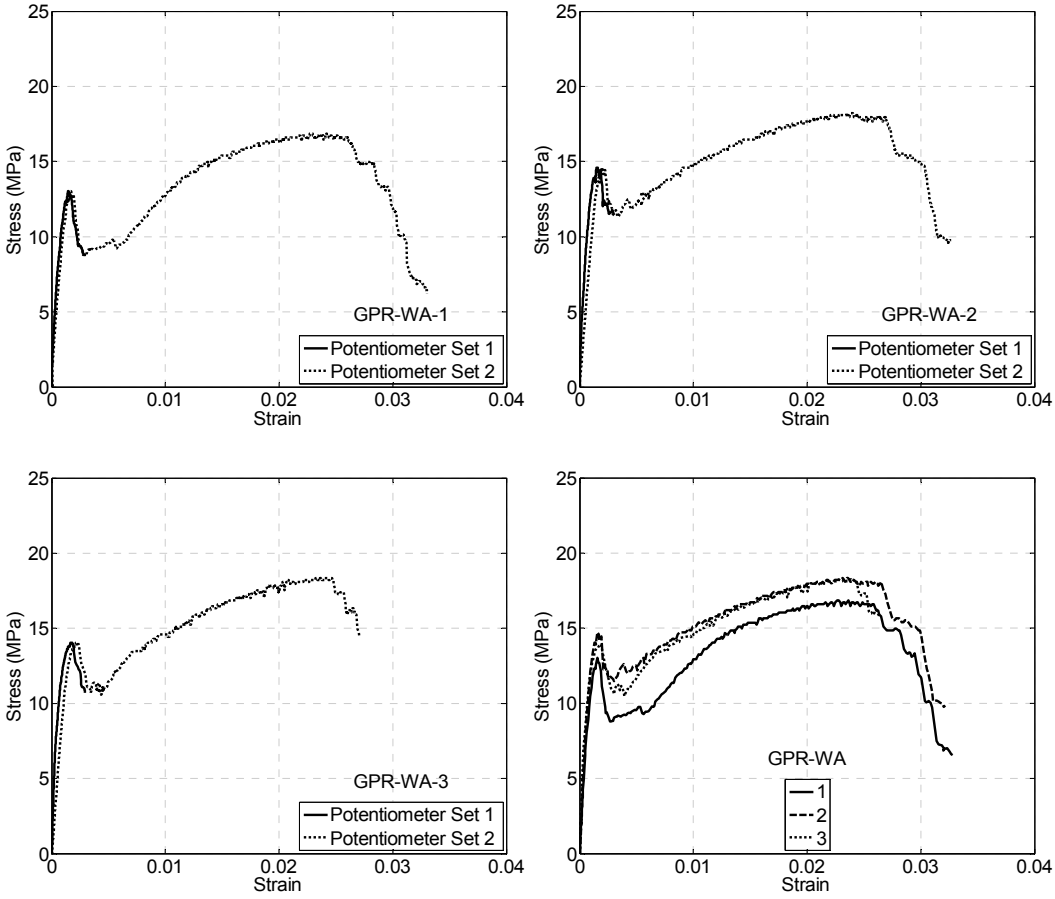

Figure B.17. Detailed Plots – Self-Reinforced Block, Type WA Spiralled-Wire (GPR-WA) Prisms

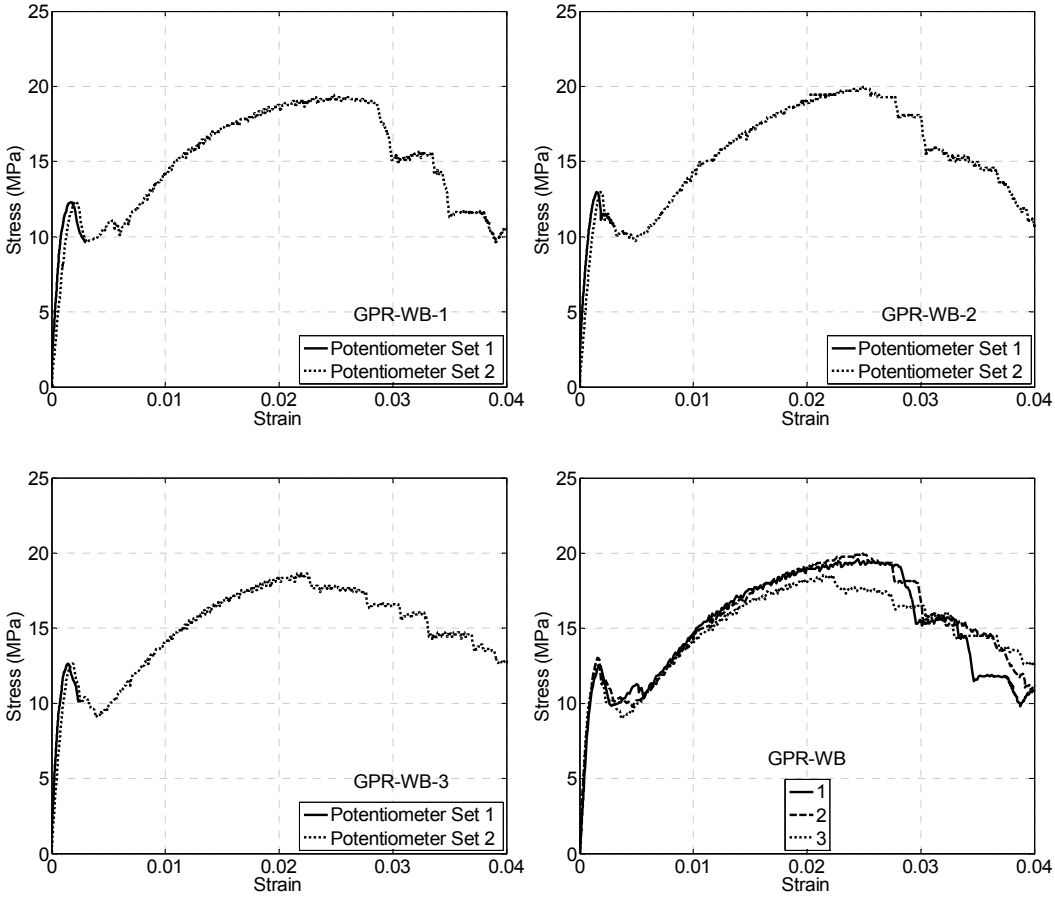

Figure B.18. Detailed Plots – Self-Reinforced Block, Type WB Spiralled-Wire (GPR-WB) Prisms

APPENDIX C
EQUATIONS FOR WALL CAPACITY PREDICTIONS

Units used for all of the following equations were N, mm and MPa.

C.1. Flexural Capacity

The following equations were used to predict the flexural strength of each of the shear walls. An iteration process was used to locate the position of the neutral axis of each wall by defining a strain criterion (maximum compressive strain of masonry) and varying the opposing (tensile) strain until equilibrium of axial load was achieved. The sum of moments from the compressive (masonry and reinforcing steel) and tensile (reinforcing steel) forces at equilibrium provided the total bending moment used to calculate the lateral load capacity of the cantilever wall.

$$P = C_m + C_s - T_s$$

C_m was derived using the trapezoid rule by dividing the compression zone of the wall into several increments. The stress for each increment was taken as that associated with the compressive masonry strain at the midpoint of the increment (assuming plane sections remain plane) from the experimental stress-strain data for the confined material (from prism tests, Figure 6.1 a)).

$C_s = \sum A_s f'_s$ where f'_s is taken as the stress associated with the compressive steel strain (assuming plane sections remain plane) from the experimental stress-strain curve for the reinforcing steel (Figure 6.1 b)).

$T_s = \sum A_s f_s$ where f_s is taken as the stress associated with the tensile steel strain (assuming plane sections remain plane) from the experimental stress-strain curve for the reinforcing steel (Figure 6.1 b)).

$$M_u = C_m \left(\frac{l_w}{2} - \frac{c}{2}\right) + \sum A_s f_s \left(d_i - \frac{l_w}{2}\right)$$

$$F_{lateral} = \frac{M_u}{h_w}$$

Where:

P axial load applied to wall
C_m compression force in the masonry (cross-section of the wall)
C_s compression force in the supported vertical reinforcement
T_s tensile force in the vertical reinforcement
A_s area of vertical reinforcement

f'_s compressive stress in vertical reinforcement
f_s tensile stress in vertical reinforcement
M_u moment resistance at defined maximum compression strain of masonry
l_w length of wall
c depth of neutral axis
d_i distance to the vertical reinforcement from the compression fibre
$F_{lateral}$ lateral force carrying capacity of the wall
h_w height of wall

C.2. Shear Capacity

C.2.1. Equations from CSA S304.1 (CSA 2004a)

$V_r = V_m + V_s$

Limited by,
$V_r \leq 0.4\sqrt{f'_m} b_w d_v \gamma_g$

Where,
$V_m = (v_m b_w d_v + 0.25 P_d)\gamma_g$

$V_s = \left(0.60 A_v f_y \frac{d_v}{s}\right)$

$v_m = 0.16\left(2 - \frac{M_f}{V_f d_v}\right)\sqrt{f'_m}$ where, $0.25 \leq \frac{M_f}{V_f d_v} \leq 1$

And,
$\gamma_g = 1$ for fully grouted masonry

$d_v = 0.8 l_w$ when flexural reinforcement distributed along length

10.16.5.3.1:
"within the potential plastic hinge region the factored shear resistance contributed by the masonry and the axial compressive load shall be reduced by one half."

C.2.2. Equations from Paulay and Priestley (1992)

$V_r = V_m + V_s$

Limited by,
$v_i = \frac{V}{td} \leq 0.15 f'_m$ and $v_i \leq 1.8$ MPa In potential plastic hinge regions and,

$v_i \leq 0.2 f'_m$ and $v_i \leq 2.4$ MPa For other regions

Where,

$V_m = v_m A_v$

$A_v = 0.8 l_w t$ (for a fully grouted wall)

In all regions except potential plastic hinges:

$v_m = 0.17\sqrt{f'_m} + 0.3\left(P_u/A_g\right)$

Limited by,

$v_m \leq 0.75 + 0.3\left(P_u/A_g\right)$ and $v_m \leq 1.3$ MPa

In plastic hinge regions (conservative recommendations):

$v_m = 0.05\sqrt{f'_m} + 0.2\left(P_u/A_g\right)$

Limited by,

$v_m \leq 0.25 + 0.2\left(P_u/A_g\right)$ and $v_m \leq 0.65$ MPa

And,

$V_s = \frac{A_{sh} f_{yh} d}{s_h}$

$d = 0.8 l_w$

Limited by,

$v_i = \frac{V}{b_w d} \leq 0.15 f'_m$ and $v_i \leq 1.8$ MPa In potential plastic hinge regions and,

$v_i \leq 0.2 f'_m$ and $v_i \leq 2.4$ MPa For other regions

Where:

V_r	total shear strength of wall
V_m	shear strength of wall provided by axial loading and masonry strength
V_s	shear strength of wall provided by shear (horizontal) reinforcement
v_i	maximum total shear stress on wall
v_m	shear strength (stress capacity) of masonry
A_v	effective shear area of wall
f'_m	compressive strength of masonry
P_u	applied axial load
A_g	gross cross-sectional area of the wall
A_{sh}	cross-sectional area of shear (horizontal) reinforcement
l_w	length of wall
t or b_w	thickness of wall
f_{yh}	yield strength of shear (horizontal) reinforcement
s_h	spacing of shear (horizontal) reinforcement